The Search for Circumbinary Exoplanets with the BEBOP Radial Velocity Survey

Matthew R. Standing

UNIVERSITY OF BIRMINGHAM

A thesis presented for the degree of
Doctor of Philosophy

School of Physics and Astronomy
College of Engineering and Physical Sciences
University of Birmingham
July 2022

Abstract

The Search for Circumbinary Exoplanets with the BEBOP Radial Velocity Survey

Matthew R. Standing

This thesis is about the field of exoplanets, with a particular focus on the search for circumbinary exoplanets with Radial Velocity (RV) observations. Chapter 1 introduces the field of exoplanet science, provides an overview of relevant techniques for exoplanet detection, discusses what we have learnt about exoplanets through their demographics, and provides background information on circumbinary exoplanets. Chapter 2 covers the data analysis techniques that were utilised in this work. It introduces Bayesian statistics and nested sampling, explains the `Kima` package used to fit Keplerian signals to RV data in this work, best practises in its use, and how planetary parameters are obtained through this analysis. Chapter 3 describes my contribution to the analysis of the RV data for the star HD-16417 (λ^2 Fornacis) and includes the full paper. In this work we constrain the parameters of a known planet host star, and in turn update the planet's parameters. Chapter 4 provides a detailed description of the Binaries Escorted By Orbiting Planets (BEBOP) survey, the main topic of work in this thesis. Previous attempts to discover circumbinary planets with RV observations are discussed, before describing how the BEBOP survey is carried out. In Section 4.3, I present my work on the calculation of detection limits for the BEBOP survey, along with the calculation of circumbinary planet occurrence rates, and present some preliminary candidate circumbinary signals. I find the BEBOP survey is sensitive to planets with masses down to that of Saturn and Neptune, and that our circumbinary planet occurrence rates agree with those from other works, including those of gas giants around single stars. Chapter 5 details the detection of the first circumbinary planet with ground-based RV observations, along with my contributions to this work. We are able to independently detect the circumbinary planet Kepler-16b, confirm its orbital parameters, and place constraints on the presence of additional planets in the system. In Chapter 6, I describe the first discovery of a circumbinary planet with RV observations alone, BEBOP-1c. This second planet in the system has a mass of 0.2 M_J and an orbital period of 215 days. We are also able to place an upper limit on the smaller inner transiting planet's mass at 23.6 $M_\oplus$ with 99% confidence. In this chapter I also describe an attempt to view the signal of the secondary star in the binary star system. Finally, in Chapter 7, I

describe additional contributions I have made to other bodies of work during my PhD, and conclude the thesis while discussing future avenues of work to increase our sensitivity to circumbinary planets with RV observations.

Acknowledgements

I would first like to thank my supervisor Amaury Triaud, whose guidance and vast knowledge on the subject made all this work possible. Thank you for giving me the opportunity to return to academia, instilling in me your passion for exoplanets, and placing your faith in me to lead such an exciting area of research. I will follow your advice for years to come, where I hope to stay in touch and continue trading results.

Thank you to my Mum and Dad for supporting me with every decision I have made. Thank you for always pushing me, and also reminding me to take breaks. Thank you for letting me and Idoia escape COVID to the Welsh country-side through both lock-downs. Without you none of this would be possible, you made me who I am today.

Thank you to all my family for supporting me and always showing interest in my work.

Thanks to all the Sun, Stars, and Exoplanets group at the University of Birmingham and beyond. Thank you to the postdocs and staff: Martin, Lalitha, Daniel, Ted, Warrick, Tanda, Bill, Guy, Andrea, and Lou for all your help, and for always finding time to answer my questions. Thanks to my fellow PhD students: Vedad, Eddie, Alex D. (big), Alex L. (little), Walter, Oli, Ben, Emma, Lindsey, Emily, George, Tom, Mat, and Sanyia. You all made the office such a fun and welcoming place to be. Thanks for all the lunchtime debates, bake-offs, fruit and biscuit competitions, Wok fresh and Seoul Plaza journeys, board game nights and D&D sessions. I hope that we'll be able to stay in touch.

I would also like to thank all the collaborators I was lucky enough to get the chance to work with during my PhD, João Faria, David Martin, and Neda Heidari.

Thanks to all my friends from Cardigan and Birmingham, my Cardiff coursemates, housemates, and squash friends for helping me to take my mind off work after a long day with a few games of Warzone/Battlefield, board games, or a few pints.

Thank you to all of those that helped and supported me on my many observing runs in France and Chile, including remotely. Thank you to the observatory staff at La Silla, Paranal, OHP and ASTEP, also to the observers including the SPECULOOS team for showing me the ropes and helping me with any questions/problems I had.

I would like to acknowledge the Science Technology and Facilities Council (STFC) for funding my research, and thank you to my thesis committee.

Finally, and perhaps most importantly, I'd like to thank Ido. Thank you for supporting me through the difficult times, coming with me to sunny Birmingham, reading this whole thesis, listening to every talk

(several times), and letting me explain my work and coding problems to you (you should get an honorary degree). Thank you for always being there to love and support me through the highs and lows. Thank you for helping me get through this and reminding me to go outside every once in a while. This PhD has been an adventure, and no adventure would be complete without you by my side, I love you.

Contents

Abstract v

Acknowledgements vii

Contents vii

List of Abbreviations xii

1 Introduction to exoplanets 1

1.1 What is an exoplanet? . . . 2

1.1.1 How are exoplanets named? . . . 2

1.1.2 Leading questions of the field . . . 3

1.2 Detection methods . . . 7

1.2.1 Planetary Orbital motion . . . 8

1.2.2 The Radial Velocity method . . . 10

1.2.3 The Transit method . . . 17

1.2.4 Other methods . . . 19

1.3 Observed patterns and demographics of exoplanets . . . 21

1.3.1 Planet types . . . 22

1.3.2 Exoplanet demographics . . . 23

1.3.3 Planet formation . . . 27

1.3.4 Planet migration . . . 30

1.4 Circumbinary exoplanets . . . 31

1.4.1 Circumbinary orbital stability . . . 33

1.4.2 Observational challenges . . . 34

1.4.3 Circumbinary planet demographics . . . 35

1.4.4 Planets in post-main sequence binaries . . . 37

2 Analysis of RV data 39

2.1 Bayesian statistics . . . 39

2.1.1 Nested Sampling . . . 40

2.2 The `kima` package . . . 42

2.2.1 Using `kima` to search for planetary RV signals . . . 43
2.2.2 Bayesian model comparison . . . 44
2.2.3 Testing `kima` . . . 45
2.2.4 Improvements to `kima` . . . 48
2.2.5 Best practices when using `kima` . . . 49
2.2.6 Obtaining planetary parameters from posterior samples . . . 55

3 Updating Planetary Parameters **59**
3.1 My contribution to the paper . . . 59
3.2 TESS asteroseismology of the known planet host star λ^2 Fornacis . . . 60
3.3 Time series preparation . . . 61
3.4 Modeling λ^2 For . . . 61
3.5 Radial velocity analysis of the λ^2 For system . . . 64
3.5.1 Updated characteristics λ^2 For b . . . 64
3.5.2 Additional radial velocity variability . . . 65
3.6 Discussion and conclusions . . . 66

4 BEBOP **71**
4.1 Previous circumbinary planet searches . . . 71
4.2 The BEBOP Survey . . . 72
4.2.1 Observing strategy . . . 74
4.2.2 Data sources . . . 78
4.2.3 Data quality control . . . 82
4.2.4 Target data-sheets . . . 83
4.3 Detection limits for RV surveys . . . 88
4.3.1 Calculating detection limits with `kima` . . . 89
4.3.2 BEBOP II: Sensitivity to sub-Saturn circumbinary planets using radial-velocities 91
4.3.3 Description of our observational protocol and data collection . . . 92
4.3.4 RV Analysis with `kima` . . . 94
4.3.5 Methods & Simulations . . . 94
4.3.6 Results and Discussion . . . 98
4.3.7 Conclusions . . . 101
4.3.8 Post-Keplerian effects . . . 106
4.3.9 Detection limits for the entire BEBOP south survey . . . 108
4.4 Candidate circumbinary planet signals . . . 114

5 Detection of Kepler-16b with RV observations **117**
5.1 My contribution to the paper . . . 117

5.2 BEBOP III. Observations and an independent mass measurement of Kepler-16 (AB) b – the first circumbinary planet detected with radial velocities . . . 119
5.3 Velocimetric observations on Kepler-16 . . . 121
5.4 Modelling of the radial velocities . . . 121
5.5 Discussion . . . 124

6 The BEBOP-1 system **129**
6.1 The ESPRESSO Pipeline . . . 131
6.1.1 FWHM larger in ESPRESSO compared to HARPS . . . 131
6.2 Detection of circumbinary planet TOI-1338/BEBOP-1c . . . 132
6.2.1 The First Circumbinary Planet Discovered with Radial Velocities . . . 133
6.2.2 Supporting material . . . 149
6.2.3 Collected observations . . . 149
6.2.4 Modeling of the data . . . 154
6.2.5 Stellar activity . . . 158
6.2.6 System dynamics . . . 163
6.2.7 System formation . . . 171
6.2.8 Prospects for atmospheric follow-up with JWST . . . 176
6.3 Attempt to view the secondary stars' CCF . . . 185

7 Conclusions & Future Work **189**

A Guide to the ESPRESSO Pipeline **193**

List of Figures **197**

List of Tables **211**

Bibliography **213**

List of Abbreviations

AAT Anglo-Australian Telescope.
ALMA Atacama Large Millimeter Array.
ARIEL Atmospheric Remote-sensing Infrared Exoplanet Large-survey.
ASTEP Antarctic Search for Transiting ExoPlanets.
AT Auxiliary Telescope.
AU Astronomical Units.

BEBOP Binaries Escorted By Orbiting Planets.
BF Bayes Factor.
BJD Barycentric Julian Date.

CCF Cross-Correlation Function.

DDT Director's Discretionary Time.
DEC Declination.
DNS Diffusive Nested Sampling.
DR Data Release.
DRS Data Reduction Software.

EAS European Astronomical Society.
EBLM Low Mass Eclipsing Binaries.
ESA European Space Agency.
ESO European Southern Observatory.
ESPRESSO Echelle SPectrograph for Rocky Exoplanets and Stable Spectroscopic Observations.
ETV Eclipse Timing Variations.

FAQ Frequently Asked Questions.
FIP False Inclusion Probability.
FWHM Full Width at Half Maximum.

GP Gaussian Process.
GUI Graphical User Interface.

H Hydrogen.

HARPS High Accuracy Radial velocity Planet Searcher.
HDBSCAN Hierarchial Density-Based Spatial Clustering of Applications with Noise.
He Helium.
HE High Efficiency.
HR High Resolution.

IAU International Astronomical Union.
ISM Interstellar Medium.

JWST James Webb Space Telescope.

MCMC Markov Chain Monte Carlo.

OHP Observatory Haute-Provence.

PLATO PLAnetary Transits and Oscillations of stars.

RA Right Ascension.
RAM Random Access Memory.
RMS Root Mean Squared.
RV Radial Velocity.

SB1 Single line Spectroscopic Binary.
SB2 Double line Spectroscopic Binary.
SNR Signal to Noise Ratio.
SOPHIE Spectrograph for the Observation of the PHenomena of stellar Interiors and Exoplanets.
SPECULOOS Search for Planets EClipsing ULtra-cOOl Stars.
SPOTS Search for Planets Orbiting Two Stars.

TATOOINE The Attempt To Observe Outer-planets In Non-single-stellar Environments.
TESS Transiting Exoplanet Survey Satellite.
TIP True Inclusion Probability.
TRAPPIST TRAnsiting Planets and PlanetesImals Small Telescope–South.
TSM Transmission Spectroscopy Metric.
TTV Transit Timing Variations.

UHR Ultra High Resolution.
UT Unit Telescope.

VLT Very Large Telescope.

WASP Wide Angle Search for Planets.

Chapter 1

Introduction to exoplanets

> "Space is big. Really big. You just won't believe how vastly, hugely, mind-bogglingly big it is. I mean, you may think it's a long way down the road to the chemist's, but that's just peanuts to space."
>
> Douglas Adams, *The Hitchhiker's Guide to the Galaxy*

The world was a very different place when I began my PhD in 2018. The United Kingdom was still in the European Union, the United States of America was being made "great again", no-one knew what COVID-19 was, everyone still worked in offices, Boris Johnson was no-where near being the prime minister, and the United Kingdom still had a Queen. It is strange to think back on all that has happened in the last four years as I write this thesis, but the universe, stars and planets I will discuss here have remained constant throughout it all, barely noticing any of these changes. They were here long before us, and will be here long after we have gone.

In this thesis I discuss the topic of the search for circumbinary planets with ground-based, radial velocity observations. This chapter introduces exoplanets, describes what they are, how they are discovered, and what we know about them. I then introduce the specific exoplanets targeted in this work, circumbinary planets, and discuss all that we have learnt about these objects through observations so far.[a]

Since the first discovery of a planet orbiting a sun-like star outside our solar system in 1995, 51-Pegasi b (Mayor & Queloz 1995), interest in these 'exoplanets' has increased steadily. As of today there are over 5000 confirmed exoplanets[b] with many more awaiting confirmation. This has sparked research into topics such as habitability, atmospheric analysis, and mechanisms for planet formation along with many others. The more exoplanets discovered the greater insight we obtain into understanding how planets and planetary systems form. Demographics of these exoplanets can then reveal just how common

[a] Parts of this section have been adapted from my mid-term report.

[b] https://exoplanetarchive.ipac.caltech.edu/ July-2022

our solar system is in the Universe, and how frequently planets that can support life similar to our Earth form. In turn, this can lead to answering one of the most famous questions known to humanity, *is there life elsewhere in the universe?*

1.1 What is an exoplanet?

The word 'exoplanet' comes from the Ancient Greek words, "exo", meaning outside or external, and "planetes" meaning wanderer. Exoplanet therefore refers to any planet found orbiting a star other than the Sun.

Planets are characterised in many ways, primarily based on their size, mass and temperature compared to planets in our solar system. The main categories used are: 'gas giants' such as Jupiter and Saturn, 'Neptunes' smaller gas giants such as Neptune and Uranus, 'sub-Neptunes' which have a similar composition to Neptune though smaller, and 'terrestrial' planets such as the rocky inner planets of the solar system. These categories and further sub-classes of planets are discussed in more detail in Sect. 1.3.1.

1.1.1 How are exoplanets named?

The first question I get asked when explaining that my research involves searching for exoplanets is: "Do you get to name the planets you find?" and while I always enjoy the idea of naming a planet "Planet Matt", unfortunately there exists a naming convention (nomenclature) adopted by the International Astronomical Union (IAU).

Detailed in this article by the IAU[c], the nomenclature states that the scientific designation of an exoplanet be the name of the star which hosts the planet followed by a lowercase letter designating what order planets in the system were discovered in. For example the first planet found orbiting a sun-like star, 51-Pegasi b (Mayor & Queloz 1995). The star itself is designated 51-Pegasi, and the planet is then 'b'. Stars can have names which stem from ancient Greek or Arabic (usually the brightest in the night sky), be named in order of brightness within a constellation, or be named from the catalogue which first mapped their positions followed by the number of the star in that catalogue. Common star names include HD (e.g. HD 209458) from Henry Draper's star catalogue, HIP (e.g. HIP 67851) from the HIPPARCOS satellite catalog (Esa 1997), and GJ (e.g. GJ 1214) from the Gliese (1957) index of stars.

Exoplanets can also be named based on the planet surveys which detected them. For example, the Wide Angle Search for Planets (WASP) project (Pollacco et al. 2006) name their planets as WASP-12 b (Hebb et al. 2009), for the 12$^{\text{th}}$ planetary system found by the transit survey, and first planet in that system. The TRAnsiting Planets and PlanetesImals Small Telescope–South (TRAPPIST) survey (Gillon et al. 2011) also adopts the same system with the first planet discovered by the survey being named TRAPPIST-1 b (Gillon et al. 2017).

In planetary systems with multiple planets, such as TRAPPIST-1 which has 7 transiting planets, the planets are named based on the order in which they were discovered. In this example they are named

[c] https://www.iau.org/public/themes/naming_exoplanets/

TRAPPIST-1 b, c, d, e, f, g, and h. However, this means that they will not necessarily be in alphabetic order, e.g. Kepler-90 b, c, i, d, e, f, g, h (Cabrera et al. 2014, ; where planet i was discovered after the first 6 planets).

Nature is often more complex than this, and planets have been even found in systems with multiple stars. Binary star systems are those which have two stars orbiting a common centre of mass. Planets orbiting both stars of a binary star system, known as circumbinary planets are the main topic of this thesis and are discussed in more detail in Section 1.4 & Chapter 4. Their naming follows a similar pattern as discussed above. The first circumbinary planet was the 16th planetary system discovered by the *Kepler* space telescope (Borucki et al. 2010), and therefore named Kepler-16. In a binary star system the largest and brightest star, known as the primary star, is designated 'A', the secondary star 'B', and so on for higher order systems with multiple stars. Therefore, the full name for the first circumbinary planet discovered is Kepler-16 (AB) b (Doyle et al. 2011), as the planet orbits both stars (AB). For circumbinary planets this is often shortened to Kepler-16 b. Chapter 4 describes the nomenclature we implement for circumbinary planets with the BEBOP survey, while Chapter 5 covers the Kepler-16 system in greater detail.

The stars in Kepler-16 have an orbital period of 41.08 d, and the planet orbits the binary with a period of 228.78 d. For wider binaries (i.e. those with larger orbital separations between the primary and secondary stars), planets can be found orbiting either or the stars individually. When orbiting the primary star (circumprimary), the planet is named as Ab, and when orbiting the secondary (circumsecondary), Bb. WASP-94 provides an excellent example of this binary system architecture. Its stars are separated by $>$ 2700 Astronomical Units (AU) (where an AU is approximately the distance from the Earth to the Sun), and each star hosts a planet. WASP-94 Ab is a hot-Jupiter with a mass of 0.45 M_J, orbiting the primary star in 3.95 d. While WASP-94 Bb is also a hot-Jupiter with a mass of 0.62 M_J, orbiting the secondary star with a period of 2.01 d (Neveu-VanMalle et al. 2014). A schematic of binary-planet systems can be seen illustrated in Figure 1.15.

This said, some exoplanet names can be updated by the IAU during 'naming campaigns' following a strict set of rules (see link in footnote b). Examples of planetary systems renamed in this way are those of the 55 Cancri system (Bourrier et al. 2018). The five planets in this system have been renamed as follows: b - "Galileo", c - "Brahe", d - "Lipperhey", e - "Janssen", and f - "Harriot". One of the rules listed states that planets can not be named after 'living individuals', which unfortunately rules out "Planet Matt" (for a while hopefully).

1.1.2 Leading questions of the field

To this day, we debate the processes that form planets (see Section 1.3.3), how our solar system fits in the emerging picture of exoplanetary systems, and whether habitable planets are common in our galaxy. In this section I will highlight some of the overarching questions in the field of exoplanetary science.

1.1.2.1 What planetary system architectures are possible?

In our solar system there are 8 confirmed planets along with 5 dwarf planets[d]. In the over 5000 exoplanets found to date we have discovered only one other system with as many as 8 planets, Kepler-90 (Cabrera et al. 2014) and one further with 7 planets, TRAPPIST-1 (Gillon et al. 2017). Though these systems sound similar, Kepler-90's planets all orbit within the orbital distance of the Earth, and TRAPPIST-1's planets' orbits are more compact, with all 7 orbiting well within Mercury's orbital distance (see Figure 1.1).

In opposition to compact planetary systems are those such as HR 8799 (Marois et al. 2010). Where direct imaging (Section 1.2) captured four large planets orbiting a very bright star seen in Figure 1.10. HR 8799 b, c, d, and e have masses between 5.7 – 9.1 M_J, and orbital periods between $\approx$ 45 – 460 years (16.25 – 71.2 AU). This places these four planets on orbits outside that of Saturn, and for the outer planet b at almost double the orbital distance of Pluto.

It seems that planetary systems with as many planets as the solar system exist, but may be rare. Currently, planetary detections are limited by biases present in the techniques used to discover exoplanets (see Section 1.2), favouring the detection of those with shorter orbital periods. As exoplanet surveys mature, longer period planets will be discovered, and in turn planetary systems like our solar system may yet be discovered.

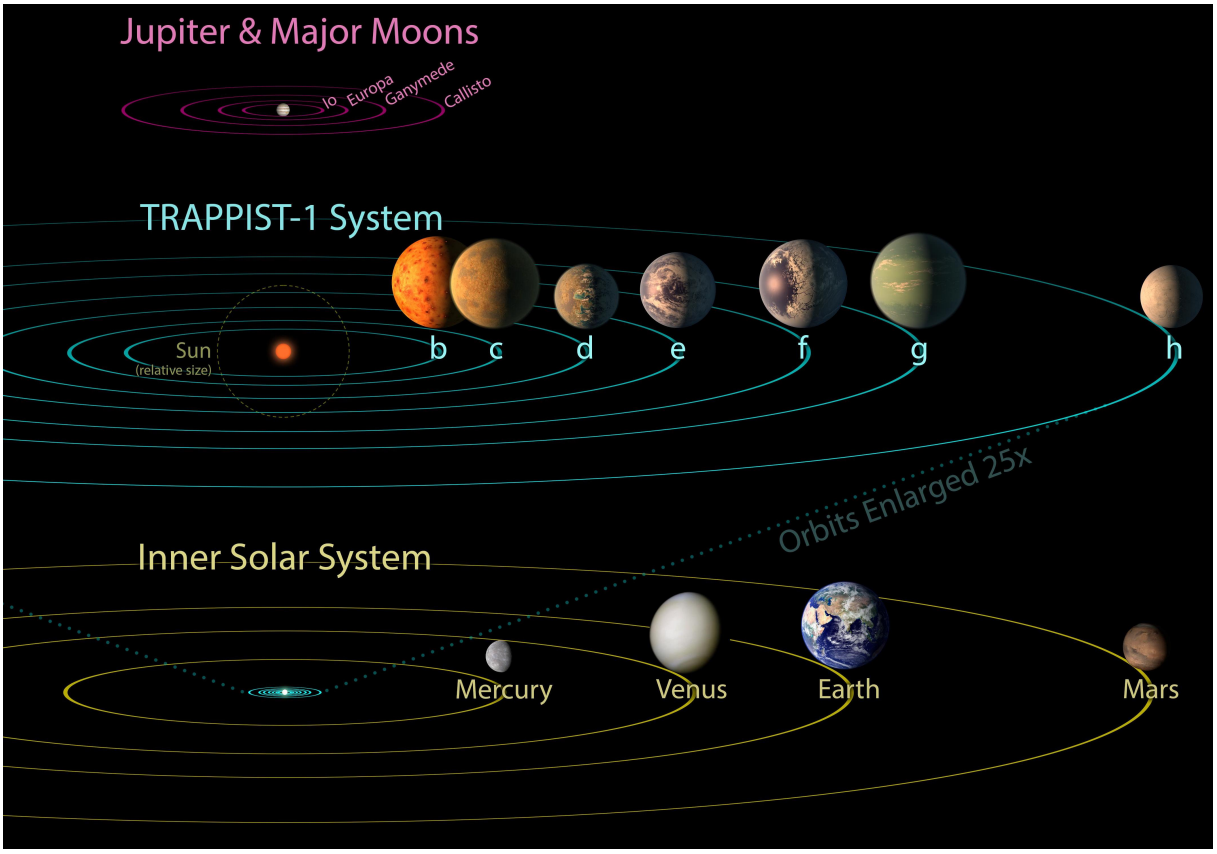

Figure 1.1: An illustration of the planets orbiting TRAPPIST-1 compared to the scale of the Solar system. All planets can be seen to orbit well within the orbital distance of Mercury. Credit: NASA/JPL-Caltech

[d]Let's not forget about Pluto (along with Eris, Ceres, Makemake, and Haumea)

1.1.2.2 Are there habitable planets like the Earth?

One of the most exciting questions in exoplanet science is whether Earth-like planets exist around other stars. The question forms the core of exoplanet science, and the search for life in the universe. The search for life is often associated with the search for Earth-like planets, for the simple reason that the Earth hosts the only life known to us in the universe. An Earth-like planet is of a similar size to Earth and orbits within the 'habitable zone' (Kasting et al. 1993) of a sun-like star. The habitable zone is the name given to the region surrounding a star where, if water is present, it can exist in liquid form on the surface of planets. The region is so named as all life on Earth requires liquid water to survive. It is important to note that an Earth-like planet in the habitable zone of a Sun-like star is *not necessarily habitable*, as the planet's composition and activity cycle of the parent star also affect habitability.

Several studies have shown that habitable zone terrestrial planets around sun-like stars appear to be common in the galaxy (Howard et al. 2010; Bashi et al. 2020; Bryson et al. 2021). With Bryson et al. (2021) estimating that the nearest habitable zone planet could be < 20 light years[e] from the Sun. Hsu et al. (2019) calculate an upper limit on the occurrence rate of planets with sizes $0.75 - 1.5 R_{\oplus}$, and periods $237 - 500$ days at $< 27\%$. Further discussion on occurrence rates can be found in Section 1.3.2.

Despite these estimates on their occurrence rates, Earth-like planets remain largely illusive, with only a handful having been discovered to date (e.g. Borucki et al. 2012; Jenkins et al. 2015; Petigura 2015). This is due to the smaller signals these objects impart on their stars, compared to the larger, more massive gas giant planets (see Section 1.2). Most of these Earth-like planets have been discovered by the dip in brightness we see as the planets travel between us and their host stars, known as the transit method. They are therefore classified by their planetary radius alone. Consequently, it is difficult to correctly characterise these objects without follow-up observations to determine their mass using the Radial Velocity (RV) method. Further details on these detection methods can be found in Section 1.2.

In the search for habitable planets, M-dwarf stars have recently become prime targets. M-dwarfs are smaller ($R \approx 0.09$ $R_{\odot}$, $M \approx 0.08$ $M_{\odot}$), and cooler than the Sun (≈ 2000 K, compared to the Sun's 6000 K), consequently their habitable zones lie closer to the stars compared to Sun-like stars. M-dwarfs are also common objects compared to other types of star (Winn & Fabrycky 2015). Any planets orbiting these smaller objects in their habitable zones impart a larger signal which, in combination to the numbers of these stellar objects, makes them good targets for exoplanet detection surveys. The only drawback is the stars themselves are fainter. The most famous exoplanet discovery around an M-dwarf star is that of TRAPPIST-1's 7 transiting planets (Gillon et al. 2017). Three of these planets, TRAPPIST-1 e, f and g, lie within the star's habitable zone (Fauchez et al. 2019). Several transit surveys are ongoing searching for planets around these cooler late-dwarf stars including Search for Planets EClipsing ULtra-cOOl Stars (SPECULOOS) (Delrez et al. 2018), which I have aided in the operation of during my PhD.

[e] A light year is the distance an object travelling at the speed of light can travel in a year.

1.1.2.3 Do Jupiter-like exoplanets allow Earth-like planets to form?

Another characteristic of our solar system is the presence of gas giant planets at large orbital periods, with terrestrial planets orbiting closer to the star. These 'Cold Jupiters', so named due to their large orbital distance from their star, appear to be common in the universe with an occurrence rate of $\approx 6.7\%$ (Wittenmyer et al. 2020). Rosenthal et al. (2021) find that $\approx 32\%$ of stars that host a Jupiter analog planet, also host an inner planet with a mass $2 - 30$ $M_\oplus$. There is a large volume of literature demonstrating that the presence of giant planets in a system strongly affects the formation of smaller terrestrial planets in the system (e.g. Raymond 2006; Morbidelli et al. 2012; Raymond & Izidoro 2017). Planet formation is discussed in greater detail in Section 1.3.3.

An example of a system with a gas giant planet at large orbital separations is the 55 Cancri system. The star (55 Cancri A) is part of a binary star system, though its secondary star (55 Cancri B) orbits at a distance of 1062 AU (Mugrauer et al. 2006), corresponding to an orbital period of approximately $36,000$ years. The primary star, 55 Cnc A is similar to the Sun in mass, radius and temperature, among other characteristics (Bourrier et al. 2018). Orbiting the primary star, 5 planets have been detected on circular orbits, similar to the orbits of the planets in our solar system. One of these planets is a gas giant (55 Cnc d) in the outer region of the system. This gas giant is similar to Jupiter with a mass of approximately 3 M_J, and an orbital distance of ~ 6 AU, compared to Jupiter's ~ 5.2 AU. The similarities between our solar system and 55 Cancri end there: the inner planets in the system all orbit within 1 AU and are larger than our terrestrial planets, with three gas giants, and a super-Earth which orbits the star in less than a day. Despite this, 55 Cancri is one of the closest solar system analogues we have discovered to date.

As we are yet to find an exoplanetary system that shares these characteristics with our solar system, does this mean that our solar system is special/different compared to these other systems? Or could it be explained by hidden planets in these systems? Are we the exception? or the Rule?

1.1.2.4 Do exoplanets have atmospheres like Earth? and are they habitable?

We know exoplanets host gaseous envelopes such as the planets in our solar system. Determining the composition of these atmospheres is an active field of research.

With the recent launch of the James Webb Space Telescope (JWST) (Gardner et al. 2006; Greene et al. 2016), acceptance of the Atmospheric Remote-sensing Infrared Exoplanet Large-survey (ARIEL) space (Tinetti et al. 2018) mission by the European Space Agency (ESA), and proposal of the Twinkle space telescope (Edwards et al. 2019), atmospheric study of exoplanets is set to provide groundbreaking results in the coming decade. These telescopes will observe the transits of exoplanets and analyse the light that passes through the atmosphere of the planet from the host star in order to determine the molecular species present in the atmosphere. Lustig-Yaeger et al. (2019) describes how atmospheric characterisation of the TRAPPIST-1 planets (Gillon et al. 2017) will be possible with the newly launched JWST. Determining the chemical composition of giant exoplanet atmospheres will provide us with information on the accretion

history of material throughout their formation (Pinhas et al. 2016). For more details on this method see Section 1.2.3.

Results can show the presence of water vapour in the atmospheres of planets, as seen in HD189733 b (Tinetti et al. 2007). Though the presence of water vapour does not mean the planet would be habitable for humans. HD189733 b is in fact a 'hot Jupiter' planet, named due to their similarities to Jupiter in size and mass, and their high temperatures due to their proximity to their host star.

By searching for specific molecular species present in exoplanet atmospheres, known as 'biosignatures', studies of exoplanet atmospheres hope to aid in the detection of life in the galaxy. A biosignature, in this context, is the presence of an atmospheric characteristic which indicates the presence of biological processes. As an example, the gas phosphine has been shown to be an excellent biosignature gas, produced mainly by bacteria on Earth (Sousa-Silva et al. 2020). Phosphine was recently detected in the atmosphere of Venus (Greaves et al. 2021), though the presence of microbial life producing this phosphine in the clouds of Venus is hotly debated.

To answer the questions posed above, we must discover many exoplanets in many orbital combinations. The methods employed to discover exoplanets continue to improve steadily, leading to more of these objects being discovered. Each discovery fills gaps in our knowledge and slowly reveals the underlying processes and patterns which will eventually allow us to pinpoint our place in the galaxy.

1.2 Detection methods

So far I have introduced exoplanets, and why we search for them. Stereotypically, astronomers are seen as scientists searching for objects they can see through a telescope. While we do *use* telescopes, we are usually unable to see any exoplanets directly. It is important to note that the distances to these exoplanets are astonishingly large. Proxima Centauri, the nearest star system to Earth is 4.2 light years away, and hosts the closest exoplanet, Proxima Centauri b. However, travelling at the speed of the fastest spacecraft in history: NASA's Parker Solar Probe (as of December 2021) at 163 $\mathrm{km\,s^{-1}}$,[f] it would take over 7700 years to reach the system!

In combination with their large distances from Earth, exoplanets are also many times fainter than their parent stars. Therefore, the majority of discovery methods must rely on the effects these planets have on their surroundings, such as their parent star, which are easier to observe with our techniques.

This section describes planetary orbital motion, along with the current techniques utilised to discover exoplanets, their success rate, sensitivity, and the advantages and disadvantages of each method. Numbers of detected exoplanets stated in this section are taken from the NASA exoplanet archive[g] as of February 2022.

[f] https://blogs.nasa.gov/parkersolarprobe/2021/11/10/space-dust-presents-opportunities-challenges-as-parker-solar-probe-speeds-back-toward-the-sun/

[g] https://exoplanetarchive.ipac.caltech.edu/docs/counts_detail.html

A number of techniques are utilised in the detection and characterisation of exoplanets, with the most successful being Radial Velocity (RV) (Lovis & Fischer 2010), transits (Winn 2010), Transit Timing Variations (TTV) (Kipping 2009), astrometry (Quirrenbach 2010), microlensing (Gaudi 2010) and direct imaging (Traub & Oppenheimer 2010). The work in this thesis mainly focuses on RV measurements, with some reference to transit data from the Transiting Exoplanet Survey Satellite (TESS) mission (Ricker et al. 2015). In this section I will briefly discuss these methods.

Figure 1.2 shows all confirmed exoplanets as of February 2022 in a mass versus period plot (data from NASA Exoplanet Archive[h]). Each exoplanet is coloured based on its discovery method, revealing some interesting patterns caused by the biases of each individual method, these will also be discussed below.

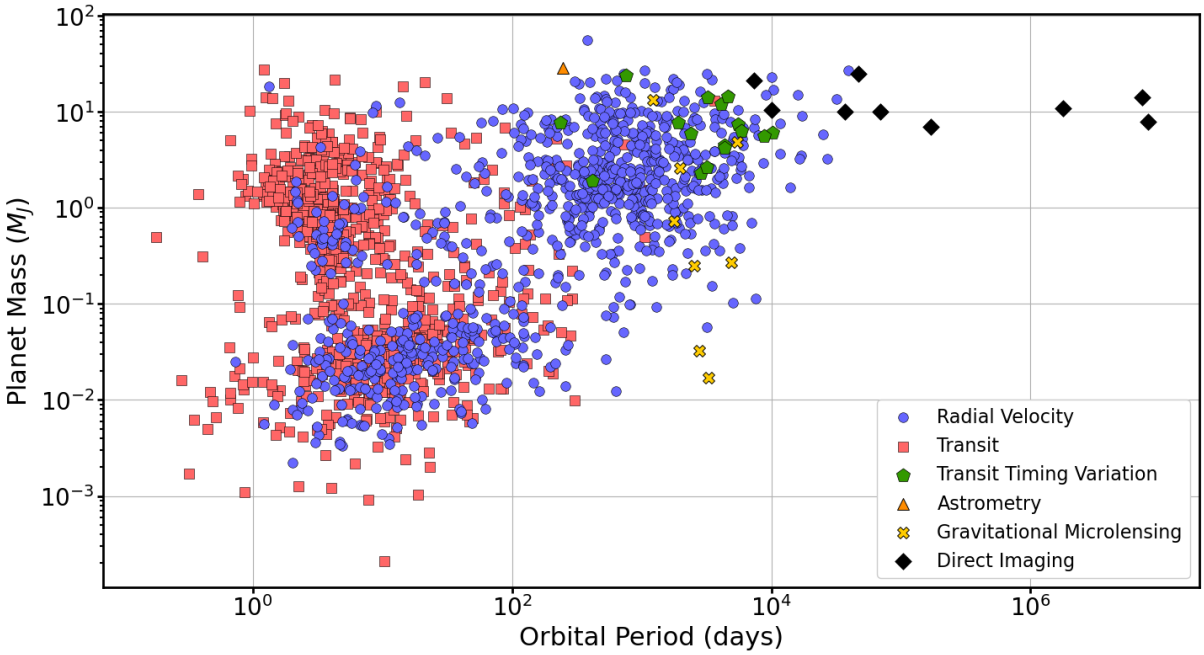

Figure 1.2: Plot of planet mass in Jupiter masses against orbital period in days for all confirmed exoplanets. Planets are coloured and shaped based on their discovery method. Data taken from the NASA Exoplanet Archive as of February 2022.

1.2.1 Planetary Orbital motion

In order to detect exoplanets, we must first understand how they move. A single planet orbiting a star follows a 'Keplerian orbit'. Each Keplerian orbit has a specific orbital period, shape and orientation. This section will describe these orbits, how they were determined, and introduce Kepler's three laws of planetary motion.

We will begin by imagining a single object orbiting a star. By observing the motion of the planets in the sky, Johannes Kepler developed three laws that describe the motion of planets orbiting the Sun. These can be applied to any orbiting body and describe a 'Keplerian orbit'. Kepler developed these laws

[h] https://exoplanetarchive.ipac.caltech.edu/index.html

based purely on observations of the planets. Here I will present Kepler's laws and briefly describe how they are obtained using Newtonian physics as in Murray & Correia (2010).

In 1609 there were competing ideas for how the planets orbited the Sun. Copernicus' heliocentric model placed the Sun at the centre of the solar system with the planets in perfectly circular orbits around it. However, this did not correctly describe the observations of Mars' orbit by Tycho Brahe. Kepler instead postulated that the planets orbited in 'elliptical' orbits with the Sun at one focus. This fit the observations and became Kepler's first law of planetary motion. Kepler released these laws in Astronomia Nova (Kepler 1609). In polar coordinates, Kepler's first law can be expressed as:

$$r = \frac{a(1-e^2)}{1+e\cos f} \tag{1.1}$$

where r is the separation between the two orbiting bodies, a is the semi-major axis of the ellipse, e the eccentricity of the ellipse between 0 and 1, and f is the true anomaly (i.e. the angle between the planet and the argument of periastron, ω, see Figure 1.6). For the case of a circular orbit where $e = 0$, equation 1.1 demonstrates that $r = a$. If $e = 1$ then the orbit is parabolic and no longer a closed path, instead extending to infinity.

The area of a section drawn from a line extending from one focus to the edge of this ellipse in time t is given by:

$$\frac{dA}{dt} = \frac{1}{2} r^2 \frac{df}{dt} \tag{1.2}$$

The equation for angular momentum L of a particle of mass m, distance r moving with an angular velocity $\frac{df}{dt}$ is given by $L = mr^2\frac{df}{dt}$, substituting this expression into equation 1.2 gives:

$$\frac{dA}{dt} = \frac{L}{2m} = \text{constant} \tag{1.3}$$

Since angular momentum is conserved, L is constant and therefore $\frac{dA}{dt}$ is also constant. This is Kepler's second law (also known as the 'law of equal areas'). This law states that a line drawn from the star to a planet will sweep out equal areas in equal times independent of the planet's location in its orbit.

Kepler's third law states that the square of a planet's orbital period is directly proportional to the cube of its semi-major axis. This can be obtained by starting with the gravitational force acting on a planet in orbit around a star:

$$F = -\frac{G\,M\,m}{r^2} \tag{1.4}$$

Where G is the gravitational constant, M is the mass of the star, m is the mass of the planet, and r the semi-major axis. Combining equation 1.4 with the acceleration of the planet $a = \omega^2 r$, using Newton's law of motion $F = ma$, simplifying and rearranging for ω gives:

$$\omega = \sqrt{\frac{GM}{r^3}} \tag{1.5}$$

The orbital period P of the planet is given by $P = \frac{2\pi}{\omega}$. Substituting equation 1.5 into this expression and squaring both sides then gives Kepler's third law:

$$P^2 = \frac{4\pi^2}{GM} r^3 \tag{1.6}$$

If P is expressed in Earth years, r in AU, and M in solar masses ($M_\odot$) then $\frac{4\pi^2}{G} = 1$ and therefore $P^2 = r^3$. These laws finally described the motion of the planets through the sky, and provided solid evidence for Copernicus' heliocentric model of the solar system adapted to include elliptical orbits.

1.2.2 The Radial Velocity method

The main detection method utilised in this thesis is the 'Radial Velocity' RV technique. It is the most established method for exoplanet discovery, and was utilised in the discovery of 51-Pegasi b, the first exoplanet discovered around a sun-like star (Mayor & Queloz 1995). This discovery revolutionised the world of exoplanet research, and introduced a new class of planet, 'hot-Jupiters' (see sect. 1.3.1). The discovery was awarded half of the Nobel prize in physics in 2019, during the first year of my PhD, an incredibly exciting time to have joined the field. Since 1995 the RV method has found over 910 planets, corresponding to $\approx$ 19% of all exoplanets discovered to date.

The radial velocity method relies on the fact that planets in stellar systems do not orbit their parent star exactly, but rather the centre of mass between the star and the planet. As a result, the star itself orbits the same centre of mass, and exhibits a small orbital motion from the gravitational pull of the orbiting planet. Consequently, we can measure the star's motion along our line of sight using the Doppler effect (Lovis & Fischer 2010). The Doppler effect, theorised by Christian Doppler in 1842, states that a wave will change its wavelength depending on the relative motion of the source and the observer. Light from a star as seen by an observer will therefore be detected at a slightly different wavelength than when emitted, dictated by the following equation (Hilditch 2001):

$$\lambda = \lambda_0 \frac{\sqrt{1 + \frac{v}{c}}}{\sqrt{1 - \frac{v}{c}}} \tag{1.7}$$

Where λ is the detected wavelength of the light, λ_0 is the wavelength of the emitted light, v is the velocity of the star with respect to us along our line of sight, and c is the speed of light in a vacuum. Therefore, when a light source moves towards us the light is shifted to shorter wavelengths (to the blue end of the spectrum), and to longer wavelengths (to the red end) when moving away.

Atomic and molecular species absorb light of particular wavelengths, which we are able to measure in a stationary reference frame known as a 'rest frame'. Molecular species present in the atmosphere of a star absorb the emitted light at these particular wavelengths (Gray 2008). Observing the light from a star through a spectrograph disperses the light to reveal the stars spectrum, along with these 'absorption lines' (see Figure 1.3). If the star is moving with respect to us, the wavelengths of the observed absorption lines are all shifted when compared to their rest frame values, according to equation 1.7.

Taking multiple absorption lines into account when calculating the instantaneous velocity of the star produces a more precise value for the velocity (Baranne et al. 1996). To achieve this, a technique known as a Cross-Correlation Function (CCF) is implemented. Calculating a CCF involves choosing a

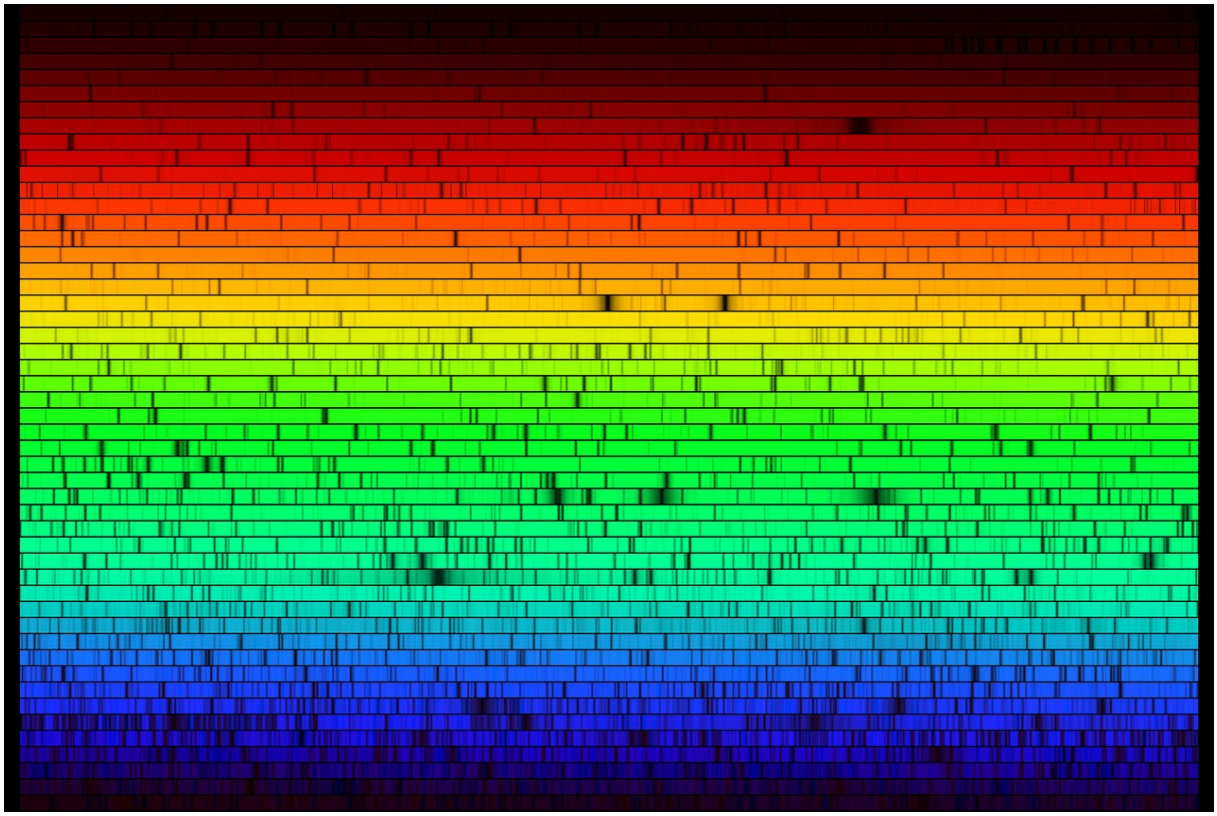

Figure 1.3: The solar spectrum. Absorption lines can be seen as the vertical dark lines in the spectrum. Credit: NOAO/NSO/Kitt Peak FTS/AURA/NSF

weighted template spectrum that closely matches the stars spectral absorption lines, and then shifting it in steps through velocity space across the observed spectra. At each step, the correlation between the template and the observed spectra is calculated, see Figure 1.4. This yields an inverted Gaussian shaped curve representing the average shape of the observed stellar absorption lines. Fitting a Gaussian to this curve and taking the value from the centre of the fit, provides the stars' instantaneous radial velocity (see Figure 1.8). Further details of the CCF method can be found in Baranne et al. (1996).

Subsequent observations provide us with the star's velocity towards or away from us over time. Folding these radial velocities onto the orbital period of the star, allows us to view the entire orbit as a sine wave, see Figure 1.5.

The radial velocity motion of a star can be expressed using the following equation (Lovis & Fischer 2010):

$$V_{\mathrm{rad}} = \sqrt{\frac{G}{(M_* + m_{\mathrm{p}})\, a\, (1 - e^2)}}\, m_{\mathrm{p}} \sin i \cdot (\cos(f + \omega) + e \cos \omega) + \gamma \tag{1.8}$$

Where G is the gravitational constant, M_* and m_p are the masses of star and planet respectively, a is the planet's semi-major axis, e its eccentricity, i is the inclination angle of the system on the sky. f is known as the 'true anomaly', i.e. the angle between the orbital position of the planet and the periastron direction (the closest distance from the planet to the star in the orbit). ω is the argument of periastron, i.e. the angle between the line of nodes and the periastron direction, see Figure 1.6. γ is the systemic

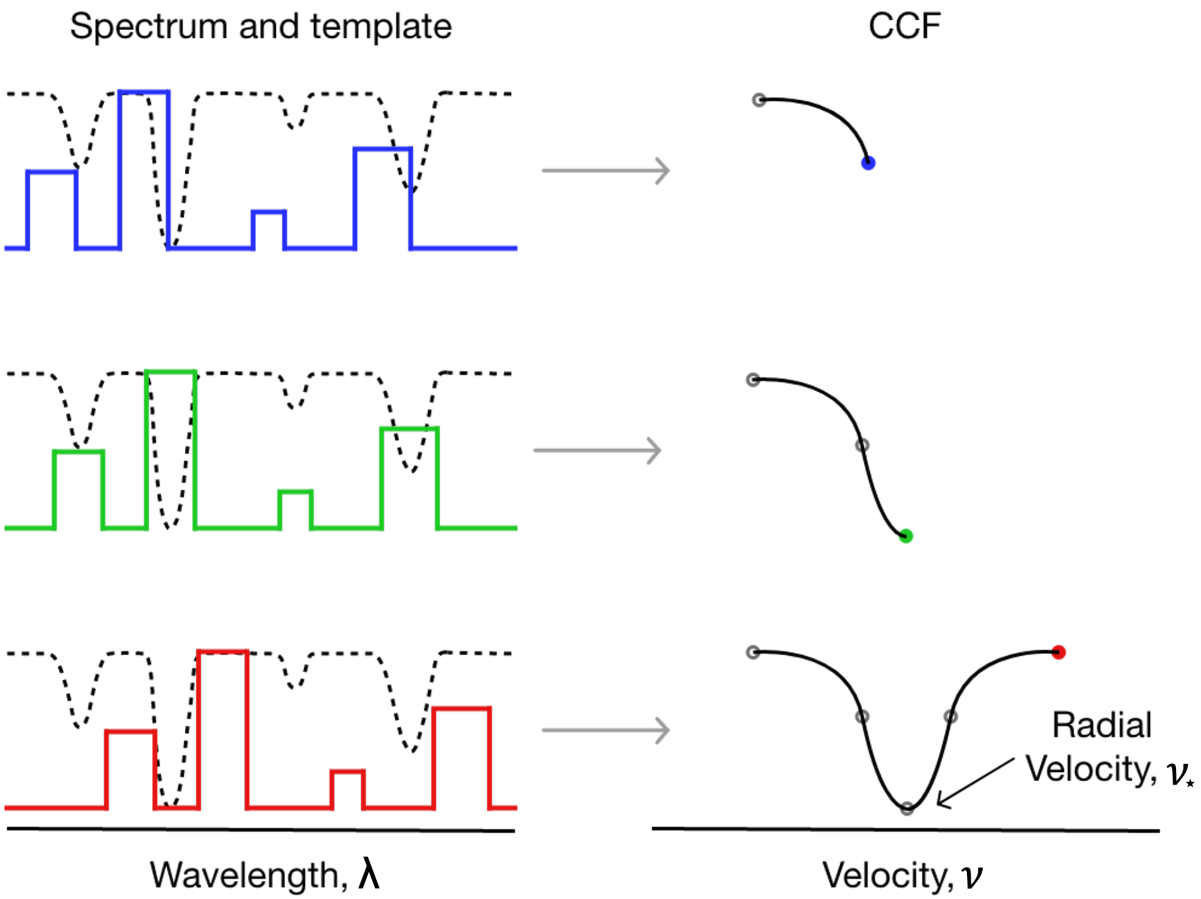

Figure 1.4: Figure of the cross correlation method for calculating the Radial Velocity RV of a star adapted from Roy et al. (2016). Left: Black dashed observed stellar absorption spectra and coloured template spectra in wavelength space. Colours represent the shifting of the template from shorter (blue) wavelengths to longer (red) wavelengths. Green represents the wavelength at which the template matches the observed spectra. Right: Resulting Cross Correlation Function CCF calculated at each step. The instantaneous radial velocity is then obtained from the centre of a gaussian fit to the CCF.

velocity of the system, i.e. the constant radial velocity of the centre of mass of the system after removing the motion of the Earth (Hilditch 2001; Lovis & Fischer 2010). From equation 1.8, we can see that with an eccentricity of 0 (a circular orbit) the radial velocity is a *cosine* curve with a semi-amplitude K given by:

$$K = \sqrt{\frac{G}{(M_* + m_\mathrm{p})\, a\, (1 - e^2)}}\, m_\mathrm{p} \sin i \tag{1.9}$$

The semi-amplitude is measured as half the peak to peak amplitude of the radial velocity, seen in Figure 1.5. Equation 1.9 can also be written in terms of P using Kepler's second law (Hilditch 2001):

$$K = \frac{2\pi\, a \sin i}{P(1 - e^2)^{1/2}} \tag{1.10}$$

It is also possible to express Equation 1.9 in a more practical scaling relation (Lovis & Fischer 2010):

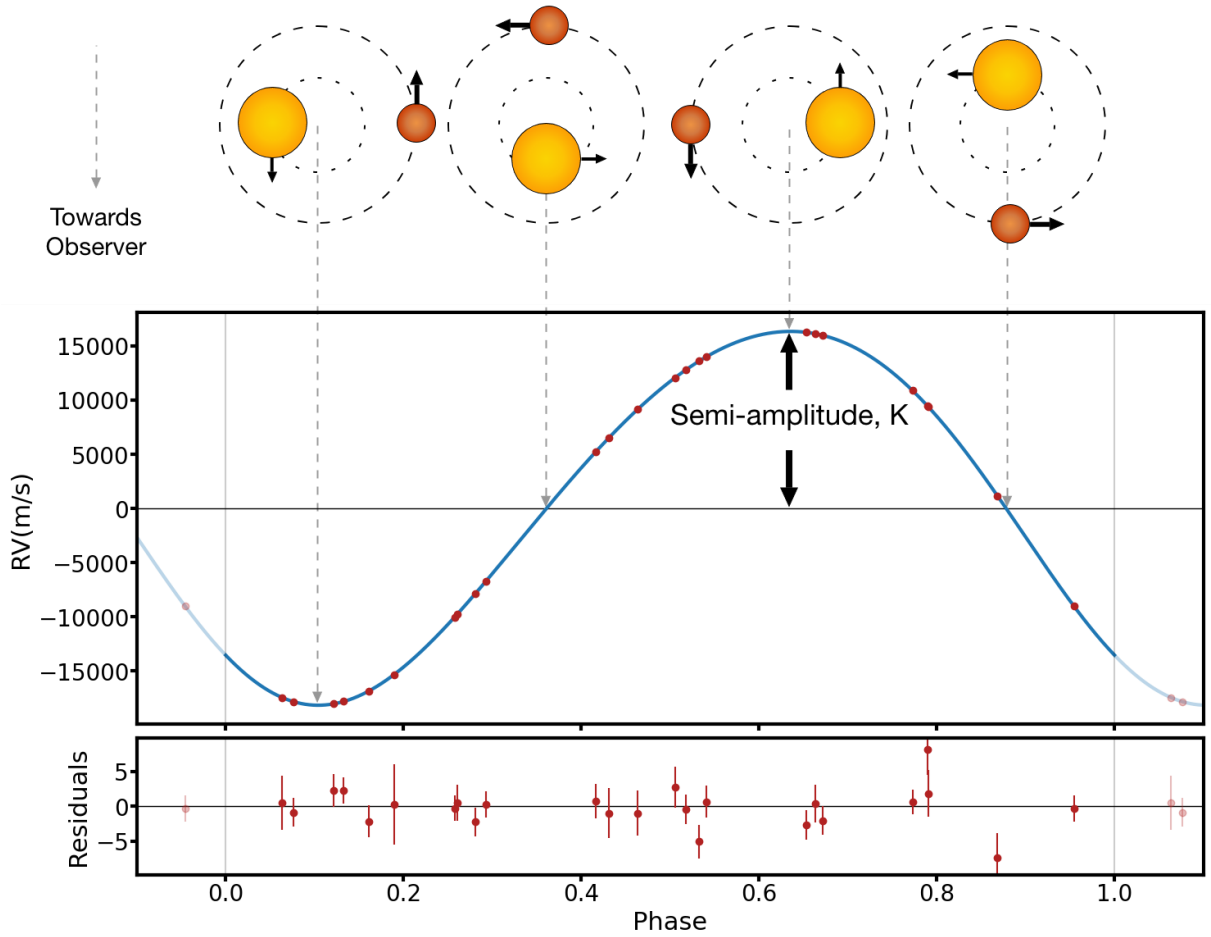

Figure 1.5: Top: Schematic of a binary star systems orbital motion at four different times through one orbit. Bottom: Phased radial velocity plot showing the same orbit of the binary star J1928-38. Red points are RV data from the HARPS spectrograph as part of the BEBOP survey (see Chapter 4). The blue line is a Keplerian RV signal fit to the data. The semi-amplitude K of the binary signal is shown. Inspired by Martin (2017a).

$$K = \frac{28.4329 \text{ m s}^{-1}}{\sqrt{1-e^2}} \frac{\text{m}_2 \sin \text{i}}{\text{M}_\text{J}} \left(\frac{\text{m}_1 + \text{m}_2}{\text{M}_\odot} \right)^{-2/3} \left(\frac{\text{P}}{1 \text{ yr}} \right)^{-1/3} \tag{1.11}$$

Rearranging equation 1.9 for $m_p \sin i$, assuming $m_p << M_*$ gives:

$$m_\text{p} \sin i = K \sqrt{\frac{(1-e^2)\, M_* \, a}{G}} \tag{1.12}$$

Obtaining K from the radial velocity measurements allows the minimum mass ($m_p \sin i$) of the planet to be calculated. As we are only able to measure the projection of the star's radial velocity along our line of sight, without knowing the inclination angle (i) of the orbit, the true mass of the planet cannot be determined. The inclination angle of the orbit can be determined from other detection methods, such as if the orbiting object transits the parent star (see Section 1.2.3). For planets orbiting binary star systems (see Section 1.4), if the binary stars experience eclipses, this reveals the inclination angle of the system (Triaud et al. 2013).

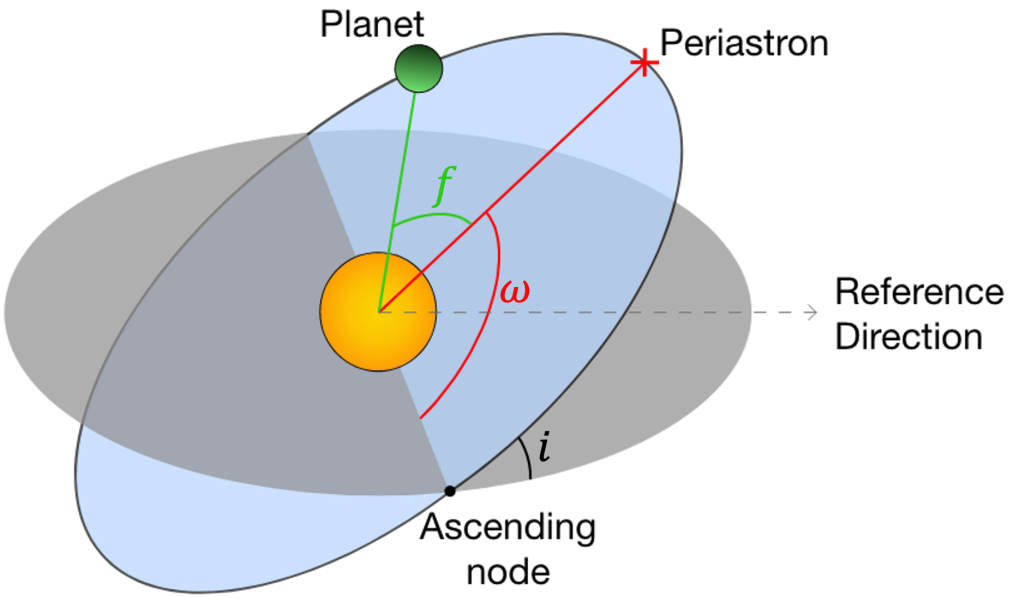

Figure 1.6: Schematic of planetary orbit around a single star. The periastron is the location on the planets orbit where it is closest to its star. f is known as the 'true anomaly' and denotes the angle from the periastron direction to the orbital position of the planet. ω is the argument of periastron, and denotes the angle from the line of nodes to the periastron direction. i is the orbital inclination of the system. Figure adapted from Rebound Orbital elements.

Radial velocities are often used for follow-up observations of candidate planets from transit observations for this reason. Since transit observations provide the radius of the planet along with the inclination angle of its orbit, RV follow-up can then provide accurate mass and density information, essentially mitigating the method's primary drawback, and enabling further characterisation of these exoplanets Bouchy & Queloz (2007).

From equation 1.9 we can see that the radial velocity method has a bias towards massive planets at shorter orbital separations from their host star which produce larger semi-amplitude signals. The method also allows for the eccentricity of a planet's orbit to be measured directly. As each set of measurements map the motion of the systems centre of mass, multi-planetary systems can be discovered with this method (providing sufficient data is available). It is also able to detect the presence of large planets on long orbits, with minimal monitoring observations over long time-spans. Though it can take years to confirm the planetary nature of these orbits, Figure 1.2 demonstrates that the majority of long period planets have been discovered using the radial velocity technique.

Using equation 1.10 we can calculate the semi-amplitude radial velocity signal that solar system planets induce on the Sun. The largest planet in the solar system, Jupiter, imparts a 12.4 m s^{-1} RV signal.

Whereas, the Earth imparts only 0.09 $\mathrm{m\,s^{-1}}$ (9 $\mathrm{cm\,s^{-1}}$). The most precise spectrographs available today, e.g. HARPS (Pepe et al. 2002), and ESPRESSO (Pepe et al. 2021), can reach precisions of $\lesssim 1\ \mathrm{m\,s^{-1}}$, see Section 4.2.2. If this were the only factor at play, we would be on the cusp of detecting habitable zone exoplanets around sun-like stars. Unfortunately, due to stellar activity, scatter is introduced to RV measurements of the order of $\sim$ 10's of $\mathrm{m\,s^{-1}}$ for the Sun (Dumusque et al. 2015). Without accounting for these effects, terrestrial planets in sun-like stars' habitable zones remain just out of reach for current RV techniques and instruments, for now...

1.2.2.1 Stellar activity & RV precision

Since radial velocities are obtained from the Doppler shift of a star's spectral lines, any stellar activity that has an effect on the spectral line profiles can alter the radial velocity values obtained from the cross correlation function (CCF). The Gaussian shape of a CCF has a specific width measured by its Full Width at Half Maximum (FWHM), slope of its bisector (the mid-points of lines spanning from one end to the other of the CCF (Baştürk et al. 2011)), and mean centre value revealing the star's radial velocity. Assuming the shape of a CCF is approximated by a Gaussian allows us to calculate an uncertainty on the RV through (Lovis & Fischer 2010; Bouchy & Queloz 2007):

$$\sigma_{\mathrm{RV}} \sim \frac{\sqrt{\mathrm{FWHM}}}{C \cdot \mathrm{SNR}} \tag{1.13}$$

Where FWHM is the Full Width at Half Maximum of the CCF, C is its contrast (depth divided by continuum level), and SNR is its Signal to Noise Ratio. It follows that the narrower and deeper the CCF, the more precise the measured RV value. The FWHM measures how broad the spectral lines from the star are. The faster a star rotates (indicated by a higher $v \sin i$ value), the broader the spectral lines we observe become (Doyle et al. 2014). This is due to the relative motion of both hemispheres of the star with respect to Earth. As the star rotates, the spectral lines of the hemisphere rotating towards us will be slightly blueshifted, while an opposing redshift will be observed for the opposite hemisphere. The averaged spectral lines from the entire star will consequently become wider in response. Therefore, the faster a star rotates, the wider the CCF becomes, and the FWHM increases along with the uncertainty on the obtained RV value.

Starspots represent a form of stellar activity which can introduce a variation of the RV measurements, similar to that of an orbiting planet. Starspots are dark spots on a star's surface caused by the local magnetic field at the surface (Strassmeier 2009). A starspot warps the shape of the observed CCF, by blocking light from a small area of the star's surface. The blocked light appears as a small bump on the absorption lines. See Figure 1.7 for an example of how starspots affect the spectral profile of a star.

The bump occurs at shorter wavelengths when light is blocked on the hemisphere of the star rotating towards Earth, and at longer wavelengths when blocking light from the hemisphere rotating away from Earth. The bisector slope of a CCF provides a measure of the change in slope of the bisector, the span, between the top and bottom of the CCF, and therefore any assymetry in the profile (Figure 1.8). Subsequent observations of the star may occur when the spot has rotated to a different location on the

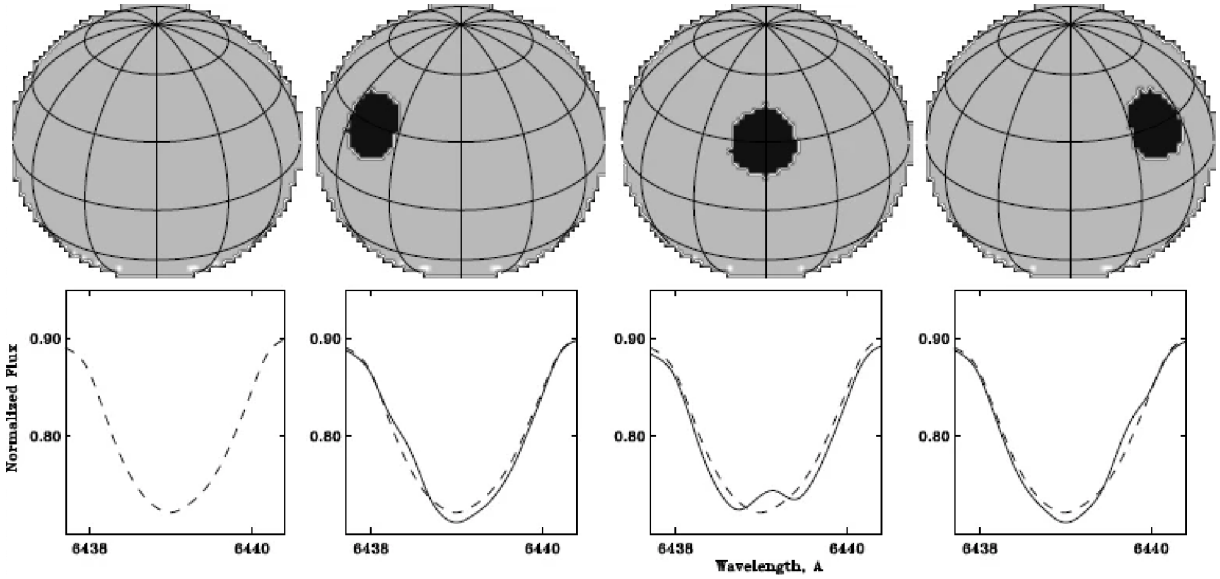

Figure 1.7: Figure from Berdyugina (2005) illustrating the effect of a starspot on the spectral line profile of a star. The dashed lines in the lower row of plots indicate a model with no spots present, and the solid lines those of the star with the spot.

stellar surface, introducing a change in the bisector values. Since the shape of the CCF is changed by the spots, variations in the central RV values can be introduced, which mimic that of the presence of an orbiting planet. Queloz et al. (2001b) demonstrated this effect for HD 166435. Plotting the bisector values against the RV values for the star revealed an anti-correlation. Thus proving that the RV modulation observed was not caused by a planet, but rather starspots on the rotating stellar surface. Queloz et al. (2001b) also described how measuring variations in the Ca II H and K absorption lines can be used as a proxy for surface magnetism on stars following work carried out in Baliunas et al. (1998). Since starspots are related to the stellar magnetic field (Berdyugina 2005; Strassmeier 2009), observing these Ca II H and K lines can indicate whether stellar activity is causing any RV variations observed. Other activity indices (or indicators) which can be used similarly are Hα and Na I (Gomes da Silva et al. 2011). See Chapter 6 for further details along with a practical application of using these indices to check for RV signals caused by stellar activity.

Another aspect of stellar activity that can affect the shape of the observed CCF is that of granulation on the stellar surface. Granulation (or macroturbulence) consists of granules (pockets of material rising to the surface of the star), and lanes (inter-granule sections that sink into the star). The granules, as they are rising to the surface are blue shifted. Whereas the cooler sinking lanes are red shifted. However, since the hot granules are brighter than the cool lanes, a net blue shift is observed across the star. This skewes the lines to the blue end of the spectrum slightly, while broadening each line (Doyle et al. 2014). The greater the level of granulation on a star the stronger this effect becomes. The broader the lines, and therefore the larger the FWHM of a star, the lower the resolution of the CCF and in-turn the RV precision. Further information can be found in Doyle et al. (2014).

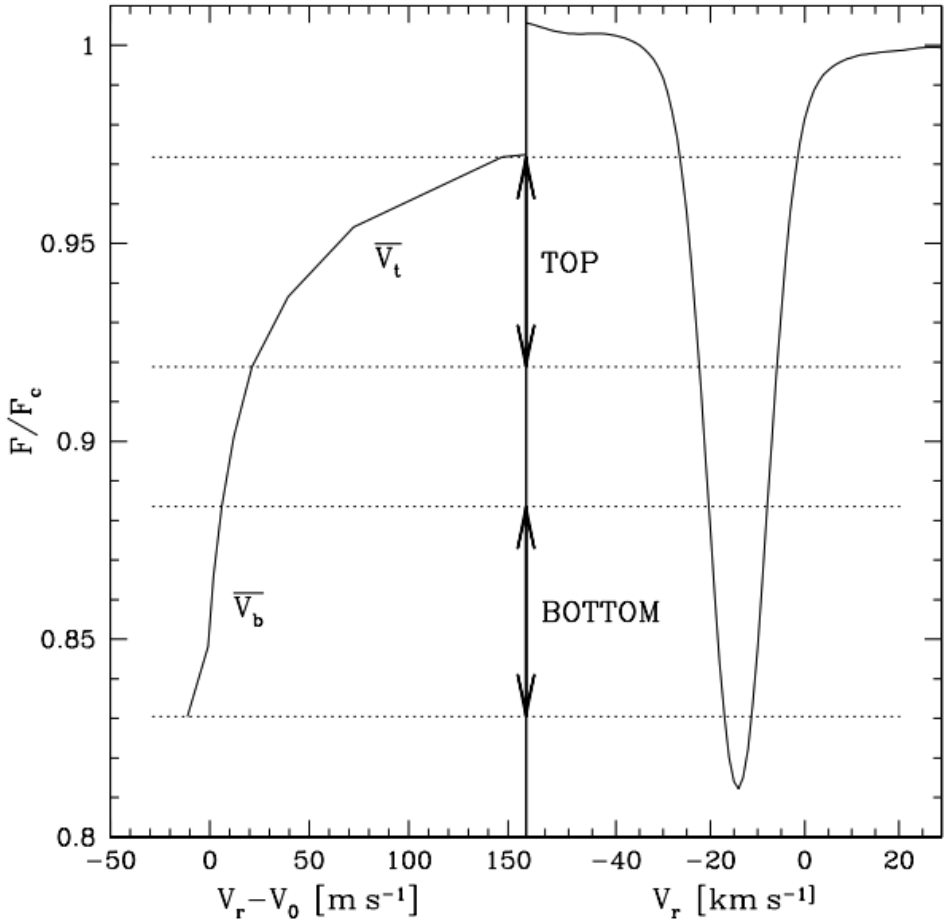

Figure 1.8: Right: CCF of HD166435 spectra. Left: bisector of the CCF. Here we can see the boundaries which define the top and bottom of the bisector slope, V_0 is an arbitrary offset. Both plot CCF contrast against RV. Figure from Queloz et al. (2001b).

1.2.3 The Transit method

The transit method uses photometry (the measure of brightness) to search for dips in a star's brightness caused by planets (or other objects) obscuring them along our line of sight. These dips in brightness are called transits, and occur on the 'primary transit' (or 'eclipse', where the planet crosses its parent star and blocks its light), and the 'secondary transit' (when the planet travels behind the star, and any reflected light from the planet is blocked, producing a smaller dip). Monitoring the brightness of the star over time yields the star's 'lightcurve', which can be seen in Figure 1.9. Any transits seen in the lightcurve can indicate the presence of an orbiting planet, and the time between primary transits reveals the orbital period of the planet.

For a transit to be observed, the inclination of the orbit must be such that the planet crosses the star along our line of sight. Transits are therefore highly dependent on the orientation of the system. Consequently, if a system is not oriented along our line of sight, any orbiting planets may never transit the star and remain undetected. The probability of a planet to transit its star is given by the following equation (Winn 2010):

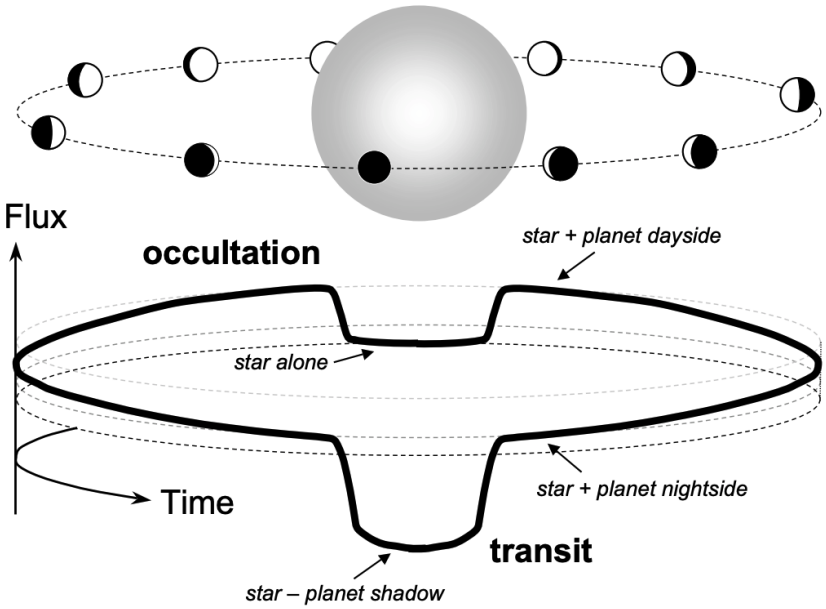

Figure 1.9: An illustration of transits and occultations from Winn (2010). As can be seen, there is a dip in brightness as the planet passes in front of the star, the "transit". The combined flux from the system increases slightly as the planets day side comes into view. Then as the "occultation" occurs, the reflected component of stellar flux is blocked by the star and the total flux decreases to the stellar value.

$$p = R_*/a \tag{1.14}$$

Where p is the probability of transit, R_* is the radius of the parent star and a is the planet's semi-major axis (the distance at which the planet orbits its host star). This equation demonstrates the transit methods large bias towards detection of planets on short close orbits, due to their higher transit probability. This bias is clearly evident in Figure 1.2, where the majority of transit detections are at short orbital periods. To search for transiting planets with longer orbital periods, transit missions must stare at the same area of the sky for long periods of time to observe repeat transits.

With two major space based missions *Kepler* (Borucki et al. 2010), and *TESS* (Ricker et al. 2015), the transit method is the most successful exoplanet detection method to date. There have been over 3750 transiting exoplanets discovered, corresponding to the majority of exoplanet discoveries on record at $\approx$ 77%. The higher number of transit detections can be attributed to the main advantage of transit observations, that large areas of the sky can be monitored for transits simultaneously.

Though transits are responsible for the majority of planet detections, it is unable to ascertain the mass of detected planets without the presence of transit timing variations (Section 1.2.3.2). To measure the planetary mass, radial velocity observations are often used to follow-up a planetary transit discovery (see Section 1.2.2). This serves to confirm the planetary nature of the transit, but also since the planet transits, the inclination of the system must be $i \approx 90°$. Determining the inclination angle this way allows the RV method to reveal the system's absolute mass.

1.2.3.1 Atmospheric characterisation

Transits can also reveal more information about the planet than just its presence. From the transit's depth, the planetary radius can be calculated relative to the size of the host star. If the transit depth varies with wavelength, transmission spectroscopy can be carried out, unlocking the secrets of the planet's atmosphere (Seager & Sasselov 2000). As light from the star filters through any atmosphere that may be present around the planet, molecular species in the atmosphere absorb the light from its host star at certain wavelengths. Consequently, the planet's transit becomes deeper at those wavelengths, translating as an apparent increase in radius. Plotting the transit depth against wavelength then reveals the atmospheric composition of the planet's atmosphere. This is known as transmission spectroscopy.

The ARIEL mission (Tinetti et al. 2018), chosen by the ESA to be launched in 2028, along with the newly launched JWST (Gardner et al. 2006; Greene et al. 2016) will both utilise this technique to provide exciting new insights into exoplanet atmospheres.

1.2.3.2 Transit Timing Variations

Variations in the timing of transits can also be an indicator of further bodies present in the planetary system. Gravitational effects from a second planet, or even an 'exomoon', can cause a periodic perturbation from the expected transit time of the planet. This is a method known as Transit Timing Variation TTV. It can identify non-transiting objects orbiting in the system and works towards mitigating some of the bias discussed above. It can also be used to provide an estimate on the mass of circumbinary planets (see Section 1.4). A more detailed description of the TTV method can be found in Agol & Fabrycky (2018).

1.2.4 Other methods

I will briefly mention the other methods used to discover and characterise exoplanets and point to further material.

Astrometry measures the position of stars over time, and tracks their motion across the sky. It detects the presence of an orbiting planet by searching for a "corkscrew" motion of a star. The "corkscrew" is caused by the gravitational interaction of the star-planet system as they orbit the systems common centre of mass. This method not only reveals the planets semi-major axis, but also the systems orbital inclination (i), providing absolute masses for any planets present. The astrometric signal of an exoplanetary system (θ) is given by (Quirrenbach 2010):

$$\theta = \frac{m_{\rm p}}{M_{\rm star}} \frac{a}{d} \tag{1.15}$$

where d is the distance from the observer to the star. As can be seen by equation 1.15, astrometry is therefore most sensitive to massive planets at large orbital separations from their parent star, such as the gas giants in our solar system. This makes it better at detecting similar systems to our solar system than the RV method, even though they are both based on the same gravitational interaction.

Unfortunately, since the levels of precision required for these measurements are difficult to achieve from the ground, and the orbital periods this method is sensitive to are long, exoplanets are difficult to detect with this method. As detectors improve, and the Gaia satellite (Gaia Collaboration et al. 2016) releases more data, such as the newly released Gaia Data Release (DR) 3 (Vallenari et al. 2022), astrometry promises to provide a number of exoplanet discoveries in the more sparsely sampled outer regions of stellar systems with absolute masses for the planets (Holl et al. 2022). Further information on this technique can be found in Quirrenbach (2010).

Gravitational Microlensing occurs when a foreground star passes close to an observer's line of sight to a distant background star. The gravity of the foreground star warps space-time and acts as a lens for the light from the background star, magnifying its brightness as a function of time. If this foreground star has a planet orbiting around it, the planet can further perturb the light, magnifying it further. This method is able to detect planets with wide separations from their parent stars. The timespan of a microlensing event is related to the mass of the planet involved following (Gaudi 2010):

$$t_{E,p} = q^{1/2} t_E \tag{1.16}$$

where $t_{E,p}$ is the duration of the planetary event, q= m_p/M, the ratio of the planetary mass (m_p) to the stellar mass, and t_E the duration of the entire event. with the duration of the order of a few days for Jovian-mass planets, and a few hours for Earth-mass planets (Gaudi 2010).

An advantage this method provides is the ability to detect free-floating planets. These objects, predicted by planet formation theories, are planets which have been ejected from their star systems and no longer orbit a host star. No other detection method is able to detect these near invisible objects. However, due to the nature of microlensing events, the foreground and background stars being independent bodies, the event cannot be repeated, and the method relies on chance alignments. To improve the probability of detections microlensing surveys observe dense star fields, though the microlensing event rate remains low. To date microlensing surveys have detected over 120 exoplanets, further information on this method can be found in Gaudi (2010).

Direct imaging is a method that does exactly what it says, directly imaging an exoplanet by spatially resolving it from its parent star. Though this sounds like the simplest method covered so far, it has difficult physical limitations to overcome. The parent stars are several orders of magnitude brighter than their orbiting planets, and can therefore easily hide any reflected light from the planets. For this reason, planets discovered by this technique have large orbital separations from their host star. The method requires large mirrors to spatially resolve the faint planets, limiting direct imaging to ground based observations, and introducing additional noise sources to the observations of the already faint targets in the form of atmospheric distortion. Despite these limitations, direct imaging has detected 57 exoplanets to date, and yields impressive images such as the four planets seen orbiting HR 8799 in Figure 1.10.

Unfortunately, planetary masses are difficult to obtain from direct imaging, therefore astrometry or radial velocity observations are used in tandem with direct imaging to determine the masses of exoplanets discovered with this technique.

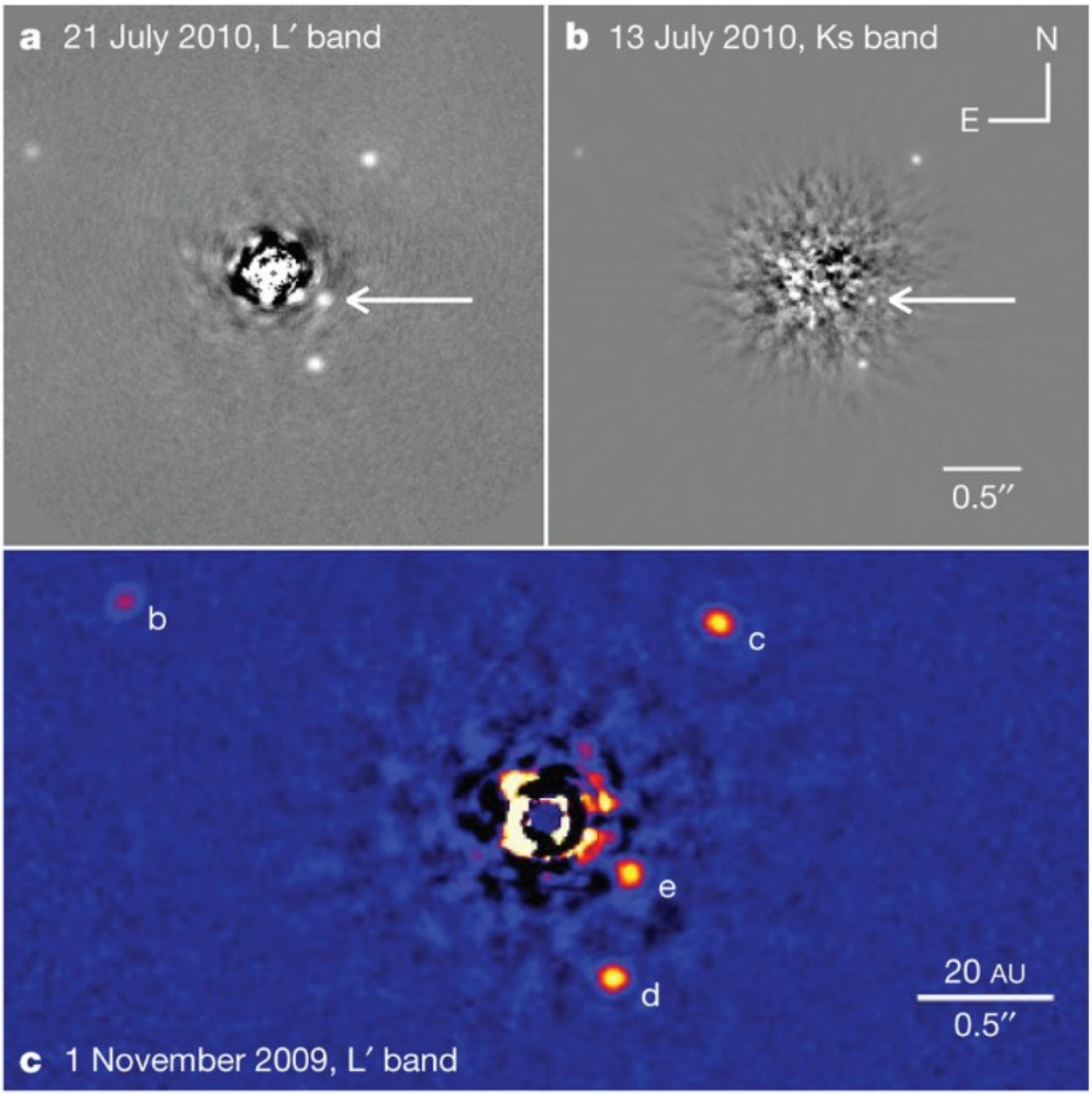

Figure 1.10: Direct imaging of quadruple exoplanet system HR 8799, obtained from Marois et al. (2010). A time-lapse of the planets' motion over 7 years is also available by clicking here.

This method provides an unique opportunity to image the light from an exoplanet directly, allowing spectral information to be obtained, in-turn providing information on atmospheric composition. It also allows the planet's orbit to be constrained accurately, even in face on planetary systems. Further information on this method can be found in Traub & Oppenheimer (2010).

1.3 Observed patterns and demographics of exoplanets

In this section I will briefly describe what has been learnt about exoplanets from the discovery methods outlined above. I will discuss the types of planets detected, the demographics and patterns observed, and theories on their formation.

1.3.1 Planet types

In the solar system there exists a diverse selection of planets. From the small, rocky and hot Mercury, the habitable Earth, the giant Jupiter and Saturn, and the cold distant Neptune. Despite this diversity, exoplanet detections have continued to push the boundaries of our understanding of planets and the mechanics that apply to them.

The first planet discovered around a sun-like star, 51-Pegasi b (Mayor & Queloz 1995), was no exception. The planet was unlike any other we knew: it is around half the mass of Jupiter, and would be the second largest planet in our solar system. Despite this, it orbits its star every 4.23 days, this corresponds to the planet being around 7.5 times closer to its star than Mercury is to the Sun. Prior to this discovery an arrangement such as this was unheard of, and the discovery sparked the invention of a new class of planet, 'Hot Jupiters' (described below).

Below I will introduce the classes of exoplanets which have been populated with exoplanet discoveries following 51-Pegasi b. These classes will be referred to throughout this thesis, and occurrence rates for these planet classes are discussed in Section 1.3.2.

Gas giants are the largest class of planets and include our Jupiter and Saturn. They have large Hydrogen (H) and Helium (He) envelopes surrounding a solid core. The Gas giant category also contains sub-categories; **'Hot Jupiters'**, so named for their size and extremely high temperatures from their proximity to their parent stars, with orbital periods < 10 days (Huang et al. 2016; Dawson & Johnson 2018). Due to the biases of the detection methods discussed in Section 1.2, hot Jupiters are the easiest to discover due to their large transit and radial velocity signal. This makes gas giants the most numerous class of exoplanets, as can be seen by the large number of high mass exoplanets in Figure 1.2. Other types of gas giant planets include **'Warm Jupiters'**, which are Gas giant planets that orbit with orbital periods $10 - 200$ days (Huang et al. 2016; Dawson & Johnson 2018), and **'Cold Jupiters'** which are Gas giant planets that have orbital periods > 100 days (Wittenmyer et al. 2020) similar to Juipter and Saturn.

Neptunes also fall into the broad gas giant category, but with smaller masses similar to that of Neptune at 17.5 $M_\oplus$.

Sub-Neptunes are smaller than gas giants at approximately $5 - 10$ $M_\oplus$, though they still posses a large H and He envelope with a planetary radius > 2 $R_\oplus$ (Bean et al. 2021).

'Super-puffs' are a rare but intriguing sub-class of exoplanet. They are so called as their atmospheres appear to be inflated, with radii > 4 $R_\oplus$ while their mass is between $1 - 10$ $M_\oplus$ (Chachan et al. 2020), giving them an incredibly low density. Some of the lowest density exoplanets that have been discovered are in the Kepler-51 system, where all three planets have densities < 0.1 g cm^{-3} (Libby-Roberts et al. 2020)[i].

Terrestrial planets are rocky planets which may also have a gaseous envelope, though the majority of their mass is primarily from its rocky core. They tend to have masses less than approximately $5 - 10$ $M_\oplus$, as it is thought that during formation larger planets are more likely to develop into giant planets or sub-Neptunes by capturing large amounts of gas (Seager & Lissauer 2010). Terrestrial planets also have

[i]Less dense than a Victoria sponge cake! https://bakerpedia.com/processes/specific-gravity-cakes/

sub-categories such as **'Super-Earths'** which are terrestrial planets larger than the Earth at $1 - 10M_{\oplus}$ (Mayor et al. 2011).

The most exciting sub-category of the terrestrial planets are **'Earth-like'** exoplanets. These are of similar mass, size and temperature to Earth, in an Earth-like orbit around a Sun-like star. Unfortunately, these objects are not necessarily habitable. For an exoplanet to be considered habitable, liquid water must exist on its surface. This is only possible if the planet orbits within its stars 'habitable zone' (Kasting et al. 1993), where the planet's surface temperature is not too hot (from being too close to the star) and not too cold (from being too far from it). This explanation gives rise to the alternative name for habitable zone the 'Goldilocks zone', as the temperature within this region is "just right" for liquid water to be present.

1.3.2 Exoplanet demographics

Now that we have discussed how exoplanets are discovered and the ways in which we classify them, we can explore some patterns that have emerged from observations.

1.3.2.1 Radius gap

When studying the size distribution of sub-Neptunes and terrestrial planets discovered by the *Kepler* space telescope, Fulton et al. (2017) found an intriguing pattern had developed. Terrestrial planets with periods < 100 days demonstrated a deficit of planetary radii between $1.5 - 2.0R_{\oplus}$. Figure 1.11 from Fulton et al. (2017) illustrates this phenomenon, and shows that short period terrestrial planets appear to fall into one of two distinct size regimes, $< 1.5R_{\oplus}$, and $2.0 - 3.0R_{\oplus}$. This phenomenon was dubbed the "radius valley" or "Fulton gap". They postulated that the amount of low-density gas a terrestrial planet possesses at these radii govern the overall size of the planet.

It was first predicted by Owen & Wu (2013), and later shown by Owen & Wu (2017) & Van Eylen et al. (2018) that the bi-modal nature of the distribution between super-Earths at $\approx 1.5R_{\oplus}$ and sub-Neptunes at $\approx 2.5R_{\oplus}$, could be explained by photoevaporation models. Photoevaporation is the process of stellar-radiation driven dispersion of gas from the envelope of planets. Planetary cores large enough to be able to hold onto their gaseous envelopes in the presence of stellar radiation fall into the sub-Neptune category, while smaller cores are less likely to be able to preserve their entire envelope, and their radius consequently diminishes into the super-Earth category (Owen & Wu 2013). This provided a new name for the phenomena, the "photoevaporation valley". However, recent studies claim that the valley can also be explained by different planet formation pathways for the two size regimes (Venturini et al. 2020; Luque & Pallé 2022).

1.3.2.2 Occurrence rates

Before the discovery of exoplanets, the only planets known to us were the Solar system planets. We had no method of determining if planet formation in the galaxy was a rare or common occurrence. Today, with

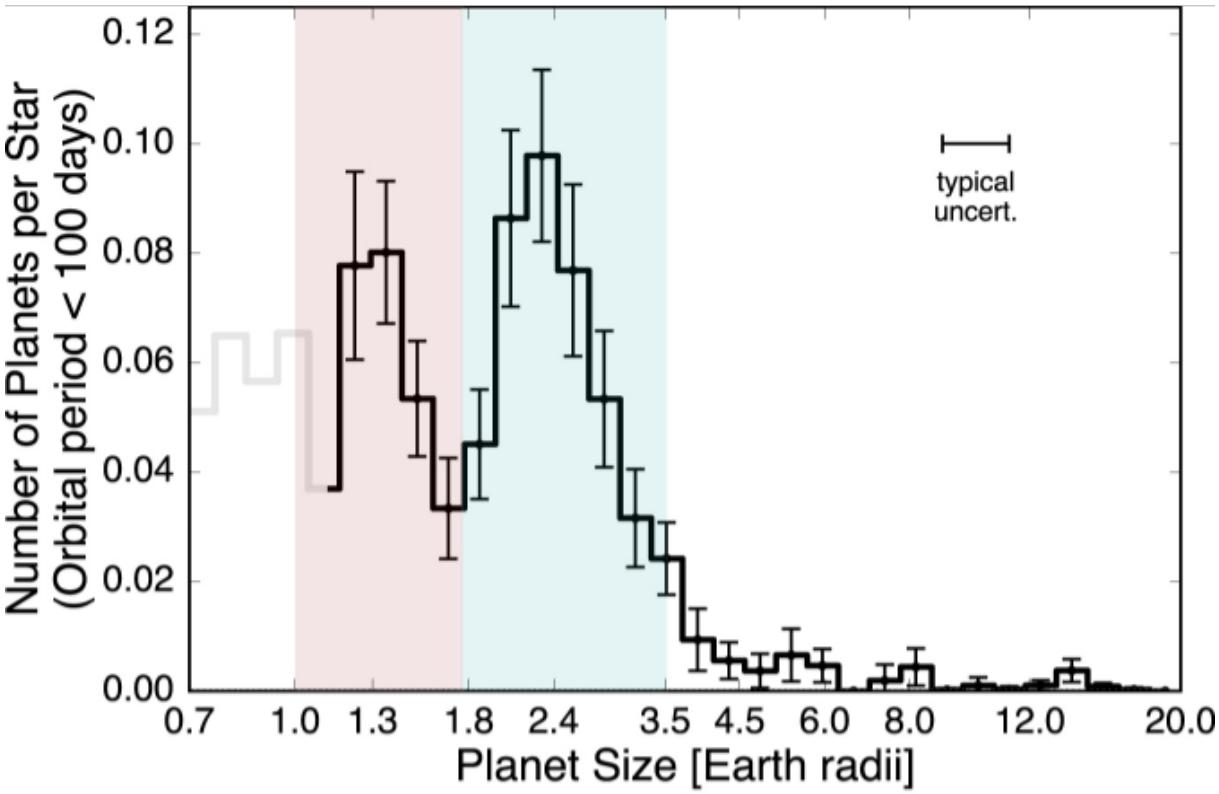

Figure 1.11: Histogram of number of planets per star with orbital periods < 100 days against planet radius, modified from (Fulton et al. 2017). Shaded regions illustrate the radius definitions of super-Earths (red) and sub-Neptunes (blue).

almost 5000 discovered exoplanets we are able to place constraints on the occurrence rates of individual categories of exoplanets around an array of stellar host types.

Gas giants

Despite being the most numerous planet type detected, hot Jupiters are heavily impacted by the detection biases outlined in Section 1.2. They appear to be rarer in nature than our detections imply, Mayor et al. (2011) find the data is consistent with a 0.9% occurrence rate of hot Jupiters with periods < 11 days. Using *Kepler* data Steffen et al. (2012) conclude that systems which contain hot Jupiter planets are less likely to contain giant planets at longer orbital periods, and Winn & Fabrycky (2015) state that systems hosting hot Jupiters tend to have less planets with orbital periods between 10 – 100 days. These results hint at chaotic formation process for systems containing hot Jupiters see Section 1.3.3. Gas giant planets with orbital periods < 1 year appear to be less abundant than smaller planets, and ≈ 10% of Sun-like stars host giant planets with orbital periods shorter than a few years (Winn & Fabrycky 2015). While Wittenmyer et al. (2020) demonstrate that 'Cold Jupiters' (i.e. gas giants at long orbital periods) have an occurrence rate of 6.73%. In addition, Bryan et al. (2019) show that in the presence of an inner 'Super Earth' (a terrestrial planet larger than Earth), the occurrence rate for Jupiter like companions increases to ≈ 39%. This agrees with the finding that the giant planets discovered have a broad range of orbital eccentricities from 0 – 0.9, with a mean of ≈ 0.2 (Winn & Fabrycky 2015). In contrast, smaller planets have eccentricities < 0.1, with even smaller eccentricity distributions for small planets in multiplanetary

systems. A higher eccentricity could indicate that these planets have interacted with other planets during their formation process, ejecting them from the system and in turn exciting their own eccentricities (Dawson & Murray-Clay 2013). A planet forming disk (see Section 1.3.3) around a metal-rich star could contain more solid material, form more planets and lead to these larger number of planetary interactions.

There also appears to be a correlation between the abundance of heavier elements (metals[j]) in a stars atmosphere with the presence of planets. Giant planets appear to be more common around stars with higher metallicities (Gonzalez 1997; Santos et al. 2004; Fischer & Valenti 2005; Winn & Fabrycky 2015), whereas smaller planet occurrence does not appear to be associated with this characteristic (Sousa et al. 2008; Buchhave et al. 2012; Winn & Fabrycky 2015).

Small planets

Smaller planets have been found to be more common than their giant counterparts (Mayor et al. 2011), with Howard et al. (2010) and Bashi et al. (2020) finding that $\approx 20\%$ of stars harbor a short period Earth mass planet. For Sun-like stars, the likelihood of hosting a compact multi-planetary system of smaller planets with orbital periods < 1 year is as high as 50% (Mayor et al. 2011; Winn & Fabrycky 2015), with Howard et al. (2012) and Mulders et al. (2015) finding that smaller planets are more common around stars with a smaller mass than giant planets. Considering only habitable zone terrestrial planets, Bryson et al. (2021) find that a conservative occurrence rate of planets with radii between $0.5 - 1.5\ R_\oplus$ orbiting sun-like stars is approximately $37 - 60\%$. Latham et al. (2011) found that small planets are more likely to be found in multi-planetary systems than their giant counterparts, this also supports the fact that smaller planets have a lower range in eccentricities, while giant planets are found to be more eccentric.

With the number of exoplanets increasing steadily, these occurrence rate predictions can only improve in the years to come. Further details on planetary occurrence rates can be found in Winn & Fabrycky (2015).

1.3.2.3 Peas in a pod

The *Kepler* space telescope is the most successful exoplanet detection mission to date. It discovered over 3000 (including K2) transiting exoplanets by monitoring the brightness of thousands of stars in a stationary field of view (Borucki et al. 2010). When studying the $\approx$ 350 multi-planetary systems discovered by *Kepler*, Weiss et al. (2018) noticed that the radii of the planets within the same system are correlated with each other. The orbital period ratios of the planets are also correlated. Figure 1.12 from Weiss et al. (2018) demonstrates this even spacing of planets.

Furthermore, it became apparent that the systems with smaller planets have smaller period ratios between the planets. This hints at the presence of either an underlying mechanism during planet formation, or orbital dynamics shortly after planetary formation. An additional pattern seen in Figure 1.12, is that the largest planets in these systems appear to orbit further from their parent stars. In fact, Weiss et al. (2018) calculated that the outer planet is the largest 65% of the time. The figure also reveals possible locations of undiscovered planets in these systems by taking note of the gaps in each row.

[j] Astronomers refer to any elements heavier than hydrogen and helium as metals

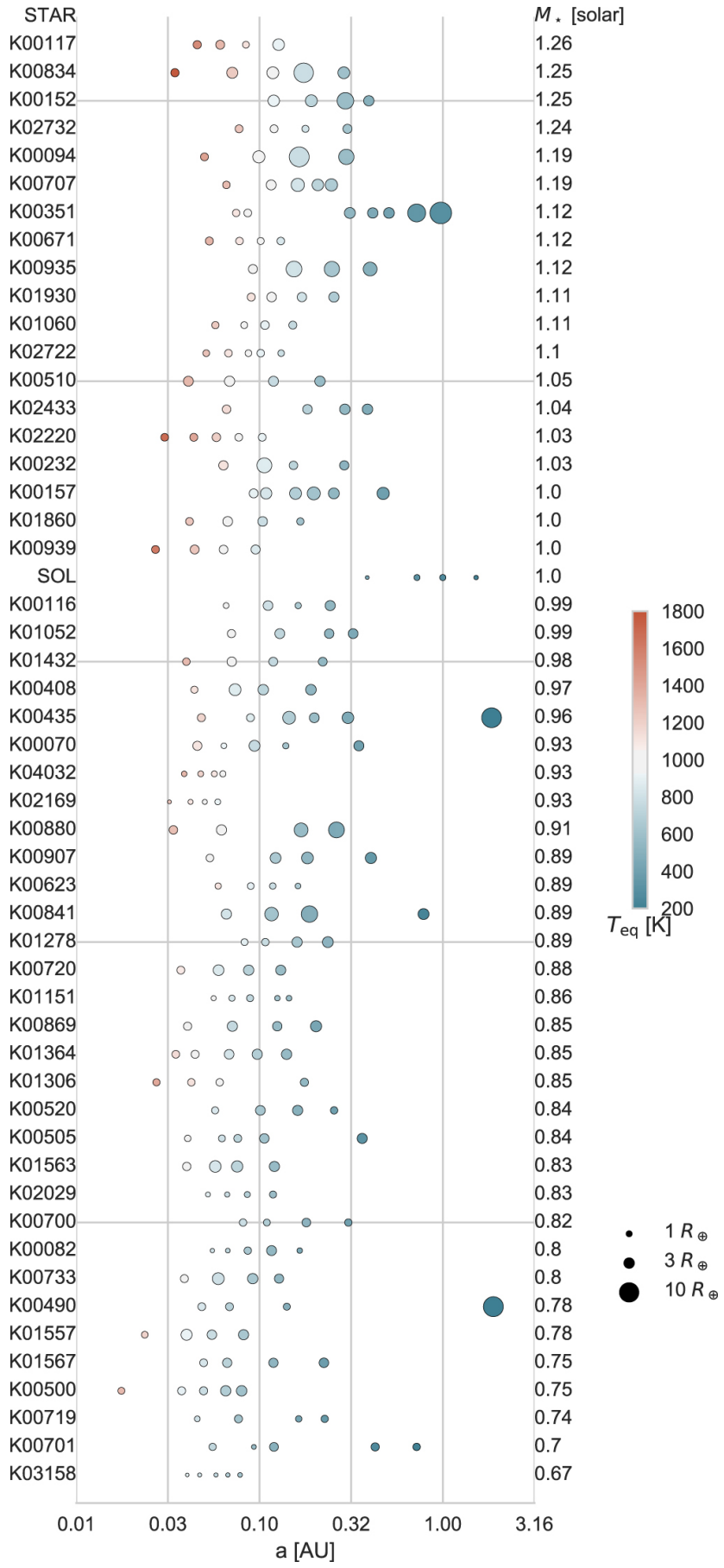

Figure 1.12: Plot from Weiss et al. (2018) which shows the system architectures of *Kepler* multi-planetary systems with at least 4 planets. Each row depicts a planetary system (name left), and each planet is plotted against its semi-major axis (AU) in log space. The size of each point depicts the planet's radius, and colour depicts their equilibrium temperature.

1.3.2.4 Post-main-sequence planets

Exoplanets have also been found around evolved stars such as pulsars. Pulsars are neutron stars which spin rapidly, and as such have strong magnetic fields. Pulsars emit radiation in two beams from their magnetic poles. As the neutron star rotates (if aligned with Earth) these breams are observed with extremely regular periods, similar to the light from a lighthouse. Periodic deviations in the timing of these observed beams can be used to detect the presence of orbiting planets. The first three exoplanets were in fact discovered in this way by Wolszczan & Frail (1992); Wolszczan (1994). Evidence for asteroids (planetessimals) around white dwarfs have been found in the form of metal pollution in white dwarf atmospheres (e.g. Vanderburg et al. 2015; Croll et al. 2017). Due to their formation, white dwarfs typically only contain carbon and oxygen (Veras 2016). If any are observed with other elements present, it is assumed that these elements must have accreted onto the surface of the star from a sub-stellar object (Veras 2016).

It is important to note, that any planets surrounding these evolved stars may have formed after violent stages in the stellar life-cycle. Pulsars form after the star undergoes a supernova explosion which is likely to destroy any orbiting planets, while white dwarfs are remnant stellar cores after the star sheds its outer layers. Therefore, planets orbiting these stars likely formed after these stages, and are unlike the other exoplanets discussed in this thesis.

1.3.3 Planet formation

The ways which any of these planets form, including our Earth, is still largely a mystery to us. However, a number of theories have emerged based on observations of exoplanets and their demographics described above. In this section I will briefly introduce some of these theories and describe how planets form from a disk of gas and dust surrounding a star.

Stars form from the Interstellar Medium (ISM), the clouds of gas and dust within galaxies. Over-densities in the ISM undergo gravitational collapse to form a protostar, with the surrounding material flattening into a disk due to conservation of angular momentum. This disk of material continues accreting onto the star and is known as an accretion (or circumstellar) disk. Once the protostar reaches hydrostatic equilibrium (i.e. when the pressure from fusion in its core is equally balanced with the gravitational forces causing the contraction of the gas), it stops accreting material, and is now referred to as a star (Roberge & Kamp 2010). The remaining material in the surrounding disk becomes known as the protoplanetary disk, and is where planet formation takes place.

Observations of our solar system reveal that the planets all lie in a single plane in circular orbits around the Sun, the logical reasoning for this configuration is that the planets all formed from a single disk of material surrounding the Sun, its protoplanetary disk. It is possible to infer a minimum mass for the disk by calculating the mass required to provide the planets with the amount heavy elements we observe today (Chambers 2010). Recent observations with the Atacama Large Millimeter Array (ALMA) reveal these protoplanetary disks in-situ around their stars. Figure 1.13 shows an ALMA image of the HL Tau system (ALMA Partnership et al. 2015). The bright regions correspond to thermal emission from the disk, but what is astonishing is the detail with which we are able to view the structure of the protoplanetary disk.

Dark bands in the disk correspond to regions which have been thinned of material by an orbiting body, or protoplanet. Further details on protoplanetary disks can be found in Roberge & Kamp (2010).

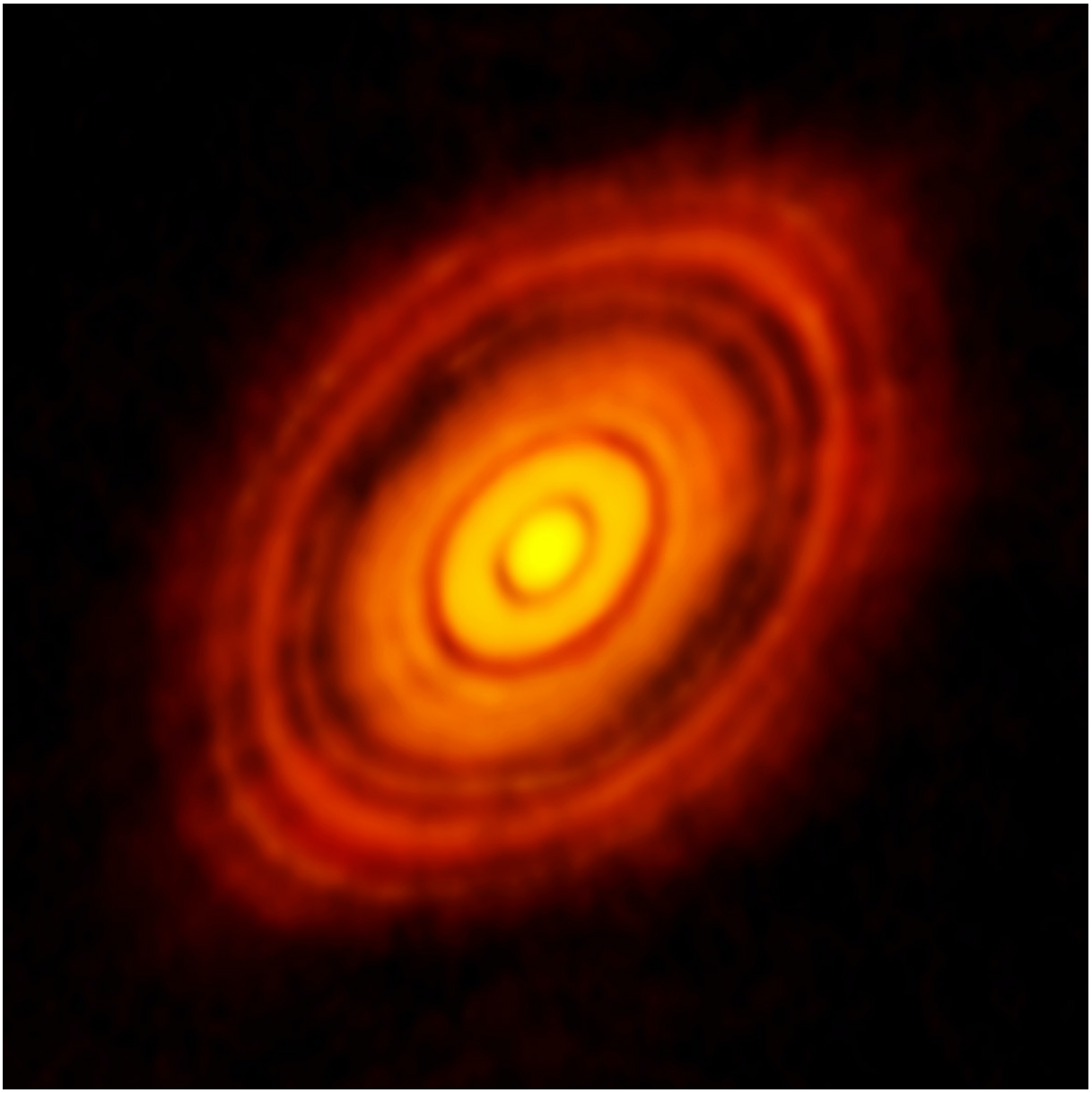

Figure 1.13: ALMA dust continuum image of the protoplanetary disk surrounding the star HL Tau from ALMA Partnership et al. (2015).

1.3.3.1 Rocky cores

In the protoplanetary disk, planet formation begins as microscopic dust grains coalesce into larger 'pebbles' a few cm in size (Izidoro & Raymond 2018). These pebbles continue to grow through collisions, and gravitational attraction, and coalesce into larger bodies known as 'planetesimals' which are approximately a few kilometers across (asteroids) (Chambers 2010; Izidoro & Raymond 2018). The efficiency of this growth depends on how turbulent the disk is. The more turbulent, the higher the velocity

of the particles hindering their ability to coalesce, instead colliding and fragmenting (Chambers 2010). The larger the planetesimal, the greater its gravitational interaction with the material in the disk, and consequently, the faster it can accrete mass. This stage of planet formation is known as 'runaway growth' (Raymond et al. 2014; Izidoro & Raymond 2018).

Once a planetesimal reaches approximately 100 times the mass of an average planetesimal (0.01 – 0.1 $M_\oplus$), it is referred to as a planetary embryo and planet formation enters the 'oligarchic' growth stage Chambers (2010); Raymond et al. (2014); Izidoro & Raymond (2018). During oligarchic growth each region of the disk is dominated by an embryo. These embryos continue to grow by accreting planetesimals and interacting with one another. If Mercury or Mars formed via this process they could be leftover planetary embryos (Raymond et al. 2014).

Planetary embryos continue to accrete mass from the disk. To explain the existence of super-Earths and sub-Neptunes Lambrechts & Johansen (2012) postulated that at this stage, if the disk mass is still dominated by pebbles, planetary embryos would accrete pebbles efficiently and quickly grow to several $M_\oplus$, and referred to this process as 'pebble accretion'. Once planetary embryos reach this mass they obtain thick gaseous envelopes from the disk, increasing the drag on passing pebbles and planetesimals, in turn increasing their chance of capture (Chambers 2010). Once a planetary embryo grows it perturbs the surrounding disk through gravitational interactions, opening a gap in material in the disk and a pressure bump outside its orbit (Izidoro & Raymond 2018). This stops pebbles from migrating inwards and slows the growth of the embryo.

This final stage of planet formation is known as 'late-stage' growth, and involves oligarchic growth of leftover material and numerous chaotic collisions of these large planetary embryos (Raymond et al. 2014; Izidoro & Raymond 2018).

1.3.3.2 Gas giant formation

Formation of gas giant planets place constraints on the formation processes described above. For a gas giant planet to form, a planetary embryo must first obtain a mass of $\approx 10\,M_\oplus$ before runaway gas accretion is able to take place, which in turn allows the planet to achieve the masses known of gas giant planets (D'Angelo et al. 2010). The embryo must achieve this mass before the protoplanetary disk dissipates, which is believed to occur in approximately $1 - 10$ Myr (Haisch et al. 2001; Lissauer & Stevenson 2007; D'Angelo et al. 2010). Forming these planets in these short timescales require a large amount of available mass in the disk. It is therefore thought that gas giants form outside of the "snow line" where the distance from the star provides temperatures which allow for water ice to form, leading to greater amount of solid material (D'Angelo et al. 2010). The pebble accretion model described above (Lambrechts & Johansen 2012) provides a mechanism for these planets to obtain large masses in timescales shorter than the disk lifetime. As large planets form they open a gap in the protoplanetary disk, starving the planet of material (D'Angelo et al. 2010). Pebbles continue to be accreted as they experience gas drag from the disk and migrate through the gap towards shorter orbital periods (D'Angelo et al. 2010; Lambrechts & Johansen 2012).

Lack of mass in the disk at < 0.1 AU from the star means that in-situ formation of observed hot Jupiter exoplanets is unlikely. The favoured formation scenario for these extreme objects is that they formed outside the "snow line" and then migrated inwards (Section 1.3.4) to their observed locations (Lin et al. 1996; Bodenheimer et al. 2000; Fabrycky & Tremaine 2007).

There is a large volume of literature demonstrating that the presence and formation of giant planets in a system can strongly affect the formation of terrestrial planets in the system. Raymond (2006) and Raymond & Izidoro (2017) demonstrate through N-body simulations that the location of a giant planet can inhibit the growth of terrestrial planets within the habitable zone. They suggest that for the formation of habitable water rich planets a giant planet must be located at > 3.5 AU. This is supported by Morbidelli et al. (2012), where they find that planetesimals scattered by giant planets outside the snow line can deliver water to inner terrestrial planets.

1.3.4 Planet migration

Radial migration of planets in the disk is a mechanism which determines the final orbital location for many planets. It explains the observed orbital radii of hot-Jupiters and circumbinary planets which are thought to be unable to form in-situ, but rather form at larger orbital radii and migrate inwards (see Section 1.4). Here I will briefly discuss the two types of migration thought to occur to planets within the disk, and how planetary orbits might change without the presence of the disk.

1.3.4.1 Type-I migration

Planets excite spiral density waves in the gaseous disk, one within the orbital radius of the planet, and one outside (Lubow & Ida 2010; Ormel et al. 2012). These density waves each exert a torque on the planet, the inner causes the planet to increase angular momentum, and the outer causes the planets angular momentum to decrease. The outer wake's torque is slightly greater than that of the inner wake, thus decreasing the planets angular momentum and causing the planet to migrate inwards (Ward 1997; Lubow & Ida 2010), this is known as type-I migration.

1.3.4.2 Type-II migration

Type-II migration occurs in the instance where a planet is large enough ($\gtrsim 0.2$ M_J) to clear a gap in the disk around its orbit (Lin & Papaloizou 1986; Lubow & Ida 2010). Torques acting on the planet from the material inside its orbit, balance those from the material outside the orbit, locking the planet in the gap. The planet then migrates inwards along with the disk as it is accreted to the star (Lin & Papaloizou 1986; Lubow & Ida 2010).

Unfortunately, the estimated timescales for each of these migration types are far too short and would result in any planets quickly migrating through the disk and fall into the host star (Lubow & Ida 2010). There are many competing theories as to mechanisms which could slow the migration of the planet. Discrepancies in disk density at certain orbital radii could slow type-I migration, or additional currently

unknown torques could be acting on planets slowing their migration (Alibert et al. 2004; Lubow & Ida 2010; Morbidelli & Raymond 2016). Further details on orbital migration can be found in Lubow & Ida (2010).

1.3.4.3 Dynamical instability

Planetary interactions can also vary the orbital radius of planets in a system. During migration, planets can find themselves in orbits which cross that of other planets, or close enough so that they can interact gravitationally. If this occurs the planets orbits can be changed drastically. Giant planets migrating through the disk can excite the eccentricities of smaller planets or even eject them from the system entirely (Raymond et al. 2014). Even after disk dispersal, if surviving planetary orbits are unstable they will eventually interact with each other, exciting eccentricity or ejecting planets entirely. Raymond et al. (2014) shows that in the presence of several gas giant planets interacting via dynamical instabilities, smaller planets are ejected from the system and eccentricities of the remaining giant planets are excited. This could explain the large range of eccentricities observed for gas giant planets (Winn & Fabrycky 2015). Planet-planet scattering is another potential formation pathway for eccentric hot Jupiters. Eccentric gas giant planetary orbits (caused by planet-planet scattering) could be circularised by star-planet interactions (Nagasawa et al. 2008; Beaugé & Nesvorný 2012; Raymond et al. 2014).

1.4 Circumbinary exoplanets

This thesis focuses on the discovery of circumbinary planets. These are exoplanets that orbit around a tight binary star system, with their orbits enclosing that of the binary star pair. Planets in binary systems have been at the forefront of works of science fiction for decades (see Figure 1.14), and were long hypothesised to exist in nature (e.g. Borucki & Summers 1984; Schneider 1994). The first confirmed circumbinary planet was not detected until 2011 by Doyle et al. (2011) (see Section 1.4.4 for a discussion on the first circumbinary planet discovered orbiting a pulsar in Thorsett et al. (1999)). In this section I will describe circumbinary planets, their orbital characteristics, list their discoveries to date, and describe their demographics. For a description of the search for circumbinary planets carried out in this thesis see Chapter 4.

Figure 1.15 demonstrates the possible architectures of exoplanets within binary star systems. Circumprimary planets only orbit the primary star of a binary system, while circumsecondary planets orbit the secondary star. Collectively these orbits are also known as "s-type" (satellite-type) orbits, though henceforth will be referred to as circumprimary/secondary only. Similarly, circumbinary orbits are also known as "p-type" (planet-type) orbits, but will henceforth be referred to as circumbinary only.

In Section 1.3.2, I established that current estimates for the presence of giant planets around single Sun-like stars were of the order $\approx$ 10%, and small planets up to 50% (Winn & Fabrycky 2015). In comparison, binary (or even higher order) star systems comprise around half of all stellar systems containing Sun-like stars in the galaxy (Duquennoy & Mayor 1991; Raghavan et al. 2010). Yet, despite

Figure 1.14: Luke Skywalker stares longingly at the binary sunset on his circumbinary home planet of "Tatooine", as John Williams's "Binary Sunset" theme swells into its crescendo. *Star Wars IV - A New Hope* (Lucas et al. 1977).

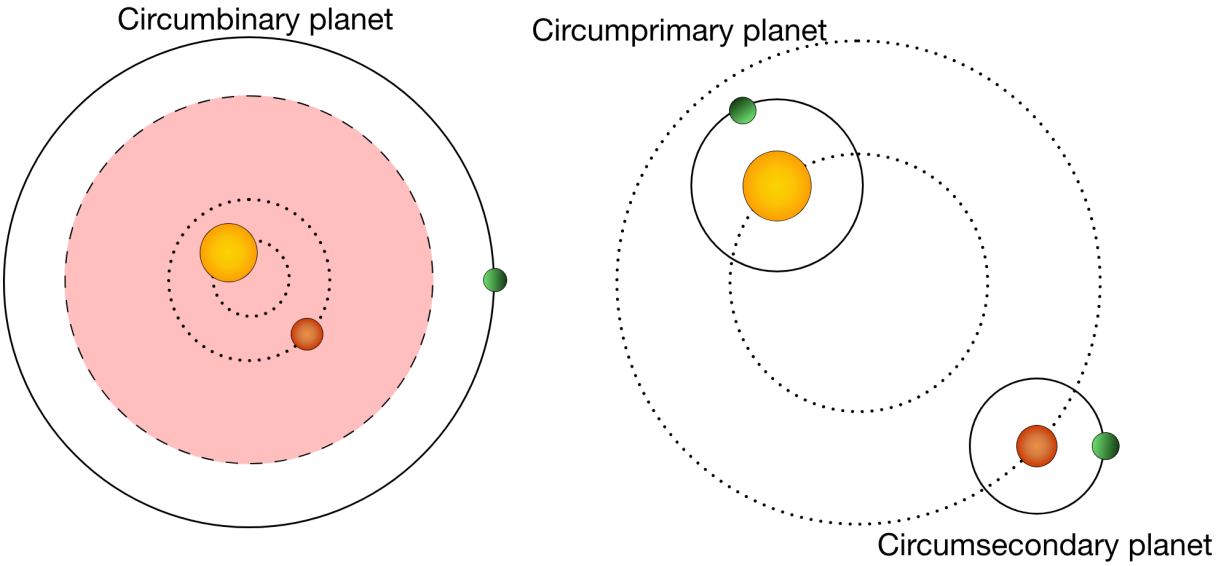

Figure 1.15: Schematic of planetary orbits within binary star systems. Left: A circumbinary planetary system, consisting of a close binary with the primary star (yellow), and secondary star (red), orbited by a circumbinary planet (green). The red shaded region surrounding the binary depicts the instability region. Right: A circumprimary/secondary planetary system, within a wide binary. The primary star (yellow) is orbited by a circumprimary planet (green), and the secondary star (red) is orbited by a circumsecondary planet (green). Adapted from Martin (2017a).

856 eclipsing binaries with binary orbtial periods between 5 – 50 days (the binary periods of known circumbinary planet hosts) being observed by *Kepler* (Slawson et al. 2011), only 12 circumbinary planets have been discovered by *Kepler* around 10 binaries (Table 1.1, Figure 4.25). Another two circumbinary planets have been discovered by *TESS*, TIC-1729b (Kostov et al. 2021), and TOI-1338b (Kostov et al. 2020) a system which is investigated further in Chapter 6.

Table 1.1: Orbital parameters for discovered circumbinary planets and their binary hosts.

System name	M_A ($M_\odot$)	M_B ($M_\odot$)	P_{bin} (days)	e_{bin}	P_p (days)	M_p ($M_\oplus$)
Kepler-16[1,2]	0.654	0.1964	41.078	0.15994	228.776	105.8 ± 5.1
Kepler-34[3]	1.048	1.021	27.796	0.52087	288.822	69.9 ± 3.2
Kepler-35[3]	0.888	0.809	20.734	0.1421	131.458	40.4 ± 6.4
Kepler-38[4]	0.949	0.249	18.795	0.103	105.595	< 122
Kepler-47 b[5,6]	0.957	0.342	7.448	0.0288	49.514	2.1 ± 23.7
Kepler-47 d	-	-	-	-	187.3	19.0 ± 23.8
Kepler-47 c	-	-	-	-	303.158	3.2 ± 2.2
Kepler-64[7,8]	1.47	0.37	20.000	0.204	138.51	< 169
Kepler-41[9]	0.82	0.542	10.116	0.0365	66.262	67 ± 22
Kepler-453[10]	0.934	0.194	27.322	0.051	240.503	< 16
Kepler-1647[11]	1.221	0.968	11.259	0.1602	1107.592	483 ± 206
Kepler-1661[12]	0.841	0.262	28.163	28.163	175.06	17 ± 12
TOI-1338[13]	1.127	0.3128	14.609	14.609	95.174	33 ± 20
TIC-1729[14]	1.238	1.202	19.658	19.658	204.046	981.3 ± 5.7

Notes: 1 - Triaud et al. (2022), 2 - Doyle et al. (2011), 3 - Welsh et al. (2012), 4 - Orosz et al. (2012b), 5 - Orosz et al. (2012a), 6 - Orosz et al. (2019), 7 - Schwamb et al. (2013), 8 - Kostov et al. (2013), 9 - Kostov et al. (2014), 10 - Welsh et al. (2015), 11 - Kostov et al. (2016), 12 - Socia et al. (2020), 13 - Kostov et al. (2020), 14 - Kostov et al. (2021)

In addition to these transit detections, HD 202206b a circumbinary planet candidate (Correia et al. 2005), later to be re-classified as a brown dwarf (Benedict & Harrison 2017), Kepler-16b (Triaud et al. (2022), Chapter 5), and TOI-1338/BEBOP-1c (Chapter 6) are the only circumbinary planets detected with radial velocities so far. 2MASS0103(AB)b (Delorme-1b) a circumbinary planet/brown dwarf (Delorme et al. 2013), and HD 106906b (Bailey et al. 2014; Lagrange et al. 2016) have been discovered with direct imaging. There have also been some microlensing discoveries such as OGLE2007-BLG-349(AB)b (Bennett et al. 2016), which we are unfortunately unable to confirm due to the nature of microlensing events (Section 1.2). Circumbinary planets have also been discovered around post-main sequence binary stars such as NN Ser (Beuermann et al. 2010). These are discussed in more detail in Section 1.4.4.

The low detection rate of these planets can partly be explained by innate difficulties in observations of binary star systems, along with difficulties for planet formation in these unique stellar environments.

1.4.1 Circumbinary orbital stability

The dearth of discovered circumbinary planets leads to the question of planetary stability in this orbital arrangement. Numerous studies have been carried out in this area, the most heavily cited being Holman & Wiegert (1999) and Mardling & Aarseth (2001). Holman & Wiegert (1999) build on the work of Dvorak et al. (1989) and demonstrate using numerical simulations that there exists a region of instability surrounding the binary extending out to $\approx 3\ a_{bin}$, depending on the eccentricity of the binary, following (Holman & Wiegert 1999):

$$\frac{a_c}{a_{bin}} = (1.6 \pm 0.04) + (5.1 \pm 0.05)e_{bin} + (-2.22 \pm 0.11)e_{bin}^2 + (4.12 \pm 0.90)\mu_{bin} + (-4.27 \pm 0.17)\, e_{bin}\, \mu_{bin} + (-5.09 \pm 0.11)\mu_{bin}^2 + (4.61 \pm 0.36)\, e_{bin}^2\, \mu_{bin}^2 \quad (1.17)$$

Where a_c is the "critical semi-major axis" or instability limit, a_{bin} is the semi-major axis of the binary, e_{bin} the binaries eccentricity, and μ_{bin} the binary mass ratio = $M_2/(M_1 + M_2)$, where M_1 and M_2 refer to the masses of the primary and secondary stars respectively. A rough approximation leading from these analyses is that $a_c/a_{bin} \approx 3$ (Martin 2017a). Transforming this into binary period using Kepler's third law gives $P_c \approx 3^{3/2} P_{bin} \approx 5 P_{bin}$. Any orbit crossing this instability limit (illustrated by the red shaded region in Figure 1.15) would be ejected from the system, while planetary orbits outside this limit are stable. With the median orbital period of the *Kepler* eclipsing binary catalogue at 2.8 days (Martin 2018), the constraint of the instability limit leads to planetary orbital periods > 14 days. Thus placing circumbinary planets at longer orbital periods than the majority of planets discovered by the transit technique (see Figure 1.2).

1.4.2 Observational challenges

The majority of circumbinary planets found to date have been detected by the transit method, specifically while monitoring eclipsing binary systems by the *Kepler* (Borucki et al. 2010) and *TESS* (Ricker et al. 2015) transit missions (Table 1.1). Circumbinary planets have a high likelihood to transit their host stars due to their orbital precession caused by three body orbital dynamics (Martin & Triaud 2015). If the binary itself is eclipsing the transit likelihood is nearly 100% (Martin & Triaud 2015). This likelihood to transit provides an opportunity to perform atmospheric spectroscopy (Section 1.2.3) on the atmospheres of cool transiting planets (Martin & Triaud 2015). Unfortunately, the same orbital precession also leads to periods where no transits are observed for years (Martin & Triaud 2014; Martin 2017b). Martin (2017b) finds that the majority of the *Kepler* transiting circumbinary planets are in a transiting configuration < 50% of the time, with some spending even less at < 20%. Thus, the chances for circumbinary planet detection via the transit technique are maximised by missions utilising long stares such as *Kepler*, and the upcoming *PLATO* mission (Rauer et al. 2014). Figure 1.16 shows the lightcurve of Kepler-16 from Doyle et al. (2011). In around ≈ 600 days of monitoring by the *Kepler* space telescope only 3 transits of the planet are observed. *TESS*'s observing strategy makes it less efficient in discovering these objects in comparison to *Kepler* as it observes a 'sector' of the sky for 27 days before moving on to another, not returning to observe the same field for months. Many circumbinary planet transits are likely missed by *TESS*. Despite this, *TESS* has discovered two circumbinary planets thus far, TOI-1338 b (Kostov et al. 2020), and TIC-1729 b (Kostov et al. 2021). TOI-1338 b was discovered in the mission's 'continuous viewing zone' at the ecliptic where longer lightcurve monitoring is possible, whereas TIC-1729 b was discovered within a single TESS sector as it transited the primary star and then the secondary star 5 days later (Kostov et al. 2021).

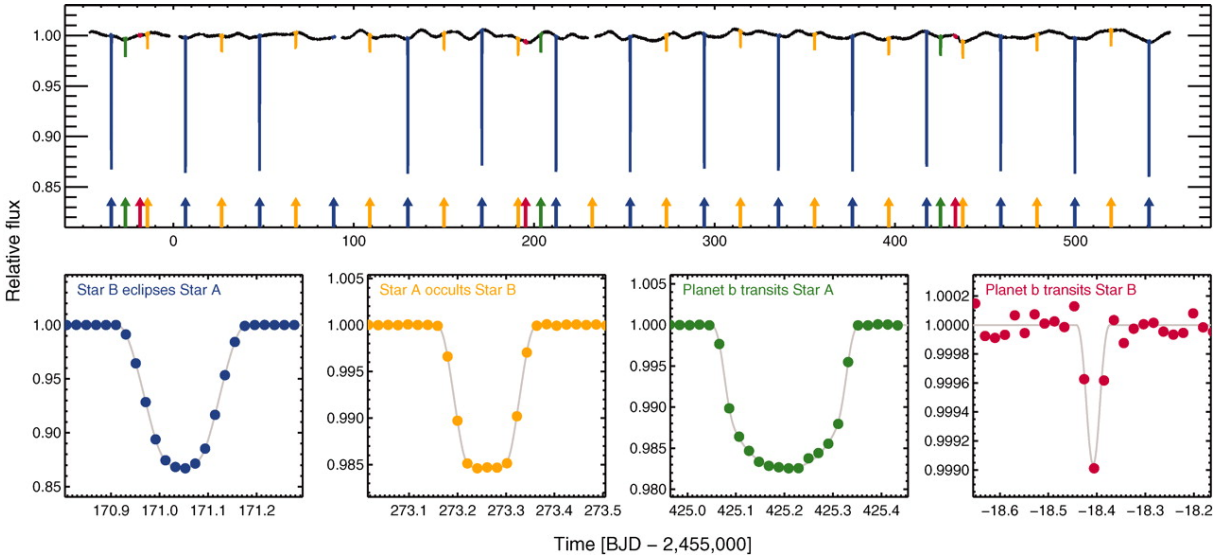

Figure 1.16: Lightcurve of Kepler-16 from Doyle et al. (2011) over ≈ 600 days. Primary eclipses of the binary are marked in blue, secondary binary eclipses in yellow. The transits of the planet as it passes in front of the primary star green, and the transits of the planet in front of the secondary star in red.

Attempts have been made to discover these planets with radial-velocities through The Attempt To Observe Outer-planets In Non-single-stellar Environments (TATOOINE) (Konacki et al. 2009) (named after the Star Wars planet in Figure 1.14), and BEBOP (Martin et al. 2019) (see Chapter 4). The process is complicated by contamination of the observed spectra from the second star in many cases, along with the presence of post-Keplerian effects (discussed in more detail in Chapter 4). It is possible to avoid this spectral contamination through observing only binary star systems where the secondary star is far smaller and fainter than the primary star (known as Single line Spectroscopic Binarys (SB1s)). This results in the secondary spectra being too faint to be detected by our instruments, and yields RV measurements akin to single stars. Further discussion on the detection of circumbinary planets using radial velocities can be found in Chapter 4. Therefore, to date only two circumbinary planets have been detected using RV observations. A detection of Kepler-16 b by the BEBOP project (Triaud et al. 2022) covered in detail in Chapter 5, and the discovery of a second planet BEBOP-1c in the TOI-1338/BEBOP-1 system, discussed in Chapter 6 (Standing et al. (In review)).

1.4.3 Circumbinary planet demographics

Most circumbinary planets found to date seem to lie close to their instability limit, at approximately $6xP_{bin}$ (Winn & Fabrycky 2015; Martin 2018) (see Figure 1.17). The only exceptions are Kepler-1647 b, along with the outer planets in Kepler-47, and TOI-1338/BEBOP-1 (Chapter 6) the only known multi-planetary circumbinary systems. Welsh et al. (2014) suggest this is either a natural preference for the planets following their formation, or the result of an observing bias. Martin & Triaud (2014) simulated the circumbinary planet population from *Kepler*, and could not reproduce this phenomenon with an observing bias alone (Martin 2018). This leads to the assumption that circumbinary planets are observed in this region due to an effect from their formation. Meschiari (2012); Paardekooper et al. (2012); Lines

et al. (2014), and Pierens et al. (2020) find that perturbations in the protoplanetary disk excited by the binary inhibit planet formation close to the binary. Therefore, circumbinary planets must form $\gtrsim 4$ AU and migrate inwards, via the processes discussed in Section 1.3.3, coming to rest near the instability region (e.g. Nelson 2003; Pierens & Nelson 2013; Kley & Haghighipour 2014; Pierens & Nelson 2018).

All detected circumbinary planets have a radius ≥ 3 $R_\oplus$ (Winn & Fabrycky 2015). Martin & Fitzmaurice (2022) propose a theoretical explanation for these observations, as opposed to the observing bias where larger planets are easier to detect. Using N-body integrations of planetary migrations in a circumbinary disk, Martin & Fitzmaurice (2022) find that the known circumbinary planets do not exist within any unstable regions, and that smaller planets are more likely to be ejected during migration when compared to their larger brethren.

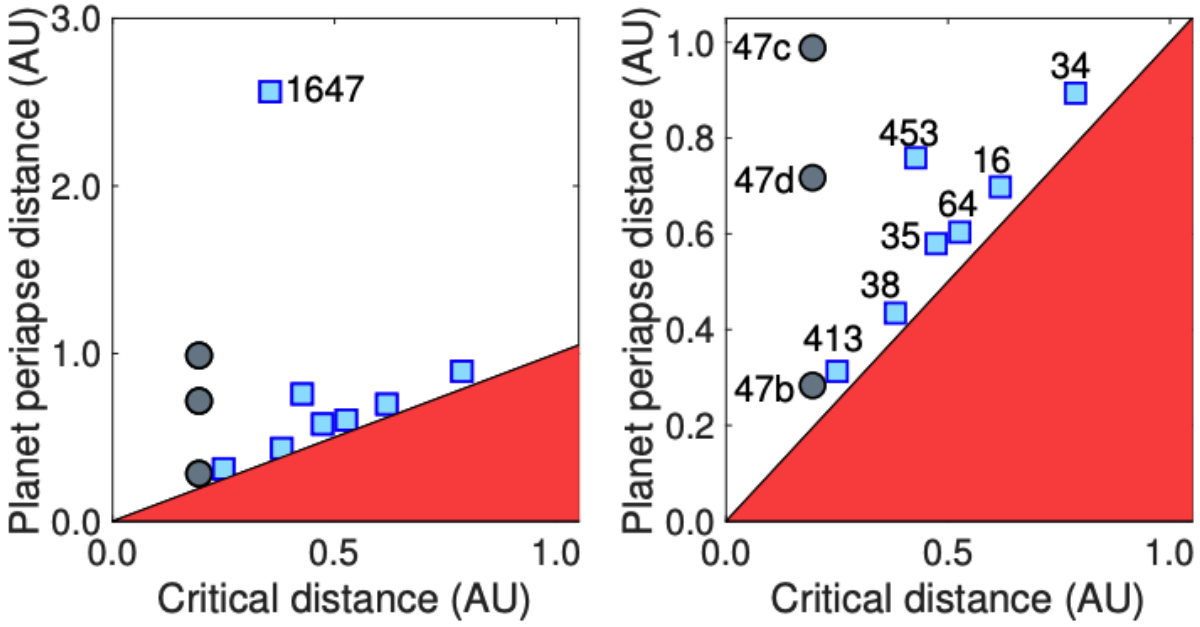

Figure 1.17: Plot of *Kepler* circumbinary planet periapse distance, $a_p(1 - e_p)$ against the instability limit from Equation 1.17. The red region depicts the unstable region surrounding the binaries. Kepler-47's multi-planetary system is depicted by the grey circles in comparison to the blue squares for the single planet systems. The right hand plot is zoomed in to the instability limit excluding Kepler-1647. Planets are labelled by their *Kepler* numbers. Plot taken from Martin (2018).

The occurrence rates for circumbinary planets with radii > 6 $R_\oplus$ and orbital periods < 300 days is approximately 10% (Armstrong et al. 2014) around binaries with orbital periods between $7 - 41$ days. This is compatible with the occurrence rates observed around single stars (Section 1.3.2) (Martin 2018).

When sorting circumbinary host systems by binary period, it seems that the circumbinary planets all orbit binaries within the longer-period half of the distribution (Winn & Fabrycky 2015). Martin & Triaud (2014) confirm this phenomenon does not seem to be an observational bias, and if confirmed supports the theory that close binary stars with periods $\lesssim 5$ days form through a different mechanism such as orbital shrinking via tidal circulation (Fabrycky & Tremaine 2007).

With RV follow-up ability limited, the masses for circumbinary planets are obtained from the Transit Timing Variation (TTV) method described in Section 1.2.3.2. In eclipsing binary systems it is possible

to infer the mass of an orbiting circumbinary planet by tracking the timing of the primary and secondary binary eclipses (Eclipse Timing Variations (ETV)'s).

Figure 4.25 in Chapter 4 shows that most circumbinary planet masses detected with TTV's only have upper limits on the masses. This is as the ETV amplitudes are short, of the order of seconds or minutes (Chapter 6), and demonstrates the need to determine accurate circumbinary planet masses. With current RV observations of TOI-1338/BEBOP-1 yielding no sign of TOI-1338b, an upper limit on the planet's mass can be placed at 23.6 $M_\oplus$ with 99% confidence (Chapter 6). This is lighter than the 33 ± 20 $M_\oplus$ initially estimated in Kostov et al. (2020), and yields a planetary density of < 0.39 g cm^{-3}. Therefore, the planet must be inflated, possibly to the extent of the 'super-puff' planets mentioned in Section 1.3.1. This trend may extend to other circumbinary planets, and provide and alternate solution as to why no small radius circumbinary planets have been detected (they are inflated).

1.4.4 Planets in post-main sequence binaries

The first circumbinary planet discovered is commonly quoted as Kepler-16 b (Doyle et al. 2011) (as I have mentioned in previous sections), though in reality one was discovered earlier by Thorsett et al. (1999). This discovery is often overlooked as the first circumbinary planet detection as the binary stars are a pulsar and white dwarf PSR B1620-26, both heavily evolved stars. The planet was discovered by monitoring variations in the timing of the radio pulses received by the pulsar as it rotates. The pulsar orbits a white dwarf star with a period of approximately 191 days, Sigurdsson et al. (2008) found the circumbinary planet has a mass of approximately $1 - 3$ M_J, and an orbital period of a few decades. Ford et al. (2000) propose that the planet was cast into a circumbinary orbit during stellar interactions within the globular cluster in which the system resides, i.e. it did not form in a circumbinary configuration.

Further circumbinary planet candidates have been found around evolved binary stars, including two gas giant planets with periods of 15.5 and 7.7 years orbiting a white dwarf and cool M-dwarf in the NN Ser system discovered in Beuermann et al. (2010) (later corroborated in Marsh et al. (2014)), and a circumbinary brown dwarf[k] orbiting the white dwarf and solar mass binary of V471 Tau in ≈ 30 years (Beavers et al. 1986; Guinan & Ribas 2001).

This being said, significant doubt has been cast on many of these objects. The brown dwarf candidate in V471 Tau was not detected by direct imaging in Hardy et al. (2015), and the candidate planets orbiting NN Ser were found to be dynamically unstable by Mustill et al. (2013) and Horner et al. (2014). In fact, Horner et al. (2014) find 4 of the 6 eclipse timing post main sequence circumbinary planets to be "catastrophically unstable", and suggest that underestimating uncertainties of the eclipse timings could be the cause of the planetary signals.

The methods used to discover post/pre-main sequence circumbinary planets, along with their extreme environments make them difficult to fully confirm and obtain reliable orbital parameters for, therefore this thesis will focus on the detection of circumbinary planets orbiting main sequence binary stars.

[k] A failed star which doesn't gain enough mass during its formation

In summary, circumbinary exoplanets can provide us with information on whether planet formation is affected by the presence of a second stellar object. Finding more of these objects may shine light on dominant evolution or formation scenarios in these extreme environments. My work as described in this thesis aims to discover more of these objects, constrain their masses and place detection limits on a population of binaries in an attempt to discern more accurate circumbinary planet demographics.

Chapter 2

Analysis of RV data

"Never tell me the odds!"

Han Solo, *Star Wars: The Empire Strikes Back*

In this chapter the statistical tools used for the Radial Velocity (RV) analysis in the following chapters are described. In Section 2.1 Bayesian statistics, nested sampling, and the modelling of Keplerian orbits are introduced. In Section 2.2 how these techniques are applied within `kima`, the code used to fit Keplerian models to RV data in the following chapters is described. I also describe the best practices in the use of `kima` for analysis of RV data, and how planetary parameters are obtained from the results of a `kima` run.

2.1 Bayesian statistics

In the field of exoplanets, when data is collected from observations of a star, the end goal is to establish whether there is a planetary signal present in this data. For radial velocities, the planetary signal follows a Keplerian model as seen in equation 1.8 and Figure 1.5. The parameters for each Keplerian model are K, P, e, f, ω, γ and i as in Section 1.2.2. The values that these parameters can assume for a model are referred to as its 'parameter space'. A single point in parameter space provides a single value for each parameter which calculate a model Keplerian signal. We must then fit this model signal to the data and calculate the probability that the parameters of our model are correct given the data. To calculate this probability we utilise Bayesian statistics.

Bayesian statistics is built on the idea that "*probability is a measure of the degree of belief about a proposition*" (Trotta 2008). In our case, this is the probability that the proposed planetary model caused the observed data, which is described by the Bayes theorem (Bayes & Price 1763; Trotta 2008):

$$p(H|d) = \frac{p(d|H)\, p(H)}{p(d)} \tag{2.1}$$

Where H represents the parameters of our model or hypothesis, d the data, and a lower case p a probability distribution. $p(H|d)$ is the posterior probability of the hypothesis given the data. $p(d|H)$ is known as the likelihood, and represents the likelihood of obtaining the data given the hypothesis is true. The prior $p(H)$ modulates the likelihood function, and allows the inclusion of any prior information available about the parameters of the model, such as unstable periods and eccentricities which can be discounted from the parameter space. In order to obtain absolute values for the parameters from the posterior distribution, the likelihood and prior distributions must be normalised by the evidence $p(d) = \sum_H p(d|H)p(H)$. The evidence sums all possible outcomes for the hypothesis.

Sampling from the posterior probability distribution then allows us to infer the areas in parameter space which have a greater probability of describing the data. The most common method of sampling this posterior distribution used in exoplanet science utilises a technique known as Markov Chain Monte Carlo (MCMC). A detailed description of this technique is beyond the scope of this thesis and further details can be found in MacKay et al. (2003), Trotta (2008) and Hogg & Foreman-Mackey (2018), though I will provide a brief description below.

An MCMC explores parameter space through the use of walkers. These walkers are allowed to 'roam' by proposing steps in parameter space. Each step must meet a certain criterion such as a certain increase in likelihood before being accepted. Their starting positions are randomised and they are then left to explore the distribution. Each step the walker makes is a recorded as a posterior sample.

Through numerous iterations the walkers move to areas of high likelihood. The initial samples from the walk are then discarded, known as the walkers' 'burn-in'. Numerous walkers are able to be used simultaneously depending on the computing power available.

Though MCMC is a powerful tool to sample the posterior distribution, the walkers can struggle to sample posterior distributions with multiple areas of high probability, known as 'multimodal'. The walkers tend to get stuck in localised areas of probability and fail to explore the parameter space efficiently, this problem can be compounded in large parameter spaces with a greater number of free parameters. For these posterior distributions another sampling method such as nested sampling is required to sample the posterior efficiently.

2.1.1 Nested Sampling

Nested sampling was chosen for use in my work as it performs reliably in cases with complicated multi-modal posteriors with widely separated areas of high likelihood (Skilling 2006).

It works by setting a number of particles throughout the prior distribution ($p(H)$), and at each iteration the particle with the lowest likelihood ($p(d|H)$) is replaced with a new particle. This new particle is sampled from the same prior distribution (generally using MCMC), with the constraint that the new particles likelihood must be higher than that of the one it replaces (Brewer et al. 2009). The removed point is recorded and assigned a value depending on the prior mass estimated at a higher likelihood to it. As this continues, particles move to higher and higher likelihoods. After a set number of iterations, the $1 - e^{-1} \approx 0.63212$ quantile is determined from the collected likelihoods. A new 'level' L_1 in parameter

space is then created, which occupies e^{-1} less of the prior parameter space (L_0). This continues creating higher and higher likelihood levels until either a set number of steps or levels have been reached, or the estimated highest likelihood level has been reached.

2.1.1.1 Diffusive Nested Sampling

The specific method of nested sampling utilised in this work is known as Diffusive Nested Sampling (DNS). DNS differs from classical nested sampling by sampling from a weighted combination of levels once the next level has been reached. I.e, once L_1 has been created, instead of sampling only from that level, DNS samples from a mixture of L_1 and L_0 weighted by an exponentially decaying function (Brewer et al. 2009).

Once the desired number of levels have been created, by choice or by reaching the maximum likelihood available, the particles are allowed to continue exploring all levels and the weightings for each level is changed to uniform. A uniform weighting results in a greater number of posterior samples, and therefore more accurate evidence estimates (Brewer et al. 2009). Allowing the particles to explore uniformly also ensures that no narrow peaks of high likelihood are missed in more complex probability distributions. Further details can be found in Brewer et al. (2009). Figure 2.1 illustrates the difference between classic and diffusive nested sampling.

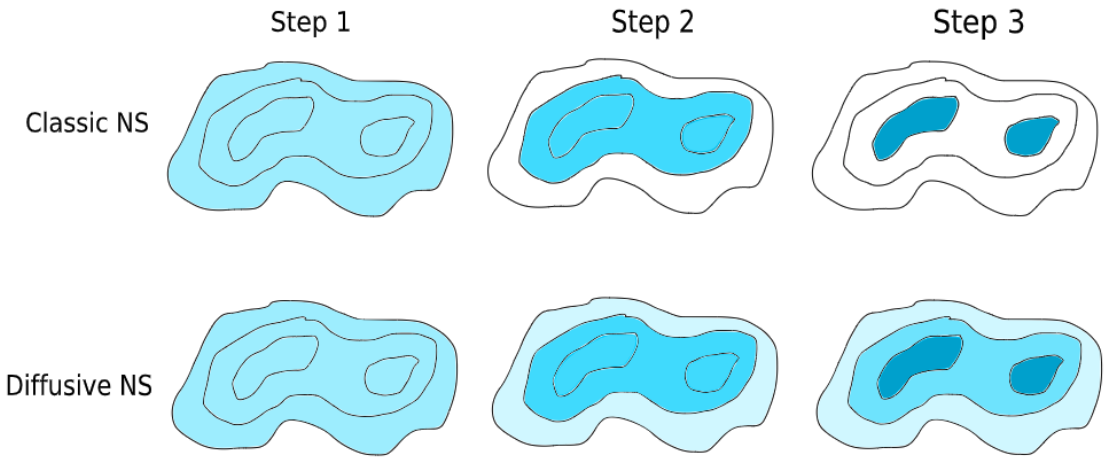

Figure 2.1: Illustration of the sampling levels at each stage for classic and diffusive nested sampling. For the bi-modal distribution shown, classic nested sampling could have difficulty exploring both islands of probability. However, diffusive nested sampling allows particles to travel more freely to isolated nodes of higher likelihood through lower levels. Figure from Brewer et al. (2009).

Due to DNS's sampling strategy, runs have two visibly separate phases as can be seen in Figure 2.2. The particles can be seen initially increasing in levels until the maximum number of levels have been reached, this is determined automatically by `DNest4` (Brewer et al. 2011). During this phase of the run, the particles can be seen to still explore some lower levels as discussed above. Following this stage, the particles are then left to explore all levels uniformly for a set number of iterations. In my work, these plots are visually inspected to ensure even exploration of the parameter space has occurred during a run.

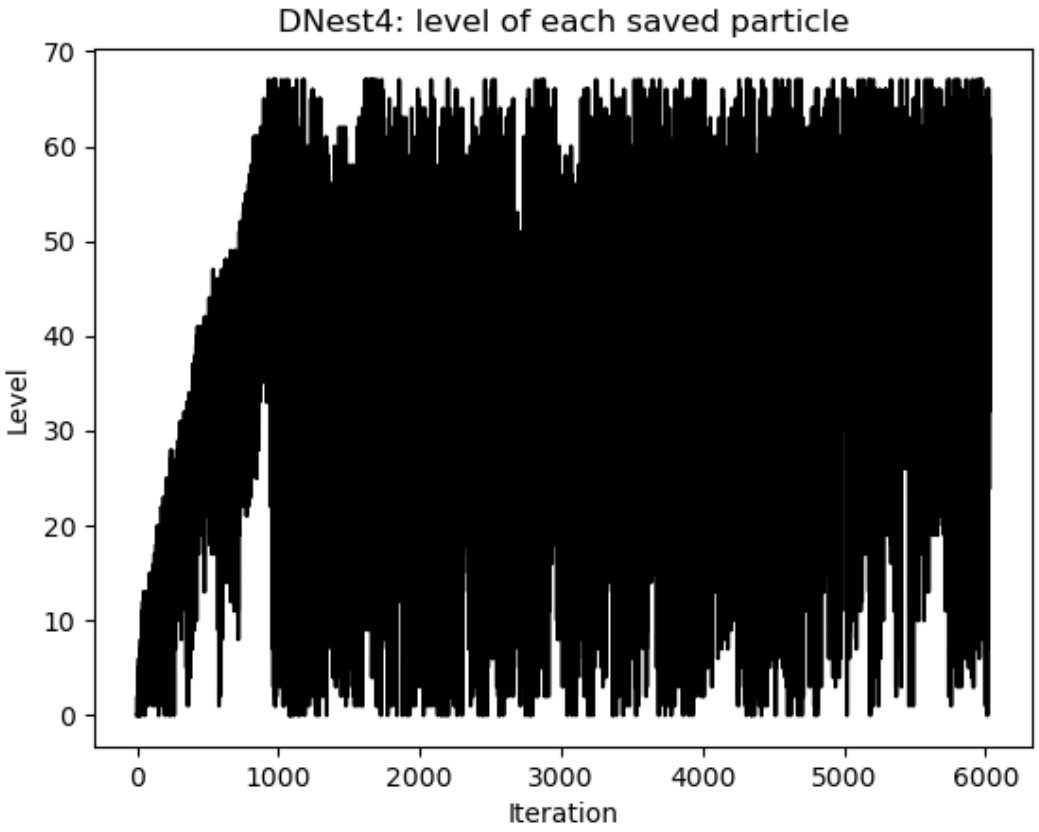

Figure 2.2: An example of a DNS run where the two stages of a run can be seen. The initial rising stage, where new likelihood levels are created until the maximum number of levels have been reached. During this stage the particle is still able to explore lower levels, allowing more freedom in exploration. Once the limit of the number of levels have been created, the particle is free to explore all levels with uniform weightings.

2.2 The `kima` package

The code used to fit Keplerian planet models to Radial Velocity (RV) data in the following sections is `kima`. Introduced in Faria et al. (2018), `kima` uses the Diffusive Nested Sampling DNS algorithm `DNest4` (Brewer et al. 2011) to sample the posterior distribution. `kima` can model RV data with a sum of $N_{\rm p}$ planetary Keplerian models, and estimate the posterior distributions of planetary parameters. Utilising a DNS approach provides `kima` with estimates on the evidence of each model, allowing for model comparison, which is discussed below.

The main advantage of `kima` and other codes such as e.g. `radvel` (Fulton et al. 2018), `pyaneti` (Barragán et al. 2019) etc, is its ability to treat $N_{\rm p}$ as a free parameter in the fit. `kima` is also efficient, written to support multi-threading, and allows for a run resulting in $\gtrsim 20,000$ posterior samples to be completed in a few hours on a standard laptop computer. For more information on `kima` such as how to install it, along with a few examples see the wiki.

2.2.1 Using kima to search for planetary RV signals

The parameters explored in a kima run are as follows: P, K, e, f and ω for each N_p. γ and σ_{jit} for each set of instrument RV values given, and an offset between each RV data file provided, if using 'multi-instrument' mode. Where P is the period of the fitted Keplerian signal, K its semi-amplitude, e its eccentricity, f its true anomaly, and ω its argument of periastron. N_p refers to the number of planetary signals fit to the data. This can be allowed to vary, and would result in $N_p \times P$,K etc, in each posterior sample. γ is the systemic velocity of the system (i.e, the velocity of the centre of the system with respect to the observer). σ_{jit} is an extra white noise 'jitter' term added to the data's uncertainty in quadrature to account for scatter. Prior distributions can be set for each of these parameters in the 'kima_setup.cpp' file.

Faria et al. (2018) have provided several example systems for kima. The first, and perhaps most straightforward to describe the output of kima, is 51-Peg. Running kima on this data as described in the wiki produces a detection of 51-Peg b as in Mayor & Queloz (1995). Running the command 'kima-showresults all' in command line then produces several standard plots of the resulting posterior samples. Figure 2.3 a) shows a phased periodogram of the highest likelihood posterior sample along with its associated RV residuals. While Figure 2.3 b) illustrates the number of posterior samples obtained for each available N_p specified, in this case N_p was allowed to uniformly explore 0 or 1 planetary signals. All resulting posterior samples are found with 1 planetary signal in the data, yielding very strong evidence in favour of a detection of planet 51-Peg b as in Mayor & Queloz (1995).

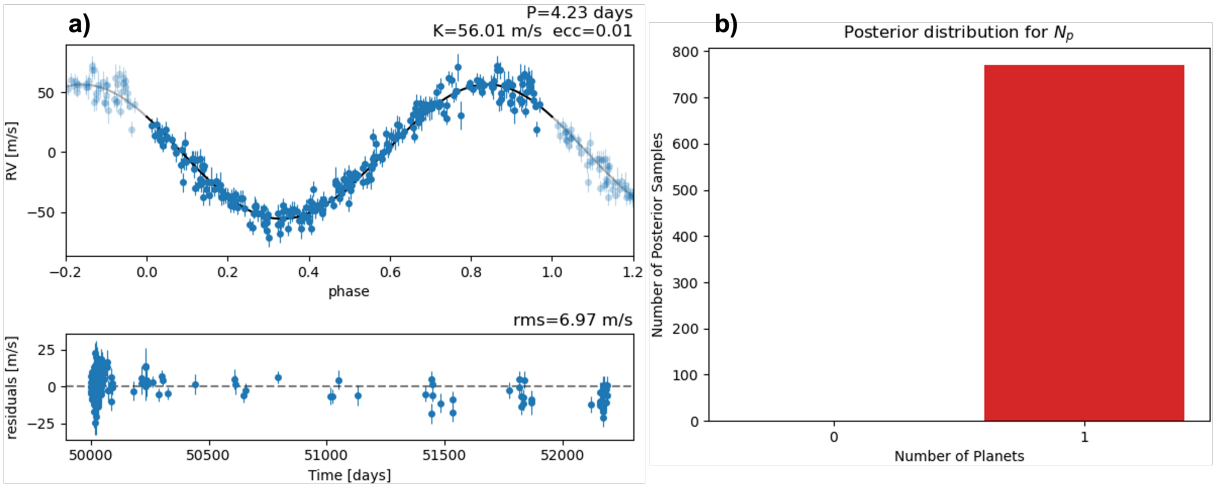

Figure 2.3: Default kima plots from posterior samples obtained from a kima run on the example data for system 51-Peg. a) Shows the phased keplerian plot of the data with the posterior Keplerian model with the highest likelihood, along with its associated residuals. b) Shows a histogram of the number of posterior samples with N_p. In this case N_p was allowed to vary uniformly between 0 and 1, as can be seen all posterior samples are found with $N_p = 1$, showing a definite detection of 51-Peg b as in Mayor & Queloz (1995).

In this case it is clear that one planetary signal can be found in the data. However, in RV surveys planetary signals are not always as clear and deciding between the number of signals present in the data can prove challenging. Below, how competing models are compared in a Bayesian framework is discussed.

2.2.2 Bayesian model comparison

When comparing two models (or hypothesis H_0, H_1) in Bayesian statistics it is possible to evaluate the ratio of their posterior probabilities (Trotta 2008):

$$\frac{p(H_0|d)}{p(H_1|d)} = B_{01}\,\frac{p(H_0)}{p(H_1)} \tag{2.2}$$

In words, the Posterior odds = Bayes factor × prior odds (Kass & Raftery 1995). This equation is obtained from Bayes theorem (Equation 2.1) ignoring the normalisation constant which depends only on the data. Here, B_{01} is known as the *Bayes factor*, and is defined as the ratio of the evidence between two competing models (Trotta 2008):

$$B_{01} \equiv \frac{p(d|H_0)}{p(d|H_1)} \tag{2.3}$$

The Bayes Factor (BF) therefore quantifies the support in favour of one model over the other. A more detailed description of the Bayes factor can be found in Kass & Raftery (1995).

For `kima` runs, the Bayes factor is utilised to compare the evidence for one model (e.g. with $N_\mathrm{p} = 1$) with another model (with $N_\mathrm{p} = 0$). This is achieved by simply calculating the ratio of the number of posterior samples obtained with $N_\mathrm{p} = 1$, to the number with $N_\mathrm{p} = 0$.

For example, Figure 2.4 shows the number of posterior samples obtained in favour of $N_\mathrm{p} = 0, 1, 2$ or 3 in a radial velocity analysis of the binary star system EBLM J0608-59 (TOI-1338/BEBOP-1, Chapter 6).

Here there are 0 samples obtained with $N_\mathrm{p} = 0$, 9 364 with $N_\mathrm{p} = 1$, 13 193 with $N_\mathrm{p} = 2$, and 12 754 with $N_\mathrm{p} = 3$. Therefore to calculate the BF in favour of $N_\mathrm{p} = 1$ over $N_\mathrm{p} = 0$ we calculate $9\,364/0 = \infty$. Since we cannot have an infinite BF, we replace the 0 with 1 sample and obtain a BF > 9 364 in favour of there being at least one planetary signal present in the data. Repeating the same process for $N_\mathrm{p} = 2$ over $N_\mathrm{p} = 1$ yields a BF = 1.41, and $N_\mathrm{p} = 3$ over $N_\mathrm{p} = 2$, BF = 0.97.

Once calculated, Bayes factors are interpreted against the Jeffreys' scale (Jeffreys 1961) as a measure of evidence strength. Table 2.1 taken from Standing et al. (2022) shows the evidence strength of each BF value. For the purpose of planetary detection, we take BF ≥ 150 as our detection threshold.

For use in the BEBOP survey (see Chapter 4) we also assign additional BF evidence thresholds to aid in our identification of planetary candidates. We use a BF > 6 to identify targets worthy of further observations. In theory, the BEBOP survey is blind, meaning all targets are observed homogeneously. However in the case that a target has a BF > 6 in favour of a planet, we obtain more observations to confirm the candidate signal. We use a BF > 12 as a threshold for 'moderate' evidence, > 35 as a > 3σ detection threshold (truly 3σ corresponds to a BF = 21 (Trotta 2008)), and BF > 70 to alert of targets with increasing evidence. When a target reaches a BF > 140 we target them more thoroughly with observations to confirm them at the established > 150 threshold. These additional levels are discussed in more depth in Standing et al. (2022), Section 4.3.4.

Returning to the BF values calculated for J0608-59, the BF > 9 364 (for $N_\mathrm{p} = 1$) passes the required 150 detection threshold, and therefore corresponds to strong evidence of there being at least one planetary

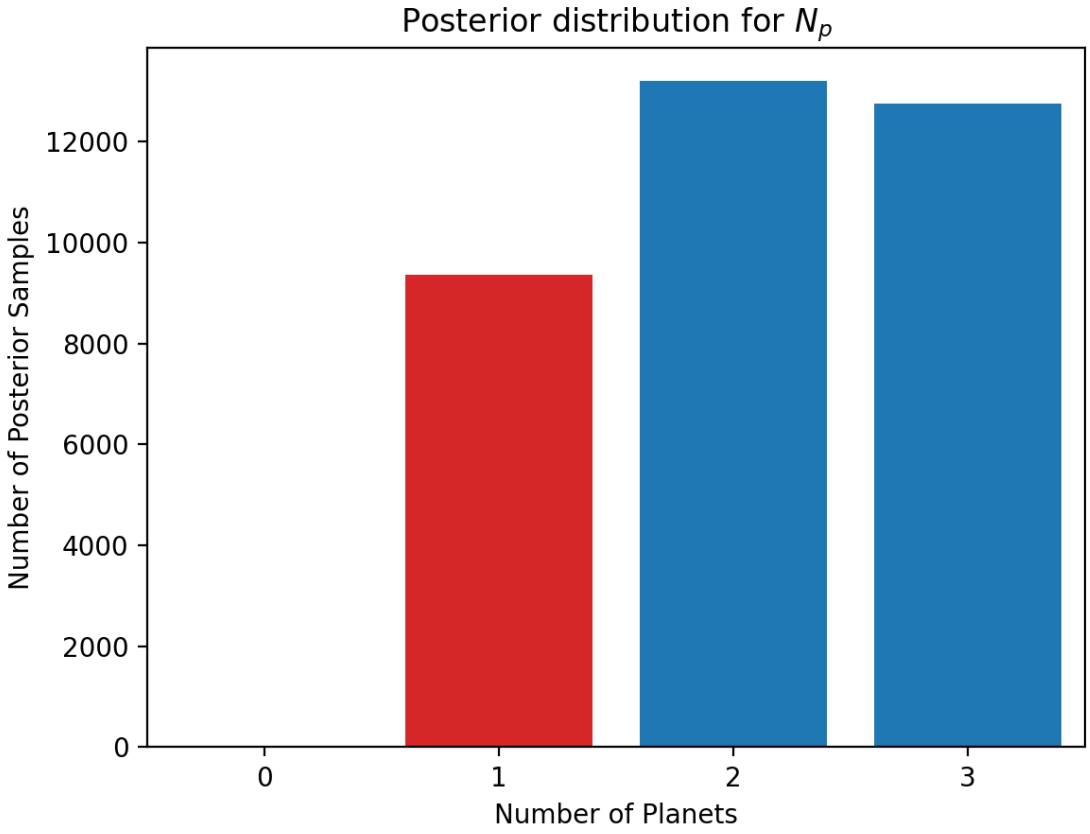

Figure 2.4: Histogram of the number of posterior samples with associated N_p from a `kima` run on radial velocity data for the Low Mass Eclipsing Binaries (EBLM) J0608-59 (TOI-1338/BEBOP-1) system (Chatper 6). The chosen N_p is decided from the Bayes factor as discussed in the text, and is displayed in red.

Table 2.1: Table of Bayes Factors (BF) along with corresponding probability, sigma values (standard deviations away from the mean of a normal distribution), and the "Jeffreys' scale" from Standing et al. (2022); Trotta (2008).

BF	Probability	sigma	Evidence strength
$\lesssim 3$	< 0.750	$\lesssim 2.1$	Inconclusive
3	0.750	2.1	Weak
12	0.923	2.7	Moderate
150	0.993	3.6	Strong

signal present in the data. Whereas, BF = 1.41 (for $N_p = 2$) yields inconclusive evidence for two planetary signals in the data. In this example we can claim the detection of a single planetary signal in the data. Further discussion on the J0608-59 system can be found in Chapter 6 (Standing et al. (In review)).

2.2.3 Testing `kima`

Once `kima`'s robust ability to detect planets was established, various planetary Radial Velocity (RV) signals were tested to identify any shortcomings of the algorithm. These tests are discussed briefly below.

2.2.3.1 One eccentric Vs. Two circular planets

When analysing Radial Velocity (RV) data it is important to remember that all Keplerian RV signals linearly add to each other, and are combined in the motion of the star. This could lead to incorrect interpretation of Keplerian signals. For example, in the case of two planets in a 2:1 orbital resonance (i.e, the outer planet's orbital period is roughly twice that of the inner planet) their influence on the star can appear as a single planet on a more eccentric orbit (e.g. Anglada-Escudé et al. 2010; Wittenmyer et al. 2013; Boisvert et al. 2018; Wittenmyer et al. 2019). Anglada-Escudé et al. (2010) describe this effect to be most prominent when the outer planet is the more massive of the two, and exaggerated by poor observational sampling of the orbits. Furthermore, they find that around 35% of published eccentric single planet systems cannot be distinguished from two planet circular orbit systems in this 2:1 orbital resonance. To correctly distinguish between these two configurations, the number of observations $N_{\rm obs}$ on the systems must be increased, ensuring evenly sampled orbits of the planets in question.

To test `kima`'s response to such an orbital configuration, I wrote a python script to simulate RV observations. The script can include random deviations in observation night, along with times within the nights. It also introduces a level of scatter to the data points which could be tailored to a specific system's residual Root Mean Squared (RMS) scatter. The simulated data was run through `kima` with no additional scatter, and included scatter to test the simulation script. In both instances `kima` found the inserted signal.

Taking the 51-Pegasi planet system (Mayor & Queloz 1995) as inspiration, RV data for a two planet system in 2:1 resonance with $P_1 = 4.23$ d, and $P_2 = 8.46$ d was simulated with the same cadence (observation times) as the ELODIE observations for 51-Peg. Eccentricity was kept low $e = 0.01$, and they were given the same phase. The masses of the planets were varied in several combinations, the outer having double the mass of the inner planet, the same mass, and the same semi-amplitude signal for both.

Running `kima` on each system, and then systematically lowering the semi-amplitude signals on each system yielded the same result as predicted in (e.g. Anglada-Escudé et al. 2010; Wittenmyer et al. 2013; Boisvert et al. 2018; Wittenmyer et al. 2019). Both planets were detected with low eccentricities in the tests until the signal strength of the planets were just below the level of the residual RMS scatter of the data, then, only a single planet was detected. This planet had the same period as the simulated outer planet at 8.46 d, though its eccentricity was much larger than simulated at $e > 0.3$. Thus confirming the findings of Anglada-Escudé et al. (2010); Wittenmyer et al. (2013); Boisvert et al. (2018), and Wittenmyer et al. (2019). Care must be taken to ensure sufficient orbital coverage of data when eccentric planetary solutions are proposed.

`kima`'s ability to correctly characterise the orbits of multi-planetary systems single stars down to the residual noise level of the input data had been confirmed. Since the main targets involved in this work are primarily binary star systems, below I will describe our initial testing of `kima` on our preliminary binary RV data sets.

2.2.3.2 Challenges in analysing RV signals of binary stars and circumbinary planets

Radial Velocity (RV) measurements of binary stars pose some unique challenges in their observation and analysis. For example, contamination of the observed primary stars' spectra by the light of the secondary star can interfere with the RV extraction process mentioned in Section 1.2.2. This is explained in greater detail in Chapter 4, and can be overcome by observing binary stars where the secondary is sufficiently small and faint, so as not to contaminate the observed spectra.

Even then, the RV motion of the primary star is dominated by the signal of the secondary due to its size. The secondary star imposes an RV signal with semi-amplitude (K) of the order of several km s^{-1}. Fitting the data for the large binary signal, whilst also fitting for further additional circumbinary planetary signals is a unique problem in exoplanet science, and must be treated carefully. Any deviations in the fitted orbital parameters of the binary can introduce signals at resonances with the binary orbital period in parameter space.

For a large portion of our parameter space, circumbinary orbits would be unstable due to the instability region (Holman & Wiegert 1999) discussed in Section 1.4. This region extends out to roughly $5 \times P_{\rm bin}$, and sampling from this region wastes computational time and hinders the sampling of other areas of the parameter space where circumbinary planet orbits are stable. Additionally, fitting for the binary signal and any planetary companions with the same prior distribution in semi-amplitude is inefficient. Values for the semi-amplitude must be allowed to be sampled up to several km s^{-1} to account for the binary. While it is obvious that only one signal appears at this strength in our data, any additional planetary signals are expected with semi-amplitudes < 100 m s^{-1}. Therefore, the parameter space between $100 - 10\,000$ m s^{-1} offers no advantage to our fits and only serves to dilute the posterior samples obtained.

Due to the large signal of the binary, we are able to place very tight constraints on its orbital parameters. For example, mean uncertainties on the period of the binaries can be constrained to < 5.8 minutes, mean semi-amplitude uncertainties to < 10 m s^{-1}, and mean eccentricity uncertainties to < 0.0006, with our RV data alone. Originally `kima` only had the ability to set one set of priors for its sampling. It became apparent that when searching for circumbinary signals in the data, placing tight priors on the binary along with separate priors on the remaining stable parameter space, would improve the sampling efficiency considerably minimising run-time.

Furthermore, Kima fits static Keplerian signals to the data. This poses no problem for single star systems, however, for binary systems with circumbinary planets present it can lead to the divergence of the data from the fit over long timescales. This is due to the orbital precession of the binary driven by the circumbinary planet discussed in Section 1.4 and Martin & Triaud (2015). Figure 4.20 in Chapter 4 demonstrates this divergence over time for an N-body simulated J0310-31 binary and planet system, as $\omega_{\rm bin}$ varies within the timespan of the data. Allowing $\omega_{\rm bin}$ to vary with a linear apsidal precession term ($\dot{\omega}_{\rm bin}$) within `kima` can account for this, though this work is ongoing and will appear in Baycroft et al.

(2022) in prep.

2.2.4 Improvements to `kima`

Each posterior sample obtained from `kima` has the orbital parameters of up to $N_{\rm p}$ planetary signals within it. A limitation with this method is that `kima` does not check whether these orbits would be stable within each proposed system. For example, two circular planets in a 2:1 resonance could be stable in a planetary system. Though if either planet is highly eccentric their orbits would cross, they would gravitationally interact, and one (usually the least massive planet) would be ejected from the system. Calculating the stability of each proposed posterior sample would be computationally expensive and difficult to implement within the code. Below a functionality implemented in `kima` to discount any unstable posterior samples from analysis is discussed, along with the changes made to `kima` in order to allow for more rigorous fitting of binary RV data.

2.2.4.1 Crossing orbits

During testing with `kima`, I noticed that posterior samples were being gathered which resulted in inherently unstable orbital solutions. Each posterior sample from `kima` contains the parameters for $N_{\rm p}$ planetary signals. Some of which would lead to crossing orbits and in nature the ejection of these planets from the system.

If a planetary orbit has $e \neq 0$, there exists a point where the planet will be at its closest separation from its host star, known as its "Periastron", and consequently its furthest separation "Apastron". These are governed by the following equations (Hilditch 2001):

$$\begin{aligned} r_{\rm peri} &= a(1-e) \\ r_{\rm ap} &= a(1+e) \end{aligned} \tag{2.4}$$

where a is the semi-major axis of the orbit and e its eccentricity. If the periastron of a planet lies within the apastron of another, then those orbits cross, and are unstable for timescales longer than a few orbital periods. The chances of observing a planetary system in this configuration is highly unlikely, and any crossing orbits suggested by `kima` should be flagged.

The crossing orbit criterion outlined above can also be expanded to include any planetary orbit whose periastron lies within its host stars "Roche limit" (or radius). The Roche limit marks the distance at which the gravitational pull of the star at the planets surface overcomes the gravitational force of the planet itself. A planet within the Roche limit of the star will be destroyed by the resulting tidal forces. The Roche limit can be calculated using the following equation (Rappaport et al. 2013):

$$R_{\rm lim} = 2.44\, R_* \left(\frac{\rho_*}{\rho_{\rm p}}\right)^{1/3} \tag{2.5}$$

where R_* is the radius of the star in question, ρ_* its density, and $\rho_{\rm p}$ the density of the planet. From Equation 2.5 it becomes clear that dense planets orbiting small, less dense stars are far less likely to fall

within this zone. As a conservative limit we implement this criterion using Solar radius and density and a planet density of 7.8 g cm^{-3}, that of a solid iron sphere.

For circumbinary planets there is no need to calculate if any orbits cross the Roche limit. Instead, we calculate if any of the proposed orbits cross into the binaries instability region (Holman & Wiegert 1999). If any of the proposed orbits' periastra lie within $\approx 3.5\,P_{\rm bin}$ (more conservative than $5\,P_{\rm bin}$ quoted in Section 1.4) they are removed from further analysis.

Figure 2.5 shows the posterior samples obtained from a kima run on binary data for EBLM J0608-59 (TOI-1338/BEBOP-1) in an eccentricity vs period plot. The blue points here represent the binaries orbital parameters, while the green points correspond to planet TOI-1338/BEBOP-1 c (Chapter 6). Black points represent other posterior samples, and the greyed points those removed by the crossing orbit algorithm described above. In this example orbits are removed from further analysis from being highly eccentric and crossing the instability region, though not many cross with the detected planet. Testing finds that this is the case for data with obvious planetary signals such as TOI-1338/BEBOP-1c or Kepler-16b (Chapter 5). However, for the identification of planetary candidates with weaker signals present in the data, removing the crossing orbits can be useful by highlighting which family of signals are plausible in the data.

It is important to note that currently when removing samples from the posterior distribution, the evidence of probabilities are not re-normalised. Therefore, in our analysis the Bayes factors are always calculated using the complete set of posterior samples. To use the crossing orbits functionality in kima type the command '*kima-showresults –help-remove-crossing*' in the command line.

2.2.4.2 Known object mode

As mentioned above, when fitting Radial Velocity RV data with a known object present (i.e, a binary star or transiting planet), there is additional information available on the system which can be used to set tight priors for a specific object.

To allow for these special cases, kima introduced a 'Known Object' mode. This mode allows individual tight priors to be set for a known object or transiting planet in the system, along with wider priors to search for additional signals in the data.

The known object mode became the default mode used in my analysis of the binary systems outlined in Chapter 4. Originally kima allowed for only one known object to be set, though this has since been increased to allow multiple unique priors to be set on the same data.

Below I will describe the best practices I reached in the use of kima during my PhD, along with the priors I utilise in runs on our binary RV data.

2.2.5 Best practices when using kima

Through testing and experimentation in the use of kima to fit our Radial Velocity (RV) data during my PhD, I have settled upon the best priors and settings for use in my analysis. Here I will detail these settings, intended as a guide for those wishing to utilise kima in the search for planetary signals, especially in the presence of a large signal, such as a binary companion, in the data.

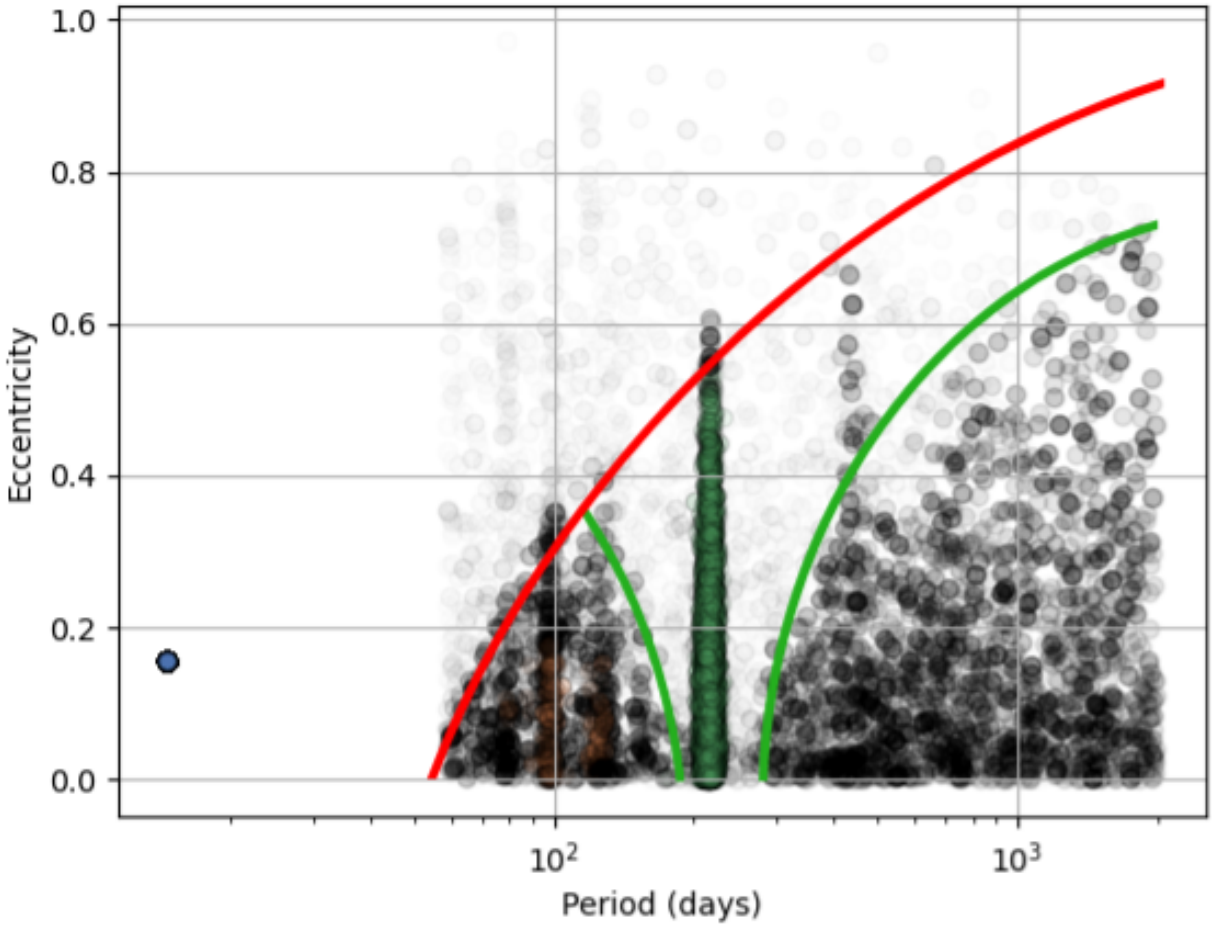

Figure 2.5: Plot of the eccentricity vs orbital period of posterior samples obtained from a `kima` run on radial velocity data for EBLM J0608-59 (BEBOP-1). The thick red line corresponds approximately to the exclusion zone created by the instability region of the binary stars, the blue cluster of points at ≈ 14.6 days. The thick green lines mark the approximate exclusion zone carved by BEBOP-1c, the green cluster of points at ≈ 220 days. Black points are valid samples which are not part of a cluster, while the orange points are clustered, representing the third densest region of samples. The faded grey points represent posterior planetary orbits which cross with another planet, or the instability region in their proposed systems.

2.2.5.1 Sampler settings

In `kima`, to set the options for the `DNest4` sampler (Brewer et al. 2011) we edit the 'OPTIONS' file. Below I will introduce each parameter, and provide the values used in my analysis in the following Chapters.

Number of particles, this parameter sets the number of MCMC particles exploring the parameter space. Brewer & Foreman-Mackey (2016) recommend 5 here, while `kima` suggests 1 or 2 suffice, especially when utilising multiple threads. In my experience 2 particles over 4 threads produce reliable and quick exploration of the parameter space. With access to more cores increasing the number of threads can speed up the sampling. Editing the 'run' file allows the user to change the number of threads. With six cores setting the number of threads to 6, and keeping the number of particles at 2 provided the fastest sampling in my experimentation.

New level interval sets the number of sample steps that will be taken with a likelihood above the current level before a new level is created. Brewer & Foreman-Mackey (2016) suggest using a default

of 10,000, while `kima` uses 5000. Through experimentation I have found 50,000 to provide effective sampling of binary RV datasets. The higher the value, the more thorough and consequently slower the exploration (Brewer & Foreman-Mackey 2016).

Save interval governs the number of steps before a sample is saved into the output files. This acts as a thinning parameter. Saving more frequently is good, but can produce large output files and use large amounts of Random Access Memory (RAM) in analysis. Brewer & Foreman-Mackey (2016) and `kima` both suggest setting the save interval to be close to or smaller than the new level interval. I have settled upon 5000 as an adequate value, though testing is required to see if a higher value may be better suited to individual needs.

Thread steps controls how many steps each thread takes independently before communicating their information about the levels with the other threads. Brewer & Foreman-Mackey (2016) and `kima` both suggest a default value of 100. I have found little reason to change this.

Maximum number of levels sets the maximum number of levels for `DNest4` to create. If left as 0, `DNest4` will attempt to determine the maximum number of levels automatically. If set to 1 it will sample from the priors only and can be used to troubleshoot prior choices. The maximum number of levels can be monitored using Figure 2.6 obtained from executing the command 'kima-showresults diagnostic'. The initial phase of DNS are shown in the upper plot where particles move left to higher likelihood (L) as levels are created, in turn decreasing the prior mass (X) (Brewer & Foreman-Mackey 2016). The lower plot in Figure 2.6 should contain a single peak as demonstrated. This shows that increasing the number of levels further will not produce any additional samples at a higher posterior weight than those already obtained (Brewer & Foreman-Mackey 2016). If a second peak appears at the left edge in this plot, then the fit should be re-run with more levels to confirm the presence of a second peak (Brewer & Foreman-Mackey 2016).

Backtracking scale length controls the degree with which the particles are allowed to drop to lower levels during sampling. The higher this value the less likely to miss any peaks in likelihood space, though it will take longer to create new levels. Brewer & Foreman-Mackey (2016) and `kima` suggest using 10 for this, and I have found no reason to deviate from this value.

Strength of forcing target weighting (Brewer et al. 2011) compensates for differences in the spacing of the created levels (Brewer & Foreman-Mackey 2016). Brewer & Foreman-Mackey (2016) and `kima` recommend a value of 100 which I also use.

Maximum number of saves controls the length of a `DNest4` sampling run. The value corresponds to the number of saved samples in the output 'sample.txt' file. The number of posterior samples (rows in the 'posterior_sample.txt' output file) is always less than this value (Brewer & Foreman-Mackey 2016). Setting the value to 0 will allow the sampler to run indefinitely until terminated. Through my experimentation I found that using $50,000 - 80,000$ would provide reliable results with $5000 - 8000$ posterior samples. To obtain reliable orbital parameters from the solution, `kima` and I suggest obtaining at least 10,000 posterior samples. This varies depending on the dataset, but I found that $100,000 - 150,000$ saves facilitates this. When calculating detection limits, as outlined in Standing et al. (2022) (Section 4.3),

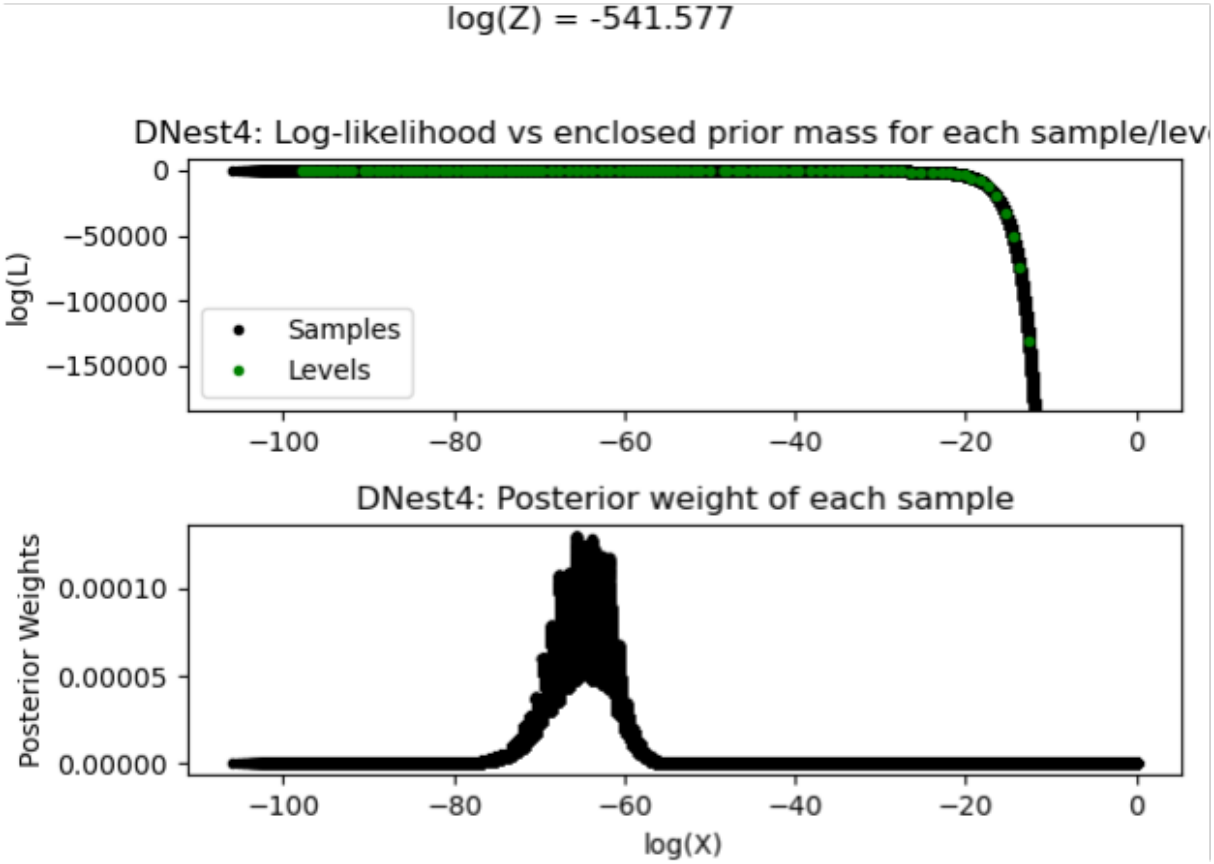

Figure 2.6: Top panel: log-likelihood (L) vs enclosed prior mass (X). Green points indicate samples at which new levels were created. Lower panel: Posterior weights of the saved particles. A successful run should show a single peak as above (Brewer & Foreman-Mackey 2016). Plot obtained from `kima`.

I recommend using at least 200, 000 saves.

Further details and description of each of these parameters can be found here, and in Brewer & Foreman-Mackey (2016).

2.2.5.2 Prior distributions

Through my use of `kima` I have experimented with various prior distributions in the fitting of Keplerian signals to Radial Velocity (RV) data. The priors used in my analysis are similar to those laid out in Faria et al. (2020), and are detailed in Standing et al. (2022) (see Section 4.3). Below I will share the priors which provided the best results in my analysis in the following Chapters.

Prior distributions are a feature of Bayesian statistics, and can be used to enforce any prior information known about the data in question. For example, in the case of a normal six-sided die there is an equal probability of each side landing face-up with any given throw. An adequate prior to represent this would be that of a uniform distribution across all faces, similar logic can be applied for RV data. For example, in our binary case, we know that there exists a region of instability surrounding the binary stars' orbit, and no circumbinary companions can orbit within this region. Therefore, priors for the period of circumbinary planets should have a lower limit close to that of this instability region. Prior distributions

should enclose the true parameters along with their associated uncertainties (Standing et al. 2022). The shape of the prior distribution is also important. For example, RV data is most sensitive to larger signals at shorter orbital periods (see Section 1.2), though planets can have any orbital periods within the stable period ranges available in a system. Therefore, a Log-Uniform (Jeffreys) prior (Jeffreys 1946) would be the most appropriate in this instance. A Log-Uniform distribution prevents the sampler from favouring longer orbital periods, which would occur if a standard uniform prior was used.

Known object binary priors

The majority of the RV data analysed in this thesis is that of binary star systems, where the reflex motion of the primary star due to the secondary is obviously present in the data. For this data we utilise `kima`'s known object mode (Section 2.2.4.2) for the secondary star, with tight priors on its parameters.

To obtain the orbital parameters for the secondary star, an initial fit on the data is carried out with wide uninformative priors. Once the orbital parameters are ascertained, tight uniform priors are placed on its orbital period, semi-amplitude, and eccentricity. Orbital periods of binary stars can be determined from RV data to within hundredths of a second, though some of our BEBOP targets (Chapter 4) have period uncertainties of the order of several minutes. Therefore, we set the prior to explore within ±0.01 days (±14.4 minutes) of the orbital period.

The semi-amplitude and eccentricity precision on the binary orbit increases with the number of measurements on a system. For the majority of the systems explored in the work of the following chapters we set the priors on the binary semi-amplitude and eccentricity to uniformly explore ±30 $\mathrm{m\,s^{-1}}$ and ±0.001 respectively. Once planetary signals are identified in a system, more observations are obtained to confirm them. With these further observations, even tighter priors can be enforced on the binary known object to increase the sampling efficiency. In Standing et al. (2022) I utilise priors of ±10 $\mathrm{m\,s^{-1}}$ and ±0.0005 on the semi-amplitude and eccentricity respectively (see Table 4.3). Placing wider priors on the binary has no effect on the parameters obtained from the fit.

For the remaining binary orbital parameters of f and ω we utilise a uniform prior from 0 to 2π. These parameters are circular, therefore there is no reason to favour a particular value. This is also the case for bodies orbiting single stars and the same priors are utilised in those instances.

Additional planetary signal or system priors

With the known object priors set, the priors for additional signals can be provided. The priors for these additional signals in binary systems are also used for single stars in the following chapters.

For the **systemic velocity** (γ) we initially set uniform priors with limits of the maximum and minimum values of the RV data. For single stars this would usually suffice, however, the span of the RV data for binary systems can be of the order of many $\mathrm{km\,s^{-1}}$. Therefore, once an estimated value is established for γ, the limits are contracted to ±100 $\mathrm{m\,s^{-1}}$ for subsequent runs.

When searching for additional signals in the data, the **number of planets** N_p parameter for the number of Keplerian signals `kima` can fit at once in the system is important. Through testing we find that more

complex models including more Keplerian signals, and consequently more parameters, is favoured in the fits. This is expected, as the more complex the model, the better it fits the data. Figure 2.4 demonstrates this effect, with the largest number of posterior samples hosting two or three planetary signals. When searching for planets in any system I utilise a uniform prior on N_p allowing the values to vary from 0 to 3. If the N_p chosen by the Bayes factor is equal to 3, then the data would be reanalysed with the upper limit on N_p increased to 5 and so on. When calculating detection limits as described in Standing et al. (2022) (see Section 4.3), N_p can be fixed to = 1. This forces `kima` to fit planetary orbits to the data and reveals what signals could cause the observed values.

For the **orbital period** (P) prior, a Log-Uniform (Jeffreys) distribution (Jeffreys 1946) is utilised. It does not favour any particular period region and allows the exploration of longer periods should the data allow it. Log-Uniform priors can also span several orders of magnitude, making them perfect for the orbital period. In binary systems, the inner limit on the period prior is determined by the instability region (Holman & Wiegert 1999). In Section 1.4 I stated that the instability region extends out to $\approx 5\,P_{\rm bin}$, though in my analysis I use a more conservative inner limit to the P prior at $3.5\,P_{\rm bin}$ to ensure that any signals near the instability limit are able to be sampled. The P prior for single stars is limited only by the Roche limit (Rappaport et al. 2013) described above, and therefore can be set to small values. As an outer limit for the period, the time-span of the data can be used. This is the span of time from the first RV point to the last, and limits the ability to reliably detect orbits at longer periods. When searching for planetary signals I would not recommend exceeding $\approx 4\times$ the time-span of the data, any signal with a longer period than this will not be detectable and will appear as a drift in the data only.

The prior for the **semi-amplitude** (K) of the RV signal is a modified version of the Log-Uniform distribution which has a knee and an upper limit. The reasons for its use are described in Standing et al. (2022) in Section 4.3.5, though I will briefly cover them here. An upper limit of 100 $\mathrm{m\,s^{-1}}$ is chosen for the distribution, as any signal greater than this would be obvious in our data. The knee in the distribution splits it into a standard Log-Uniform beyond the knee, and a uniform prior below it giving less priority to these signals (Standing et al. 2022). Gregory (2005) suggests the use of $1/10$ of the RV uncertainty as the knee value. The instrument precision used in this work typically approaches ≈ 1 $\mathrm{m\,s^{-1}}$. Therefore, the knee is placed at 0.1 $\mathrm{m\,s^{-1}}$.

As the prior for the **orbital eccentricity** (e), Kipping (2013) recommends a Beta distribution. In `kima` a Beta distribution can be utilised using the Kumaraswamy distribution (Kumaraswamy 1980). This closely resembles the Beta distribution identified in Kipping (2013) when using shape values of $\alpha = 0.867$, and $\beta = 3.03$. This distribution favours lower eccentricities, though still allows the exploration of higher values.

The final prior to set is that of the **instrumental jitter** ($\sigma_{\rm jit}$). I also utilise a Log-Uniform distribution for the jitter term, with a lower limit of 0.001 $\mathrm{m\,s^{-1}}$ out to a maximum of the smallest between $10\times$ the residual scatter of the data, or 100 $\mathrm{m\,s^{-1}}$. If the residual scatter is $>$ 100 $\mathrm{m\,s^{-1}}$ the value can be set independently, though if this is the case it is likely that the binary parameters have not been determined correctly.

Further discussion on these priors can be found in Section 4.3.5 from Standing et al. (2022), and all are shown in Table 4.3

2.2.6 Obtaining planetary parameters from posterior samples

Once the priors are set, `kima` can be run on the data. If the resulting Bayes factors for the posterior samples obtained shows evidence of a planetary candidate in the system, analysis of the posterior samples can reveal the orbital parameters of the corresponding signal. Below, the ways in which orbital parameters are obtained from the posterior samples are discussed, along with how the time of next transit/eclipse is calculated for transiting objects.

Once all effective posterior samples are obtained from `kima`, and all crossing orbits are removed as above, it becomes possible to obtain planetary parameters from these samples. Each posterior sample has N_p Keplerian signals associated with it (i.e, N_p periods, eccentricities, semi-amplitudes etc.). Unfortunately, these signals are not always consistent between posterior samples. Parameters associated with a candidate planetary signal can appear in different columns in the 'posterior_sample.txt' output file. Therefore, a natural way to isolate dense regions in parameter space is through clustering the posterior samples. Clustering involves assigning posterior samples with a value corresponding to a cluster to which it belongs. If the sample in question is part of a dense region it is assigned to a cluster, if in a sparse region it is identified as a noise point.

For the work in this thesis I utilise the Hierarchial Density-Based Spatial Clustering of Applications with Noise (HDBSCAN) clustering algorithm (McInnes et al. 2017). HDBSCAN clusters data points by drawing circles around each point. Each point in this instance is a period, semi-amplitude, or eccentricity obtained from the posterior samples. It increases the radius of these circles until a circle contains a minimum number of points required for a cluster (the only variable required for the algorithm). This yields a measure of density for each point in the parameter space, which can be used to form a density tree. The process can be visualised by comparing the method to lowering a water level over a tree, the branches which emerge from the water are the high density regions. As the water level decreases the branches merge with the trunk of all the points. Instead, by increasing the water level the position at which points branch off from the main cluster (trunk) is noted. HDBSCAN uses the minimum number of points parameter to decide whether the points splitting from the tree correspond to a cluster (i.e, number of points > min number of points), or just a few noise points (vice versa). Clusters which survive the longest before splitting, and have the largest number of points are chosen as clusters. The only caveat being that if a cluster is chosen, no other branch from the same cluster can be subsequently chosen. For further information see McInnes et al. (2017) along with the documentation.

The only input parameter needed for clustering with HDBSCAN is the minimum number of points required for a cluster to be formed. To calculate this value I first identify the number of planetary signals present in the data from the Bayes factors described above and increase this value by one. This provides the expected number of clusters present in the posterior samples, and prevents the creation of one large cluster of points. If the chosen value is zero it is manually set to equal one, allowing the calculation and

plotting of the highest likelihood signal present in the results, and the identification of candidate planets.

I then produce a histogram of the orbital periods of all posterior samples and obtain the number of samples within each period bin. Sorting these values, the number of posterior samples in the $N_p + 1$ largest bin is used as an estimate for the minimum number of points in a cluster. HDBSCAN is then run on the posterior samples in three dimensions, period (P), semi-amplitude (K), and eccentricity (e). If the number of clusters obtained is less than $N_p + 1$, the minimum number of points is reduced and clustering is repeated. All posterior samples from the known object are manually placed into an additional cluster.

Figure 2.5 demonstrates this clustering method, where the green cluster corresponds to planet TOI-1338/BEBOP-1c (Chapter 6, Standing et al. (In review)). The blue cluster is all the posterior samples obtained for the binary known object, the orange points represent the next densest region in the parameter space and may correspond to TOI-1338/BEBOP-1b (Kostov et al. 2020). The black points represent noise points, posterior samples which do not belong to any cluster, and the faded grey points those removed due to crossing orbits.

Orbital parameters can then be determined by calculating the 50$^{\text{th}}$ percentile, along with its associated uncertainties at the 16$^{\text{th}}$ and 84$^{\text{th}}$ percentiles. This can be seen in the corner plot in Figure 2.7, for the green cluster from Figure 2.5.

The minimum mass of the object can be calculated using Equation 1.12, using the combined mass of the primary and secondary stars as M_* for circumbinary planets. The semi-major axis (a) can be obtained using Kepler's third law Equation 1.6.

In Figure 2.7, T_0 is the time of periastron passage, and indicates the time at which the orbiting body passes the periastron. This can be calculated using the following equation, where in `kima` the epoch is defined as the time of the first observation:

$$T_0 = \text{Data}_0 - \frac{P \times \phi}{2\pi} \tag{2.6}$$

where Data_0 is the time of the first measurement, P the orbital period, and ϕ the mean anomaly at the epoch (i.e, the fraction of the orbit that has passed since the periastron passage).

From the time of periastron passage it becomes possible to calculate the time at which the orbiting body would transit the host star (should the system be in a transiting configuration). Firstly the true anomaly during transit is calculated using the following equation (Murray & Correia 2010; Winn 2010):

$$f = \pi/2 - \omega \tag{2.7}$$

where ω is the argument of periastron, and $\pi/2$ represents the true longitude of the planet during transit (Winn 2010). Following this, the eccentric anomaly is calculated as (Murray & Correia 2010):

$$E = 2\tan^{-1}\left[\tan\left(\frac{f}{2}\right)\sqrt{\frac{1-e}{1+e}}\right] \tag{2.8}$$

The time of transit from T_0 can then be calculated from (Murray & Correia 2010):

$$T_{\rm tran} = T_0 + \frac{P}{2\pi}\,(E - e\sin E) \tag{2.9}$$

The following chapters present the results of the analysis of several RV datasets utilising the above analysis techniques, including updating the planetary parameters of planet λ^2 Fornacis (HD16417) (Nielsen et al. 2020).

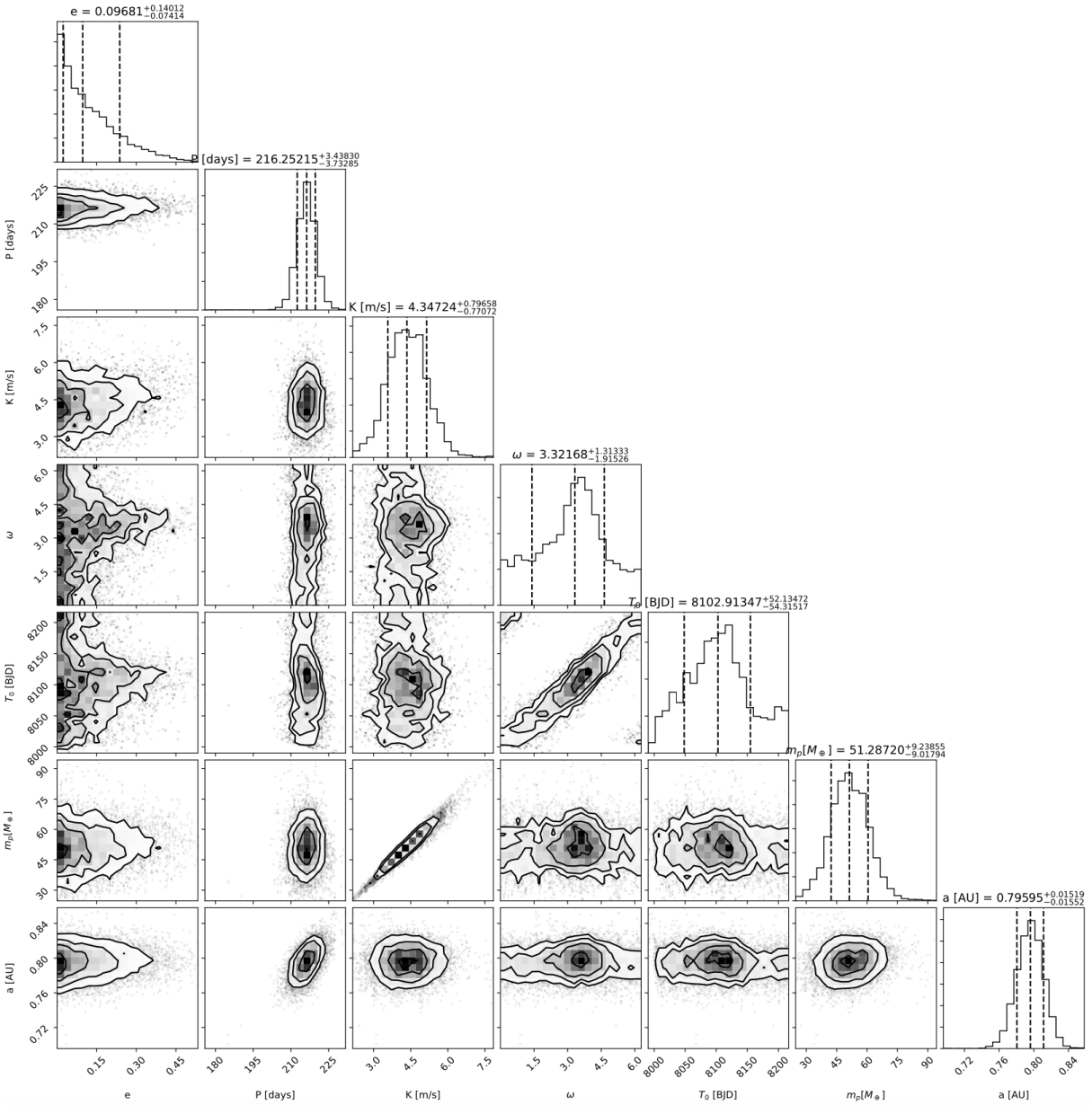

Figure 2.7: Corner plot of posterior samples from green cluster in Figure 2.5 corresponding to TOI-1338/BEBOP-1c. Figure created using corner package (Foreman-Mackey 2016).

Chapter 3

Updating Planetary Parameters

> "All you really need to know for the moment is that the universe is a lot more complicated than you might think, even if you start from a position of thinking it's pretty damn complicated in the first place."
>
> Douglas Adams, *The Hitchhiker's Guide to the Galaxy*

3.1 My contribution to the paper

Having established my data analysis methods as described in Chapter 2, I was ready to utilise them in the analysis for a scientific paper. At the end of the first year of my PhD, I was approached by Martin Nielsen and Warrick Ball from the asteroseismology group at the University of Birmingham, and asked to contribute to a paper on the use of *TESS* data (Ricker et al. 2015) to update the system parameters of a known planet host λ^2 Fornacis.

λ^2 Fornacis was one of the first Solar-like oscillators to be observed with the Transiting Exoplanet Survey Satellite (*TESS*), and as such they wanted to show that asteroseismology was possible with < 2 months of *TESS* lightcurves.

My role in this work was to analyse archival Radial Velocity (RV) data from HARPS (Mayor et al. 2003), UCLES at the Anglo-Australian Telescope (AAT), and HIRES at the Keck observatory to search for additional planets in the system, and update the known planet's parameters in the light of new stellar parameters from Martin and Warrick's asteroseismic analysis. I utilised `kima` as described in Chapter 2, and the results of my analysis can be found in Table 3.3 and are discussed in Section 4 of the manuscript below. This was my first scientific application of `kima`, and some plots will be similar to those found in the following chapters.

A&A 641, A25 (2020)
https://doi.org/10.1051/0004-6361/202037461

Astronomy & Astrophysics

TESS asteroseismology of the known planet host star λ^2 Fornacis

M. B. Nielsen[1,2,3], W. H. Ball[1,2], M. R. Standing[1], A. H. M. J. Triaud[1], D. Buzasi[4], L. Carboneau[1,4], K. G. Stassun[5], S. R. Kane[6], W. J. Chaplin[1,2], E. P. Bellinger[2,7], B. Mosser[8], I. W. Roxburgh[10,1], Z. Çelik Orhan[9], M. Yıldız[9], S. Örtel[9], M. Vrard[11,19], A. Mazumdar[20], P. Ranadive[20], M. Deal[11], G. R. Davies[1,2], T. L. Campante[11,12], R. A. García[13,14], S. Mathur[15,16], L. González-Cuesta[15,16], and A. Serenelli[17,18]

(Affiliations can be found after the references)

Received 8 January 2020 / Accepted 15 June 2020

ABSTRACT

Context. The Transiting Exoplanet Survey Satellite (TESS) is observing bright known planet-host stars across almost the entire sky. These stars have been subject to extensive ground-based observations, providing a large number of radial velocity measurements.
Aims. The objective of this work is to use the new TESS photometric observations to characterize the star λ^2 Fornacis, and following this to update the parameters of the orbiting planet λ^2 For b.
Methods. We measured the frequencies of the p-mode oscillations in λ^2 For, and in combination with non-seismic parameters estimated the stellar fundamental properties using stellar models. Using the revised stellar properties and a time series of archival radial velocities from the UCLES, HIRES and HARPS instruments spanning almost 20 years, we refit the orbit of λ^2 For b and searched the residual radial velocities for remaining variability.
Results. We find that λ^2 For has a mass of $1.16 \pm 0.03\,M_\odot$ and a radius of $1.63 \pm 0.04\,R_\odot$, with an age of 6.3 ± 0.9 Gyr. This and the updated radial velocity measurements suggest a mass of λ^2 For b of $16.8^{+1.2}_{-1.3}\,M_\oplus$, which is $\sim 5 M_\oplus$ less than literature estimates. We also detect an additional periodicity at 33 days in the radial velocity measurements, which is likely due to the rotation of the host star.
Conclusions. While previous literature estimates of the properties of λ^2 For are ambiguous, the asteroseismic measurements place the star firmly at the early stage of its subgiant evolutionary phase. Typically only short time series of photometric data are available from TESS, but by using asteroseismology it is still possible to provide tight constraints on the properties of bright stars that until now have only been observed from the ground. This prompts a reexamination of archival radial velocity data that have been accumulated in the past few decades in order to update the characteristics of the planet hosting systems observed by TESS for which asteroseismology is possible.

Key words. asteroseismology – stars: individual: HD 16417 – planetary systems – techniques: radial velocities – techniques: photometric

1. Introduction

The Transiting Exoplanet Survey Satellite (TESS, Ricker et al. 2014) observed the southern celestial hemisphere in the period from July 2018 to July 2019. The main objective of TESS is to observe short-period transiting exoplanets around bright stars. The observation strategy during the first year of operations covered almost the entirety of the southern hemisphere, observing large swaths of the sky for short periods of time (≈27 days). This is a departure from the previous space-based photometry missions CoRoT (Fridlund et al. 2006) and *Kepler* (Borucki et al. 2010), which provided photometric time series of hundreds of days or even several years for a few select fields. These time series have been a huge advantage for asteroseismology, which benefits from long observations and bright stars to make precise measurements of the oscillation modes of a star. The cohort of TESS targets extends to much brighter targets than *Kepler* and CoRoT, and so despite a lack of long baseline time series, the mission has already yielded a multitude of previously unknown variable stars, including solar-like oscillators.

The star λ^2 Fornacis (HD 16417, λ^2 For) was initially selected for observation in the TESS two-minute cadence mode based on its brightness (G-band magnitude of 5.59) and high likelihood of exhibiting solar-like oscillations, as indicated by the Asteroseismic Target List (Schofield et al. 2019). It was observed for approximately two months shortly after the beginning of the TESS mission, and is one of the first planet-host stars to be observed by TESS with confirmed solar-like oscillations (see also Huber et al. 2019; Campante et al. 2019). Previous studies of λ^2 For have yielded a wide range of physical parameters (e.g., Bond et al. 2006; Gehren 1981; Bensby et al. 2014), indicating a spectral type anywhere between G2V or G8IV. Despite the relatively short amount of time that this star was observed by TESS, the photometric variability shows an unambiguous power excess at a frequency of $\approx 1280\,\mu$Hz, caused by solar-like acoustic (p-mode) oscillations. Stars with outer convective zones like the Sun and λ^2 For oscillate with regularly spaced overtones of radial and non-radial modes with angular degree, l. These modes propagate through the interior of the star, and therefore place tight constraints on its physical properties (e.g., García & Ballot 2019). The oscillation power of λ^2 For peaks at around $1280\,\mu$Hz, which alone places the star firmly in the subgiant regime. However, going a step further and measuring the individual mode frequencies has been shown to yield estimates of the mass and radius at a precision of a few percent, and the stellar age at ≈10% (e.g., Brown et al. 1994; Lebreton & Goupil 2014; Angelou et al. 2017; Bellinger et al. 2019). This has implications for estimates of the characteristics of any potential orbiting planets, in particular with respect to the mass of the planets, but also in terms of the dynamical history of the system itself.

O'Toole et al. (2009) discovered a roughly Neptune-mass planet in a 17.25-day orbit around λ^2 For. The detection was made using radial velocity (RV) measurements from the UCLES spectrograph at the Anglo-Australian Telescope (AAT), and

the HIRES spectrograph at the Keck telescope. Since then an extensive set of HARPS (Mayor et al. 2003) data from the ESO La Silla 3.6 m telescope has become publicly available (see Table E.1). Here we combine the original observations by O'Toole et al. (2009) and the HARPS measurements to construct an almost 20-year set of RV data. This, combined with the updated estimates of the stellar mass from asteroseismology, allows us to better constrain the planet and its orbital parameters. Furthermore, the extensive RV data set and the high quality of the HARPS measurements presents an opportunity to investigate variability on timescales other than the orbit of the known planet.

The TESS time series reduction is presented in Sect. 2. The modeling process of λ^2 For is described in Sect. 3, including the power spectrum and spectral energy density SED fitting processes, which yields the seismic and non-seismic constraints, respectively. In Sect. 4 we discuss the methods used to improve the estimates of the planet and orbital characteristics of the known planet and the methods used to investigate additional periodicity in the RV measurements.

2. Time series preparation

λ^2 For was observed by TESS in Sectors 3 and 4, for a total of approximately 2 months. The photometric time series are available in a pre-reduced version from the Science Processing Operations Center (SPOC) pipeline (Jenkins et al. 2012), and in the form of pixel-level data. The SPOC pipeline removes artifacts and carries out traditional CCD data reduction activities, such as bias correction and flat-fielding, prior to performing aperture photometry. Aperture sizes are computed using the algorithm originally developed for *Kepler* postage stamps, which makes use of stellar parameters from the TESS Input Catalog (Stassun et al. 2018a) together with models of the detector and spacecraft attitude control system. Following extraction, the presearch data conditioning (PDC) algorithm removes instrumental signatures due to changes in pointing and focus, and performs corrections due to stellar crowding and aperture overfilling by the target star.

We attempted to improve on the SPOC result by manually reducing the pixel-level data. This was done using a procedure that has previously produced better signal-to-noise ratio (S/N) oscillation spectra for asteroseismic analyses of bright stars compared to the standard SPOC pipeline (Metcalfe et al., in prep.). The approach broadly mirrors that used successfully on K2 data in the past (see, e.g., Buzasi et al. 2015), and involved defining a custom photometric aperture pixel mask. In the case of λ^2 For this procedure did not reduce the noise level around the p-mode envelope, but for completeness we briefly summarize the method and the result in Appendix A. In the following sections we only use the SPOC PDC time series.

3. Modeling λ^2 For

To estimate the fundamental properties of λ^2 For we used both seismic and non-seismic constraints. The seismic constraints came from measuring the individual oscillation frequencies observed in the power spectrum of the SPOC time series, also known as peakbagging. The non-seismic constraints were derived from SED fitting. These constraints were then used by several independent modeling teams to provide estimates of the mass, radius, and age of λ^2 For. These steps are detailed in the following section.

3.1. Seismic constraints

To measure the oscillation frequencies of λ^2 For we used the SPOC flux time series as described above. Because of the low S/N of the oscillations, several independent peakbaggers[1] were tasked with finding and fitting the oscillation peaks. Initial guesses for the frequencies were found using the universal pattern approach (see Mosser et al. 2013) and by-eye inspection. The final choice of which modes to fit was based on the subset that all teams agreed on within their respective uncertainties. Each mode alone only has a ∼95% probability of not being due to background noise, whereas this manual approach also incorporates knowledge of the repeating pattern of the p-modes. In a low S/N case like λ^2 For, this repeating pattern helps identify the initial mode frequencies. The mode frequencies range from 1142 μHz to 1380 μHz, with a peak of oscillation power at $\nu_{\rm max} \approx 1280\,\mu$Hz and a separation of consecutive overtones of the same angular degree (large separation), $\Delta\nu \approx 69\,\mu$Hz.

The final list of frequencies was then fit using a Markov chain Monte Carlo (MCMC) approach, the result of which was used in the remaining analysis of λ^2 For. The model used to fit the power spectrum mirrors that used in previous peakbagging efforts such as Handberg & Campante (2011) or Lund et al. (2017). The mode frequencies and heights were treated as independent variables for each mode, and the mode widths were assumed to follow the relation by Appourchaux et al. (2014). The fit assumed a single rotational splitting and inclination axis for all oscillation modes. The background noise levels from granulation, activity, and uncorrected instrumental effects were fit concurrently with the modes, using two Harvey-like profiles (Harvey et al. 1988; Kallinger et al. 2014). We applied uniform priors on the mode frequencies, background timescales, rotational splitting, inclination angle, and the location parameters of the mode width relation (see Appourchaux et al. 2014). For the remaining model parameters we used log-uniform priors.

The posterior distribution of the model parameters was mapped using an MCMC sampler[2]. For each model parameter the median of the marginalized posterior distribution was taken as the best-fit solution, and the 16th and 84th percentile interval as a measure of the parameter uncertainties.

The power density spectrum and the resulting fit frequencies are shown in Fig. 1, and the échelle diagram in Fig. 2. Modes of angular degree $l = 3$ were not considered by any of the teams as these are typically very low amplitude, and thus require exceptional S/N to be observed. One team suggested the possible presence of mixed $l = 1$, but this could not be verified by the other teams and so they were not included in the final fit. The final list of fit frequencies is presented in Table B.1.

The fit to the power spectrum was unable to constrain the rotational splitting of the modes to less than ≈2.1 μHz, and thus the stellar rotation rate. Similarly, the seismic data were unable to constrain the stellar inclination angle. The marginalized posterior distributions of the inclination angle and rotational splitting are shown in Fig. C.1.

3.2. Stellar modeling

Three teams, identified by their principal locations, independently fit stellar models to the seismic and non-seismic data for λ^2 For. The teams independently chose stellar evolution codes, stellar pulsation codes, non-seismic observables, and fitting methods. The main choices of input physics are summarized in Table 1

[1] Peakbagging team members: MBN, IWR, MV, BM, WJC.
[2] `emcee`: Foreman-Mackey et al. (2013).

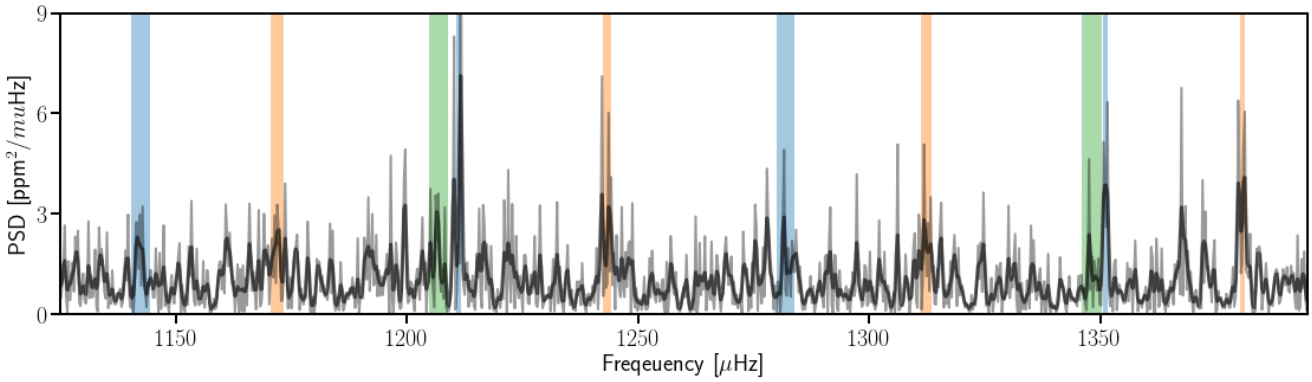

Fig. 1. Power density spectrum (gray) and the smoothed spectrum (black) around the p-mode oscillation frequencies. The 68% confidence interval of the fit mode frequencies are shown as the vertical shaded regions. Colors denote the angular degree, l, where blue is $l = 0$, orange is $l = 1$, and green is $l = 2$.

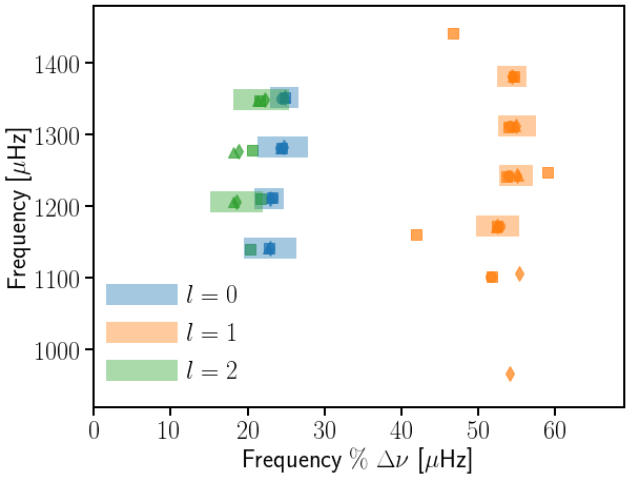

Fig. 2. Échelle diagram showing oscillation frequencies modulo the large separation ($\Delta\nu = 69.0\,\mu$Hz) supplied by each team: MV (circles), IWR (squares), MBN (diamonds), and WJC (triangles). The colors represent the angular degrees, l, that were considered. The shaded regions represent 68% confidence interval of the frequencies in the final fit. Several mixed modes (diverging modes along the $l = 1$ ridge) were suggested, but could not be verified by the other teams, and so were not included in the final fit.

and the best-fitting parameters of the models, with uncertainties, are listed in Table 2. For the frequencies derived from seismology, all the teams used either the one- or two-term surface correction by Ball & Gizon (2014). We did not enforce a line-of-sight velocity correction as this was negligible for λ^2 For (Davies et al. 2014; Soubiran et al. 2018). We describe below more complicated details of the stellar models, and how each team fit their models to the data. Our final estimates of the stellar properties are precise to 3% in mass, 2.7% in radius, and 14% in age.

3.2.1. Birmingham

The Birmingham team used Modules for Experiments in Stellar Astrophysics (MESA, r10398; Paxton et al. 2011, 2013, 2015) with the atmosphere models and calibrated mixing-length (MLT) parameters from Trampedach et al. (2014a,b) as implemented in Mosumgaard et al. (2018). The mixing-length parameter in Table 1 is the calibrated correction factor that accommodates slight differences between MESA's input physics and mixing-length model and that of the simulations by Trampedach et al. (2014a,b), rather than the mixing-length parameter $\alpha_{\rm MLT}$. The free parameters in the fit are the stellar mass M, the initial metallicity $[{\rm Fe/H}]_i$, and the age t.

The free parameters were optimized by first building a crude grid based on scaling relations, then optimizing the best model from that grid using a combination of a downhill simplex (i.e., Nelder–Mead method, Nelder & Mead 1965) and random resampling within error ellipses around the best-fitting parameters when the simplex stagnated. Uncertainties were estimated by the same procedure as used by Ball & Gizon (2017).

The objective function for the optimization was the unweighted total χ^2 of both the seismic and non-seismic data, using observed non-seismic values of $T_{\rm eff}$, [Fe/H], and $L_\star/L_\odot$. The $T_{\rm eff} = 5841 \pm 60$ K and [Fe/H] $= 0.13 \pm 0.06$ values were taken from Delgado Mena et al. (2017), with uncertainties increased to those used for most of the stars in Lund et al. (2017). The luminosity was derived from SED fitting following the procedures described in Stassun & Torres (2016), and Stassun et al. (2017, 2018b). The available photometry spans the wavelength range 0.35–22 μm (see Fig. 3). We fit the SED using Kurucz stellar atmosphere models (Kurucz 2013), with the priors on effective temperature $T_{\rm eff}$, surface gravity $\log g$, and metallicity [Fe/H] from the spectroscopically determined values. The remaining free parameter in the SED fit is the extinction (A_V), which we restricted to the maximum line-of-sight value from the dust maps of Schlegel et al. (1998). The best-fit extinction is $A_V = 0.04 \pm 0.04$. Integrating the model SED (which is unreddened) gives the bolometric flux at Earth of $F_{\rm bol} = 1.36 \pm 0.05 \times 10^{-7}$ erg s cm^{-2}. Together with the *Gaia* parallax of 39.3512 ± 0.0534 mas, this yielded a constraint for the luminosity of $\log L_\star/L_\odot = 0.436 \pm 0.015$.

3.2.2. Mumbai

The Mumbai team computed a grid of stellar models also using MESA (r10398). The grid spans masses from 1.10 to 1.38 $M_\odot$ in steps of 0.01 $M_\odot$, initial metallicities $[{\rm Fe/H}]_i$ from −0.02 to 0.36 in steps of 0.02, and mixing-length parameters $\alpha_{\rm MLT}$ of 1.81, 1.91, and 2.01. Gravitational settling, which is otherwise included in the stellar models, is disabled for models with $M_\star > 1.3\,M_\odot$, but the best-fitting models are less massive and unaffected by this choice. The grid uses two values for the length scale of core convective overshooting, using the exponentially decaying formulation by Herwig (2000): $f_{\rm ov} = 0$ (i.e., no overshooting) and 0.016.

Table 1. Stellar model settings for the different teams.

Team	Birmingham	Mumbai	Porto
Models	MESA [(a)] (r10398)	MESA [(a)] (r10398)	GARSTEC [(b)]
Oscillations	GYRE	GYRE	ADIPLS
High-T opacities	– OPAL (Iglesias & Rogers 1993, 1996) –		
Low-T opacities	– Ferguson et al. (2005) –		
Gravitational settling	– Thoul et al. (1994) –		
EoS	MESA/OPAL	MESA/OPAL	FreeEOS
Solar mixture	GN93	GS98	GN93
Helium enrichment law ($Y = \ldots$)	$1.28855Z + 0.248$	$2Z + 0.24$	$1.1843Z + 0.2485$
Nuclear reactions	NACRE	NACRE	Solar Fusion II
Atmosphere	Mosumgaard et al. (2018)	Krishna Swamy (1966)	Eddington
$\alpha_{\rm MLT}$	1.037*	1.81, 1.91, 2.01	1.811
Surface correction	BG14-1	BG14-1	BG14-2
Overshooting	None	0 & 0.016	0.02

Notes. A single entry is used where all three teams used the same input physics.
References. [(a)]Paxton et al. (2011, 2013, 2015) [(b)]Weiss & Schlattl (2008), Ball & Gizon (2014), Adelberger et al. (2011), Rogers & Nayfonov (2002), Irwin (2012), Grevesse et al. (1993), Townsend & Teitler (2013), Townsend et al. (2018), Herwig (2000).

Table 2. Model parameters for λ^2 For using seismic and non-seismic constraints.

Team	Birmingham	Mumbai	Porto	Adopted
Mass [$M_\odot$]	1.16 ± 0.02	1.17 ± 0.04	1.15 ± 0.03	1.16 ± 0.03
Radius [$R_\odot$]	1.64 ± 0.01	1.63 ± 0.04	1.63 ± 0.06	1.63 ± 0.04
Age [Gyr]	6.4 ± 0.5	5.6 ± 1.0	6.7 ± 0.8	6.3 ± 0.9
$T_{\rm eff}$ [K]	5816 ± 47	5847 ± 80	5824 ± 102	5829 ± 80
$\log g$ [cm s^2]	4.07 ± 0.01	4.08 ± 0.02	4.07 ± 0.04	4.08 ± 0.03
[Fe/H]	0.12 ± 0.07	0.09 ± 0.06	0.11 ± 0.10	0.10 ± 0.08

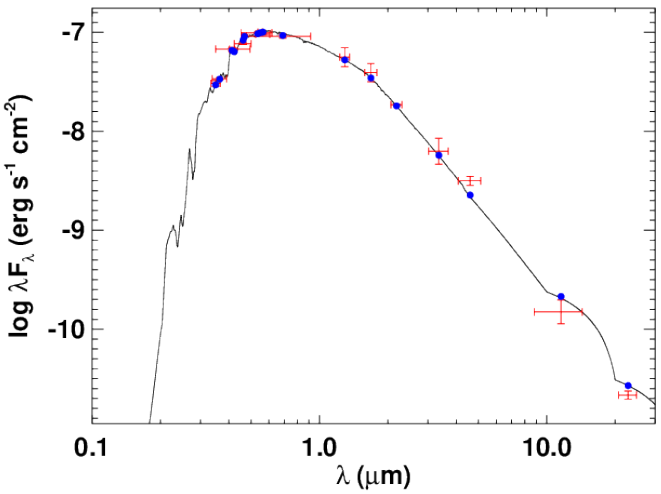

Fig. 3. Spectral energy distribution of λ^2 For. Red symbols represent the observed photometric measurements, where the horizontal bars represent the effective width of the passband. The photometric measurements are $B_T V_T$ magnitudes from *Tycho*-2, the *BVgri* magnitudes from APASS, the JHK_S magnitudes from 2MASS, the W1–W4 magnitudes from WISE, and the G magnitude from *Gaia*. Blue symbols are the model fluxes from the best-fit Kurucz atmosphere model (black).

The goodness of fit was evaluated through a total misfit defined by

$$\chi^2_{\rm Mum} = (\chi^2_{T_{\rm eff}} + \chi^2_{\log g} + \chi^2_{\rm [Fe/H]} + \chi^2_\nu), \quad (1)$$

where for $x = T_{\rm eff}$, $\log g$, or [Fe/H]:

$$\chi^2_x = \left(\frac{x_{\rm model} - x_{\rm obs}}{\sigma_x}\right)^2 \quad (2)$$

and

$$\chi^2_\nu = \frac{1}{N}\sum_i \left(\frac{\nu_{i,\rm model} - \nu_{i,\rm obs}}{\sigma_{\nu,i}}\right)^2. \quad (3)$$

The observed values of the non-seismic data were $T_{\rm eff} = 5790 \pm 150$ K, $\log g = 4.11 \pm 0.06$, and [Fe/H] $= 0.09 \pm 0.11$. The reported parameters are likelihood-weighted averages and standard deviations of the likelihood evaluated for each model in the grid, where the unnormalized likelihood is

$$\mathcal{L}_{\rm Mum} = \exp\left(-\frac{1}{2}\chi^2_{\rm Mum}\right). \quad (4)$$

3.2.3. Porto

The Porto team used Asteroseismic Inference on a Massive Scale (AIMS: Lund & Reese 2018; Rendle et al. 2019) to optimize a grid of stellar models computed with GARSTEC (Weiss & Schlattl 2008). The observed non-seismic values were taken to be $T_{\rm eff} = 5792.5 \pm 143.5$ K, metallicity [Fe/H] $= 0.09 \pm 0.10$, and luminosity $L_\star / L_\odot = 2.71 \pm 0.10$. The luminosity was determined from the relation by Pijpers (2003) using the extinction correction derived from the SED fit described in Sect. 3.2.1. The masses M in the grid ranged from 0.7 to 1.6 $M_\odot$

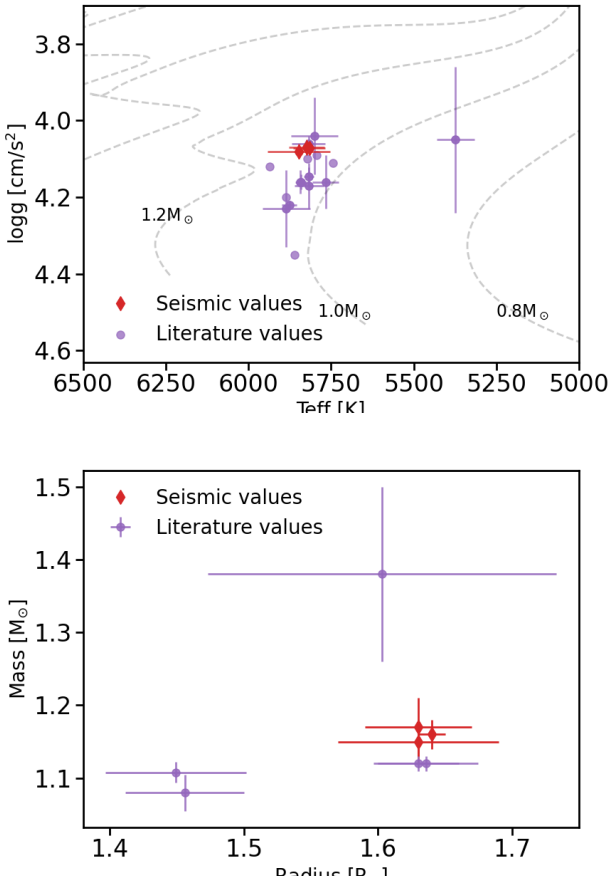

Fig. 4. *Top*: Kiel diagram showing the literature values (purple) and seismic values (red; see Table 2) of λ^2 For. Dashed lines indicate evolutionary tracks spanning a mass range of 0.8−2 $M_\odot$, in increments of 0.2 $M_\odot$. Literature values are presented in Table D.1. *Bottom*: masses and radii of the literature sources with a combination of $\log g$ with either mass or radius in comparison to the seismic estimates.

in steps of 0.01 $M_\odot$ and the initial metallicity $[\mathrm{Fe/H}]_i$ ranged from −0.95 to 0.6 in steps of 0.05. The models included extra mixing below the convective envelope according to the prescription by VandenBerg et al. (2012). The efficiency of microscopic diffusion is smoothly decreased to zero from 1.25 to 1.35 $M_\odot$ though, again, the best-fitting models are all significantly below 1.25 $M_\odot$ and therefore not affected by this choice. In addition, a geometric limit is applied for small convective regions, as described in Magic et al. (2010).

The goodness-of-fit function was the unweighted total χ^2 of the seismic and non-seismic data, as used by the Birmingham team (Sect. 3.2.1).

3.3. Adopted fundamental stellar parameters

Table 2 includes parameters averaged across the three stellar model fits. Specifically, we took the average and 1σ percentile ranges from the evenly weighted combination of the three fits.

Figure 4 shows the $\log g$ and $T_{\rm eff}$ values estimated by each team in relation to the literature values (see also Table D.1). Among the more recent literature sources the estimates of $\log g$ span a considerable range of ≈0.2 dex, and a subset of sources reported a mass ranging from $1.08^{+0.03}_{-0.02}$ $M_\odot$ to 1.38 ± 0.12 $M_\odot$, and corresponding radius between 1.45 ± 0.05 $R_\odot$ and 1.61 ± 0.13 $R_\odot$ (see bottom frame of Fig. 4, Valenti & Fischer 2005; Ramírez et al. 2014).

The asteroseismic measurements allow us to obtain robust estimates of the surface gravity, and subsequently of the mass and radius. Despite the inclusion of different model physics and approaches taken by the modeling teams in this work, the resulting estimates all fall within a few percentage points of each other in both mass and radius, with average values of $M_\star$ = 1.16±0.03 $M_\odot$ and $R_\star$ = 1.63±0.04 $R_\odot$. There is therefore agreement between the asteroseismic modeling results that λ^2 For is at the early stages of the subgiant evolutionary phase, whereas previous estimates were unable to confirm this unambiguously.

The literature estimates of the age (Valenti & Fischer 2005; Tsantaki et al. 2013; Bonfanti et al. 2016) fall within 1−2σ of the asteroseismic estimates of 6.3 ± 0.9 Gyr, with the extremes at 4.3±0.8 Gyr (da Silva et al. 2006) and 7.6±0.7 (Nordström et al. 2004).

4. Radial velocity analysis of the λ^2 For system

Since the discovery of λ^2 For b, a much larger sample of RV measurements has become available from the HARPS spectrometer at the ESO La Silla 3.6 m telescope. This presents an opportunity to update the orbital parameters of the planet based on this new data, and by using the new estimates of the stellar mass from asteroseismology. The HARPS data were downloaded via the ESO Science Portal[3]. We combined these data with the AAT and Keck data as presented by O'Toole et al. (2009) in Table 2 of that publication.

4.1. Updated characteristics λ^2 For b

We used `Kima` (Faria et al. 2018) to analyze the combined data set. `Kima` fits a sum of Keplerian curves to RV data corresponding to one or more potential planets. It uses a diffusive nested sampling algorithm (Brewer et al. 2009) to sample the posterior distribution of parameters explaining the data, where in this case the number of planets N_p was left as a free parameter. This allowed us to use `Kima` to estimate the fully marginalized Bayesian evidence of the parameter space, which was used to determine the likelihood of any number of planets that may be present and detectable in the data.

For the analysis of the RV data from λ^2 For, N_p was set as a free parameter with an upper limit of N_p = 5. Once samples of the fit posterior were obtained from `Kima` any proposed crossing orbits were removed a posteriori. The resulting posterior consists of a wide parameter space with a number of overdensities corresponding to regions of high likelihood for each of the parameters, such as orbital period P, semi-amplitude K, and eccentricity e. We identified these regions with the clustering algorithm `HDBSCAN` (McInnes et al. 2017). `HDBSCAN` identified a cluster corresponding to the orbital period of λ^2 For b. We extracted these samples from the posterior and used them to approximate the posterior probability density of the planetary orbital and physical parameters. As a result we provide

[3] The HARPS data set was collected thanks to several observing programs listed in Appendix E.1, and were obtained from: https://archive.eso.org/scienceportal/home?data_release_date=*:2019-09-18&pos=39.2442,-34.57798&r=0.016667&poly=39.318719,-34.614387,39.169781,-34.614387,39.169846,-34.541445,39.318654,-34.541445&dp_type=SPECTRUM&sort=dist,-fov,-obs_date&s=P%2fDSS2%2fcolor&f=0.122541&fc=39.318654,-34.541445&cs=J2000&av=true&ac=false&c=8,9,10,11,12,13,14,15,16,17,18&ta=RES&dts=true&sdtm=%7b%22SPECTRUM%22%3atrue%7d&at=39.2442,-34.57798

Table 3. Best-fit orbital parameters of λ^2 For b.

Parameter	Discovery paper	This work
P [days]	17.24 ± 0.01	$17.251^{+0.002}_{-0.003}$
K [m s^{-1}]	5.0 ± 0.4	4.0 ± 0.3
e	0.20 ± 0.09	$0.35^{+0.05}_{-0.05}$
$m_p \sin i$ [$M_\oplus$]	22.1 ± 2.0	$16.8^{+1.2}_{-1.3}$

Notes. Orbital parameters of λ^2 For b, where P is the orbital period, K is the RV semi-amplitude, e is the orbital eccentricity, and $m_p \sin i$ is the estimated lower limit of the planet mass. The middle column shows the values found by O'Toole et al. (2009), the right column shows the best-fit parameters from `Kima` found in this work.

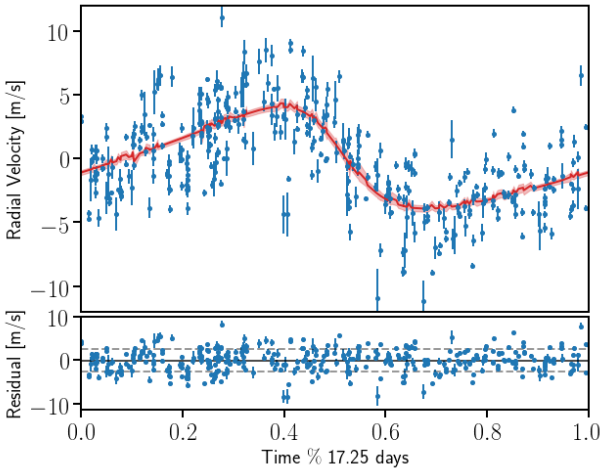

Fig. 5. *Top*: observational RV data (blue) of λ^2 For, from AAT, Keck, and HARPS, phase-folded at a period of 17.25 days. The phase-folded best-fit model is shown in red, with the model uncertainties in shaded red. *Bottom*: residual RV after subtracting the best-fit RV model. The dashed lines indicate the standard deviation, $\sigma = 2.64\,\mathrm{m\,s^{-1}}$, of the residual.

the median of the distribution of each parameter (see Figs. C.2 and C.3), and provide uncertainties estimated from the 16th and 84th percentiles, which are shown in Table 3. The best-fit model is shown in Fig. 5, along with the residual RV signal, which has a standard deviation of $\sigma = 2.64\,\mathrm{m\,s^{-1}}$.

To verify the `Kima` results, we also fit the RV data using the `exoplanet` package (Foreman-Mackey et al. 2019), which, like `Kima`, also fits Keplerian orbits, but includes the signal from stellar granulation noise as a Gaussian process in the RV model. The `exoplanet` package uses the `celerite` library (Foreman-Mackey et al. 2017) to model any variability in the RV signal that can be represented as a stationary Gaussian process. The choice of kernel for the Gaussian process was set by the quality factor which we here chose to be $Q = 1/2$ to represent a stochastically excited damped harmonic oscillator with a characteristic timescale w_0 and amplitude S_0. We applied a normal prior on w_0 based on the modeling of the TESS power spectrum presented in Sect. 3 as the granulation timescale is expected to be identical in both radial velocity and photometric variability. The granulation power in the TESS intensity spectrum is not easily converted to a radial velocity signal as seen from multiple different instruments, we therefore use a weakly-informative log-normal prior on S_0. We found that the `Kima` and `exoplanet` results were consistent within 1σ.

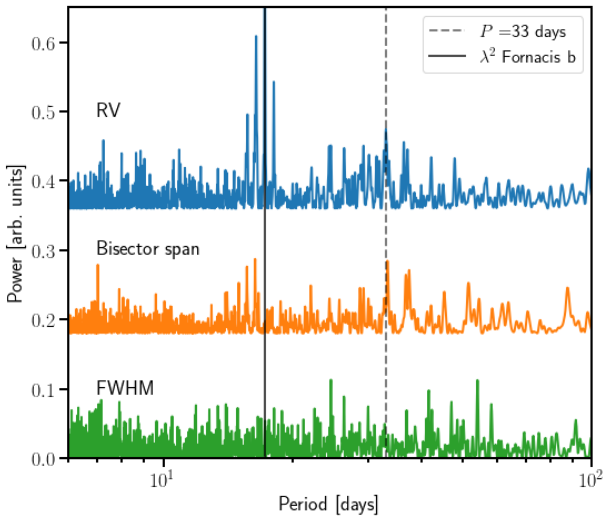

Fig. 6. Periodograms of the HARPS RV data (blue), the spectral line bisector span (orange), and the cross-correlation function full-width at half maximum (FWHM, green). The FWHM and bisector span were only available for the HARPS data, and so the AAT and Keck data are not included in the power spectra shown here. The full vertical line shows the period of λ^2 For b, and the dashed line is the secondary 33-day periodicity. The comb of peaks around the orbital period of λ^2 For b are caused by the observational window function, as is the case for many of the peaks around the 33-day periodicity.

4.2. Additional radial velocity variability

O'Toole et al. (2009) suggested the presence of a periodicity at ≈298 days, which they ultimately did not attribute to the presence of an additional planet. The posterior distribution of the fit parameters obtained from `Kima` indeed shows a periodicity at ≈300 days, but the Bayesian evidence does not support the added model complexity that comes from adding a planet at or near this orbital period. This was quantified by calculating the Bayes factor (the ratio of evidence weighted probabilities, Kass & Raftery 1995) for an increase in the number of planets from $N_\mathrm{p} = 1$, i.e., assuming only λ^2 For b exists, to $N_\mathrm{p} = 2$ (see Fig. C.2). This yielded a Bayes factor of ≈1.67, which is "not worth more than a bare mention" (Kass & Raftery 1995). This was found to be the case when testing both just the AAT and Keck data set, and with the added HARPS data.

However, using the combined data sets highlights a period at ≈33 days. Figure 6 shows the periodogram of the RV measurements, where the signal due to λ^2 For b is visible at $P = 17.25$ days, with surrounding aliases caused by the observational window function. The 33-day periodicity shows aliasing in the RV, but also appears in the bisector span, which in addition shows harmonic peaks at a period of ≈16.5 days. This signal was not discussed by O'Toole et al. (2009), and so to investigate this periodicity further we established two scenarios: first, that it is due to another planet in a wider orbit than the known planet or second, that it is due to variability induced by magnetic activity on the stellar surface.

4.2.1. Scenario 1: An additional planet

In the first scenario we consider that the 33-day signal is due to an additional planet in the λ^2 For system. From Fig. 6 a bisector span variation is apparent at this period, which is a strong indication that the signal is not a planet (see, e.g., Queloz et al. 2001). In addition, we used `Kima` to evaluate the possibility of a

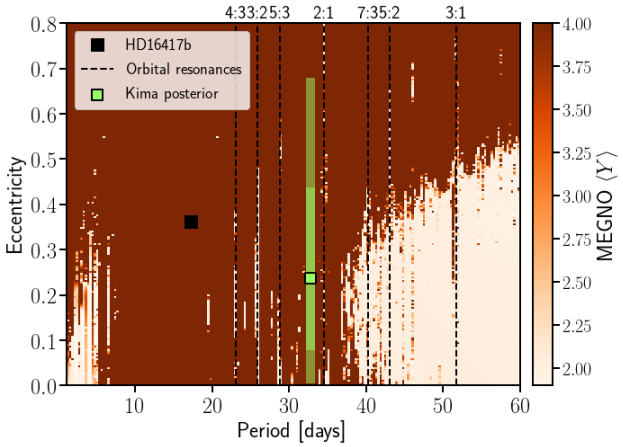

Fig. 7. Stability map (MEGNO) for a particle at different periods and inclinations, in the presence of the known planet λ^2 For b. The color bar indicates the linear scale of the MEGNO statistic, for which darker colors represent a higher degree of orbital divergence (chaos) on timescales of 10^5 orbits of λ^2 For b. Lighter shaded regions denote stable orbits. The upper range of the color bar has been truncated at a MEGNO value of 4 for clarity. The marginalized posterior distribution of the 33-day orbit is shown in green, with the median indicated by the square symbol. Orbits in resonance with λ^2 For b are indicated by vertical dashed lines. Additional resonances are not marked for clarity. The solid black square denotes the period and eccentricity of λ^2 For b.

planet in such an orbit, but the Bayesian evidence for the additional planet remains small. This in itself would suggest that the existence of a second planet is unlikely but as a final belts-and-braces measure we tested the dynamical stability of such a planet to investigate whether it could survive on timescales comparable to the ≈6.3 Gyr lifetime of the λ^2 For system.

The dynamical simulations were performed using the `REBOUND` package[4], described in detail by Rein & Liu (2012), and using the WHFast integrator (Rein & Tamayo 2015). `REBOUND` computes the Mean Exponential Growth factor of Nearby Orbits (MEGNO, Maffione et al. 2011), which is a chaos indicator on a logarithmic scale that quantifies the divergence of a test particle placed in relation to known orbiting planet, in this case λ^2 For b. These techniques have been applied to a range of exoplanetary systems (Goździewski et al. 2001; Goździewski 2002; Satyal et al. 2013, 2014; Triaud et al. 2017; Kane 2019).

Figure 7 shows the results of our dynamical simulation, where the MEGNO values are presented as a function of eccentricity and orbital period. MEGNO values $\lesssim$2 indicate very likely stable orbits, while values $\gtrsim$2 are either approaching instability (chaos), or for MEGNO $\gg$2 have already diverged at the end of the simulation. The simulations were run for 10^5 orbits of λ^2 For b, equivalent to ≈4700 years, where the configuration seen in Fig. 7 was reached after just a few hundred orbits. Figure 7 also shows the marginalized posterior distribution of the eccentricity and period obtained from `Kima`, for the 33-day periodicity. The range of periods is narrower than the symbol size (see Table 3), but the eccentricity spans a wide range. None of the orbits within the period range have MEGNO values $\lesssim$2, indicating that any orbit at this period would be unstable. A number of very narrow stable regions appear at multiple different periods. These are all likely due to resonances with λ^2 For b. However, none fall near the 33-day periodicity, excluding the possibility that a planet in this orbit could be stable due to a resonance.

[4] `rebound.readthedosc.io`

4.2.2. Scenario 2: Stellar activity

O'Toole et al. (2009) did not discus the 33-day RV variability; however, they estimated a rotation period of the star of 22−33 days, based on the measured $\log R'_{\rm HK} = -5.08$ and the age-activity relation by Wright et al. (2004). Estimates of the projected rotational velocity $v \sin i$ in the literature fall in the range 2.1−2.5 km s^{-1} (Nordström et al. 2004; Valenti & Fischer 2005; Ammler-von Eiff & Reiners 2012), which is consistent with a rotation period of 33 days when assuming a stellar radius of 1.63 $R_\odot$ and an inclined rotation axis on the order of $i \approx 50°$ relative to the line of sight to the observer.

While the asteroseismic fit included the rotation rate and inclination of the rotation axis of the star as free variables, the marginalized posteriors for these parameters (see Fig. C.1) could only constrain the rotation rate to $\lesssim$2.1 μHz. This is likely in part due to the low frequency resolution of the power spectrum (0.2 μHz) compared to the expected slow rotation rate of the star (≈0.36 μHz). Measuring rotation rates from the oscillation modes may also be further hampered by a very low angle of inclination of the rotation axis relative to the observer.

No signatures of star spots are visible in the TESS photometry, either in the SPOC or manually reduced light curves (see Fig. A.1), which might also be expected for a star with a low inclination angle and low activity level.

If this signal is indeed due to rotation, a similar period is expected in the spectral line bisector, and in some cases in the full width at half maximum (FWHM) of the cross-correlation function used to measure the RV (e.g., Dumusque et al. 2012; Gomes da Silva et al. 2012). In the case of λ^2 For the power spectra of the HARPS RV data and the bisector span (see Fig. 6) show a power excess at around 33 days, but the FWHM spectrum does not show any clear peaks at this period. Furthermore, no significant correlation was found between the residual RV, after removing the signal from λ^2 For b, and the bisector span where a negative correlation is in some cases an indication that the bisector span variation is caused by stellar activity (Huélamo et al. 2008; Queloz et al. 2009).

Using the gyrochronology relation by Barnes (2003), with the asteroseismic ages from Sect. 3 and a $B - V = 0.66$ (Ducati 2002) as input, we find that the rotation period of the star is likely between $P_{\rm rot} = 27-31$ days. While correcting the $B - V$ estimate for interstellar reddening decreases this estimated period range, we note that the Barnes (2003) relation is only calibrated for young main-sequence stars and does not account for structural evolution that occurs after stars leave the main sequence. This is expected to increase the surface rotation period as the radius of the stellar envelope increases after the main sequence (see, e.g., Fig. 3 in van Saders et al. 2016).

5. Discussion and conclusions

We used the recent release of TESS photometric data to perform an asteroseismic analysis of the star λ^2 For. This allowed us to place tighter constraints on the stellar parameters than has previously been possible. We measured individual oscillation mode frequencies of the star centered at ≈1280 μHz, which were then distributed to several modeling teams. Using different approaches and input physics each team returned estimates of the physical properties of the star that were consistent to within 1−2σ, suggesting that the application of asteroseismic constraints produces more robust estimates of the stellar properties. For the mass and radius, which are typically well constrained by asteroseismology (Lebreton & Goupil 2014; Stokholm et al. 2019), we adopted the overall values $M_\star = 1.16 \pm 0.03\, M_\odot$ and

$R_\star = 1.63 \pm 0.04\,R_\odot$. Together with a surface temperature of $T_{\rm eff} = 5829 \pm 80$ K. Previous literature estimates suggest λ^2 For could be anything from an early G dwarf to a late G-type subgiant; however, multiple modeling teams using asteroseismic constraints all place the star firmly at the start of the subgiant phase of its evolution.

The age of the system was less well constrained, despite the seismic constraint, with an estimate of 6.3 ± 0.9 Gyr, with most literature values falling within this range. This is likely due to the correlation with the other model parameters, where particularly the mass and metallicity are important for estimating the age. In our case the uncertainty on the mass estimate is caused in part by the uncertainty on the mode frequencies due to the relativity short TESS time series, while the metallicity is taken from spectroscopic values in the literature.

Following this we revisited the analysis of λ^2 For b originally performed by O'Toole et al. (2009), who discovered the Neptune-like planet. We combined the radial velocity measurements from the original publication with the now public HARPS measurements, yielding an RV time series spanning approximately 20 years. Combining this with the asteroseismic mass estimate, reduces the lower mass limit of λ^2 For b from $m_{\rm p} \sin i = 22.1 \pm 2.0 M_\oplus$ to $m_{\rm p} \sin i = 16.8^{+1.2}_{-1.3}\ M_\oplus$. The majority of this reduction is due to the long RV time series, which alone sets a lower limit of $m_p \sin i = 17.2 \pm 1.3\ M_\oplus$. The stellar mass found here using asteroseismology is ∼3% lower than that used by O'Toole et al. (2009), and as such reduces the lower limit on the planet by a similar amount.

The orbital eccentricity was also found to be significantly higher at $e = 0.35 \pm 0.05$, as opposed to the previous estimate of $e = 0.20 \pm 0.09$. We estimate the circularization timescale due to tidal interaction following an expression derived in Barker & Ogilvie (2009) and find it to be ≈1120 Gyr, which is much longer than the age of the system. The slightly higher eccentricity found here is then perhaps more consistent with this long circularization timescale, compared to the original estimate, which at a 2σ level encompasses almost circular orbits.

In addition to the revised parameters for λ^2 For b, the larger set of RV measurements also revealed a periodicity at 33 days. Despite the relatively low activity level of the star, this periodicity is more likely due to stellar rotation when compared to the case of an additional unknown planet being present in the system. Although difficult to confirm, the former scenario is consistent with the expected rotation rate of an old inactive star like λ^2 For, and we showed that the latter scenario is not possible as such an orbit would be unstable after $\sim 10^3$ years. Assuming then that the 33-day RV signal is indeed due to rotation, the relatively short 17.25 day orbit of λ^2 For b means that tidal interaction with the host star will cause the planet to gradually spiral inward into the star. Using the relation by Barker & Ogilvie (2009) we can estimate the current infall timescale to be on the order of 10^3–10^4 Gyr. This is obviously much longer than the evolutionary timescale of the host star, and so the time when the star expands to the current periastron of λ^2 For b (0.1 AU, 21.5 $R_\odot$) sets an upper limit for when the planet will be engulfed. The models presented in Sect. 3.2 suggest that this will happen in approximately 1.5 Gyr. However, the tidal interaction, and thus the infall timescale, is a strong function of the stellar radius and the orbital period (Barker & Ogilvie 2009). This will cause the infall to accelerate considerably over time and the planet will likely be engulfed well before λ^2 For expands to the current orbit.

Despite the rather modest time series that was obtained from TESS for λ^2 For, we have shown that it is still possible to measure the individual oscillation frequencies of the star. Moreover, using these frequencies, multiple modeling teams find consistent results on the percent level for the mass and radius of λ^2 For. This shows that asteroseismology is a useful tool for obtaining robust constraints on these stellar parameters, for the enormous selection of stars being observed by TESS, which previously has only been possible for select areas of the sky like those observed by CoRoT and *Kepler*. This new and much wider range of stars that TESS is observing prompts the reexamination of the wealth of archival radial velocity data that has been accumulated in the last few decades for planet hosting systems, in order to better characterize these systems.

Acknowledgements. The authors would like to thank J. P. Faria and H. Rein for useful discussions. This paper includes data collected by the TESS mission. MBN, WHB, MRS, AHMJT, and WJC acknowledge support from the UK Space Agency. AHMJT and MRS have benefited from funding from the European Research Council (ERC) under the European Union's Horizon 2020 research and innovation programme (grant agreement no 803193/BEBOP). Funding for the Stellar Astrophysics Centre is funded by the Danish National Research Foundation (Grant agreement no.: DNRF106). ZÇO, MY, and SÖ acknowledge the Scientific and Technological Research Council of Turkey (TÜBITAK:118F352). AS acknowledges support from grants ESP2017-82674-R (MICINN) and 2017-SGR-1131 (Generalitat Catalunya). TLC acknowledges support from the European Union's Horizon 2020 research and innovation programme under the Marie Skłodowska-Curie grant agreement No. 792848 (PULSATION). This work was supported by FCT/MCTES through national funds (UID/FIS/04434/2019). MD is supported by FCT/MCTES through national funds (PIDDAC) by this grant UID/FIS/04434/2019. MD and MV are supported by FEDER - Fundo Europeu de Desenvolvimento Regional through COMPETE2020 - Programa Operacional Competitividade e Internacionalização by these grants: UID/FIS/04434/2019; PTDC/FIS-AST/30389/2017 & POCI-01-0145-FEDER-030389 & POCI-01-0145-FEDER03038. MD is supported in the form of a work contract funded by national funds through Fundação para a Ciência e Tecnologia (FCT). SM acknowledges support by the Spanish Ministry with the Ramon y Cajal fellowship number RYC-2015-17697. BM and RAG acknowledge the support of the CNES/PLATO grant. DLB and LC acknowledge support from the TESS GI Program under awards 80NSSC18K1585 and 80NSSC19K0385. LGC thanks the support from grant FPI-SO from the Spanish Ministry of Economy and Competitiveness (MINECO) (research project SEV-2015-0548-17-2 and predoctoral contract BES-2017-082610). Funding for the TESS mission is provided by the NASA Explorer Program. Based in part on data acquired at the Anglo-Australian Telescope. We acknowledge the traditional owners of the land on which the AAT stands, the Gamilaraay people, and pay our respects to elders past and present. The data presented herein were in part obtained at the W. M. Keck Observatory, which is operated as a scientific partnership among the California Institute of Technology, the University of California and the National Aeronautics and Space Administration. The Observatory was made possible by the generous financial support of the W. M. Keck Foundation. The authors wish to recognize and acknowledge the very significant cultural role and reverence that the summit of Maunakea has always had within the indigenous Hawaiian community.

References

Adelberger, E. G., García, A., Robertson, R. G. H., et al. 2011, Rev. Mod. Phys., 83, 195
Ammler-von Eiff, M., & Reiners, A. 2012, A&A, 542, A116
Angelou, G. C., Bellinger, E. P., Hekker, S., & Basu, S. 2017, ApJ, 839, 116
Appourchaux, T., Antia, H. M., Benomar, O., et al. 2014, A&A, 566, A20
Ball, W. H., & Gizon, L. 2014, A&A, 568, A123
Ball, W. H., & Gizon, L. 2017, A&A, 600, A128
Barker, A. J., & Ogilvie, G. I. 2009, MNRAS, 395, 2268
Barnes, S. A. 2003, ApJ, 586, 464
Battistini, C., & Bensby, T. 2015, A&A, 577, A9
Bellinger, E. P., Hekker, S., Angelou, G. C., Stokholm, A., & Basu, S. 2019, A&A, 622, A130
Bensby, T., Feltzing, S., & Lundström, I. 2003, A&A, 410, 527
Bensby, T., Feltzing, S., & Oey, M. S. 2014, A&A, 562, A71
Bertran de Lis, S., Delgado Mena, E., Adibekyan, V. Z., Santos, N. C., & Sousa, S. G. 2015, A&A, 576, A89
Bond, J. C., Tinney, C. G., Butler, R. P., et al. 2006, MNRAS, 370, 163
Bonfanti, A., Ortolani, S., & Nascimbeni, V. 2016, A&A, 585, A5
Borucki, W. J., Koch, D., Basri, G., et al. 2010, Science, 327, 977
Brewer, B. J., Pártay, L. B., & Csányi, G. 2009, Stat. Comput., 21, 649
Brown, T. M., Christensen-Dalsgaard, J., Weibel-Mihalas, B., & Gilliland, R. L. 1994, ApJ, 427, 1013

Buzasi, D. L., Carboneau, L., Hessler, C., Lezcano, A., & Preston, H. 2015, IAU Gen. Assembly, 29, 2256843
Campante, T. L., Corsaro, E., Lund, M. N., et al. 2019, ApJ, 885, 31
Carretta, E. 2013, A&A, 557, A128
da Silva, L., Girardi, L., Pasquini, L., et al. 2006, A&A, 458, 609
Datson, J., Flynn, C., & Portinari, L. 2015, A&A, 574, A124
Davies, G. R., Handberg, R., Miglio, A., et al. 2014, MNRAS, 445, L94
Delgado Mena, E., Tsantaki, M., Adibekyan, V. Z., et al. 2017, A&A, 606, A94
Ducati, J. R. 2002, VizieR Online Data Catalog:II/237
Dumusque, X., Pepe, F., Lovis, C., et al. 2012, Nature, 491, 207
Faria, J. P., Santos, N. C., Figueira, P., & Brewer, B. J. 2018, J. Open Source Soft., 3, 487
Ferguson, J. W., Alexander, D. R., Allard, F., et al. 2005, ApJ, 623, 585
Foreman-Mackey, D., Hogg, D. W., Lang, D., & Goodman, J. 2013, PASP, 125, 306
Foreman-Mackey, D., Agol, E., Ambikasaran, S., & Angus, R. 2017, AJ, 154, 220
Foreman-Mackey, D., Czekala, I., Luger, R., et al. 2019, dfm/exoplanet v0.2.3
Fridlund, M., Baglin, A., Lochard, J., & Conroy, L. 2006, in The CoRoT Mission Pre-Launch Status - Stellar Seismology and Planet Finding, ESA Spec. Publ., 1306
García, R. A., & Ballot, J. 2019, Liv. Rev. Sol. Phys., 16, 4
Gehren, T. 1981, A&A, 100, 97
Gomes da Silva, J., Santos, N. C., Bonfils, X., et al. 2012, A&A, 541, A9
Goździewski, K. 2002, A&A, 393, 997
Goździewski, K., Bois, E., Maciejewski, A. J., & Kiseleva-Eggleton, L. 2001, A&A, 378, 569
Gray, R. O., Corbally, C. J., Garrison, R. F., et al. 2006, AJ, 132, 161
Grevesse, N., & Noels, A. 1993, in Origin and Evolution of the Elements, eds. N. Prantzos, E. Vangioni-Flam, & M. Casse, 15
Handberg, R., & Campante, T. L. 2011, A&A, 527, A56
Harvey, J. W., Hill, F., Kennedy, J. R., Leibacher, J. W., & Livingston, W. C. 1988, Adv. Space Res., 8, 117
Hearnshaw, J. B., & Schmidt, E. G. 1972, A&A, 21, 111
Herwig, F. 2000, A&A, 360, 952
Huber, D., Chaplin, W. J., Chontos, A., et al. 2019, AJ, 157, 245
Huélamo, N., Figueira, P., Bonfils, X., et al. 2008, A&A, 489, L9
Iglesias, C. A., & Rogers, F. J. 1993, ApJ, 412, 752
Iglesias, C. A., & Rogers, F. J. 1996, ApJ, 464, 943
Irwin, A. W. 2012, FreeEOS: Equation of State for Stellar Interiors Calculations
Jenkins, J. M., Twicken, J. D., McCauliff, S., et al. 2012, in The TESS Science Processing Operations Center, SPIE Conf. Ser., 9913, 99133E
Kallinger, T., De Ridder, J., Hekker, S., et al. 2014, A&A, 570, A41
Kane, S. R. 2019, AJ, 158, 72
Kass, R. E., & Raftery, A. E. 1995, J. Am. Stat. Assoc., 90, 773
Krishna Swamy, K. S. 1966, ApJ, 145, 174
Kurucz, R. L. 2013, ATLAS12: Opacity Sampling Model Atmosphere Program
Lebreton, Y., & Goupil, M. J. 2014, A&A, 569, A21
Lund, M. N., & Reese, D. R. 2018, Asteroseismology and Exoplanets: Listening to the Stars and Searching for New Worlds, 49, 149
Lund, M. N., Silva Aguirre, V., Davies, G. R., et al. 2017, ApJ, 835, 172
Maffione, N. P., Giordano, C. M., & Cincotta, P. M. 2011, Int. J. Non Linear Mech., 46, 23
Magic, Z., Serenelli, A., Weiss, A., & Chaboyer, B. 2010, ApJ, 718, 1378
Mayor, M., Pepe, F., Queloz, D., et al. 2003, The Messenger, 114, 20
McInnes, L., Healy, J., & Astels, S. 2017, J. Open Source Soft., 2
Mosser, B., Michel, E., Belkacem, K., et al. 2013, A&A, 550, A126
Mosumgaard, J. R., Ball, W. H., Silva Aguirre, V., Weiss, A., & Christensen-Dalsgaard, J. 2018, MNRAS, 478, 5650
Nason, G. 2006, Stationary and non-stationary time series, eds. H. Mader, & S. Coles (UK: Geological Society of London), 129
Nelder, J. A., & Mead, R. 1965, Comput. J., 7, 308
Nordström, B., Mayor, M., Andersen, J., et al. 2004, A&A, 418, 989
O'Toole, S., Tinney, C. G., Butler, R. P., et al. 2009, ApJ, 697, 1263
Paxton, B., Bildsten, L., Dotter, A., et al. 2011, ApJ, 192, 3
Paxton, B., Cantiello, M., Arras, P., et al. 2013, ApJS, 208, 4
Paxton, B., Marchant, P., Schwab, J., et al. 2015, ApJS, 220, 15
Pijpers, F. P. 2003, A&A, 400, 241
Prša, A., Zhang, M., & Wells, M. 2019, PASP, 131, 068001
Queloz, D., Henry, G. W., Sivan, J. P., et al. 2001, A&A, 379, 279
Queloz, D., Bouchy, F., Moutou, C., et al. 2009, A&A, 506, 303
Ramírez, I., Meléndez, J., & Asplund, M. 2014, A&A, 561, A7
Rein, H., & Liu, S. F. 2012, A&A, 537, A128
Rein, H., & Tamayo, D. 2015, MNRAS, 452, 376
Rendle, B. M., Buldgen, G., Miglio, A., et al. 2019, MNRAS, 484, 771
Ricker, G. R., Winn, J. N., & Vanderspek, R. 2014, in Space Telescopes and Instrumentation 2014: Optical, Infrared, and Millimeter Wave, Proc. SPIE, 9143, 914320
Rogers, F. J., & Nayfonov, A. 2002, ApJ, 576, 1064
Satyal, S., Quarles, B., & Hinse, T. C. 2013, MNRAS, 433, 2215
Satyal, S., Hinse, T. C., Quarles, B., & Noyola, J. P. 2014, MNRAS, 443, 1310
Schlegel, D. J., Finkbeiner, D. P., & Davis, M. 1998, ApJ, 500, 525
Schofield, M., Chaplin, W. J., Huber, D., et al. 2019, ApJS, 241, 12
Soubiran, C., Jasniewicz, G., Chemin, L., et al. 2018, A&A, 616, A7
Sousa, S. G., Santos, N. C., Israelian, G., Mayor, M., & Monteiro, M. J. P. F. G. 2006, A&A, 458, 873
Sousa, S. G., Santos, N. C., Mayor, M., et al. 2008, A&A, 487, 373
Stassun, K. G., & Torres, G. 2016, AJ, 152, 180
Stassun, K. G., Collins, K. A., & Gaudi, B. S. 2017, AJ, 153, 136
Stassun, K. G., Oelkers, R. J., Pepper, J., et al. 2018a, AJ, 156, 102
Stassun, K. G., Corsaro, E., Pepper, J. A., & Gaudi, B. S. 2018b, AJ, 155, 22
Stokholm, A., Nissen, P. E., Silva Aguirre, V., et al. 2019, MNRAS, 489, 928
Thoul, A. A., Bahcall, J. N., & Loeb, A. 1994, ApJ, 421, 828
Townsend, R. H. D., & Teitler, S. A. 2013, MNRAS, 435, 3406
Townsend, R. H. D., Goldstein, J., & Zweibel, E. G. 2018, MNRAS, 475, 879
Trampedach, R., Stein, R. F., Christensen-Dalsgaard, J., Nordlund, Å., & Asplund, M. 2014a, MNRAS, 442, 805
Trampedach, R., Stein, R. F., Christensen-Dalsgaard, J., Nordlund, Å., & Asplund, M. 2014b, MNRAS, 445, 4366
Triaud, A. H. M. J., Neveu-VanMalle, M., Lendl, M., et al. 2017, MNRAS, 467, 1714
Tsantaki, M., Sousa, S. G., Adibekyan, V. Z., et al. 2013, A&A, 555, A150
Valenti, J. A., & Fischer, D. A. 2005, ApJS, 159, 141
Vanderburg, A., & Johnson, J. A. 2014, PASP, 126, 948
VandenBerg, D. A., Bergbusch, P. A., Dotter, A., et al. 2012, ApJ, 755, 15
van Saders, J. L., Ceillier, T., Metcalfe, T. S., et al. 2016, Nature, 529, 181
Weiss, A., & Schlattl, H. 2008, Ap&SS, 316, 99
Wright, J. T., Marcy, G. W., Butler, R. P., & Vogt, S. S. 2004, ApJS, 152, 261

[1] School of Physics and Astronomy, University of Birmingham, Birmingham B15 2TT, UK
[redacted]
[2] Stellar Astrophysics Centre (SAC), Department of Physics and Astronomy, Aarhus University, Ny Munkegade 120, 8000 Aarhus C, Denmark
[3] Center for Space Science, NYUAD Institute, New York University Abu Dhabi, PO Box 129188, Abu Dhabi, UAE
e-mail: [redacted]
[4] Department of Chemistry and Physics, Florida Gulf Coast University, 10501 FGCU Blvd., Fort Myers, FL 33965, USA
[5] Department of Physics & Astronomy, Vanderbilt University, Nashville, TN 37235, USA
[6] Department of Earth and Planetary Sciences, University of California, Riverside, CA 92521, USA
[7] School of Physics, University of New South Wales, Kensington, NSW 2033, Australia
[8] LESIA, Observatoire de Paris, Université PSL, CNRS, Sorbonne Université, Université de Paris, 92195 Meudon, France
[9] Department of Astronomy and Space Sciences, Science Faculty, Ege University, 35100 Bornova, İzmir, Turkey
[10] Astronomy Unit, School of Physics and Astronomy, Queen Mary University of London, London E1 4NS, UK
[11] Instituto de Astrofísica e Ciências do Espaço, Universidade do Porto, Rua das Estrelas, 4150-762 Porto, Portugal
[12] Departamento de Física e Astronomia, Faculdade de Ciências da Universidade do Porto, Rua do Campo Alegre, s/n, 4169-007 Porto, Portugal
[13] IRFU, CEA, Université Paris-Saclay, 91191 Gif-sur-Yvette, France
[14] AIM, CEA, CNRS, Université Paris-Saclay, Université Paris Diderot, Sorbonne Paris Cité, 91191 Gif-sur-Yvette, France
[15] Instituto de Astrofísica de Canarias, La Laguna, Tenerife, Spain
[16] Dpto. de Astrofísica, Universidad de La Laguna, La Laguna, Tenerife, Spain
[17] Institute of Space Sciences (ICE, CSIC), Carrer de Can Magrans S/N, 08193 Bellaterra, Spain
[18] Institut d'Estudis Espacials de Catalunya (IEEC), Carrer Gran Capita 2, 08034 Barcelona, Spain
[19] Department of Astronomy, The Ohio State University, Columbus, OH 43210, USA
[20] Homi Bhabha Centre for Science Education, TIFR, V. N. Purav Marg, Mankhurd, Mumbai 400088, India

Appendix A: Manual time series reduction

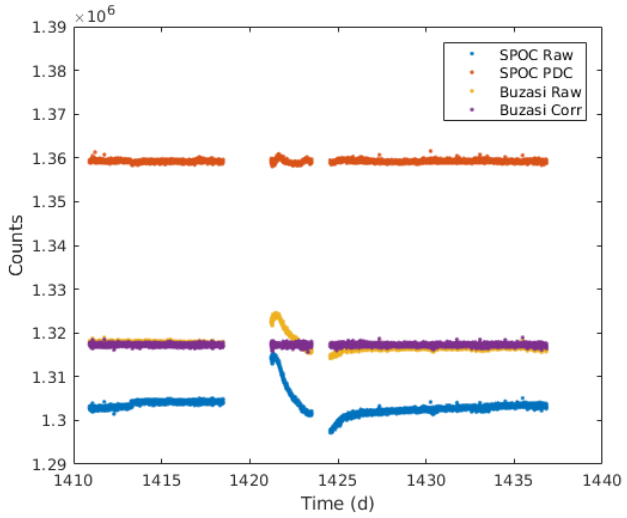

Fig. A.1. Resulting counts over time for different TESS data reduction pipelines. The Buzasi Corr time series very effectively removes most of the long-period variability; however, the SPOC time series still shows the lowest variance in the frequency range around the p-mode envelope.

For each TESS orbit we extracted a time series for each pixel and took the brightest pixel as our initial time series. The pixel time series quality figure of merit was parameterized by $q = \sum_{i=1}^{N-1} | f_{i+1} - f_i |$, where f is the flux at cadence i, and N is the length of the time series. Using the first differences of the light curve acts to whiten the time series, and thus correct for its non-stationary nature (Nason et al. 2006); similar approaches have been used in astronomical time series analysis by Buzasi et al. (2015) and Prša et al. (2019), among others.

We then iteratively added the flux of the pixels surrounding the brightest pixel. The process continued until the light curve quality stopped improving, and the resulting pixel collection was adopted as our aperture mask. The light curve produced by our aperture mask was then detrended against the centroid pixel coordinates by fitting a second-order polynomial with cross terms. Similar approaches have been used for K2 data reduction (see, e.g., Vanderburg & Johnson 2014).

Figure A.1 shows the resulting time series, compared to that derived by the SPOC. In this case, low-frequency noise was somewhat improved over the SPOC light curve product, but noise levels at the frequencies near the stellar oscillation spectrum were not. We accordingly used the SPOC light curve for the analysis outlined above.

Appendix B: Peakbagging frequencies

Table B.1. Oscillation frequencies ν with angular degree l of λ^2 For.

l	ν [μHz]
0	$1142.23^{+2.08}_{-2.00}$
1	$1171.79^{+1.55}_{-1.41}$
2	$1206.95^{+1.96}_{-2.13}$
0	$1211.30^{+0.44}_{-0.69}$
1	$1243.36^{+0.80}_{-0.92}$
0	$1282.05^{+1.83}_{-1.98}$
1	$1312.27^{+1.29}_{-0.97}$
2	$1348.67^{+1.81}_{-2.70}$
0	$1351.17^{+0.43}_{-0.44}$
1	$1380.81^{+0.45}_{-0.58}$

Notes. The frequency resolution of the data set is $\Delta T^{-1} = 0.2067\,\mu$Hz.

Appendix C: Posterior distributions

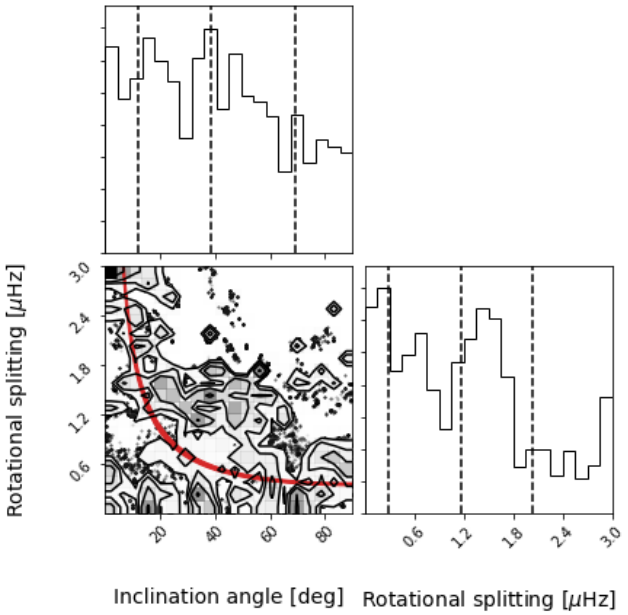

Fig. C.1. Corner plot of the rotational splitting and inclination angle posterior distributions from the seismic fit, consisting of 10^5 samples. The marginalized posterior distributions are shown in the diagonal frames. The dashed vertical lines show the 16th, 50th, and 84th percentiles of the distributions at $i = 38^{+31}_{-26}$ degrees and $\nu_{rot} = 1.2 \pm 0.9\,\mu$Hz for the inclination and rotational splitting respectively. The lower left frame shows a 2D histogram of the distributions (black). The shaded red curve shows the rotational splittings corresponding to $v \sin i = 2.5 \pm 0.1\,\mathrm{km\,s^{-1}}$ from Ammler-von Eiff & Reiners (2012) and a stellar radius of $R_\star = 1.63 \pm 0.04\,R_\odot$.

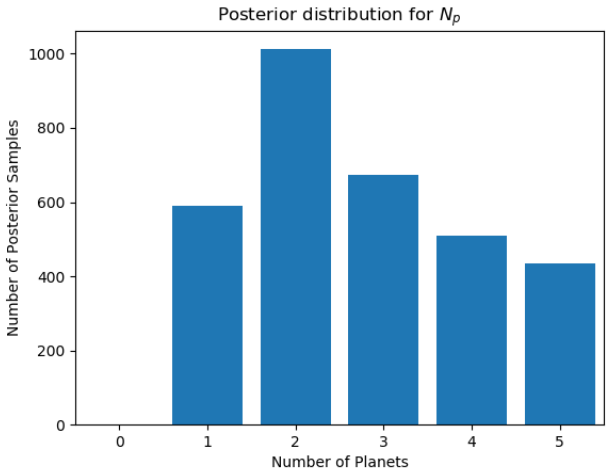

Fig. C.2. Marginalized posterior of the N_p parameter in the `Kima` fit to the RV measurements of λ^2 For. The number of samples in each bin corresponds to the likelihood, while the ratio of the height of each bin indicates the Bayes factor of one configuration over another. Comparing the cases of $N_p = 0$ and $N_p = 1$ the Bayes factor is effectively infinite, indicating that there is at least one planet in the system. In contrast, the ratio between $N_p = 2$ and $N_p = 1$ is low, with a Bayes factor of 1.67, suggesting that there is little evidence to support a two-planet configuration.

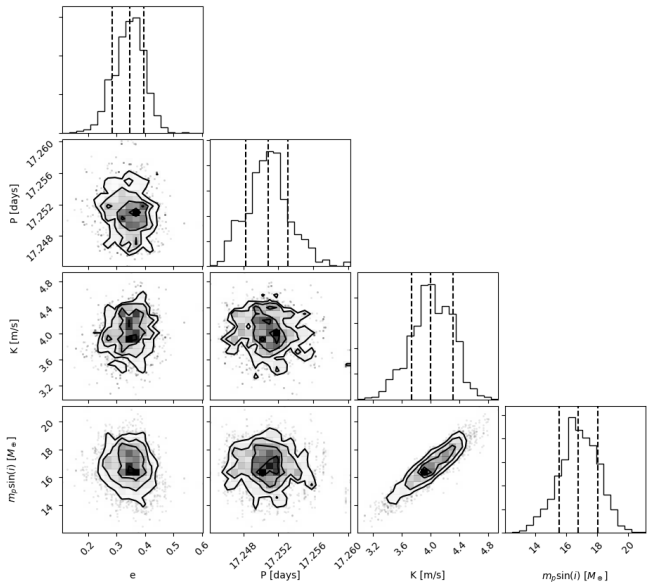

Fig. C.3. Corner plot of the orbital parameters from the `Kima` fit: the eccentricity e, the orbital period P, velocity semi-amplitude K, and the projected planet mass M.

Appendix D: Stellar properties literature values

Table D.1. Literature sources for $T_{\rm eff}$ and $\log g$ values shown in Fig. 4.

Source	$T_{\rm eff}$ [K]	$\log g$ [cm s^{-2}]
Hearnshaw & Schmidt (1972)	5793	4.09
Gehren (1981)	5860	4.35
Bensby et al. (2003)	5800 ± 70	4.04 ± 0.1
Valenti & Fischer (2005)	5817 ± 44	4.17 ± 0.06
da Silva et al. (2006)	5936 ± 70	4.12
Gray et al. (2006)	5745	4.11
Bond et al. (2006)	5374 ± 57	4.05 ± 0.19
Sousa et al. (2006)	5876 ± 22	4.22 ± 0.01
Sousa et al. (2008)	5841 ± 17	4.16 ± 0.02
Tsantaki et al. (2013)	5843 ± 12	4.16 ± 0.03
Carretta (2013)	5821	4.1
Ramírez et al. (2014)	5817 ± 15	4.146 ± 0.024
Bensby et al. (2014)	5885 ± 72	4.23 ± 0.1
Datson et al. (2015)	5766 ± 40	4.16 ± 0.07
Bertran de Lis et al. (2015)	5841	4.16
Battistini & Bensby (2015)	5885	4.2
Bonfanti et al. (2016)	5818	4.06 ± 0.02
Delgado Mena et al. (2017)	5841 ± 17	4.16 ± 0.02

Appendix E: HARPS observing programs

Table E.1. HARPS observing program PIs and IDs for data used in this work.

PI	Program ID
Diaz	198.C-0836
Doellinger	078.C-0751
Doellinger	079.C-0657
Doellinger	081.C-0802
Doellinger	082.C-0427
Hatzes	074.C-0102
Mayor	072.C-0488
Udry	091.C-0936
Udry	183.C-0972
Udry	192.C-0852

Chapter 4

BEBOP

> "In the face of overwhelming odds, I'm left with only one option: I'm going to have to science the shit out of this."
>
> Andy Weir, *The Martian*

This chapter is about the main body of work in this thesis: the attempt to discover circumbinary planets with Radial Velocity (RV) observations. In Section 4.1, I describe historical attempts to discover circumbinary planets with RV observations. Following this, in Section 4.2, the Binaries Escorted By Orbiting Planets (BEBOP) RV survey is introduced, along with its observational strategies, data sources, and techniques used to monitor the progress of the survey and identify candidate circumbinary planets. In Section 4.3, I describe detection limits for RV surveys, and my first first-author paper which details a new method to calculate detection limits for use in the BEBOP survey. Before introducing some promising candidate circumbinary planets from the BEBOP survey in Section 4.4. Parts of this section have been adapted from my mid-term report.

4.1 Previous circumbinary planet searches

Due to the instability region surrounding tight binaries (Section 1.4, Holman & Wiegert (1999)), circumbinary planets have longer orbital periods and separations from their host stars when compared to the majority of exoplanets found to date. This larger orbital separation lends itself to the direct detection method (Section 1.2) for detection of long period circumbinary planets. In 2014, an attempt to detect these planets using direct imaging was made by the Search for Planets Orbiting Two Stars (SPOTS) survey (Thalmann et al. 2014; Bonavita et al. 2016; Asensio-Torres et al. 2018). Using the Very Large Telescope (VLT) they observed a total of 163 tight binaries, and were unable to detect any circumbinary planets in the range 30-300 AU. This allowed them to place an upper limit on circumbinary planet occurrence rate

of planets with masses between 2 and 15 M_J < 10.5%, with a best fit frequency of 1.95% (Asensio-Torres et al. 2018), which is in agreement with the occurrence rate of 'Cold Jupiters' of $6.73^{+2.09}_{-1.13}$% found by Wittenmyer et al. (2020). A few circumbinary planets have been discovered with direct imaging techniques as discussed in Section 1.4.

To check for the presence of circumbinary planets with shorter orbital periods, other detection techniques are required. Transits have detected the majority of circumbinary planets around tight binaries (see Section 1.4). Of the 14 transiting circumbinary planets, accurate masses (different from zero mass by $> 2\sigma$) from binary ETV's are only available for 6 of them (see Table 1.1). Therefore, to accurately characterise these objects through determining their masses, Radial Velocity (RV) detections are required.

In 2009, an attempt to discover circumbinary planets, known as The Attempt To Observe Outer-planets In Non-single-stellar Environments (TATOOINE) RV survey, was introduced (Konacki 2005; Konacki et al. 2009, 2010). This survey searched 13 non-eclipsing, Double line Spectroscopic Binary (SB2) systems, and collected high-resolution RV data. SB2 systems are those where both stars of the binary are of similar brightness, and therefore spectral lines from both stars are resolved with a spectrograph. This leads to two minima present in the obtained CCF (see Section 1.2.2), complicating the RV extraction process. See Figure 4.10 for an example of CCF's calculated from 10 different Spectrograph for the Observation of the PHenomena of stellar Interiors and Exoplanets (SOPHIE) observations of a SB2 target as part of the BEBOP survey. The complication introduced by these double CCF's produces a large residual Root Mean Squared (RMS) scatter with an amplitude comparable to the RV signal of large gas giant planets, obscuring them from detection.

The TATOOINE survey obtained a median residual RMS of 18 $m\,s^{-1}$ on the majority of their targets, with their best target (HD 9939) reaching an RMS of 7 $m\,s^{-1}$ (Konacki et al. 2009). For SB2 binary targets, this level of precision is impressive and poses no problem for the determination of the binary orbits, as the mass of the secondary star is large and imposes an RV semi-amplitude (K) signal of several $km\,s^{-1}$. However, a scatter of 18 $m\,s^{-1}$ can easily hide the presence of planetary signals in the data.

Unfortunately, TATOOINE was unable to detect any circumbinary planets with their observations, and therefore suggested future RV surveys target SB1 binaries to reduce this unwanted residual scatter. Observing SB1 binary targets yield RV precision akin to that of single stars, since the spectral lines from the faint secondary star are not detected with current optical spectrographs. The system can therefore be treated as a single star with a particularly massive RV signal caused by the secondary. With precise RV observations, removing this binary signal can be done easily, and allows for the search for circumbinary planetary companions.

4.2 The BEBOP Survey

The Binaries Escorted By Orbiting Planets (BEBOP) survey is a Radial Velocity (RV) survey which expands on the work of Konacki et al. (2009) by observing primarily SB1 eclipsing binary systems (Martin et al. 2019). Observing SB1 binary targets means that a second set of spectral lines are not

observed, as only the brightest star's lines are present in the spectrum. Typically, the primary stars for the BEBOP binary targets are > 4 magnitudes brighter than their secondaries (Standing et al. (2022), Section 4.3).

BEBOP's aim is to discover circumbinary planets while minimising detection biases involved with transit discoveries, probing longer period orbits, with less dependence on the system inclination. A large RV survey promises to increase the sample size of these so-far illusive and mysterious celestial bodies. BEBOP aims to provide a deeper insight into circumbinary planet demographics (e.g. Martin & Triaud 2014; Armstrong et al. 2014), formation processes (e.g. Paardekooper et al. 2012; Pierens et al. 2020), and orbital evolution (e.g. Penzlin et al. 2021).

Observations began in the Southern hemisphere in 2013, with many of its binary targets being selected from the EBLM project (Triaud et al. 2013; Gómez Maqueo Chew et al. 2014; von Boetticher et al. 2017; Triaud et al. 2017; Gill et al. 2019). The EBLM project observed binaries with low mass secondary stars identified by the WASP consortium (Pollacco et al. 2006). Since then, BEBOP has also expanded to include eclipsing binaries identified by *TESS* (Ricker et al. 2015), such as TOI-222 (Lendl et al. 2020).

The southern survey observed a total of 72 SB1 binaries with the High Accuracy Radial velocity Planet Searcher (HARPS) spectrograph (Mayor et al. (2003), Section 4.2.2) from April 2018. The primary sample consisted of 50 of these targets which received a median of 22 observations each. From these initial observations, 16 candidate planetary signals were identified, along with 14 systems which demonstrated signs of stellar activity. These active targets were removed from the sample. Currently, BEBOP observes 48 southern SB1 binaries in its primary sample. The primary sample now includes those with candidate planetary signals to be confirmed with further observations, along with targets which show no signs of stellar activity. The targets with no current candidate signals are observed to probe for lower mass, and longer period planetary signals. The secondary sample consists of an additional 49 binary targets for use as back-up observations in adverse weather conditions. These are targets which have uncertain binary parameters, or those with a high level of residual scatter present, hindering the search for planetary signals.

In addition to the southern survey, BEBOP observes 60 binary targets in the Northern hemisphere (with an additional 40 targets available as back-up). The northern survey began in 2018 on the SOPHIE spectrograph (Perruchot et al. (2008), Section 4.2.2). Due to the larger number of targets diluting observations, poor weather and the COVID-19 pandemic, we have obtained fewer observations in the northern hemisphere than expected. These factors, coupled with a lower instrumental precision (when compared to HARPS), has adversely affected our ability to identify candidate signals in comparison to our southern sample. Observations are still ongoing in both hemispheres and candidate circumbinary signals begin to emerge from the noise with each observation.

In the northern hemisphere a few SB2 binary targets are also occasionally observed, with the aim of solving the double-line binary problem in the future, allowing circumbinary planet signals around them to be detected.

The nomenclature used for BEBOP targets comes from the WASP naming convention for EBLM

binaries, and provides information on the targets' sky coordinates. As an example, EBLM J0608-59 (see Chapter 6 for further discussion on this target) is located at a Right Ascension (RA) of 06h 08m, and a Declination (DEC) of -59°.[a]

BEBOP's primary and secondary southern targets have a similar median brightness at ≈ 11 m_v, while the TATOOINE sample is far brighter at 6.2 m_v. This is also reflected in BEBOP's northern sample. Figure 4.1 shows the median brightness of BEBOP's southern and northern targets, in comparison to those observed by TATOOINE.

Despite the brightness of TATOOINE's targets, Figure 4.2 illustrate the effectiveness of observing SB1 targets in BEBOP. Median uncertainties for BEBOP's southern primary sample and secondary sample are 5.5 and 7.9 $m\,s^{-1}$ respectively, whereas the median uncertainty for the TATOOINE sample is 16 $m\,s^{-1}$. This is also the case for BEBOP's northern targets, with the primary sample's median uncertainty reaching 10.1 $m\,s^{-1}$. The secondary sample in the North for BEBOP is only observed in bad conditions and suffers from few observations for each target. In Figure 4.2, taking only targets with 12 or more observations (the minimum number required to accurately characterise the binary orbit), the secondary sample has a median uncertainty of 11.1 $m\,s^{-1}$. Figure 4.3 confirms the uncertainty values with the primary samples in both hemispheres having median Signal to Noise Ratio (SNR) slightly above the secondary targets. This is expected since the secondary targets are usually observed in worse conditions. Comparing the median uncertainties for the primary samples in the two hemispheres, we can see that BEBOP's southern observations yield RV uncertainties which are half those of the northern sample. This can be explained by the difference in instrumental precision and resolution from the HARPS spectrograph in the South, when compared to that of the SOPHIE spectrograph used in the North, in combination with the average conditions available at both observatories, see Section 4.2.2.

4.2.1 Observing strategy

BEBOP is a 'blind' survey, meaning that observations are obtained uniformly across all observable targets. Performing a blind survey inhibits 'observers bias'[b] and ensures fair and equal treatment of each target in the survey. Resulting survey statistics will therefore be more analogous to the underlying demographics of circumbinary planets, and produce more robust detection limits (Standing et al. (2022), Section 4.3). Once candidate circumbinary planets reach a strong enough statistical significance (Bayes Factor (BF) > 140), targeted observations of the host binary are carried out until sufficient data is obtained, which allows the planet to be formally detected (Standing et al. (2022), Section 4.3).

The original goal of the Southern survey was to obtain 20 observations on each binary in the sample (Martin et al. 2019), though this has since been increased to 30, to increase our sensitivity to circumbinary planets with smaller masses. Each observation has a duration of 1800 s typically (with the brightest targets this is lowered to 900 s). The Northern survey aims to collect 55 observations on each binary, more than

[a] RA is a measure of East/West in hours as it depends on the rotation of the Earth, and DEC is a measure of North/South or elevation on the night sky.

[b] 'Observers bias' in this context refers to where an observer will carry out more observations on a promising target to confirm a planetary candidate when compared to the remaining survey targets, thus biasing the statistics of the overall sample.

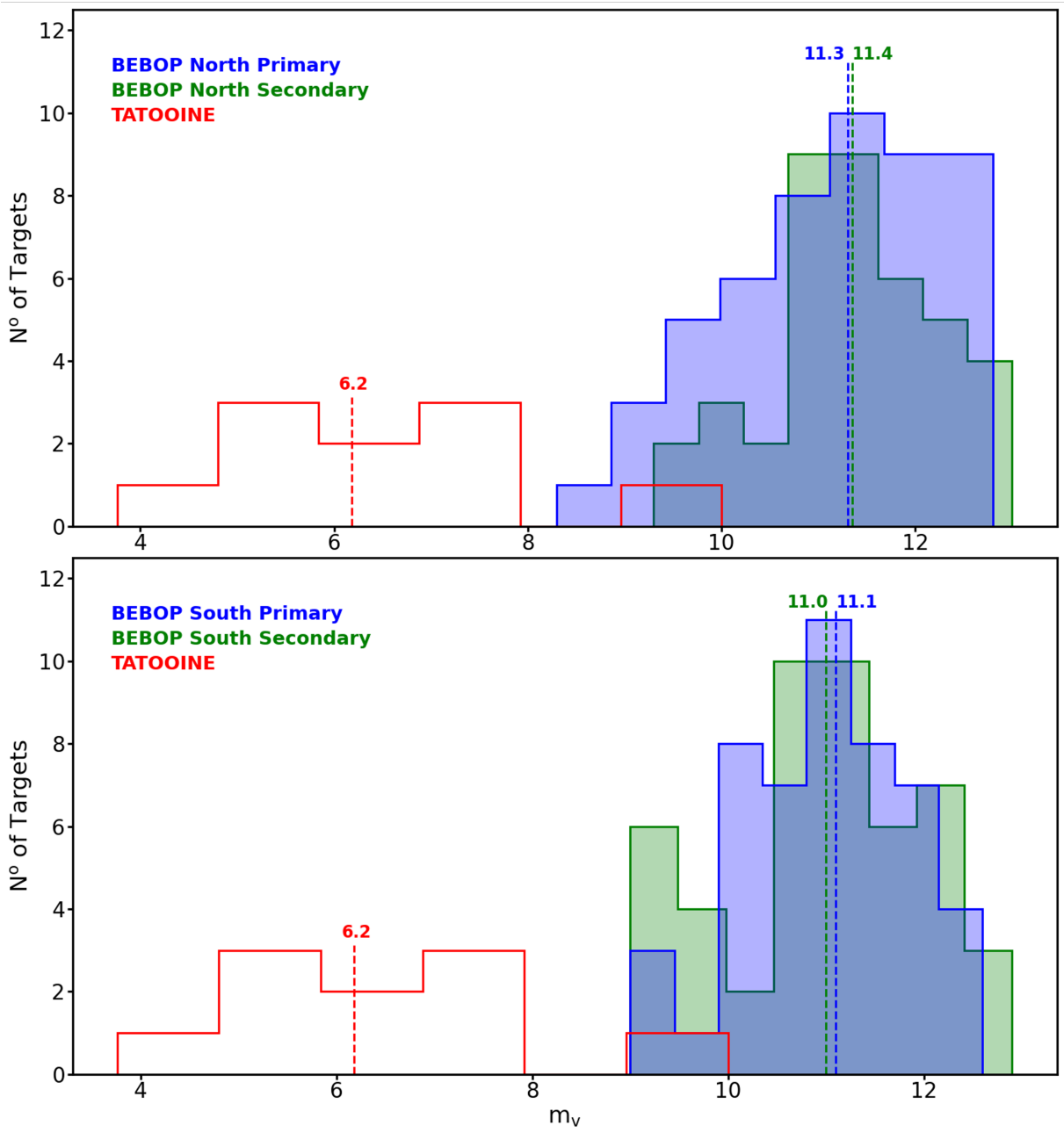

Figure 4.1: Histograms of the visual magnitude of BEBOP's northern (top), and southern (bottom) SB1 binary targets, in comparison to TATOOINE's SB2 binary target sample in red. The blue and green histograms represent BEBOP's primary and secondary samples respectively. Median values for each sample are indicated by the dotted lines in their respective colours.

in the Southern survey due to lower instrumental precision (Section 4.2.2). 1800 s integration times allow an increased SNR to be obtained, thus decreasing the uncertainty on the RV precision as in Equation 1.13 (Lovis & Fischer 2010). A concern with the use of longer integration times when observing binary stars with a spectrograph is that the spectral lines may shift during the 1800 s integration, thus affecting the observed RV value. However, as the CCF represents the average of all spectral lines, the calculated RV values are representative of the average velocity of the star at the middle of the integration. The FWHM

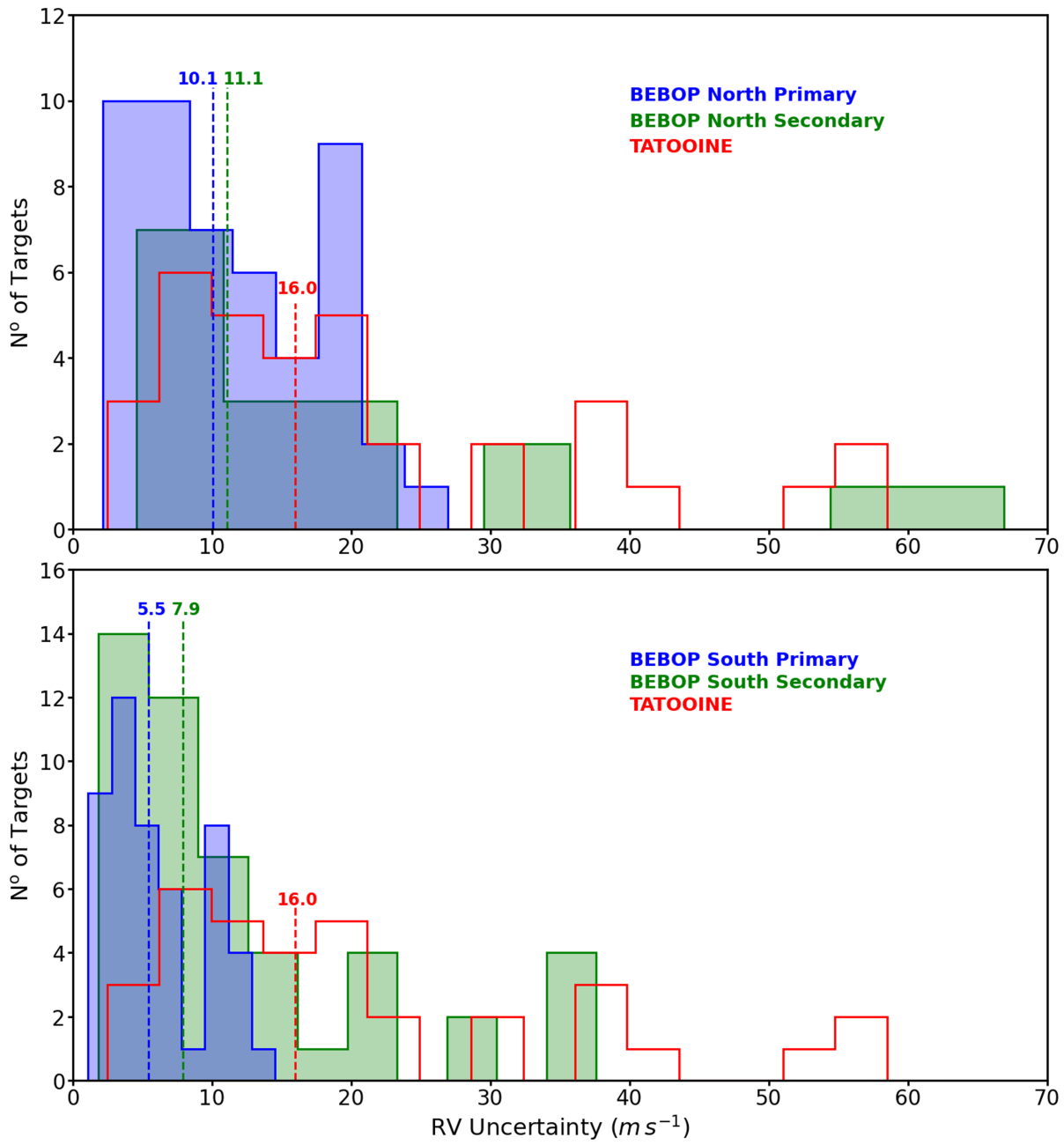

Figure 4.2: Histogram of median RV uncertainties obtained in observations with the HARPS spectrograph (Mayor et al. 2003) for BEBOP's northern (top), and southern (bottom) SB1 binary targets, in comparison to TATOOINE's SB2 binary target sample. Colours and median values in both plots are depicted as in Figure 4.1. The TATOOINE sample consists of the uncertainties for the primary and secondary stars for each of their SB2 binary targets from each individual instrument.

may be affected slightly, impacting the obtained RV uncertainty. To verify the magnitude of this effect, we take the binary target from BEBOP which has one of the shortest orbital periods (P $\approx$ 5.18 d) and largest semi-amplitude signal (K $\approx$ 44.318 km s^{-1}) as an example. This target, EBLM J0543+30, provides a measure of the worst possible case for this effect. At the peak of the orbital motion curve (position 1 or 3 in Figure 1.5) the radial velocity of the primary star in J0543+30 varies by $\approx$ 11 m s^{-1} during a 30 minute exposure. However, at the position in the orbit where the primary star is moving perpendicular

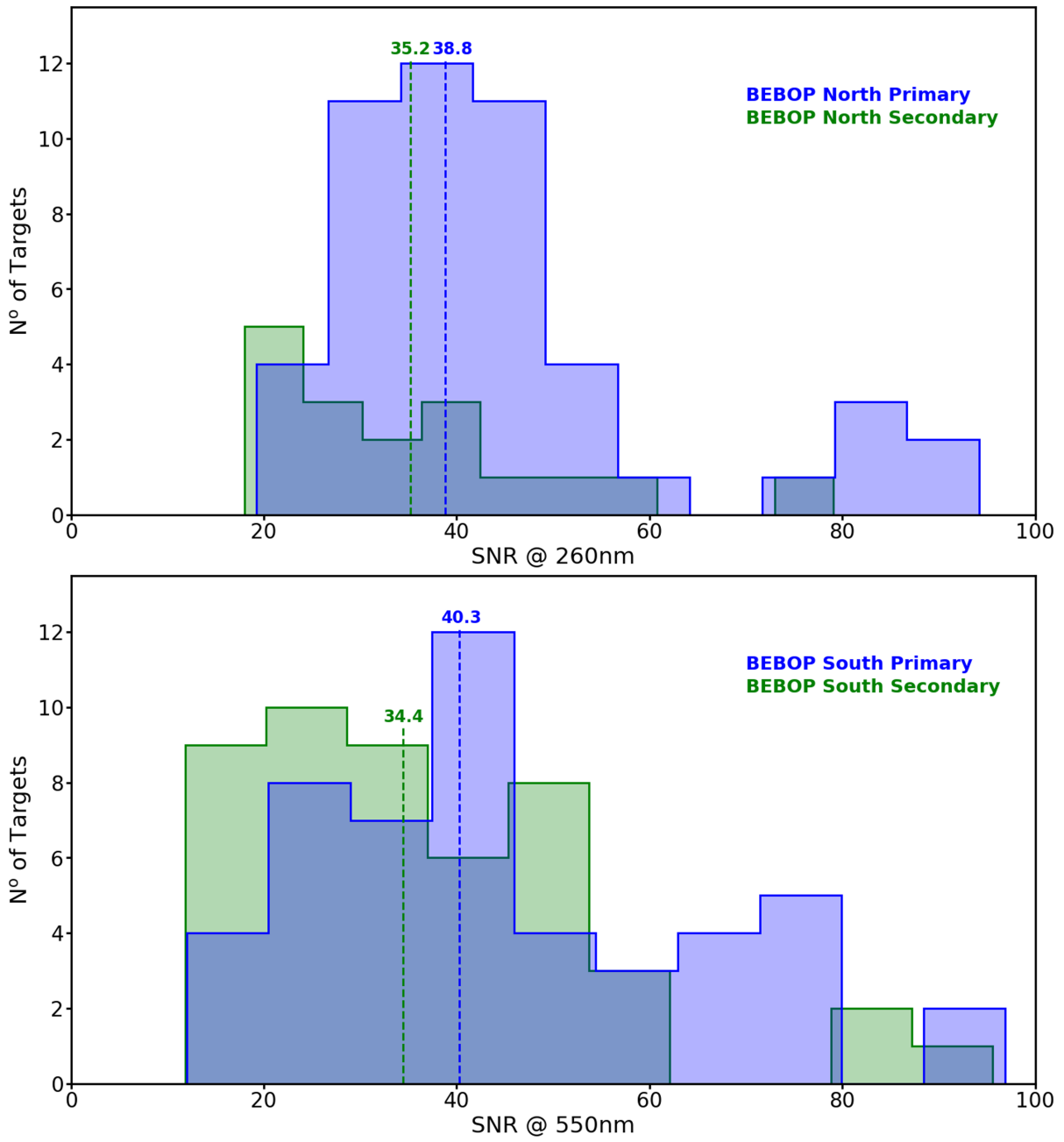

Figure 4.3: Top: Histogram of median SNR at 260 nm obtained in observations with the SOPHIE spectrograph (Perruchot et al. 2008) for BEBOP's northern SB1 binary targets. Bottom: Histogram of median SNR at 260 nm obtained in observations with the HARPS spectrograph (Mayor et al. 2003) for BEBOP's southern (bottom) SB1 binary targets. Colours and median values in both plots are depicted as in Figure 4.1.

to us (position 2 or 4 in Figure 1.5) the observed radial velocity changes by $\approx 1.1\,\mathrm{km\,s^{-1}}$ during the same exposure. Despite this large variation, the median uncertainty for observations of J0543+30 is $5.28\mathrm{m\,s^{-1}}$. Calculating the average uncertainty of our observations on this target using Equation 1.13, yield a similar result with no obvious differences between observations taken at the peak of the binary motion, or at the maximum velocity gradient. We can therefore conclude that the motion of the binary during the integration time of each observation does not have an effect on the obtained RV uncertainties.

Observations are carried out homogeneously throughout the observing period, on average every $\approx$ 6 nights, allowing for the detection of longer period planetary orbits. Observations are taken with an airmass[c] of < 1.6, and $> 30°$ separation from the Moon to avoid contamination from reflected sunlight. Good seeing conditions are also requested (< 2 arcseconds at La Silla, $\lesssim 4$ arcseconds as Observatory Haute-Provence (OHP)), though this is not always possible.

4.2.2 Data sources

The BEBOP survey began its observations in 2013 with the CORALIE[d] spectrograph on the Swiss 1.2 m telescope at the La Silla observatory in Chile (Figure 4.4). CORALIE is an echelle spectrograph with a resolving power $R = 50\,000$ (Queloz et al. 2001a). In total, 1519 spectra were obtained with CORALIE, and results from the analysis of this data can be found in Martin et al. (2019). The results obtained from this data are limited by the stability of the CORALIE spectrograph. With a mean uncertainty of $\approx 22\ \mathrm{m\,s^{-1}}$ across our target binaries, we were limited in our search for planets.

Therefore, following a successful pilot programme (Martin et al. 2019), in April 2018 BEBOP switched to observing with the HARPS spectrograph (Mayor et al. 2003) on ESO's 3.6 m telescope at La Silla (Figure 4.5). With a resolving power $R = 115\,000$ (Mayor et al. 2003), HARPS allows BEBOP to explore the presence of sub-Saturn mass planets around our binary targets (Standing et al. (2022), Section 4.3). With HARPS we have collected a total of 2260 spectra with a mean uncertainty of $\approx 6.6\ \mathrm{m\,s^{-1}}$. We utilise the Obj_AB mode in our observations, which places fibre B of the instrument on the sky (with fibre A on the target). This allows for the subtraction of any contamination from Moon light in our observations, at the expense of utilising HARPS's most accurate mode (Standing et al. (2022), Section 4.3). Our HARPS data are reduced with the HARPS Data Reduction Software (DRS) version 3.5, hosted at the Observatory of Geneva (Lovis & Pepe 2007). Further details on the data reduction can be found in Standing et al. (2022) (Section 4.3).

In the northern hemisphere, BEBOP observes with the SOPHIE spectrograph on the 1.93 m telescope at the OHP (Perruchot et al. 2008) (Figure 4.6). SOPHIE has a resolution $R = 75\,000$ when observing in High Resolution (HR) mode, and $R = 40\,000$ when observing in High Efficiency (HE) mode where resolution is sacrificed in exchange for higher throughput (Triaud et al. (2022), Chapter 5). BEBOP utilises both modes depending on the brightness of the observed target. Like the Obj_AB mode on HARPS, SOPHIE has two fibres which we utilise in the same manner with fibre A on the target, and B on the sky to remove any lunar contamination. Further details on our observations with SOPHIE can be found in Triaud et al. (2022), Section 5.3.

Our final RV data source for the BEBOP survey is the highly competitive Echelle SPectrograph for Rocky Exoplanets and Stable Spectroscopic Observations (ESPRESSO) spectrograph on the VLT

[c] Airmass is a measure of the volume of atmosphere through which the telescope must look to observe the star, a value of 1 indicates the star is directly overhead

[d] CORALIE is not an acronym, the instrument was named after the daughter of an engineer from the OHP (https://www.eso.org/public/teles-instr/lasilla/swiss/coralie/).

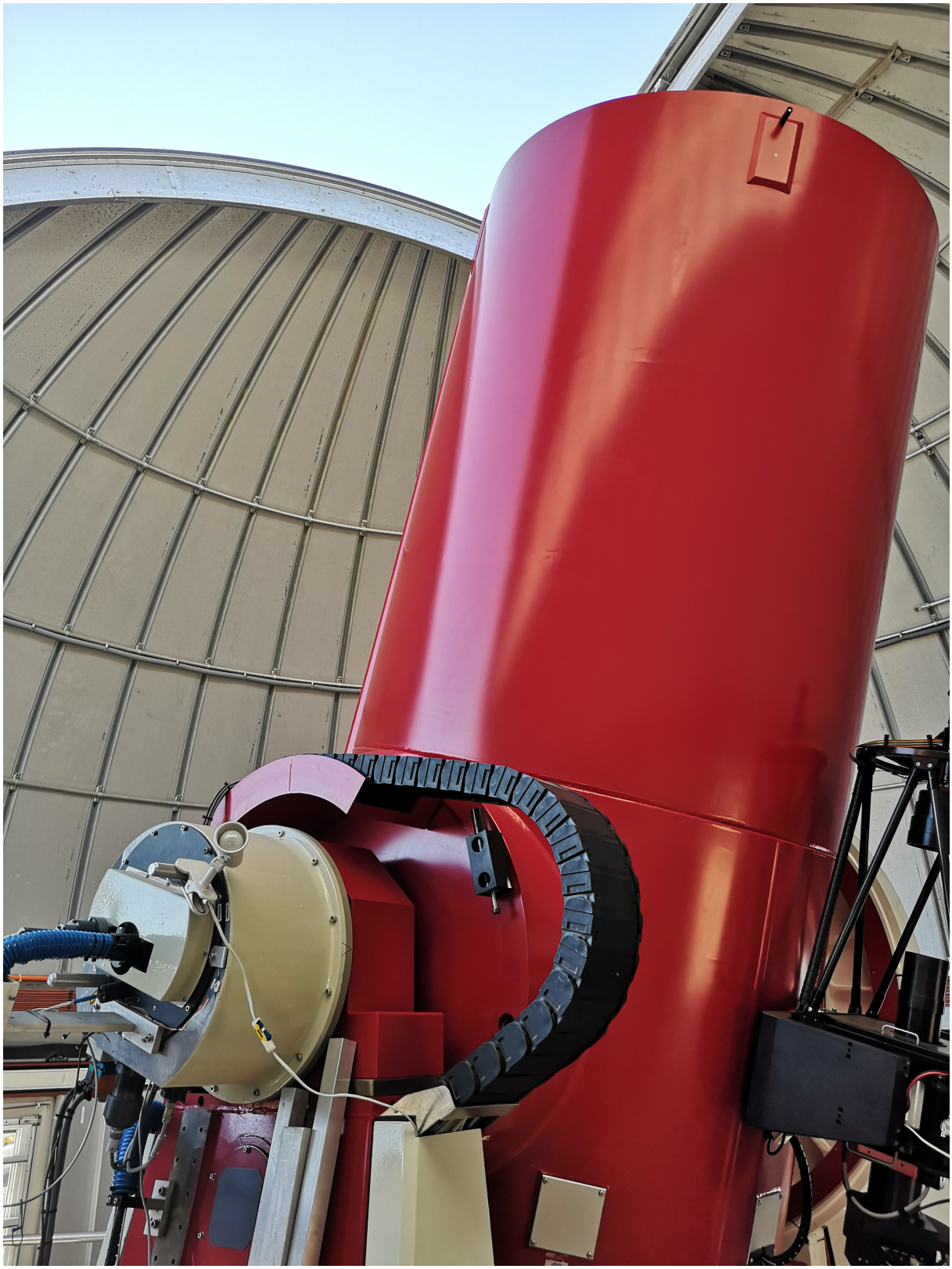

Figure 4.4: A picture of the Swiss 1.2 m telescope located at European Southern Observatory (ESO)'s Las Silla Observatory in Chile taken when I visited in 2019, just before being invited for pisco sours with the Swiss observers at the start of the night.

Figure 4.5: A picture of myself at ESO's 3.6 m telescope located at the Las Silla Observatory in Chile when I visited in 2019.

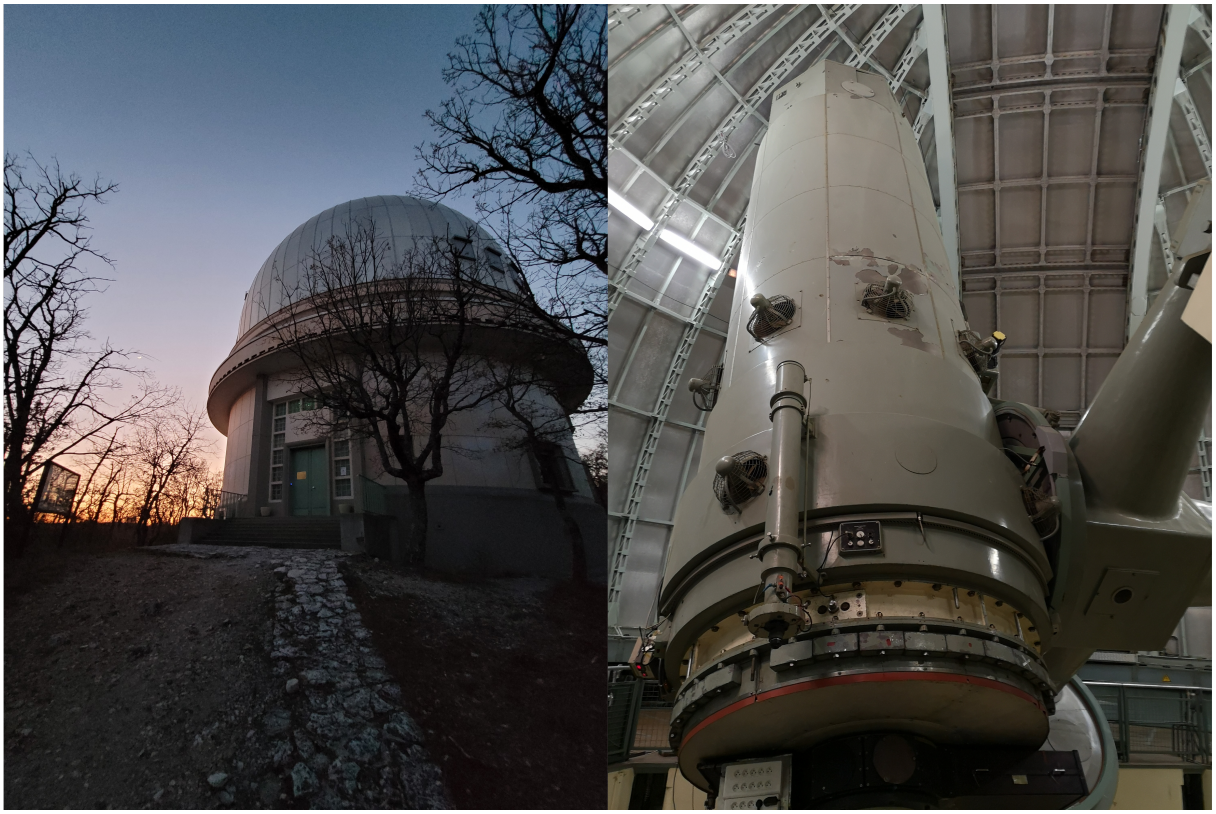

Figure 4.6: Left: A Picture of the dome housing the 1.93 m telescope located at the OHP in France taken at twilight during one of my many observing runs there. Right: A picture of the 1.93 m telescope within the dome.

telescope in Paranal observatory in Chile[e] (Pepe et al. 2021). The VLT consists of four individual 8.2 m Unit Telescope (UT)'s which can be used in unison, or individually as in our case (Figure 4.7). ESPRESSO can collect light from each of the four UT's, along with several other instruments, allowing for ease of observation scheduling. Using 1-UT, ESPRESSO has a resolution $R = 140\,000$ in HR mode (with an efficiency of 11%), and $R = 190\,000$ in Ultra High Resolution (UHR) mode (sacrificing some efficiency down to 5% and halving the sky aperture). It is therefore the highest resolution spectrograph utilised for the BEBOP programme.

I obtained time on the ESPRESSO spectrograph to observe a single target, EBLM J0608-59 (also known as TOI-1338), renamed as BEBOP-1 in Chapter 6. Details on data treatment and observational strategy for this target with ESPRESSO can be found in Chapter 6. My ESPRESSO observations of BEBOP-1, with an exposure time of 900 s in HR mode, have a mean uncertainty of 2.7 $\mathrm{m\,s^{-1}}$. On the same target our HARPS observations have a mean uncertainty of 5.7 $\mathrm{m\,s^{-1}}$ (with double the exposure time at 1800 s), and CORALIE observations a mean uncertainty of $\approx 25\ \mathrm{m\,s^{-1}}$ (with an exposure time in the range of 600-1800 s).

[e]The 2008 James Bond film, Quantum of Solace uses Paranal observatory as one of their filming locations

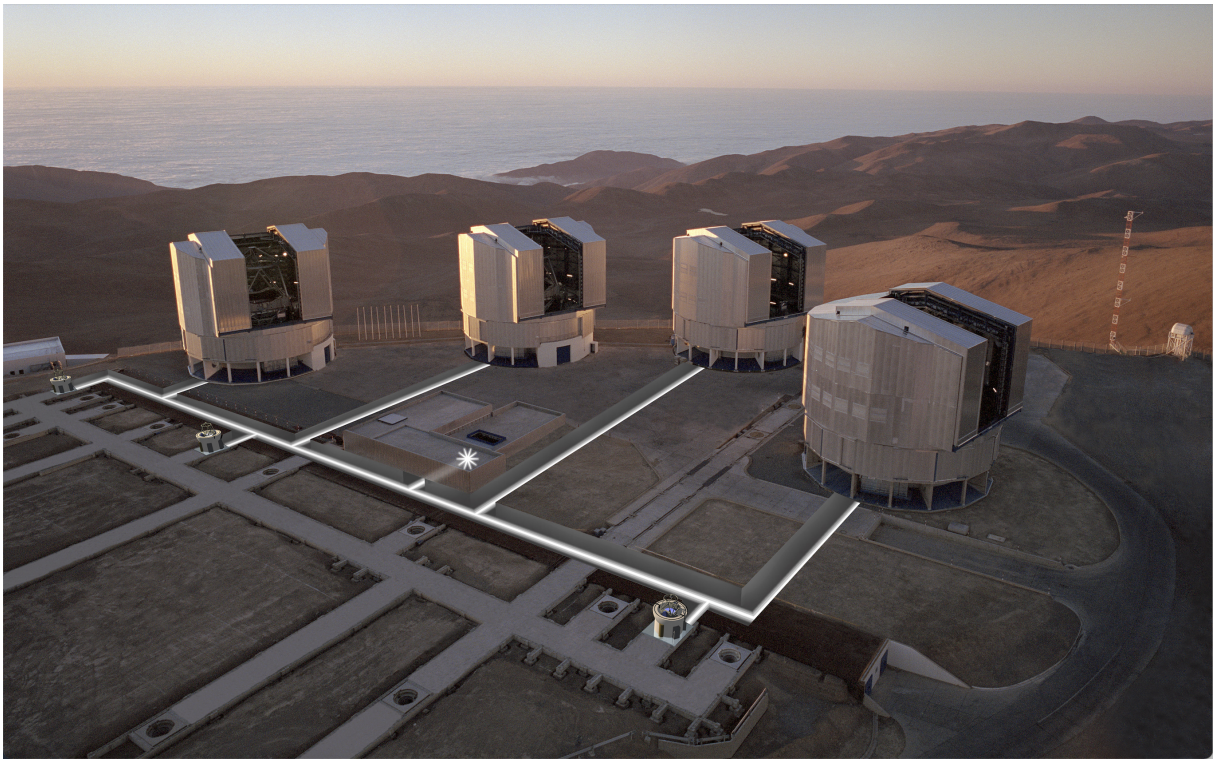

Figure 4.7: A picture of the four 8.2 m UT's of the VLT at Paranal observatory, Chile. Superimposed are the light tunnels connecting to the instruments such as the ESPRESSO spectrograph used in this work. Also visible are the three smaller 1.8 m Auxiliary Telescope (AT)'s. Image credit: ESO.

4.2.3 Data quality control

For a radial velocity (RV) survey such as BEBOP, it is important to assure the data obtained from observations conforms to a particular quality. Data quality can refer to the Signal to Noise Ratio (SNR) of each observation, which is affected by weather conditions during each observation (e.g. cloudy conditions, or high seeing[f]). To minimize these effects, observatories are placed in dry, high, and dark sky sites, such as La Silla in Chile located in the Atacama desert, one of the driest areas on Earth at an altitude of over 2000 m. The low humidity decreases the risk of clouds, and the altitude minimises atmospheric interference by lowering the airmass to targets.

To keep track of these low-quality data points, I created data quality sheets which are plotted when we receive new data points. An example of a data sheet for target J0228+05 can be seen in Figure 4.8. If a target has observations from several instruments, a sheet is generated for each individual instrument. In this example, I show the overview sheet for data from all instruments. Each sheet has several sub-plots displaying the FWHM, bisector, SNR at 550 nm, and RV uncertainty of each observation. The top panel of each sheet contains useful dataset statistics. Data points which lie further than 2σ from the median of each instrument in any of the four panels are flagged with a red 'X'. Observation numbers 24 and 40, seen in the orange HARPS data for this target, have an SNR approximately 3 times lower than the median,

[f]Seeing is a measure of the turbulence of the Earth's atmospheric layers. It affects observations by varying refractive indices causing the target stars point source to move on the image plane of a detector during an observation.

and consequently over double the median uncertainty of the other HARPS observations for this target. This can be explained by poor observing conditions on these nights. Tracking observations such as these, informs us of observing time wasted due to bad weather. This information can then be reported to the organisations running the telescopes prior to requesting additional observations. Data points which are only outliers in SNR are not removed from analysis.

Data quality, as described here, also refers to the activity indicators such as the bisector span and FWHM. Targets which exhibit strong stellar activity through bisector correlation, or FWHM modulation (Queloz et al. 2001b; Santos et al. 2002), as described in Section 1.2.2, are removed from the main target list as described in Standing et al. (2022) (Section 4.3). On occasion, the incorrect star is mistakenly observed. This can be identified easily if the point is very discrepent ($> 10\sigma$) in FWHM, bisector, or simply after fitting for the RV signal. In which case, the outlying observation is removed immediately. Since each of our targets are eclipsing binaries, observations could have been taken during the primary eclipse of the binary stars. The observation would then be affected by the Rossiter-McLaughlin effect (Rossiter 1924; McLaughlin 1924; Winn et al. 2011; Triaud 2018), the obtained RV values would be affected, and therefore all measurements corresponding to eclipse times are removed before further analysis. On average around 2 to 4 outlier points are identified and removed for each target.

A more robust method of determining outliers for removal before RV analysis is currently under development by the BEBOP team. It fits each set of points with a model as described in Hogg et al. (2010). It is utilised and described further in Chapter 6 and will be published in Baycroft at al. (In prep).

4.2.3.1 CCF Inspection

BEBOP specifically targets SB1 binary targets. If a new target is added to the observing catalogue, once observed, it requires confirmation that the spectral lines from the secondary star are not detected by the spectrograph. To do this, I created CCF datasheets in addition to the data quality sheets described above.

Figure 4.9 shows the CCF data-sheet for SB1 target J0310-31. This figure allows the motion of the observed binary CCF to be viewed. In this figure, each row in each plot is a single observation of J0310-31. If any patterns visible in these plots demonstrate motion which does not follow that of the primary star motion, then the secondary stars' spectrum is likely visible and moving in opposition to the primary star.

Figure 4.10 shows a similar CCF data-sheet, but for SB2 target HD 78418. Here we can clearly see a secondary CCF minimum in each observation, moving in opposition to the primary star. If a new target demonstrated this secondary CCF from the first few observations, it would be cut from the target list, and no further observations would be taken on the target.

4.2.4 Target data-sheets

Once data passes the above data quality visual analysis (Section 4.2.3), `Kima` is run on the data as described in Chapters 2 and 3. This stage is carried out after each observing period (roughly twice a year), to identify any candidate signals present in the newly obtained data.

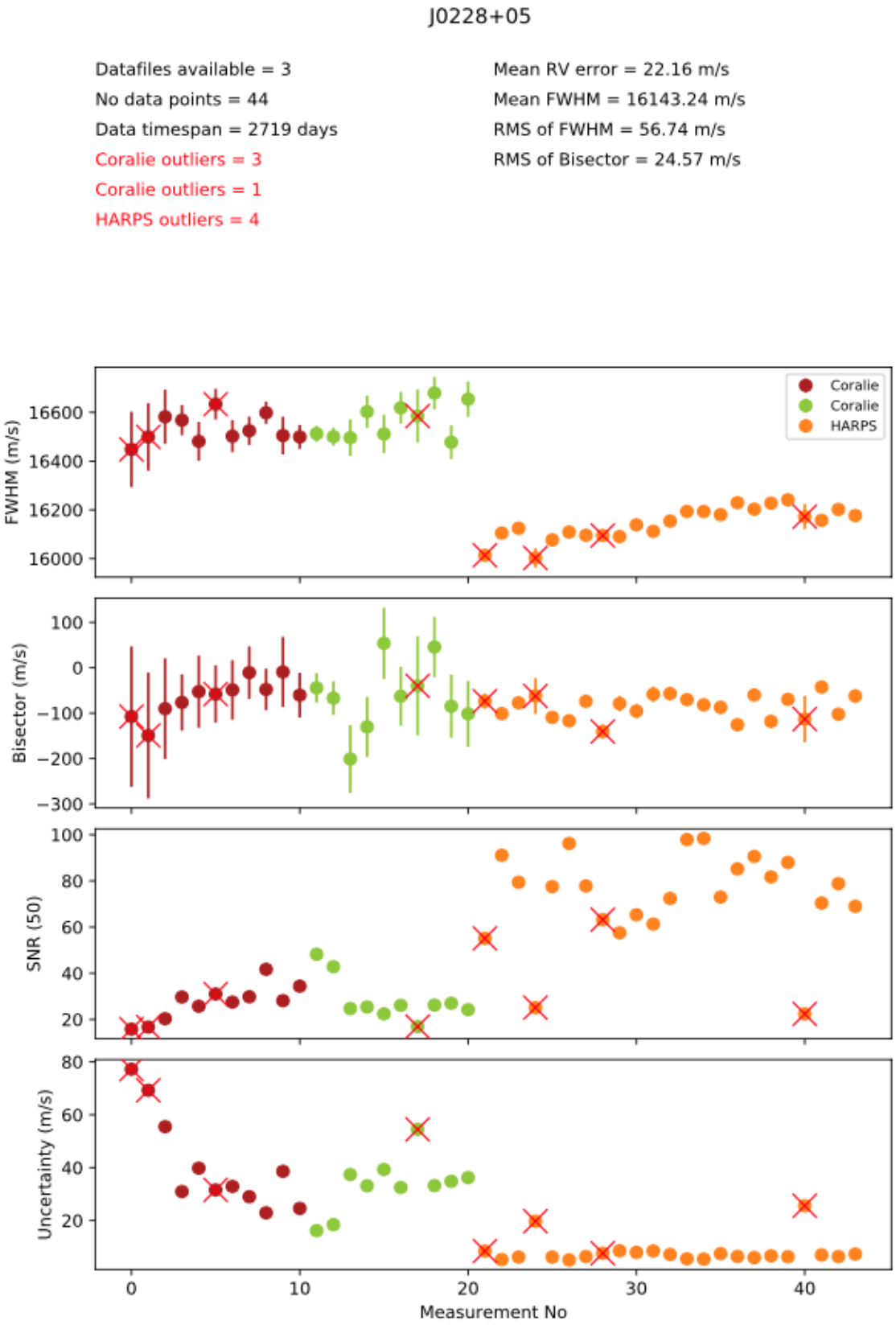

Figure 4.8: Combined instrument data quality sheet for CORALIE, and HARPS J0228+05 data. Dataset statistics can be found in the top panel. The remaining panels are plots of FWHM, Bisector, SNR (at 550 nm), and RV uncertainty against measurement number. Datapoints which lie further than 2σ from the median values in each window (per instrument) are indicated by red crosses. There are two CORALIE instruments in this plot as a fibre change introduced an RV offset. Observations before and after the change are therefore treated as from separate instruments.

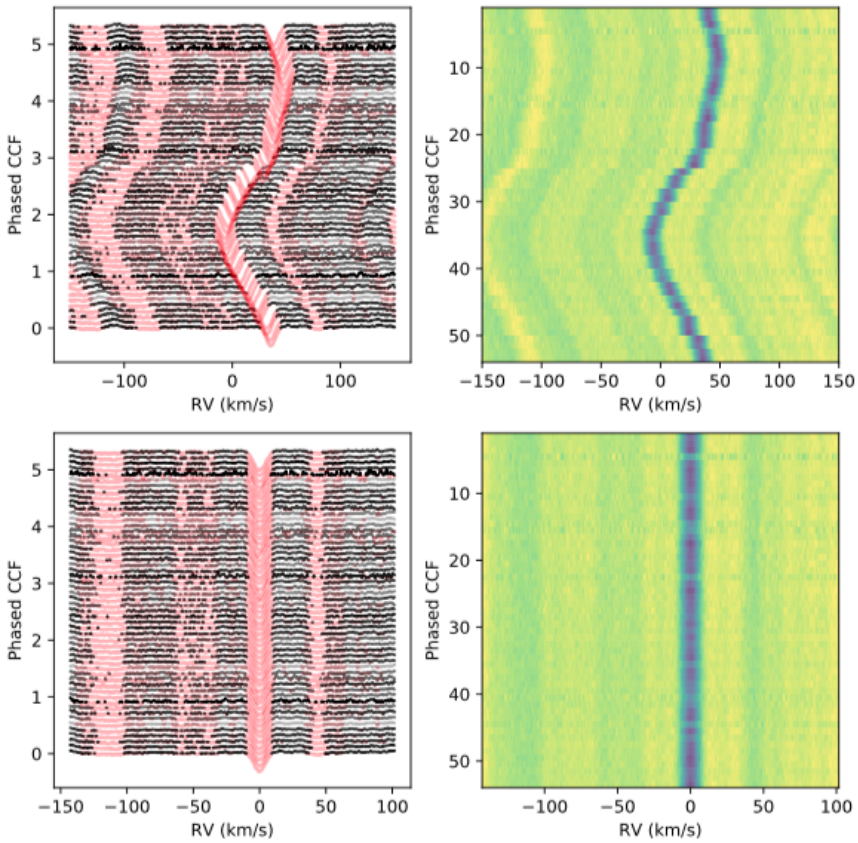

Figure 4.9: Plot of the phase folded CCF curves from SB1 J0310-31 observations. Each row in each of the four plots corresponds to a different observation. The lower row of plots has the binary CCF centered at 0 km s^{-1}. Plots in the left column have values below the median for each observation shaded red. Plots in the right column are the same phase diagrams drawn with a colour-map.

I developed a wrapper for `kima`, which allows full control over the priors and which systems are run through a single spreadsheet. True/False 'boolean' values indicate which systems are to be run, and which data-sheets are to be produced. The number of known objects present in the data, prior distribution values for the known object, along with the remaining parameter space to be explored can also be set. The wrapper is run by executing the command '`python BEBOP_control.py`' in the `kima` directory. Once posterior samples are obtained, my wrapper produces a number of plots and saves them to a folder indicating the number of planetary signals explored, the number of saves used in the run, and the time of the run.

Plots which are created at this step that have not yet been discussed, include the overview data-sheet for the system in question, along with 'planet sheets' for any known objects, and the most likely signal present in the data.

An example of the overview data-sheet for target J0608-59 (BEBOP-1, Chapter 6) can be seen in Figure 4.11. This data-sheet demonstrates the case of a system with a detected planetary signal. The N_p histogram indicates a Bayes Factor (BF) of infinity in favour of a single planetary signal in addition to the binary in the data. Infinity is calculated as no posterior samples were obtained with 0 planetary signals, this means that there are 'effective sample size' (35 311) posterior samples with at least $N_p = 1$.

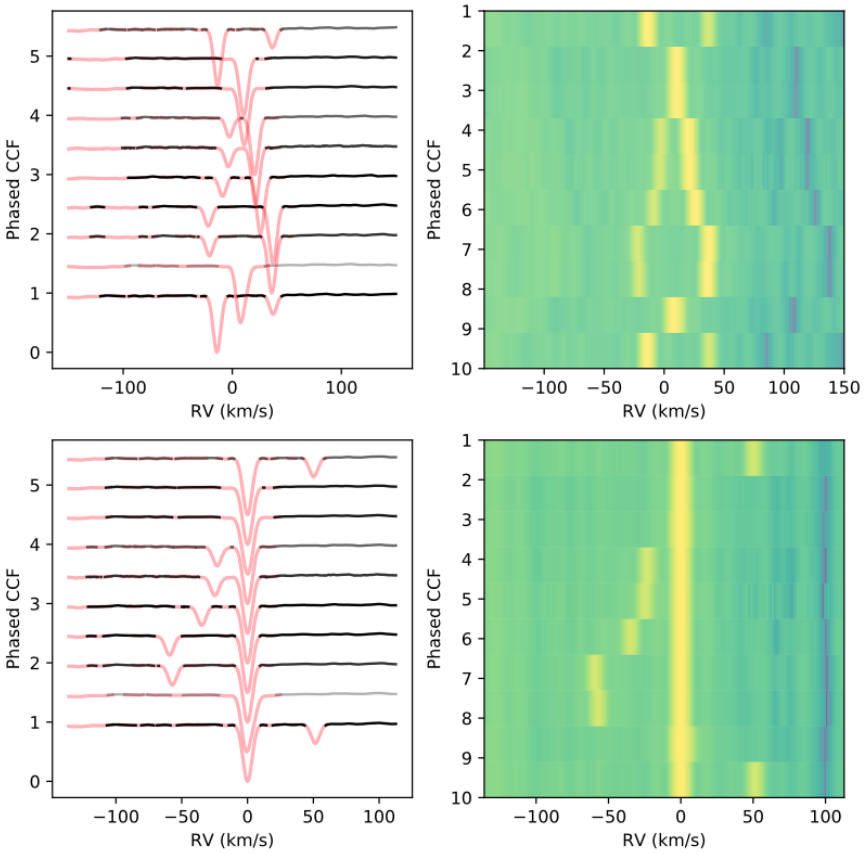

Figure 4.10: Plot of the phase folded CCF curves from 10 SOPHIE observations of SB2 HD 78418. Plots are the same as in Figure 4.9. A second CCF can be seen clearly in all observations moving in opposition to the primary star.

Assuming a single $N_p = 0$ posterior sample allows for a Bayes Factor to be calculated at $> 35\,311$. The period histogram at the bottom of the plot shows that the majority of posterior samples are found containing a signal with an orbital period of ≈ 215 days. The bisector span plot shows no correlation of bisector with the residual RV values, indicating no stellar activity being present. If an anti-correlation were to show here, the target could be demoted to the back-up target list for observations, or observations ceased entirely. Figure 4.12 shows an example of a bisector plot demonstrating an anti-correlation between bisector and RV for binary EBLM J0407-23. Future iterations of these plots will be adapted to remove statistics which have become less important for monitoring candidate signal progression.

In addition to the 'master' datasheet, a sheet is created for each orbital signal present in the chosen model, along with a corner plot of its associated cluster in parameter space (see Figure 2.7). In the case of J0608-59 (BEBOP-1), we obtain a plot of the binary star's signal seen in Figure 4.13, and one for the additional keplerian signal, BEBOP-1c, seen in Figure 4.14. Parameters above both of these figures are the posterior sample values used to calculate the Keplerian signals, true values for the binary and planetary signal are determined from the posterior sample distributions as described in Chapter 2.

If no signal is formally detected by `kima` in BEBOP data, a model with $N_P = 0$ is preferred containing only the known binary signal. In this case, for plotting only, the code selects the highest likelihood

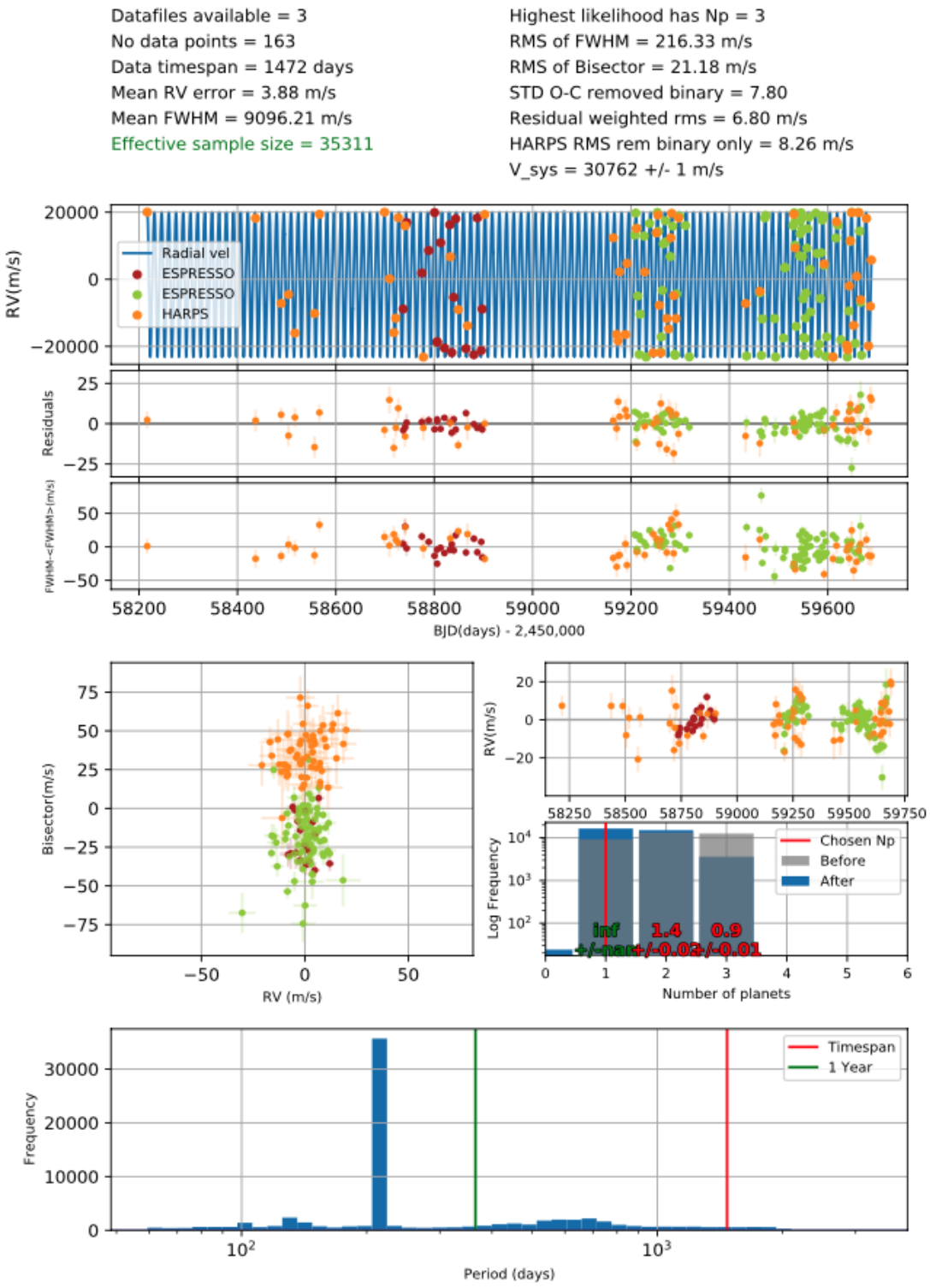

Figure 4.11: Data-sheet produced from a `kima` run on J0608-59 (BEBOP-1, Chapter 6) data. The statistics at the top provide quick-look information. The following two plots show the highest likelihood posterior sample with the chosen number of planetary signals (N_p) along with its residuals. Orange points show the HARPS data, and the red and green points show ESPRESSO data before and after a calibration lamp change respectively (Faria et al. 2022). The third plot shows the FWHM - mean FWHM, with all three plots against BJD (days) - 2,450,000. Below this on the left is a plot of the bisector slope vs RV value for each data-set. The upper plot to the right of the bisector plot shows the residual values having subtracted the only the binary star's signal. Below this, the plot shows a modified version of Figure 2.4, log(number of posterior samples) vs number of planets. The associated Bayes Factors for each number of signals are plotted above their associated number, with the vertical red line indicating the chosen N_p signals displayed in the plots. The grey histogram represents the raw `kima` posterior samples, and the blue histogram shows number of posterior samples in each bin after having removed any crossing orbits. The lowest plot in the data sheet shows a histogram of the number of posterior samples vs orbital period. The red line on this plot indicates the timespan of the data, and the green line a year.

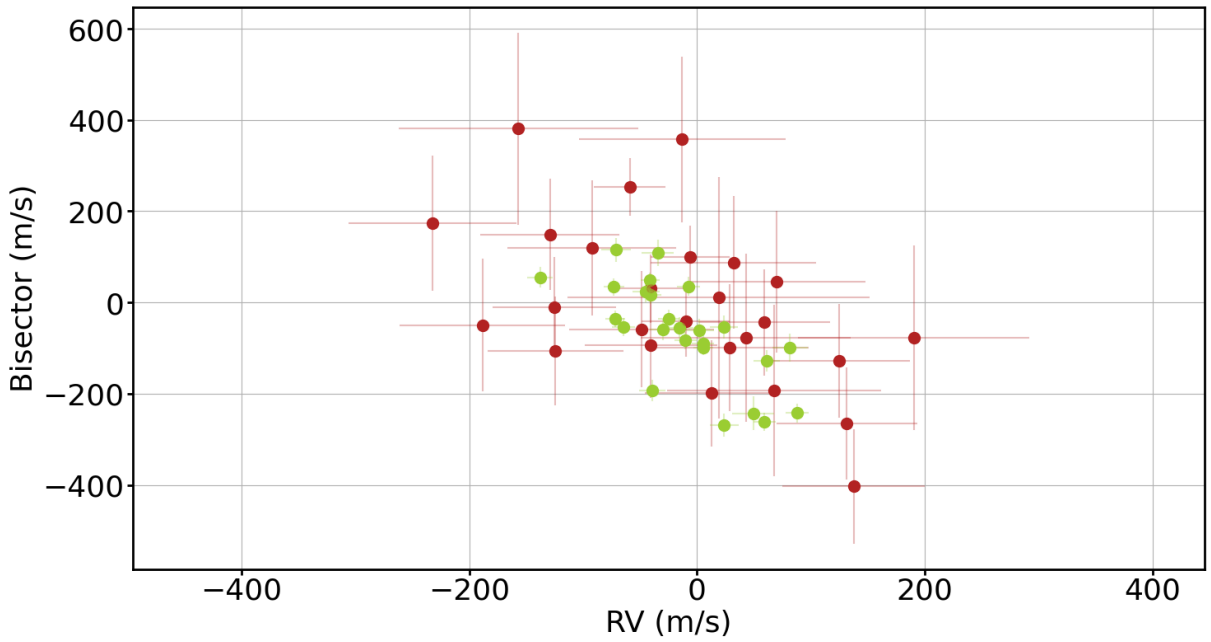

Figure 4.12: Plot of bisector slope against residual RV values after having subtracted the binary signal for southern target EBLM J0407-23. Red and green data points are CORALIE and HARPS data respectively with associated uncertainties. Anti-correlation here indicates the presence of stellar activity.

posterior sample with $N_P = 1$ providing the eccentricity of the additional Keplerian signal $e < 0.1$. It plots this solution as a visual indicator of the highest likelihood signal allowed by the data.

4.3 Detection limits for RV surveys

For several months during my PhD, the La Silla observatory in Chile, and the Observatory Haute-Provence in the South of France were both closed due to the ongoing COVID-19 pandemic. With these observatories being the primary source of RV data for the BEBOP survey, I found myself at a loss as to what to do without any new observations. Candidate exoplanets for the survey could not be confirmed without further observations, therefore I diverted my attention from confirmation of candidate circumbinary planet signals with new data, to what planetary signals could be detected with our current data. By calculating the signal strength we are sensitive to with our RV data, we can determine the 'detection limits' of our survey. A detection limit for RV surveys is a threshold in semi-amplitude signal strength (or mass) vs period where any signal above this limit should be detected, and any signal below is still undetectable with current observations alone.

Traditionally, detection limits for RV surveys are calculated with injection and recovery tests (e.g. Cumming et al. 2008; Howard et al. 2010; Mayor et al. 2011). In this method, any planetary signals are removed from the data, and a single Keplerian signal with a specific set of orbital parameters and signal strength is inserted. An attempt is then made to detect the inserted signal. The process is repeated over a fine grid of signal strengths varying all parameters, and results in a grid map of parameter space which demonstrates what signals are detectable in the data. Unfortunately, this process requires countless

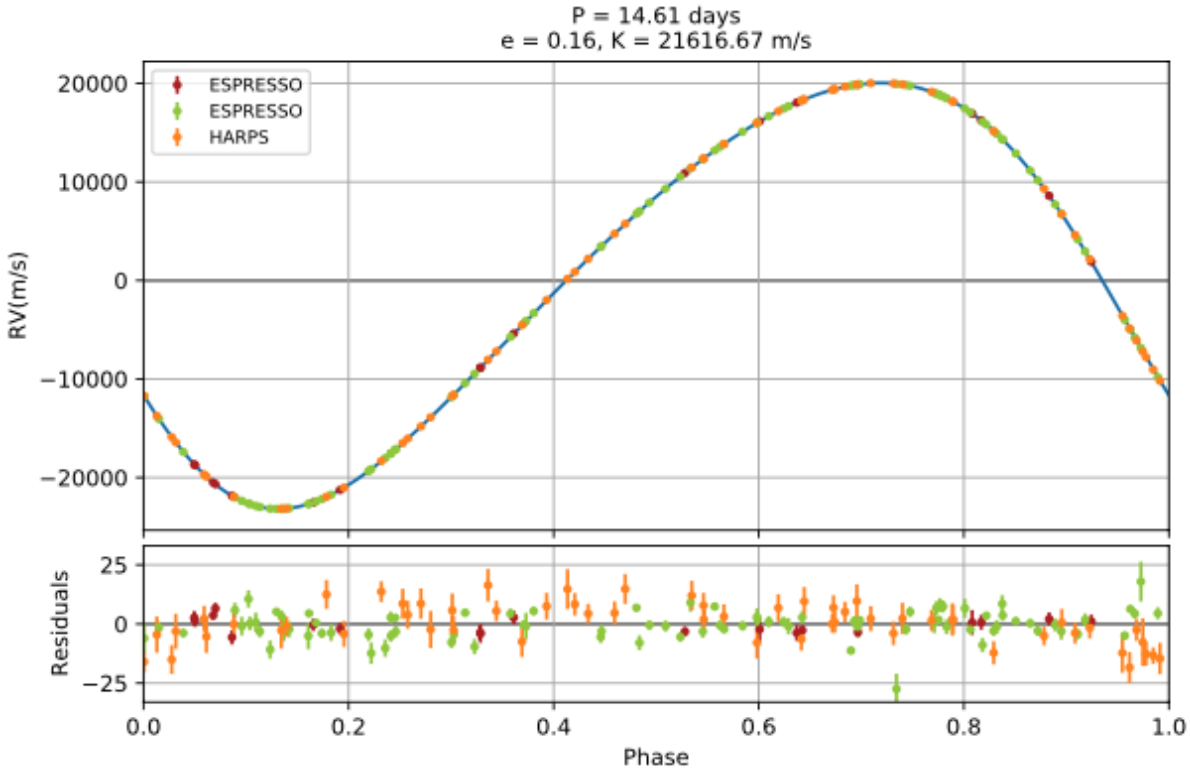

Figure 4.13: Phased Keplerian binary Radial Velocity (RV) signal for J0608-59 calculated from the highest likelihood posterior sample obtained. Above are the exact parameters from the posterior sample used to calculate the model. O-C residuals are plotted below. Orange points show the HARPS data, and the red and green points show ESPRESSO data before and after a calibration lamp change respectively (Faria et al. 2022).

simulations and retrieval attempts to produce accurate detection limits, and is therefore a computationally expensive process.

4.3.1 Calculating detection limits with `kima`

It is possible to calculate detection limits on Radial Velocity (RV) datasets using `kima`. Conceptually the method works as the Diffusive Nested Sampling (DNS) algorithm utilised by `kima`, when forced to fit an additional planetary signal to a dataset, explores all parameter space and returns a map of signals which are compatible with the data. The upper limit of the posterior samples' semi-amplitudes obtained in this way is therefore a threshold of detection. Forcing the algorithm to fit an additional planetary signal to the data is conceptually similar to the method described in Tuomi et al. (2014). `kima` is therefore able to produce detection limit for a system with a single run on the dataset. Greater details are given in the following paper.

The method was tested with a number of injection recovery tests. This lead to the first publication from my PhD 'BEBOP II: Sensitivity to sub-Saturn circumbinary planets using radial-velocities', which can be found below. I lead the following research, carried out the simulations and tests, created the plots, and wrote and organised the manuscript. Co-author contributions are as follows: Amaury H. M. J. Triaud provided insights into testing, revised and assisted with the generation of the manuscript. João

P. Faria assisted with the choice of prior distributions used, and contributed to the text. David V. Martin contributed to the text.

The journal of observations providing the RV data used in the below analysis has been removed from the paper included below to save space, it can be found in the online version, alternatively I would be happy to provide it upon request.

Monthly Notices of the ROYAL ASTRONOMICAL SOCIETY

MNRAS 511, 3571–3583 (2022) https://doi.org/10.1093/mnras/stac113
Advance Access publication 2022 January 25

BEBOP II: sensitivity to sub-Saturn circumbinary planets using radial-velocities

Matthew R. Standing [1]★ Amaury H. M. J. Triaud [1] João P. Faria,[2,3] David V. Martin [4]† Isabelle Boisse,[5] Alexandre C. M. Correia [6,7] Magali Deleuil,[5] Georgina Dransfield [1] Michaël Gillon [8] Guillaume Hébrard,[9] Coel Hellier,[10] Vedad Kunovac [1] Pierre F. L. Maxted [10] Rosemary Mardling,[11] Alexandre Santerne [5] Lalitha Sairam [1] and Stéphane Udry.[12]

[1]*School of Physics and Astronomy, University of Birmingham, Edgbaston, Birmingham B15 2TT, UK*
[2]*Depto. de Física e Astronomia, Faculdade de Ciências, Universidade do Porto, Rua do Campo Alegre, P-4169-007 Porto, Portugal*
[3]*Instituto de Astrofísica e Ciências do Espaço, Universidade do Porto, CAUP, Rua das Estrelas, P-T4150-762 Porto, Portugal*
[4]*Department of Astronomy, The Ohio State University, 4055 McPherson Laboratory, Columbus, OH 43210, USA*
[5]*LAM, Aix Marseille Univ, 13007 Marseille, France*
[6]*CFisUC, Departamento de Física, Universidade de Coimbra, P-3004-516 Coimbra, Portugal*
[7]*IMCCE, UMR8028 CNRS, Observatoire de Paris, PSL Université, 77 av. Denfert-Rochereau, F-75014 Paris, France*
[8]*Astrobiology Research Unit, University of Liège, Allée du 6 août 19 (B5C), B-4000 Liège (Sart-Timan), Belgium*
[9]*Institut d'astrophysique de Paris, UMR7095 CNRS, Université Pierre & Marie Curie, 98bis boulevard Arago, F-75014 Paris, France*
[10]*Astrophysics Group, Keele University, Keele, Staffordshire ST5 5BG, UK*
[11]*School of Physics and Astronomy, Monash University, Victoria 3800, Australia*
[12]*Observatoire astronomique de l'université de Genève, Chemin Pegasi 51, CH-1290 Versoix, Switzerland*

Accepted 2022 January 11. Received 2021 December 10; in original form 2021 October 8

ABSTRACT

BEBOP is a radial-velocity survey that monitors a sample of single-lined eclipsing binaries, in search of circumbinary planets by using high-resolution spectrographs. Here, we describe and test the methods we use to identify planetary signals within the BEBOP data and establish how we quantify our sensitivity to circumbinary planets by producing detection limits. This process is made easier and more robust by using a diffusive nested sampler. In the process of testing our methods, we notice that contrary to popular wisdom, assuming circular orbits in calculating detection limits for a radial-velocity survey provides overoptimistic detection limits by up to 40 per cent in semi-amplitude with implications for all radial-velocity surveys. We perform example analyses using three BEBOP targets from our Southern HARPS survey. We demonstrate for the first time a repeated ability to reach a residual root mean squared scatter of 3 m s^{-1} (after removing the binary signal), and find that we are sensitive to circumbinary planets with masses down to that of Neptune and Saturn, for orbital periods up to 1000 d.

Key words: techniques: radial velocities – planets and satellites: detection – binaries: eclipsing – stars: low-mass.

1 INTRODUCTION

Circumbinary planets are planets which orbit around both stars of a central binary system. Long postulated (e.g. Borucki & Summers 1984; Schneider 1994), most unambiguous discoveries have only been made in the past decade thanks to the transit method. In total, 14 circumbinary planets have been identified orbiting 12 main-sequence eclipsing binaries. The *Kepler* space telescope discovered 12 of these planets orbiting 10 binaries (Doyle et al. 2011; Welsh et al. 2012; Orosz et al. 2012a, b, 2019; Kostov et al. 2013, 2014, 2016; Schwamb et al. 2013; Welsh et al. 2015; Socia et al. 2020), and since two have been discovered in *TESS* photometry: EBLM J0608-68 b/TOI-1338 b (Kostov et al. 2020) and TIC 17290098 b (Kostov et al. 2021).

Despite these successes, circumbinary configurations remain largely elusive on account of their longer orbital periods. Martin (2018) and references therein, show how most circumbinary planets found to date lie just outside of the circumbinary stability limit, as described by Holman & Wiegert (1999), which incidentally places them often close or within the habitable-zones of their parent stars.

Binary-driven orbital precession means that most circumbinary planets find themselves in transiting configurations only ≈ 25 per cent of the time (Martin 2017), while their presence would be visible 100 per cent of the time in radial-velocity measurements. With sufficient precision, radial-velocities have the potential to be more efficient at detecting circumbinary planets than the transit method, particularly since the Doppler method is also much less sensitive to orbital inclination and period (e.g. Martin et al. 2019).

Despite these advantages, no circumbinary planet has been discovered by the Doppler method so far. Only one has been detected in follow-up, a recent recovery of Kepler-16 b by our project

★ E-mail:
† NASA Sagan Fellow

(Triaud et al. 2022). To unlock more information on circumbinary formation mechanisms, the demographics of circumbinary planets need to increase, along with accurate physical and orbital parameters.

To this end, Konacki et al. (2009) launched a Doppler survey in an attempt to detect circumbinary planets with radial velocities alone, with 'The Attempt To Observe Outer-planets In Non-single-stellar Environments' (*TATOOINE*) survey. Unfortunately, TATOOINE was unable to discover any planetary companions during their survey. This is likely due to the type of binary stars that were observed. TATOOINE observed double-lined (SB2) binary star systems. With spectra from both stars visible within a spectrograph, complex deconvolution methods need to be applied to recover the individual components' velocities with high precision and accuracy. Konacki et al. (2009) found their best binary target was HD 9939 ($V = 7$). Their ten radial-velocity measurements on this target from Keck HIRES have uncertainties of $1-4\,\mathrm{m\,s^{-1}}$, but they find a residual root mean squared (rms) scatter of $7\,\mathrm{m\,s^{-1}}$. This rms is calculated after the data have been fitted for binary Keplerian models, which we refer to as *residual rms* for the remainder of this paper. To achieve this level of rms scatter on an SB2 is impressive, though combining all their data on this target yielded a 99 per cent confidence detection limit of $\sim 1\,\mathrm{M_{Jup}}$ (Konacki et al. 2009). Results on other targets typically yield residual rms in excess of $10\,\mathrm{m\,s^{-1}}$. In the end, Konacki et al. (2010) recommend that single-lined binaries might be the next step forward, a step that we took.

Martin et al. (2019) introduced our Binaries Escorted By Orbiting Planets (BEBOP) survey. BEBOP currently only targets proven single-lined (SB1) eclipsing binary targets, where only the spectrum of the primary star, typically an F or G dwarf, is visible. We note here, that whilst the binary mass ratios of the BEBOP and TATOOINE samples are biased towards low and high values, respectively, Martin (2019) showed that circumbinary planets exist around all mass ratios with no discernable preference. Our binary sample was identified while confirming transiting hot Jupiters with the Wide Angle Search for Planets (*WASP*) survey (Pollacco et al. 2006; Triaud et al. 2013; Triaud et al. 2017). First, we used the CORALIE spectrograph, on the 1.2-m *Euler* telescope at La Silla, Chile (Martin et al. 2019), and have now extended the survey to HARPS, at the ESO 3.6-m telescope, also in Chile (Pepe et al. 2002a), as well as with SOPHIE, at the OHP 193-cm telescope in France (Perruchot et al. 2008).

In this paper, we detail and test our detection and observational protocols for the BEBOP survey, which have improved since Martin et al. (2019). To fit our data, we now use a diffusive nested sampler called KIMA (Faria et al. 2018). Contrary to our previous method, we now measure evidence for the presence of a circumbinary planet, accounting for Ockham's razor, and can marginalize our results over as-of-yet undetected planets. With KIMA , we investigate our detection sensitivity to circumbinary planets, and we use it to produce robust detection limits. We also test our detection protocol by injecting circumbinary planets into our HARPS data and retrieve them with KIMA . We show that, after removing the binary signal, we repeatedly achieve a detection limit for circumbinary planets at masses as low as Neptune's, paving our way to actual detections.

This paper is organized as follows. In Section 2, we describe our observing strategy for the BEBOP survey along with statistics of data gathered to date. Secondly in Section 3, we provide a brief overview of the KIMA DNS package, along with justification of its use within the BEBOP survey. In Section 4, the data analysis and simulation methods used are described. In Section 5, we display the results of our detection limit and simulation recovery analysis, and discuss the effect of the results on the BEBOP survey before concluding in Section 6.

2 DESCRIPTION OF OUR OBSERVATIONAL PROTOCOL AND DATA COLLECTION

The current BEBOP sample consists of a total of 113 single-lined eclipsing binaries which do not exhibit strong stellar activity, or the presence of a tertiary star. Fifty four in the Southern hemisphere, with HARPS, and fifty nine in the Northern hemisphere, with SOPHIE; observations still ongoing in each. The Southern sample was established from the EBLM programme, which identified low-mass eclipsing binaries from WASP false-positives (Triaud et al. 2013, 2017; Swayne et al. 2021). The data we use in this paper are exclusively from our Southern sample, for which we have now accumulated over 1200 HARPS spectra, an average ∼23 individual radial-velocity measurements per target. The Southern data are obtained from a preliminary proof-of-concept run (Prog.ID 099.C-0138) and a 78 night programme seeking planetary candidates that commenced between 2018 April and 2020 March (Prog. ID 1101.C-0721). BEBOP has been awarded a further large programme (Prog. ID 106.212H), which began in 2020 September to confirm a number of candidate planetary signals, the results of which will be published in future work.

2.1 Observational protocol

All systems are observed as homogeneously in time as is possible, with 1800 s exposures, at an average cadence of one measurement every ≈6 nights except when a system is no longer visible. All measurements are taken at airmass < 1.6. We attempt to cover as much of the yearly visibility as is feasible. All measurements are taken using the OBJ_AB mode of HARPS, which places the B fibre on the sky rather than on a simultaneous Fabry–Pérot calibration lamp, with the A fibre placed on our science target (Pepe et al. 2002a). Whilst the OBJ_AB mode prevents us from reaching the most accurate mode of HARPS, this gives us a chance to subtract moonlight contamination from our spectra, which can introduce a secondary spectral component, something our sample is designed to avoid. Since most our systems have V magnitudes between 9 and 12, photon noise rarely reaches down to the $1\,\mathrm{m\,s^{-1}}$ long-term stability of the instrument (Lovis & Pepe 2007; Mayor et al. 2009), removing the need for simultaneous calibration. Calibration of the instrument is done at the start of night using Fabry–Pérot and Th-Ar calibration lamps as is now standard on HARPS (Coffinet et al. 2019).

The data is analysed on a bi-monthly basis for quality control (for instance, verifying whether the residual residual rms around the binary solution is low enough to allow exoplanet detections). Exoplanet candidate identification are done only once a year. We chose on purpose to perform those candidate searches rarely in order to avoid falling into observer's bias. A homogeneously observed data set also provides more robust detection limits. On account of the rather long orbital periods expected for circumbinary planets (50+ d; Martin 2018), we are only now reaching the ability to confirm exoplanetary candidates.

A similar procedure is performed with SOPHIE, on the Northern sample. It will be more specifically described once SOPHIE data are presented for publication.

2.2 Data collection reduction and outlier removal

Observations are obtained using the HARPS instrument on the ESO 3.6-m telescope situated at the La Silla observatory in Chile (Mayor et al. 2003). Reduction of the spectroscopic data was carried out by the HARPS pipeline (Lovis & Pepe 2007). A Cross Correlation Function (CCF; Baranne et al. 1996; Pepe et al. 2002b) is created by comparing the spectra obtained by the spectrograph with a G2 or K5 template mask spectra (depending on the spectral type of the primary star in question). We remind here, that our targets are chosen such that the spectra of the secondary star is too faint to be detected. Typically our primary stars are >4 magnitudes brighter than the secondaries. This allows us to safely ignore the secondary CCF and treat each system as a single-star system (spectroscopically speaking; Martin et al. 2019). The correlation is evaluated at 0.5 km s^{-1} intervals and the CCF indicates with its lowest point the radial velocity at which the mask corresponds most closely with the targets' spectra. The CCF is fit with an inverted Gaussian profile and its mean recorded as the radial-velocity.

Various shape metrics are obtained from the CCF itself, such as the span of the inverse of the mean bisector slope (bisector span) and the full width at half-maximum (FWHM). These are often used as indicators of stellar activity (Queloz et al. 2001; Santos et al. 2002) but mainly they track the quality of our observation and whether any radial-velocity displacement is caused by a change in the shape of the CCF, or by a translation of the CCF, which is what we are after.

Eleven systems (9 on HARPS and 2 with SOPHIE) with particularly strong anti-correlation have been dropped from the observing schedule. A anti-correlation between bisector span and RV is likely caused by starspots on the surface of the target creating parasitic signals (e.g. Queloz et al. 2001).

Prior to fitting our radial-velocities, we clean any obvious outliers from our data. First, we exclude any observations mistakenly obtained on a star other than our target. This is often seen as a significant difference in the spectrum's signal-to-noise ratio and in the FWHM. Secondly, we remove any measurement likely affected by the Rossiter–McLaughlin effect (e.g. Triaud 2018). To find which measurements are affected, we fit a Keplerian binary model to the radial velocities, and from the fit parameters compute when eclipses would happen.

In the third step, we examine the distribution of all bisector span and FWHM measurements of a given system, and exclude measurements that are further from the mean by more than 3σ. We also perform target per target visual inspections of these metrics and flag systems where the bisector span and/or the FWHM appear to show a long-term trend.

2.3 Choice of targets and observation summary

For this paper, we select three systems from within the full BEBOP South sample. We choose our Southern sample for this exercise as we have obtained more high precision data with a longer baseline than what is currently available in BEBOP North. We select these three from the sample for several reasons. The first is that no planetary or stellar activity signal are currently visible.

Secondly, we select amongst the systems with the lowest radial-velocity uncertainty, and lowest rms scatter, after having removed the contribution of the secondary star to the radial velocities of the primary (that we refer to as *residual rms*). We do this to specifically demonstrate BEBOP's ability to recover circumbinary planets with signals of a few m s^{-1}. Of our 41 Southern targets with more than the average of 23 spectra, we have identified 17 with a residual

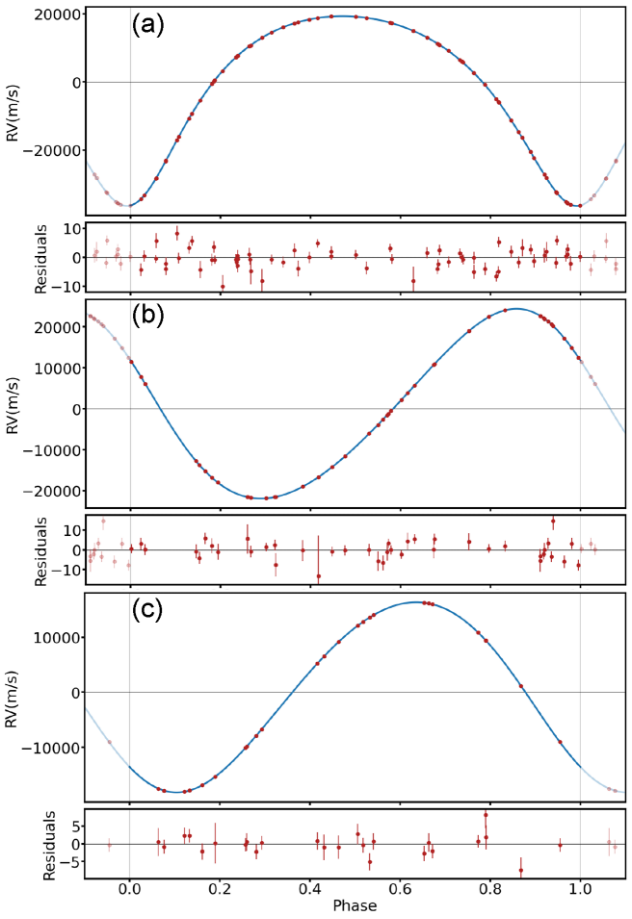

Figure 1. Best fit phased RV models for (a) = J0310-31, (b) = J1540-09, (c) = J1928-38 with associated residuals. Doppler motion of the primaries seen here are caused by the secondary stars. Residuals have an rms = 3.2, 3.8, and 3.0 m s^{-1}, respectively.

rms < 10 m s^{-1}, corresponding to roughly 42 per cent of the sample. While 27 of these targets (66 per cent) have an rms < 17 m s^{-1}. Three systems are selected from within these, which we now describe:

(1) EBLM J0310-31 (J0310-31 thereafter) has been part of the preliminary survey for BEBOP on HARPS, and of the first extensive observing campaign. This is the target for which the largest number of spectra has been obtained. In total, 65 RV data points are available, obtained between 2017-7-9 and 2020-1-2. These measurements also have the lowest mean uncertainty of the survey $\overline{\sigma_{\rm RV}} = 2.13$ m s^{-1}. J0310-31's residual rms = 3.16 m s^{-1}, which is one of the smallest we obtain so far. All these make J0310-31 the ideal target to test our procedures to compute detection limits, as well as perform injection-recovery tests on. See Fig. 1 for a phased plot of our RV data for J0310-31, along with our best-fitting model and residuals.

(2) EBLM J1928-38 (J1928-38 for short). Its residual rms = 2.96 m s^{-1}, better than J0310-31, close to its mean photon noise uncertainty $\overline{\sigma_{\rm RV}} = 2.67$ m s^{-1}. Only 25 measurements have been obtained on J1928-38 so far, which makes it more representative of the current state of the survey than J0310-31 is. These were collected between 2018-6-4 and 2019-9-14.

(3) EBLM J1540-09 (henceforth J1540-09) has $\overline{\sigma_{\rm RV}}$ = 3.86 m s^{-1}, and rms = 3.75 m s^{-1}, for 41 available spectra, observed from 2017-4-20 to 2020-3-6.

These targets were analysed using the KIMA RV analysis package (see next section). Their parameters can be found in Table 1. All data can be accessed in tables A5–A7 of appendix A. All measurements for these three systems are used, with no outliers found within those three data sets.

3 RV ANALYSIS WITH kima

For the analysis of the radial velocities and the calculation of detection limits, we use the KIMA package presented in Faria et al. (2018). The code models the RV timeseries with a sum of Keplerian functions from N_p orbiting planets, estimating the posterior distributions for all the orbital parameters.

To sample from the joint posterior distribution, KIMA uses the Diffusive Nested Sampling (DNS) algorithm from Brewer, Pártay & Csányi (2011). Together with posterior samples, DNS provides an estimate for the marginal likelihood, or evidence, of the model, which can be used for model comparison (e.g. Brewer 2014; Feroz, Balan & Hobson 2011). Fixing the values of N_p in sequence, we can use the ratio of the evidences to compare models with different number of planets. In addition, since DNS can be used in a trans-dimensional setting (Brewer & Donovan 2015), the number of planets in the system N_p itself can be a free parameter in the analysis, and its posterior distribution can be estimated together with that of the orbital parameters. The posterior probability for each N_p value then allows for the same model comparison, with the advantage of being obtained from a single run of the algorithm.

The DNS algorithm samples from a mixture of distributions which is not directly the posterior. A total number of samples N_s from this target distribution results in a smaller number of effective samples N_{eff} from the posterior distribution. We obtain $N_{eff} > 20\,000$ effective samples for each model, which is more than enough to accurately characterize the posterior.

Keplerian parameters are estimated from the effective posterior samples via the clustering algorithm HDBSCAN (McInnes, Healy & Astels 2017). First, crossing orbits are removed from the posterior samples. Those are proposed Keplerian orbits that cross with each other, or those with an eccentricity which would cause their orbit to cross into the instability region of the binary and are therefore unphysical (e.g. Dvorak, Froeschle & Froeschle 1989; Holman & Wiegert 1999; Doolin & Blundell 2011; Mardling 2013). HDBSCAN is applied on the remaining posterior samples, highlighting dense regions in parameter space. The cluster corresponding to the Keplerian signal is plotted with the CORNER package (Foreman-Mackey 2016). Parameters are determined as the 50th percentile of the cluster, with 1σ uncertainties estimated from the 14th and 84th percentiles.

To decide between competing models that fit our data, we use the *Bayes factor* (BF, here onwards). The BF is the ratio of the Bayesian evidence of the two competing models, and provides a measure of the support in favour of one over the other (Kass & Raftery 1995; Trotta 2008). Table 2 adapted from Trotta (2008) shows how the BF is measured and introduces the Jeffreys' scale (Jeffreys 1961) as a measure of evidence strength.

To guide our identification of planetary candidates, we follow the same Jeffreys' scale, but use custom thresholds that affect what response we have to the system. Like Trotta (2008), we use BF = 12 as a threshold for 'moderate' evidence. To identify planetary candidates worthy of additional follow-up (to apply for additional telescope time for instance), we use BF > 6. Regularly, 3σ marks a detection in Astronomy. To make sure we are over that value, we place a threshold at BF = 35. Any system reaching that level continues to be observed as any other, but we analyse its data more regularly than once a year. To visually track increasing evidence for a planetary signal, we place an additional division at BF = 70. Finally, we place our upper threshold BF = 140, after which observations cease to

Table 1. Updated binary, system, and derived parameters for the investigated binary systems. Uncertainties are given in the brackets, as the last two significant figures, except for σ_{jit} where uncertainties can be significantly asymmetric.

	EBLM J0310-31	EBLM J1540-09	EBLM J1928-38
System properties			
TIC	89045042	32431480	469755925
TYC	7019-784-1	5600-377-1	7931-842-1
Gaia DR2	5057983496155992448	6317098582556256000	6739146911148825344
α (deg)[a]	03:10:22.62	15:40:08.99	19:28:58.85
δ (deg)[b]	−31:07:35.7	−09:29:02.2	−38:08:27.2
Vmag	9.33(02)[b]	10.865(38)[c]	11.20(12)[b]
Distance (pc)[d]	147.29(84)	206.0(1.8)	257.7(2.2)
M_A ($M_\odot$)[a]	1.26(10)	1.18(10)	0.980(80)
Binary parameters			
P_{bin} (d)	12.6427937(17)	26.338279(14)	23.322972(22)
K_A (km s^{-1})	27.87218(52)	23.17988(87)	17.26333(52)
e_{bin}	0.308724(19)	0.120452(38)	0.073151(38)
ω_{bin} (rad)	3.243410(80)	1.09802(37)	2.39117(75)
T_{peri} (BJD2450 000)	7934.64483(13)	7839.4468(15)	8258.5885(28)
System parameters			
γ (km s^{-1})	29116.0(10)	−55395.95(65)	16558.05(62)
σ_{jit} (m s^{-1})	$2.77^{+0.45}_{-0.41}$	$1.48^{+1.32}_{-1.45}$	$0.089^{+1.153}_{-0.085}$
Derived parameters			
M_B ($M_\odot$)	0.408(20)	0.444(23)	0.268(14)
a_{bin} (AU)	0.1260(31)	0.2037(53)	0.1720(44)

Note. [a]Martin et al. (2019) [b]Høg et al. (2000) [c]Munari et al. (2014) [d]Gaia Collaboration, Brown et al. (2018)

Table 2. Table of BF along with corresponding probability, sigma values (standard deviations away from the mean of a normal distribution), and the 'Jeffreys' scale' adapted from Trotta (2008).

BF	Probability	Sigma	Evidence strength
$\lesssim$3	<0.750	$\lesssim$2.1	Inconclusive
3	0.750	2.1	Weak
12	0.923	2.7	Moderate
150	0.993	3.6	Strong

be blind and we start to target specific epochs that represent poorly sampled orbital phases, or alternate solutions (eccentricity, $2 \times P_{\rm p}$, etc). We use the thresholds described here in our insertion/recovery exercise below.

Contrary to a regular planetary system, a circumbinary SB1 system is dominated by the reflex motion caused by the secondary star (typically tens of km s^{-1}) and extremely well-constrained by the data. In addition, we know there cannot be a planet at an orbital period $\lesssim$4 $P_{\rm bin}$ due to the instability region (Dvorak et al. 1989; Holman & Wiegert 1999; Doolin & Blundell 2011; Mardling 2013).[1] In contrast, we have no idea whether a planet is within the system, or what its parameters might be. By default, KIMAapplies a common prior for all the orbiting objects (secondary, or planet) in a given model, which is not well-adapted to our case. Particularly, there is no doubt that there is a secondary star in the system, and as such no need for the nested sampler to test that hypothesis.

In this context, KIMA can instead use the so-called *known object* mode, where a specific set of priors can be placed on the binary properties, and another set of priors is used to explore the presence/parameters of putative planets. At each step, KIMA then fits for the binary (the *known object*) and any additional Keplerian signal present in the data. Using this mode, the nested sampler only computes evidence for $\geq$1 Keplerian function, therefore only testing for the presence of circumbinary planets ($\geq$0 planets).

A typical KIMA run with 200 000 saves, resulting in $N_{\rm eff} \approx$ 25 000–35 000 posterior samples (depending on data set) takes $\approx$180 min on a standard laptop computer.

4 METHODS AND SIMULATIONS

Here, we describe our methods, which are used similarly on all the systems we monitor in the survey. First, we give a simple parametrization of the model. Then, we detail and justify the priors we use within KIMA (see also Table 3). We then demonstrate using KIMA to produce robust and fully Bayesian detection limits. Following that, we perform a more traditional insertion-recovery test of static Keplerian signals to compare with our KIMA detection limits. We then test the validity of injecting static Keplerian signals in comparison to N-body simulations. Finally, we discuss how our process compares with previous methods for detection limits, both for single and binary stars.

[1]In practice, the stability limit is dependent on other parameters such as the eccentricities, orbital alignments, relative orbital phases, and mean motion resonance, as most recently explored by Quarles et al. (2018). It is therefore possible that KIMA would return unstable circumbinary configurations. However, any such solutions would have their stability rigorously tested with N-body models prior to claiming a detection.

Table 3. Prior distributions used in RV model for binary and planetary signals in KIMA.

Parameter	Unit	Prior distribution	
		Binary	Planet
$N_{\rm p}$		1	$\mathcal{U}(0, 3)$ or 1
P	d	$\mathcal{U}(P_{\rm bin} \pm 0.01)$	$\mathcal{LU}(4 \times P_{\rm bin}, 1 \times 10^3$ or $\times 10^4)$
K	m s^{-1}	$\mathcal{U}(K_{\rm A} \pm 10)$	$\mathcal{MLU}(0.1, 100)$
e		$\mathcal{U}(e_{\rm bin} \pm 0.0005)$	$\mathcal{K}(0.867, 3.03)$
ϕ		$\mathcal{U}(0, 2\pi)$	
ω		$\mathcal{U}(0, 2\pi)$	
$\sigma_{\rm jit}$	m s^{-1}	$\mathcal{LU}(0.001, 10 \times$ rms)	
γ	m s^{-1}	$\mathcal{U}(V_{sys} \pm 100)$	

Note. $N_{\rm p}$ denotes the Number of Planetary Keplerian signals to fit to the data. $P_{\rm bin}$ and $e_{\rm bin}$ denote the Period and eccentricity of the binary respectively. $K_{\rm A}$ denotes the semi-amplitude of the primary star, caused by the secondary. $\mathcal{U}$ denotes a uniform prior with an upper and lower limit, $\mathcal{LU}$ is a log-uniform (Jeffreys) prior with upper and lower limits, $\mathcal{MLU}$ is a modified log-uniform prior with a knee and upper limit, and $\mathcal{K}$ is a Kumaraswamy prior (Kumaraswamy 1980) which takes two shape parameters.

4.1 Model setup

With KIMA, we assume independent, static Keplerian orbits for the binary and any circumbinary planets. This neglects the fact that the orbits of the planet and binary will evolve through three-body interactions (e.g. Martin & Triaud 2014; Kostov et al. 2014). Martin et al. (2019) however found such interactions to be negligible with respect to the CORALIE BEBOP survey. We will briefly verify if this assumption still holds with our more precise HARPS data in Section 4.4, where we test the injection and retrieval of N-body simulated RV signals.

The Keplerian models we fit to the data are defined by the following parameters. For the binary we have $P_{\rm bin}$ (the orbital period), $K_{\rm A}$ (the semi-amplitude of the primary star, caused by the secondary), $e_{\rm bin}$ (the binary's orbital eccentricity), $\omega_{\rm bin}$ (the argument of periastron), and $\phi_{\rm bin}$ (the starting phase of the orbit). We can calculate the time of periastron passage from these parameters using $T_{\rm peri} = t_0 - (P \times \phi)/(2\pi)$, where t_0 is the chosen epoch. The number of planets in the system is referred to as $N_{\rm p}$. Planetary parameters are defined like for the binary, but written with a subscript p, e.g. $P_{\rm p}$ for a planet's orbital period.

In addition, we fit for the systemic velocity γ, and for a *jitter* term, $\sigma_{\rm jit}$ that rescales the uncertainties on the data. An increase in this parameter is penalized when computing the likelihood. We can also fit for offsets in data between instruments, but this not necessary for the three systems we analyse here.

4.2 Prior distributions

We use priors similar to those laid out in Faria et al. (2020), but adapted to circumbinary planets. As described in Section 3, we treat the signal produced by the secondary star as an *known object*, taken to be obviously present in the data and place tight priors on its parameters. We only compute Bayesian evidence for any additional signals to the inner binary. This is an advantage of using KIMA, both the orbit of the binary and any additional signal are fit to the data simultaneously, each posterior sample obtained has a corresponding binary fit. Table 3 shows the prior distributions utilized in our analysis.

The secondary's orbital parameters prior distributions are based on values from an initial fit. We take the mode of each binary parameter and set to the prior to uniformly explore a range around that value.

That range is determined from fitting all of the binaries in our sample. For instance, we explore ± 0.01 d around the orbital period, and $\pm 10\,\mathrm{m\,s^{-1}}$ around the semi-amplitude (Table 3). While these might seem tight, the typical precision obtained on $P_{\rm bin}$ and $K_{\rm A}$ is 100 times less than the prior ranges we set (see Table 1). As such, the binary priors we chose are wide enough to enclose the true parameters and their uncertainties.

To search for additional signals besides the binary (i.e. circumbinary planets), we use a uniform distribution for γ, ϕ, ω, and $N_{\rm p}$, as there is no reason to favour any particular value within these parameter spaces.

For planetary eccentricities, we utilize a Kumaraswamy distribution (Kumaraswamy 1980), using values for our shape parameters as $\alpha = 0.867$ and $\beta = 3.03$ as justified in Kipping (2013), closely resembling the Beta distribution described there. A Kumaraswamy distribution favours lower values but still permits the exploration of higher eccentricities when the data allows.

The most sensitive parameter to sample when determining robust detection limits is planetary semi-amplitudes $K_{\rm p}$. For this reason, we use a transformed Log-Uniform (Jeffreys) prior. We cap the upper range, choosing $100\,\mathrm{m\,s^{-1}}$ (any signal greater than this would be obvious in our data). Thanks to various tests, we noticed that setting a specific lower limit to $K_{\rm p}$ influenced our ability to recover planets and estimate robust detection limits. When we set the lower limit too high (e.g. $1\,\mathrm{m\,s^{-1}}$), it excludes any signals $< 1\,\mathrm{m\,s^{-1}}$ in strength that could lie formally undetected in our data, but effectively ignoring any contribution they may have on other signals and parameters. If instead we set the limit too low (e.g. $0.01\,\mathrm{m\,s^{-1}}$), the sampler does not explore the higher $K_{\rm p}$ sufficiently (since they become relatively less likely). This can bias the detection limit to lower $K_{\rm p}$ due to low number statistics in the posterior, producing overconfident detection limits.

Instead of setting a lower value we insert a *knee*, to give less priority to signals below a set value. Gregory (2005) advises using a knee at $1\,\mathrm{m\,s^{-1}}$, which was 1/10 of their typical RV uncertainty. As our survey utilizes RV data from both SOPHIE, HARPS, and ESPRESSO, our uncertainties approach $1\,\mathrm{m\,s^{-1}}$, we set our knee to $0.1\,\mathrm{m\,s^{-1}}$. For values of $0 < K_{\rm p} < 0.1\,\mathrm{m\,s^{-1}}$, the distribution acts as a uniform prior, whereas for $K_{\rm p} \geq 0.1\,\mathrm{m\,s^{-1}}$, the priors follow the usual Jeffreys prior (see Gregory 2005).

For all other parameters, we employ Log-Uniform (Jeffreys) priors since the range of values can span several orders of magnitudes. This goes for $\sigma_{\rm jit}$ and $P_{\rm p}$.

The lower limit for the $P_{\rm p}$ prior is set to $4 \times P_{\rm bin}$, following the instability region (see Section 3). This is a slightly conservative estimate for the instability region. For completeness, we explored the effect of placing a lower limit at $P_{\rm p} < P_{\rm bin}$. Results were similar, with the only effect being that posterior samples were dispersed over a larger parameter space resulting in a coarser posterior.

We place the upper limit at $P_{\rm p} = 1 \times 10^3$ d, roughly the time-span of our longest observed systems: J0310-31. For simplicity and to allow for a fair comparison, this limit is used for all three systems. We increase the maximum limit to 2×10^4 d to generate detection limits, as described in Section 4.3, and witness how the detectable semi-amplitude increases with increasing orbital period after exceeding the time-span of the data. When seeking planetary candidates, we prefer using a maximum period of 1×10^3 d, which saves computational power and ensures a finer sampling of the posterior. The presence of a planetary signal with $P_{\rm p} > 1 \times 10^3$ d in our data would be identifiable as an overdensity of posterior samples at the upper limit of this prior. In which case, we adjust this limit as required. The limit on $P_{\rm p}$ will extended as we accumulate more data.

4.3 Detection limit method

A unique feature of a diffusive nested sampler such as KIMA is that when forced to explore higher $N_{\rm p}$ than is formally detected, the sampler will produce a map of all signals that are compatible with the data. Since those proposed signals remain formally undetected, the posterior naturally produces a detection threshold. In our case, this is made simpler by KIMA's *known object* mode (see Section 3), and the fact that no planets have been detected in those three systems thus far. We describe in Section 5.3 how we calculate a detection limit when a planetary signal is already present in the data.

Later, we compare our results to a more traditional insertion-recovery test, the method of choice to assess detectability and measure occurrence rates in radial-velocities surveys (Cumming et al. 2008; Konacki et al. 2009; Bonfils et al. 2013; Martin et al. 2019; Rosenthal et al. 2021; Sabotta et al. 2021).

Using a diffusive nested sampler like KIMA also provides immediate advantages over insertion-recovery test. KIMA samples all orbital parameters in a fine manner. Particularly, this means that all orbital phases, all eccentricities, and all periastra are sampled when typically only a small number of phases are tested, and that eccentricities are nearly always forced to zero. Detection limits obtained with KIMA marginalize over more orbital parameters than is computationally feasible with insertion-recovery tests, and KIMA assumes Keplerian signals, rather than sinusoidals (see next section).

To create a detection limit, we run KIMA with priors as in Table 3 except that we fix $N_{\rm p} = 1$. KIMA marginalizes over all allowed parameter space, searching for any possible Keplerian signals producing a reasonable likelihood, in the process, ruling out Keplerians that would otherwise have been detected.

A key to producing a robust detection limit is to produce a well-sampled posterior. For each system we compute three runs, ensuring $>20\,000$ samples are obtained in each. To gather consistent results, we set the number of saves in KIMA to 200 000. The resulting ($K_{\rm p}$, $P_{\rm p}$) posterior's density is plotted in Figs 2 and 3 as a grey-scale hexbin, with the detection limit being the top envelope.

To compute the detection limit, we separate the posterior in log-spaced bins in $P_{\rm p}$, and within each bin, we evaluate the maximum 99th percentile of the $K_{\rm p}$ distribution. This is done with the caveat that ≥ 2 posterior samples must lie above the chosen sample in a given bin. We do this to prevent the detection limit from being affected by small number statistics in individual bins. We calculate a detection limit for each of the three runs we perform on each system, which we show with faded blue lines in Figs 2 and 3. We also draw the detection limit obtained when combining all posterior samples from the three runs into a single sample, with a solid blue line. Proceeding this way allows us to produce a mean detection limit and to obtain a visual estimate of the uncertainty of that limit for each bin. Overall, all runs are compatible with one another. We stop computing the detection limit for all $P_{\rm p}$ exceeding the first $P_{\rm p}$ bin where the number of samples in the top 10 per cent of $K_{\rm p}$ prior is larger than three, which is where the posterior is affected by the upper limit set for the $P_{\rm p}$ prior.

4.4 Injection and recovery tests

The seminal (single-star) radial-velocity surveys of Cumming et al. (2008), Mayor et al. (2011), and Howard et al. (2010) used injection and recovery methods as a means of determining injection limits. First, all known planets are removed from the data. Then a sinusoid of varying amplitude, period and phase is used to model a putative exoplanet, and applied to the data. Following that, a periodogram of

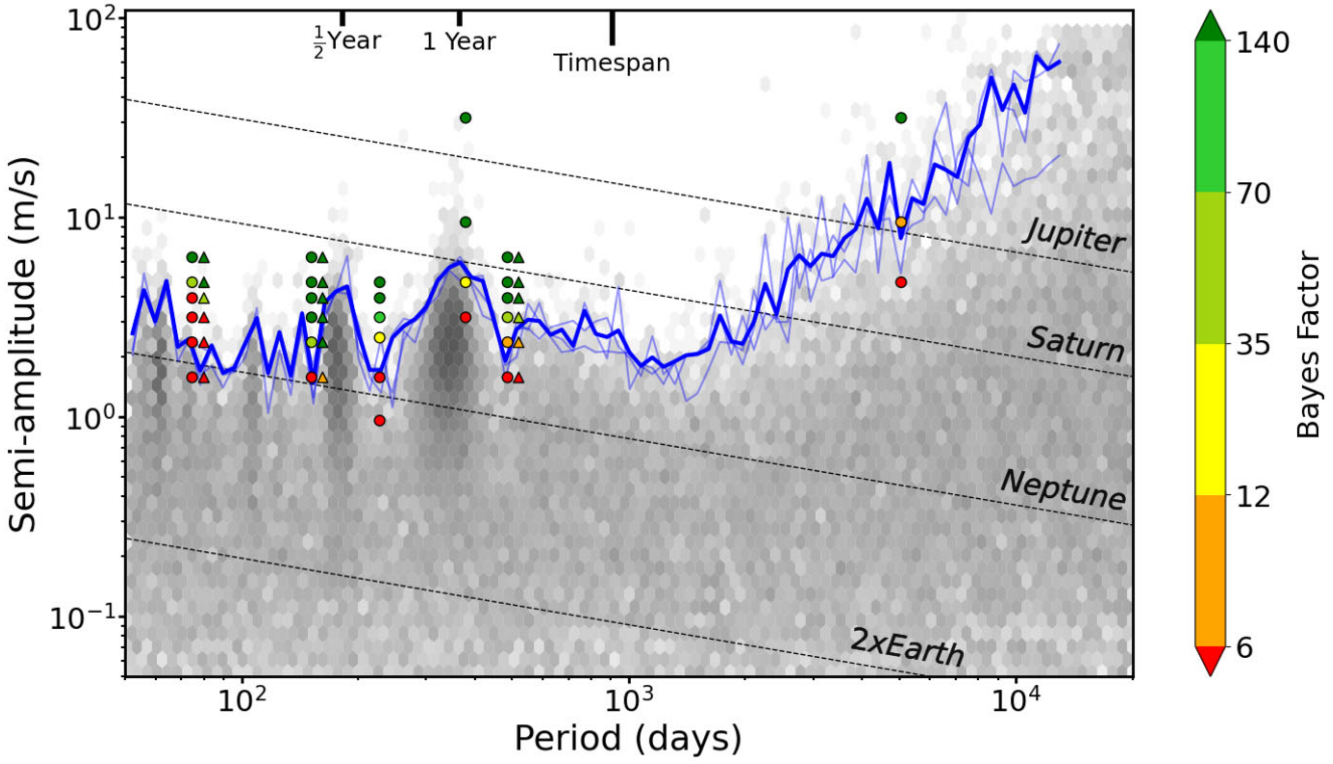

Figure 2. Hexbin plot denoting the density of posterior samples obtained from three separate KIMA runs on J0310-31 with N_p fixed =1, as a grey-scale. Faded blue lines show detection limits calculated from each individual run on the system as described in the text. The solid blue line shows the detection limit calculated from all posterior samples combined. Coloured symbols indicate the BF results of injection/recovery tests and correspond to the colour bar on the right-hand side. Circles are for injected static Keplerian sinusoidal signals, whereas triangles are for N-body simulated injected signals. The Keplerian and N-body signals are injected at the same orbital periods but are represented slightly offset horizontally here for visual clarity. The faded red dashed lines show masses of Solar system planets for comparison.

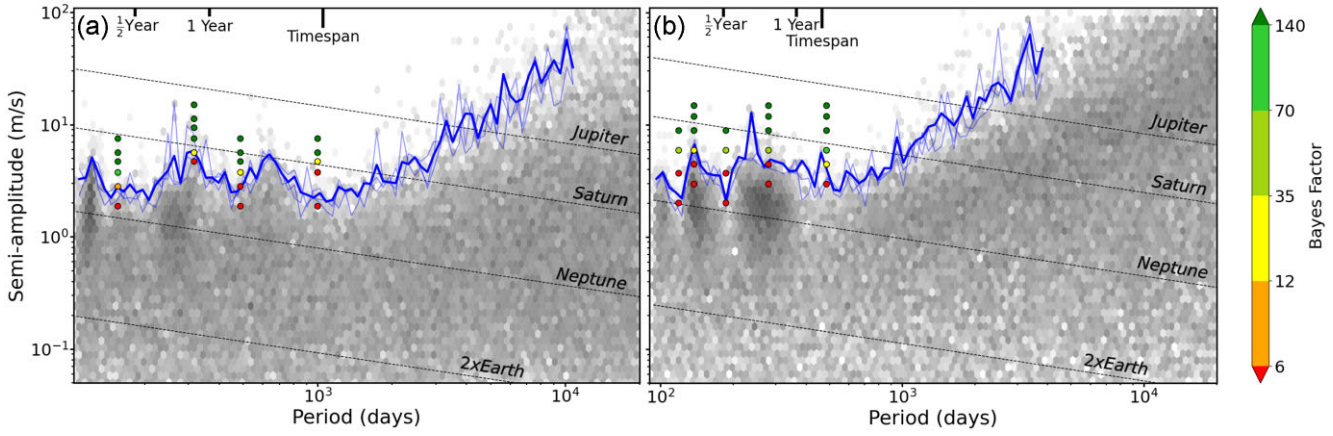

Figure 3. Same as in Fig. 2, but for three separate KIMA runs on J1540-09 (a), and J1928-38 (b) with N_p fixed =1. All injected signals here are static Keplerian sinusoidal.

the data (typically a Generalized Lomb–Scargle) is computed. If it produces a peak below a certain false alarm probability (typically < 1 per cent) near the injected period, the simulated planet is considered 'detected'. By reproducing this procedure over a grid of P_p and K_p inserted signal, it is possible to find out for which values the planet is no-longer detectable. Martin et al. (2019) followed this approach for the CORALIE BEBOP survey, with one key difference that the planet signal was injected to a radial-velocity data set where the binary signal had already been removed.

Whilst this traditional approach may appear similar to ours, in practice they are distinct. When we use our Bayesian approach with KIMA to produce detection limits, we answer the question ''what is compatible with the data?", whereas with an insertion-recovery test, we ascertain ''can this *specific* signal be found?".

Here, we create injection-retrieval tests for our three targets. There are two purposes of this. First, we investigate compatibility between our Bayesian KIMA -derived limit and the more traditional approach of injecting static Keplerian signals. Secondly, we follow the approach

of Martin et al. (2019) to inject not just static sinusoids but an N-body derived signal using REBOUND, including all dynamical interactions between the planet and binary, to test the validity of the previous step.

We add one circumbinary planet signal to the original data, and do so for a number of planetary semi-amplitudes K_p and orbital periods P_p. KIMA is then used to recover any Keplerian signals in the modified data set with the resulting BFs providing a measure of signal recovery success.

The choice of K_p and P_p at which we inject simulated signals is informed by the data itself. For K_p, values are chosen as multiples of the residual rms of each system. Values used can be found for each system in appendix A, tables A1–A4.

For P_p, there are three periods we test for all three targets. The first is $5.9 \times P_{bin}$, which is similar to known circumbinary systems (Martin 2018) and slightly offset from the often unstable 6:1 mean-motion resonance (Quarles et al. 2018). We also test $12 \times P_{bin}$ and 486 d ($365 \times 4/3$, to avoid but be close to the 1 yr alias). In some cases, we also simulate specific orbital periods, coinciding with features of the detection limits described in Section 4.3.

Each inserted signal has an eccentricity $e_p = 0.01$ (small but non-zero), and argument of periastron $\omega_p = 0$.

Then, we run KIMA as described previously, using priors as in Table 3, including a uniform prior on $N_p = U(0, 3)$, reproducing how we conduct an open search of the system. BFs are computed from each run and results are plotted in Figs 2 and 3 as coloured points. Their values can also be found in tables A1–A4 in appendix A.

The binary and putative circumbinary planets for the three chosen periods are then simulated for the J0310-31 system using the REBOUND N-body code (Rein & Liu 2012), with the IAS15 integrator (Everhart 1985; Rein & Spiegel 2015). First, we remove the best-fitting binary model from J0310-31's observed radial-velocity measurements, producing residuals. Then, we use REBOUND to simulate a radial-velocity model of the binary and putative planet at each epoch of observation. We add this model to the residuals. Doing this preserves the scatter, uncertainties, and observational cadence obtained in reality. KIMA is ran once again on each N-body simulated data set, and BFs computed and compared to those resulting from the injected static Keplerian signals. We discuss the result of this test in Section 5.3. All BF values are plotted in Fig. 2 as coloured triangles offset to the right-hand side, and can also be found in appendix A table A2.

5 RESULTS AND DISCUSSION

We begin by providing updated parameters on the three binary systems investigated. Then, we discuss the calculated detection limits for each binary system, along with how they compare to our Keplerian injection and recovery tests. Following this, we discuss and present our results from the comparison between Keplerian and N-body simulation injection and recovery. We discuss how nested sampling provides more robust detection limits. Particularly, we describe how traditional insertion-recovery exercises overestimate their ability to retrieve planets by assuming zero eccentricity.

5.1 Updated binary parameters

Table 1 shows updated orbital parameters from our most recent data for the systems investigated in this work. We provide 1σ uncertainties for each parameter, in parenthesis. Uncertainties are symmetric and varying only in the second significant figure, where the largest of the two values were taken. σ_{jit} is the only parameter that demonstrated an asymmetric distribution (tending to zero), where we consequently provide asymmetric uncertainties. Values agree with Martin et al. (2019) to within $1–2\sigma$ for all parameters other than ω_{bin} and correspondingly T_{peri}. Improvements in parameter precision of around 70 per cent are to be attributed to the increased number of high-precision measurements acquired using the HARPS spectrograph.

5.2 Detection limit results

Figs 2 and 3 show the results of our detection limit analysis for EBLM J0310-31, J1540-09, and J1928-39, respectively. The grey-scale *hexbins* show the density of posterior samples from all KIMA runs on the targets. The faded blue lines are the calculated detection limit from three individual run containing 200 000 saves, and >20 000 posterior samples. The solid blue line is calculated from all posterior samples combined. Coloured dots represent the results for each individual injection and recovery test as outlined in Section 4.4. The colour of these points represent the BF discussed in Section 3, and measure the probability of recovery for the injected Keplerian signals. Every sample in the posterior used to compute detection limits involves a free fit of the binary as a well as a proposed planetary signal, producing a detection limit that marginalizes over the binary parameters, an essential element for BEBOP.

From these plots, it is evident that different runs of KIMA produce consistent detection limits with one another. The only inconsistencies are due to a low number of samples within a particular bin, a situation easily resolved by increasing the number of saved posterior samples. We also note that the posterior below the limit is uniformly sampled across parameter space, an indication of the reliability of the method we followed.

The detection limit plots also show many features that are regularly seen in detection limits for exoplanets using the radial-velocity method. For all three systems, we see an increased density of posterior samples, and a consequently raised detection limit near 0.5 and 1 yr orbital periods, corresponding to yearly aliases, caused by seasonal gaps in observations. In addition, we observe that our detection capability is broadly horizontal for P_p below the timespan of our data. Then, it increases linearly in log until it hits the upper limit of the P_p prior. For J0310-31, we reach a mean *K*p detection of $1.49\,m\,s^{-1}$, for J1540-09, we get 2.06 , and $2.15\,m\,s^{-1}$ for J1928-38. For these three systems, we outperform any produced by the TATOOINE survey (Konacki et al. 2010) despite our systems being fainter by an average four magnitudes, validating our choice to monitor single-lined binaries to seek circumbinary exoplanets. These detection limits can be translated into masses, which are shown by additional lines in Figs 2 and 3. Typically, we are sensitive to planets with masses between Neptune's and Saturn's for orbital periods between 50 and 1000 d respectively, a milestone.

Injection-recovery test results are consistent with the detection limits obtained with KIMA at almost all orbital periods tested on each system. The largest deviation can be seen in Fig. 2 for J0310-31 at 74.59 d. Where the detection limit is approximately $2\,m\,s^{-1}$ lower than the recovered injected signal strength. This is the only location where such a deviation is observed.

Fig. 4 is an example of how the value of the BF evolves with the number of posterior samples during a KIMA run. Our example is J0310-31 data, with an injected planetary signal with $P_p = 227.57$ d, and $K_p = 3.16\,m\,s^{-1}$. The uncertainty on the BF (blue area) is estimated assuming a multinomial distribution. We use this figure as an indicator for fit convergence, i.e. once the line asymptotes on a BF value, the fit has converged.

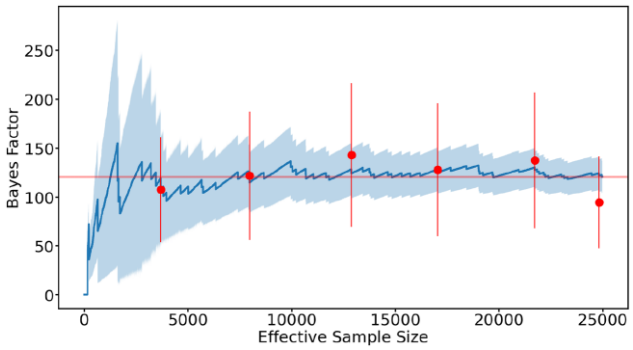

Figure 4. Plot of BF versus number of posterior samples from a KIMA run with a 227.57 d, 3.16 m s^{-1} injected signal in J0310-31. In blue, we show the cumulative BF as a function of the number of posterior samples. The blue line shows the BF values, and and their running uncertainty are drawn as the shaded blue region. We add one red dot after 10 $N_p = 0$ samples to show the BF value then, with their uncertainties. The horizontal red line shows the final BF value calculated with all posterior samples.

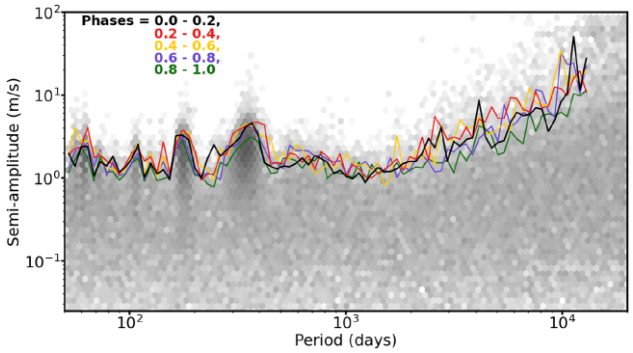

Figure 5. Hexbin plot of posterior samples for J0310-31 as in Fig. 2. The coloured lines here indicate the detection limits calculated with the posterior samples split into five even phase bins with the black line representing the phase bin containing $\phi = 0$.

We also check how often we recover the Keplerian signal we insert. We find that orbital parameters of injected signals detected with BF > 35 are typically recovered to within 3σ or 10 per cent of their original values, except those with periods close to one or half a year. This is true for injected Keplerian signals, as well as the REBOUND injected signals.

The chosen phase of the injected Keplerian signal could, in principle, cause the discrepancy between the methods seen at $P_p = 74.59$ d for J0310-31. Fig. 5 shows the same posterior samples as those in Fig. 2 but split into five different phase bins, with a detection limit calculated for each. Doing this is simple with KIMA, we simply select all posterior sample within a specific phase bin and reproduce the method in Section 4.3. As can be seen in the figure, varying phase has little effect on the detection limit, which is the case for each target investigated. This consistency seen between phase bins further demonstrates how robust and consistent our detection limits are. This also highlights the usefulness and importance of using nested samplers such as KIMA to compute detectability curves.

5.3 REBOUND simulation results comparison

Results from systems simulated using REBOUNDare shown in Fig. 2, as coloured triangles offset to the right from similar, but Keplerian-only

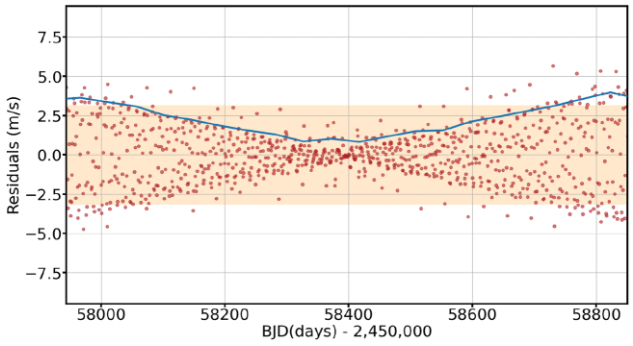

Figure 6. Plot of residual radial-velocity amplitude as a function of time, after removing a Keplerian binary signal from N-body simulated J0310-31 radial-velocity data set. Simulated data are computed with REBOUNDincluding the binary and an orbiting circumbinary planet with $P_p = 74.59$ d and $K_p = 6.32$ m s^{-1}. To reveal the Newtonian perturbation, we plot one point for each night over the entire duration of our data set. The blue line depicts 1.3 × rms within bins 45 d wide. We use this line as a visual guide to the amplitude of the effect. The shaded orange region illustrates the rms scatter obtained on the data we collected on J0310-31. The *bow-tie* shape of the residuals is caused by apsidal motion of the binary ($\dot{\omega}_{bin}$), caused by the planet, which a Keplerian model does not include.

simulations. The only evident deviation between the two simulations occurs at the shortest period investigated (74.59 d) here, the BF for the REBOUND simulated data is higher for $K_p = 3.95$ m s^{-1}.

The agreement in those results (see table A2 in appendix A) confirms that assuming Keplerian functions has no obvious detriment to circumbinary planet detection within our current data just like for any planetary system so far, and as we had already seen in Martin et al. (2019) with more imprecise CORALIE data. This simply means that assuming a static Keplerian signal is sufficient for discovery. However, dynamical fits are known to be useful to constrain the physical and orbital parameters of circumstellar planetary systems (e.g. GJ 876; Correia et al. 2010), and would likely be the case for circumbinary systems, as they have been for HD 202206 (Correia et al. 2005; Couetdic et al. 2010), a system comparable to a circumbinary configuration.

To better understand the non-Keplerian signal, we visualize the amplitude of the Newtonian interactions in Fig. 6. We use REBOUNDto simulate nightly RV data, for $K_p = 6.32$ m s^{-1} at $P_p = 74.59$ d (the shortest period and highest mass planetary signal simulated in this work, producing the largest Newtonian perturbation), over the timespan of our data on J0310-31. Fig. 6 depicts the residuals after fitting and removing the Keplerian binary and planetary signals from the N-body simulated data set. The residuals show that N-body model diverges from the Keplerian model due to apsidal precession ($\dot{\omega}_{bin}$). However, for the timespan of our current data that divergence remains comparable to the residuals' rms. Assuming Newtonian effects are non-negligible will likely cease to be valid for longer time-series.

5.4 Post-Newtonian effects

Radial-velocity measurements of binary stars are also affected by weaker effects, such as tidal distortion, gravitational redshift, transverse Doppler and light time travel effects (Zucker & Alexander 2007; Konacki et al. 2010; Arras et al. 2012; Sybilski et al. 2013). KIMA assumes purely Keplerian functions, ignoring these effects, here we explore what impact this may have on our fit, and particularly on our ability to retrieve planets.

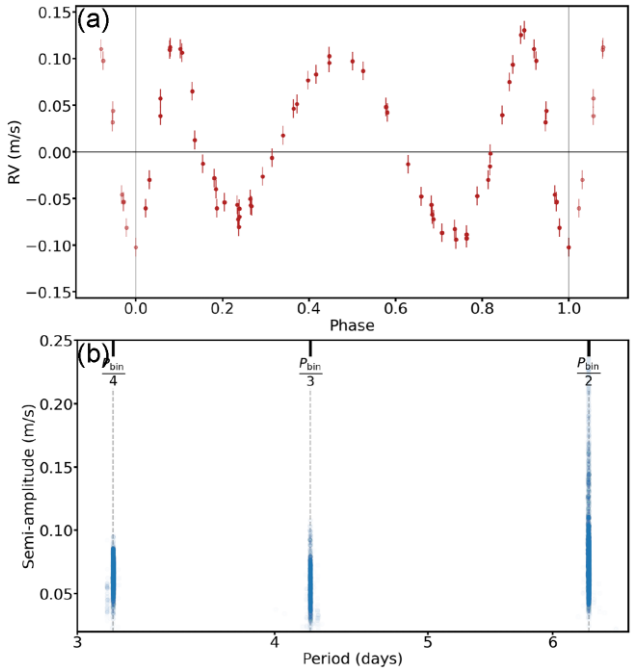

Figure 7. (a) Phased RV residuals from the best-fitting model of J0310-31 simulated binary and additional post-Newtonian effects only. Residuals have an rms = $0.07\,\mathrm{m\,s^{-1}}$. (b) Semi-amplitude versus period plot of posterior samples from a KIMA run on the residuals seen in plot (a). Posterior samples are located at half, third, and a quarter of J0310-31's binary orbital period.

We calculate the magnitude of tidal distortion on our RV measurements as in Arras et al. (2012), and find their amplitude is $< 0.7\,\mathrm{m\,s^{-1}}$ for the three systems we investigate in this paper, an insignificant contribution to the observed RV scatter. We do note however, that for the shortest period binaries in the BEBOP survey, the magnitude of this effect becomes significant (with respect to the rms of the systems) and should be accounted for in any further analysis.

Computing equations from Zucker & Alexander (2007) for the parameters of each of our three systems, we find the magnitude of transverse Doppler effects to be $< 2.2\,\mathrm{m\,s^{-1}}$, and the peak to peak variation $< 1.6\,\mathrm{m\,s^{-1}}$. Similarly, we find the magnitude and peak to peak variation of light time travel effects is $< 2.7\,\mathrm{m\,s^{-1}}$. The only relativistic effect found to be greater than the rms on these systems is that of gravitational redshift, with a maximum amplitude of $13.9\,\mathrm{m\,s^{-1}}$ but a peak to peak variation of $< 6.5\,\mathrm{m\,s^{-1}}$.

To better asses the impact of these effects on our work, we simulate a purely Keplerian binary signal for J0310-31 using the same cadence as our observations were obtained in, and add these post-Newtonian effects. We then fit the data using KIMA. Fig. 7(a) shows residuals after removing the best-fitting Keplerian model of the binary. The residuals have an amplitude of $\approx 0.1\,\mathrm{m\,s^{-1}}$ and a signal phasing with the binary (as expected). This shows that most of the post-Newtonian effects are absorbed by the Keplerian fit.

We now use KIMA once more, to ''search for a planet" in these residuals, in order to study how the algorithm behaves in the presence of additional coherent signals. The posterior of that fit is plotted in Fig. 7(b), and demonstrates the periodicity of these remaining signals at harmonic periods of the binary with low semi-amplitude.

Individually these effects boast significant amplitudes, but as their functional forms resemble, and phase, with a Keplerian, only small differences are produced. Our simulations show that the majority of the post-Newtonian signals are absorbed into our fit.

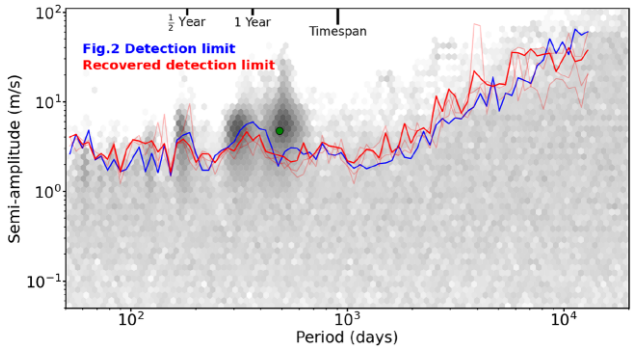

Figure 8. Hexbin plot of posterior samples obtained from three separate KIMA runs on J0310-31 with an additional 486 d signal located at the green point, with N_p free between 0 and 3. The blue line shows the detection limit as seen in Fig. 2. Faded red lines show detection limits calculated from each individual run on the system after having removed the most likely $N = 1$ signal from the data. The solid red combines all these posterior samples together.

They are absorbed primarily into the systemic velocity, and lead to a small underestimation of the secondary's semi-amplitude. For J0310-31, ignoring post-Newtonian effects in this experiment creates an underestimated $K_\mathrm{A} \approx 4\,\mathrm{m\,s^{-1}}$, corresponding to a 0.01 per cent deviation. We conclude that these effects do not affect the detection limits of this paper greatly, and can be safely ignored for our purposes.

5.5 Detection limits in the presence of planetary signals

Detection limits thus far are all generated from our current data on systems purposefully chosen with no candidate planetary signals. The ultimate goal of the BEBOP survey is to detect RV signals of circumbinary planets in our data. Once a system is found to have a planetary signal, a detection limit is required to rule out the presence of additional companions above our calculated mass limit. To this end, we calculate the detection limit for J0310-31 with our N-body simulated data set containing an injected $4.74\mathrm{m\,s^{-1}}$, 486 d signal. A signal of this strength is easily detected in the data (see table A2 in appendix A for its BF value). We identify the injected signal as in Section 4.4, with N_p varying uniformly from 0 to 3, as is standard for the survey. Fig. 8 shows the resulting posterior samples, along with a green dot illustrating the semi-amplitude and orbital period of the injected signal. To obtain a recovered detection limit, we subtract the Keplerian signal corresponding to the posterior model with the highest likelihood from the simulated data. Once subtracted, we run KIMAagain as in Section 4.3 and calculate the red recovered detection limit from the resulting posterior samples. The blue line seen in Fig. 8 is taken from Fig. 2 for reference, and the recovered red line closely resembles the original blue detection limit. We note that while this approach is not strictly Bayesian, it recovers the correct detection limit, and is expected to affect only a few systems (with planets) within the survey.

5.6 The dangers of assuming circular orbits

Thanks to our use of KIMA to produce detection limits, we are able to explore the effect of assuming $e_\mathrm{p} = 0$ on detection limits for exoplanet radial-velocity surveys.

Most often detection limits are produced with multiple insertion-recovery tests. To increase efficiency, and remain computationally tractable, a number of assumptions are made. Circular orbits are generally assumed in the inserted signals used to calculate detection

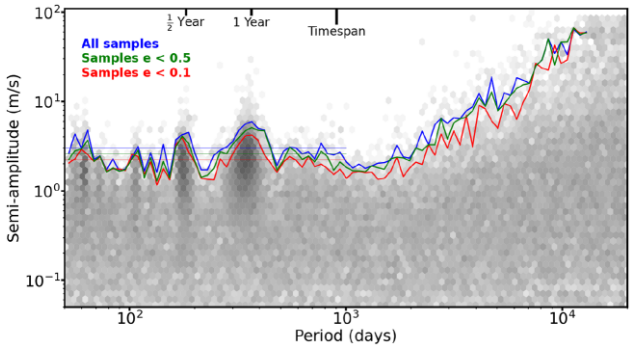

Figure 9. Hexbin plot of posterior samples and blue detection limit for J0310-31 as in Fig. 2. The red and green lines here indicate the same limit calculated from posterior samples with eccentricities <0.1 and <0.5, respectively. Horizontal coloured lines show the mean semi-amplitude of the three coloured detection-limits out to 1000 d.

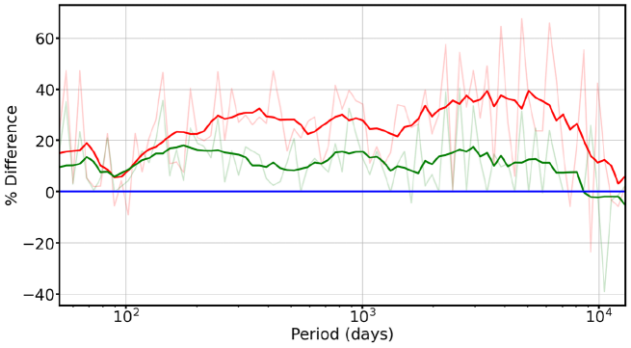

Figure 10. Plot of the percentage difference between detection limits calculated with all posterior samples, and posterior samples with eccentricities <0.1 and <0.5 in red and green, respectively, for J0310-31 from Fig. 9. Solid coloured lines represent a running mean taken on the faded coloured lines.

limits because this removes two dimensions: e_p and ω_p (e.g. Cumming et al. 2008; Zechmeister, Kürster & Endl 2009; Howard et al. 2010; Bonfils et al. 2011; Mayor et al. 2011; Bonfils et al. 2013; Martin et al. 2019; Sabotta et al. 2021).[2] In addition, a short number of discrete planet phases ϕ_p are usually sampled (e.g. 10; Martin et al. 2019 or 12; Zechmeister et al. 2009; Bonfils et al. 2011, 2013).

Commonly when orbits are assumed circular, investigators invoke Endl et al. (2002) as a justification. Endl et al. (2002) investigated the effect of eccentricity on their detection limit for HR 4979, using insertion and recovery. They test five planetary orbital periods P_p, each with *one* corresponding semi-amplitude K_p, and vary e_p over 9 values and ω_p over 4, creating 180 (P_p, K_p, e_p, ω_p) signals.[3] They only test one phase angle ϕ_p. At the time, producing these simulations represented a significant computational effort, however, nowadays this appears as a rather coarse grid. From this exercise, Endl et al. (2002) conclude that eccentricity can affect detection limit calculations, but find that their detection limits assuming $e_p = 0$ are valid for $P_p \gtrapprox 365$ d, so long as the simulated Keplerian has $e_p \lesssim 0.5$. More recently, Cumming & Dragomir (2010) also concluded that assuming circular orbits provides a good agreement with upper semi-amplitude limits for $e_p \lesssim 0.5$ when recovering signals with a periodogram. These particular results have been invoked to justify the assumption of circular orbits ever since.

Interestingly, for $P_p \leq 365$ d (Endl et al. 2002) find their detection limit is only valid if the inserted signal has $e < 0.3$. However, this recommendation has not been followed, and assuming circular orbits for short period is prevalent throughout the literature. From our analysis, we can show how eccentricity affects the detection limit over the entire period range. Our KIMA runs contain >70 000 posterior samples that naturally explore all orbital parameters.

Fig. 9 shows the same detection limit for EBLM J0310-31, as calculated before, in blue using all posterior samples. Alongside, we plot a red detection limit produced in exactly the same way, except using only samples with $e_p < 0.1$, and green with $e_p < 0.5$ (the limit stated by Endl et al. 2002; Cumming & Dragomir 2010). For the three systems explored in this work, the red detection limit is systematically lower, by an average of 24.7 per cent or $\sim 1\,\mathrm{m\,s^{-1}}$ for periods < 1000 d. The green detection limit is also systematically lower by an average of 13.3 per cent or $\sim 0.6\,\mathrm{m\,s^{-1}}$ for the same periods. Fig. 10 demonstrates how the two lower detection limits differ from the original for J0310-31 with period. We note an increase in divergence from the original detection limit at P_p exceeding the timespan of the data (> 1000 d here), to a maximum of 39.9 per cent at ∼4000 d. This maximum difference corresponds to $3.5\,\mathrm{m\,s^{-1}}$ ($\sim 120\,M_\oplus$). Our results are consistent with Wittenmyer et al. (2006) who are able to exclude planets with masses $\gtrsim 2\,M_{Jup}$ by assuming $e_p = 0$, and masses $\gtrsim 4\,M_{Jup}$ if instead they assume $e_p = 0.6$ at a given $P_p \sim 4300$ d, a 50 per cent difference, comparable to our 40 per cent.

Here, we remind the reader that we assume a Kumaraswamy distribution as our prior on e_p, which already favours low e_p, as is seen in observations (Kipping 2013). Even though circumbinary planets discovered thus far are known to have relatively low eccentricities (e < 0.15 Martin 2018), we strongly caution against assuming circular orbits when calculating detection limits in any survey, particularly at long orbital periods. Fixing $e_p = 0$ when calculating detection limits overestimates the success of the programme by a significant amount (up to $120\,M_\oplus$ or $0.4\,M_{Jup}$ in our case).

This exercise demonstrates the superiority of a diffusive nested sampler in establishing robust detection limits, which are crucial to infer the sensitivity of radial-velocity surveys, and consequently, the occurrence rates of exoplanets.

6 CONCLUSIONS

We analyse high-precision radial-velocities obtained as part of a large-scale, ongoing, radial-velocity survey that seeks circumbinary planets using radial velocities obtained with HARPS, ESPRESSO, and SOPHIE, in both hemispheres, on single-lined eclipsing binaries. This survey is called BEBOP (Binaries Escorted By Orbiting Planets). We then detail an observing and Bayesian analysis protocol and test it on data collected for three single-lined binaries within the survey. Our analysis shows for the first time, a repeated ability to detect circumbinary planets with masses between Neptune's and Saturn's, for orbital periods within 1000 d with as few as 25 spectra in the span of a year. Fig. 11 displays a mass versus period plot of the detection limits from this work (blue) along with confirmed exoplanets (grey circles; NASA exoplanet archive[4] Akeson et al. 2013), transiting circumbinary planets (magenta diamonds), and Solar system planets for comparison. This figure demonstrates our

[2]Circularity is assumed for recovery since most use a periodogram. With KIMA, the full Keplerian is used for exploration and recovery.
[3]Strangely, Endl et al. (2002) only mention 110 signals.

[4]https://exoplanetarchive.ipac.caltech.edu/index.html

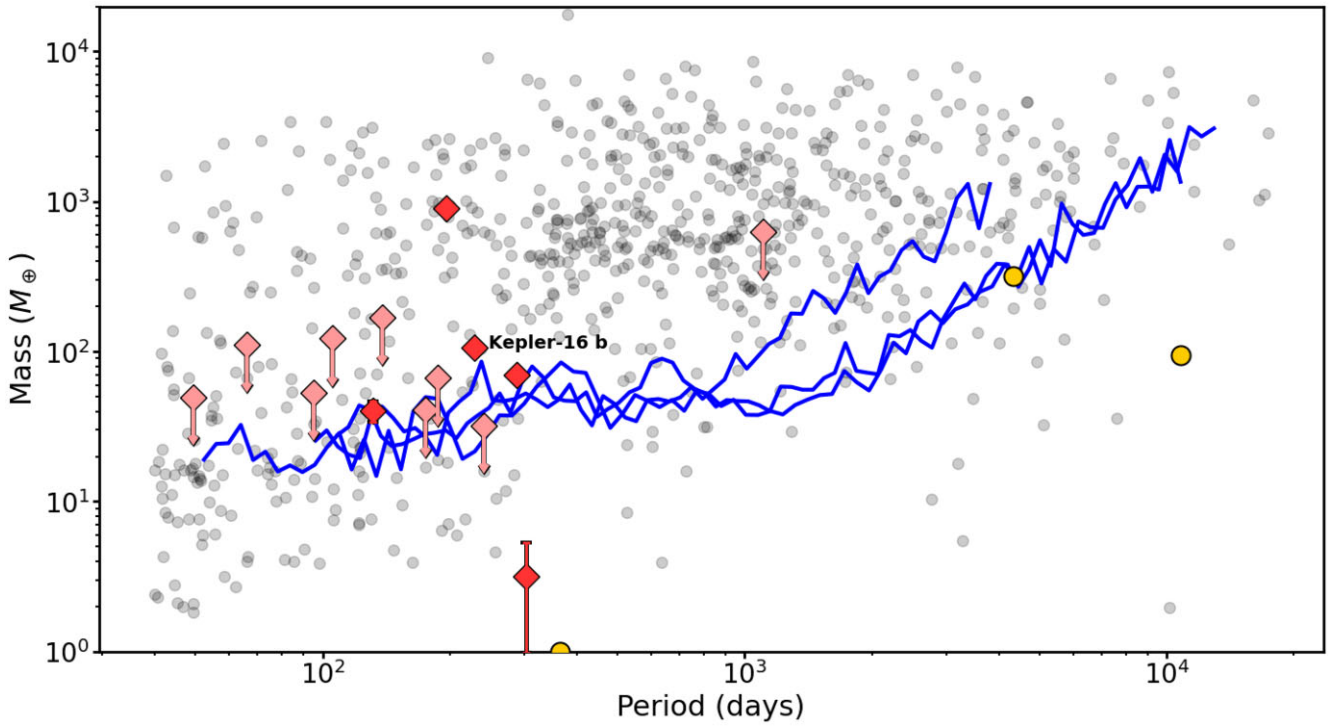

Figure 11. Mass versus period plot showing the three detection limits from this work as blue lines in comparison to confirmed exoplanets as grey circles, and transiting circumbinary planets as pink diamonds. Solar system planets are depicted as yellow dots for reference. Circumbinary planets in order of increasing period; Kepler-47 b, Kepler-413 b, TOI-1338 b, Kepler-38 b, Kepler- 35 b, Kepler-64 b, Kepler-1661 b, Kepler-47 d, TIC-1729 b, Kepler-16 b, Kepler-453 b, Kepler- 34 b, Kepler-47 c, Kepler-1647 b. Arrows illustrate planets with upper mass limits with the symbol placed to give a 2σ upper limit.

ability to detect sub-Saturn mass circumbinary planets at periods up to 1000 d. Our data are able to detect a large fraction of currently known systems. We note though that many circumbinary planet detections made with eclipse timing variations are upper limits only.

We also present a method to compute detection limits on radial-velocity data by using a diffusive nested sampler, without the need to assume circular orbits as is the norm. We then show that this method is superior than the usual injection-recovery tests. Assuming circular orbits when determining detection limits generates overoptimistic detection limits by an average of $\sim 1\,\mathrm{m\,s^{-1}}$ (24.7 per cent) at periods < 1000 d, and up to $120\,\mathrm{M_\oplus}$ at periods > 1000 d. We therefore strongly caution against assuming circular orbits when calculating detection limits, and suggest KIMA as a way for exoplanet surveys in general to extract accurate sensitivity limits and occurrence rates with fewer assumptions.

Thanks to the protocols and tests described in this paper, the BEBOP survey is now ready to produce circumbinary planet candidates following Bayesian evidence, and able to compute occurrence rates that can be compared to those already established from photometric methods (Armstrong et al. 2014; Martin & Triaud 2014). Producing occurrence rates and upper limits on the occurrence of circumbinary planets will be done by simply combining all KIMA produced detection limits.

ACKNOWLEDGEMENTS

We would like to thank the staff at ESO's La Silla observatory for their hard work and assistance throughout this project, especially during the COVID pandemic. We also thank all of the observers who took part in the HARPS timeshare and were instrumental in collecting data for this projects. We particularly thank X. Dumusque and F. Bouchy for their work organizing the timeshare. We would also like to thank our reviewer, Maciej Konacki for his comments which helped improve the manuscript.

This research received funding from the European Research Council (ERC) under the European Union's Horizon 2020 research and innovation programme (grant agreement no. 803193/BEBOP) and from the Leverhulme Trust (research project no. RPG-2018-418). MRS would like to acknowledge the support of the UK Science and Technology Facilities Council (STFC). We thank H. Rein for helpful discussion regarding this work. This work made use of the ASTROPY, NUMPY, PANDAS, SCIPY, CORNER, and MATPLOTLIB packages. We also use of label_line.py by Luke Zoltan Kelley. The French group acknowledges financial support from the French Programme National de Planétologie (PNP, INSU). ACMC acknowledges support by CFisUC projects (UIDB/04564/2020 and UIDP/04564/2020), GRAVITY (PTDC/FIS-AST/7002/2020), ENGAGE SKA (POCI-01-0145-FEDER-022217), and PHOBOS (POCI-01-0145-FEDER-029932), funded by COMPETE 2020 and FCT, Portugal.

DATA AVAILABILITY

The data we used is available for download at the ESO public archive.[5] Search for Prog. ID 099.C-0138 and 1101.C-0721.

REFERENCES

Akeson R. L., 2013, Publications of the Astronomical Society of the Pacific, 125, 989

[5] http://archive.eso.org/eso/eso_archive_main.html

Armstrong D. J., Osborn H. P., Brown D. J. A., Faedi F., Gómez Maqueo Chew Y., Martin D. V., Pollacco D., Udry S., 2014, MNRAS, 444, 1873
Arras P., Burkart J., Quataert E., Weinberg N. N., 2012, MNRAS, 422, 1761
Baranne A. et al., 1996, A&AS, 119, 373
Bonfils X. et al., 2011, A&A, 528, A111
Bonfils X. et al., 2013, A&A, 549, A109
Borucki W. J., Summers A. L., 1984, Icarus, 58, 121
Brewer B. J., 2014, preprint (arXiv:1411.3921)
Brewer B. J., Donovan C. P., 2015, MNRAS, 448, 3206
Brewer B. J., Pártay L. B., Csányi G., 2011, Stat. Comput., 21, 649
Brown A. G. A., 2018, Gaia Data Release 2. Summary of the contents and survey properties, 616, A1
Coffinet A., Lovis C., Dumusque X., Pepe F., 2019, A&A, 629, A27
Correia A. C. M. et al., 2010, A&A, 511, A21
Correia A. C. M., Udry S., Mayor M., Laskar J., Naef D., Pepe F., Queloz D., Santos N. C., 2005, A&A, 440, 751
Couetdic J., Laskar J., Correia A. C. M., Mayor M., Udry S., 2010, A&A, 519, A10
Cumming A., Butler R. P., Marcy G. W., Vogt S. S., Wright J. T., Fischer D. A., 2008, PASP, 120, 531
Cumming A., Dragomir D., 2010, MNRAS, 401, 1029
Doolin S., Blundell K. M., 2011, MNRAS, 418, 2656
Doyle L. R. et al., 2011, Science, 333, 1602
Dvorak R., Froeschle C., Froeschle C., 1989, A&A, 226, 335
Endl M., Kürster M., Els S., Hatzes A. P., Cochran W. D., Dennerl K., Döbereiner S., 2002, A&A, 392, 671
Everhart E., 1985, in Carusi A., Valsecchi G. B., eds, IAU Colloq. 83: Dynamics of Comets: Their Origin and Evolution. An Efficient Integrator that uses Gauss-Radau Spacings, Vol. 115, Reidel, Astrophysics and Space Science Library, p. 185
Faria J. P. et al., 2020, A&A, 635, A13
Faria J. P., Santos N. C., Figueira P., Brewer B. J., 2018, JOSS, 3, 487
Feroz F., Balan S. T., Hobson M. P., 2011, MNRAS, 415, 3462
Foreman-Mackey D., 2016, JOSS, 1, 24
Gregory P. C., 2005, ApJ, 631, 1198
Høg E. et al., 2000, A&A, 355, L27
Holman M. J., Wiegert P. A., 1999, AJ, 117, 621
Howard A. W. et al., 2010, Science, 330, 653
Jeffreys H., 1961, Theory of Probability. Oxford University Press,Oxford
Kass R. E., Raftery A. E., 1995, J. Am. Stat. Assoc., 90, 773
Kipping D. M., 2013, MNRAS, 434, L51
Konacki M., Muterspaugh M. W., Kulkarni S. R., Hełminiak K. G., 2009, ApJ, 704, 513
Konacki M., Muterspaugh M. W., Kulkarni S. R., Hełminiak K. G., 2010, ApJ, 719, 1293
Kostov V. B. et al., 2014, ApJ, 784, 14
Kostov V. B. et al., 2016, ApJ, 827, 86
Kostov V. B. et al., 2020, AJ, 159, 253
Kostov V. B. et al., 2021, ApJ,162,42
Kostov V. B., Mccullough P. R., Hinse T. C., Tsvetanov Z. I., Hébrard G., Díaz R. F., Deleuil M., Valenti J. A., 2013, ApJ, 770, 52
Kumaraswamy P., 1980, JHyd, 46, 79
Lovis C., Pepe F., 2007, A&A, 468, 1115
Mardling R. A., 2013, MNRAS, 435, 2187
Martin D. V. et al., 2019, A&A, 624, A68
Martin D. V., 2017, MNRAS, 465, 3235
Martin D. V., 2018, Populations of Planets in Multiple Star Systems. Springer International Publishing AG, New York, p. 156
Martin D. V., 2019, MNRAS, 488, 3482
Martin D. V., Triaud A. H. M. J., 2014, A&A, 570, A91
Mayor M. et al., 2003, The Messenger, 114, 20
Mayor M. et al., 2009, A&A, 507, 487
Mayor M. et al., 2011, The HARPS search for southern extra-solar planets XXXIV. Occurrence, mass distribution and orbital properties of super-Earths and Neptune-mass planets. preprint (arXiv:1109.2497)
McInnes L., Healy J., Astels S., 2017, JOSS, 2, 205
Munari U. et al., 2014, AJ, 148, 81
Orosz J. A. et al., 2012a, Science, 337, 1511
Orosz J. A. et al., 2012b, ApJ, 758, 87
Orosz J. A. et al., 2019, AJ, 157, 174
Pepe F. et al., 2002a, The Messenger, 110, 9
Pepe F., Mayor M., Galland F., Naef D., Queloz D., Santos N. C., Udry S., Burnet M., 2002b, A&A, 388, 632
Perruchot S. et al., 2008, in McLean I. S., Casali M. M., eds, Proc. SPIE Conf. Ser. Vol. 7014, Ground-Based and Airborne Instrumentation for Astronomy II. SPIE, Bellingham, p. 70140J
Pollacco D. L. et al., 2006, PASP, 118, 1407
Quarles B., Satyal S., Kostov V., Kaib N., Haghighipour N., 2018, ApJ, 856, 150
Queloz D. et al., 2001, A&A, 379, 279
Rein H., Liu S. F., 2012, A&A, 537, A128
Rein H., Spiegel D. S., 2015, MNRAS, 446, 1424
Rosenthal L. J. et al., 2021, APJS, 255, 67
Sabotta S. et al., 2021, A&A, 653, 15
Santos N. C. et al., 2002, A&A, 392, 215
Schneider J., 1994, Planet. Space Sci., 42, 539
Schwamb M. E. et al., 2013, ApJ, 768, 127
Socia Q. J. et al., 2020, AJ, 159, 94
Swayne M. I. et al., 2021, MNRAS, 506, 306
Sybilski P., Konacki M., Kozłowski S. K., Hełminiak K. G., 2013, MNRAS, 431, 2024
Triaud A. H. et al., 2017, A&A, 608, A129
Triaud A. H. M. J. et al., 2013, A&A, 549, A18
Triaud A. H. M. J., 2018, The Rossiter-McLaughlin Effect in Exoplanet Research. Springer International Publishing AG, New York, p. 2
Triaud A. H. M. J., 2022, BEBOP III. Observations and an independent mass measurement of Kepler-16 (AB) b - the first circumbinary planet detected with radial velocities, MNRAS
Trotta R., 2008, Contemp. Phys., 49, 71
Welsh W. F. et al., 2012, Nature, 481, 475
Welsh W. F. et al., 2015, ApJ, 809, 26
Wittenmyer R. A., Endl M., Cochran W. D., Hatzes A. P., Walker G. A. H., Yang S. L. S., Paulson D. B., 2006, AJ, 132, 177
Zechmeister M., Kürster M., Endl M., 2009, A&A, 505, 859
Zucker S., Alexander T., 2007, ApJ, 654, L83

This paper has been typeset from a TEX/LATEX file prepared by the author.

APPENDIX A: INJECTION AND RECOVERY RESULTS AND RADIAL VELOCITY DATA

Here we present the results of our insertion/recovery tests for each of our three target systems in tables A1 to A4, Numbers in the tables are Bayes factors calculated from our `kima` runs. We also present our RV data on the systems in tables A5 to A7.

This paper has been typeset from a TEX/LATEX file prepared by the author.

Table A1. J0310-31 Keplerian insertion and recovery results

Semi-amplitudes	Periods					
	$5.9 \times P_{\rm bin}$ = 74.59d	$12 \times P_{\rm bin}$ = 151.71d	$18 \times P_{\rm bin}$ = 227.57d	$30 \times P_{\rm bin}$ = 379.28d	486.67d	$400 \times P_{\rm bin}$ = 5057.12d
$10 \times$ RMS = 31.6m s^{-1}	-	-	-	-	-	inf
$3 \times$ RMS = 9.48m s^{-1}	-	-	-	inf	-	8.3
$2 \times$ RMS = 6.32m s^{-1}	inf	-	-	-	-	-
$1.5 \times$ RMS = 4.74m s^{-1}	39.7	inf	-	25.7	5946	0.8
$1.25 \times$ RMS = 3.95m s^{-1}	3.2	5860	984.83	-	409.2	-
RMS = 3.16m s^{-1}	-	1070.7	120.6	0.9	44.7	-
$0.75 \times$ RMS = 2.37m s^{-1}	-	63.7	16.4	-	7.6	-
$0.5 \times$ RMS = 1.58m s^{-1}	-	5.8	2.5	-	-	-

Table A2. J0310-31 Rebound simulated N-body insertion and recovery results

Semi-amplitudes	Periods		
	$5.9 \times P_{\rm bin}$ = 74.59d	$12 \times P_{\rm bin}$ = 151.71d	486.67d
$2 \times$ RMS = 6.32m s^{-1}	inf	-	-
$1.5 \times$ RMS = 4.74m s^{-1}	980	inf	1378.8
$1.25 \times$ RMS = 3.95m s^{-1}	60.5	inf	264.5
RMS = 3.16m s^{-1}	5.2	7020	41.5
$0.75 \times$ RMS = 2.37m s^{-1}	-	217.4	7
$0.5 \times$ RMS = 1.58m s^{-1}	-	11.3	-

Table A3. J1540-09 Keplerian insertion and recovery results

Semi-amplitudes	Periods			
	$5.9 \times P_{\rm bin}$ = 155.4d	$12 \times P_{\rm bin}$ = 316.06d	486.67d	999d
$3 \times$ RMS = 11.25m s^{-1}	-	inf	-	-
$2.5 \times$ RMS = 9.38m s^{-1}	-	inf	-	-
$2 \times$ RMS = 7.5m s^{-1}	inf	637.3	inf	inf
$1.5 \times$ RMS = 5.63m s^{-1}	2811.7	14.5	1276.8	291
$1.25 \times$ RMS = 4.69m s^{-1}	464.5	3.6	223.2	29.5
RMS = 3.75m s^{-1}	72.6	-	23.2	3.7
$0.75 \times$ RMS = 2.81m s^{-1}	8.4	-	3.6	-
$0.5 \times$ RMS = 1.88m s^{-1}	1.5	-	0.9	0.7

Table A4. J1928-38 Keplerian insertion and recovery results

Semi-amplitudes	Periods				
	$5.1 \times P_{\rm bin}$ = 118.95d	$5.9 \times P_{\rm bin}$ = 137.61d	$8 \times P_{\rm bin}$ = 186.58d	$12 \times P_{\rm bin}$ = 279.87d	486.67d
$5 \times$ RMS = 14.8m s^{-1}	-	-	-	-	inf
$4 \times$ RMS = 11.84m s^{-1}	-	inf	-	inf	inf
$3 \times$ RMS = 8.88m s^{-1}	2919	1362.6	6413	inf	inf
$2 \times$ RMS = 5.92m s^{-1}	49.8	21	47.8	58.9	138.4
$1.5 \times$ RMS = 4.44m s^{-1}	-	2.4	-	2.9	14.3
$1.25 \times$ RMS = 3.7m s^{-1}	2.3	-	2.9	-	-
RMS = 2.96m s^{-1}	-	-	-	-	2.4

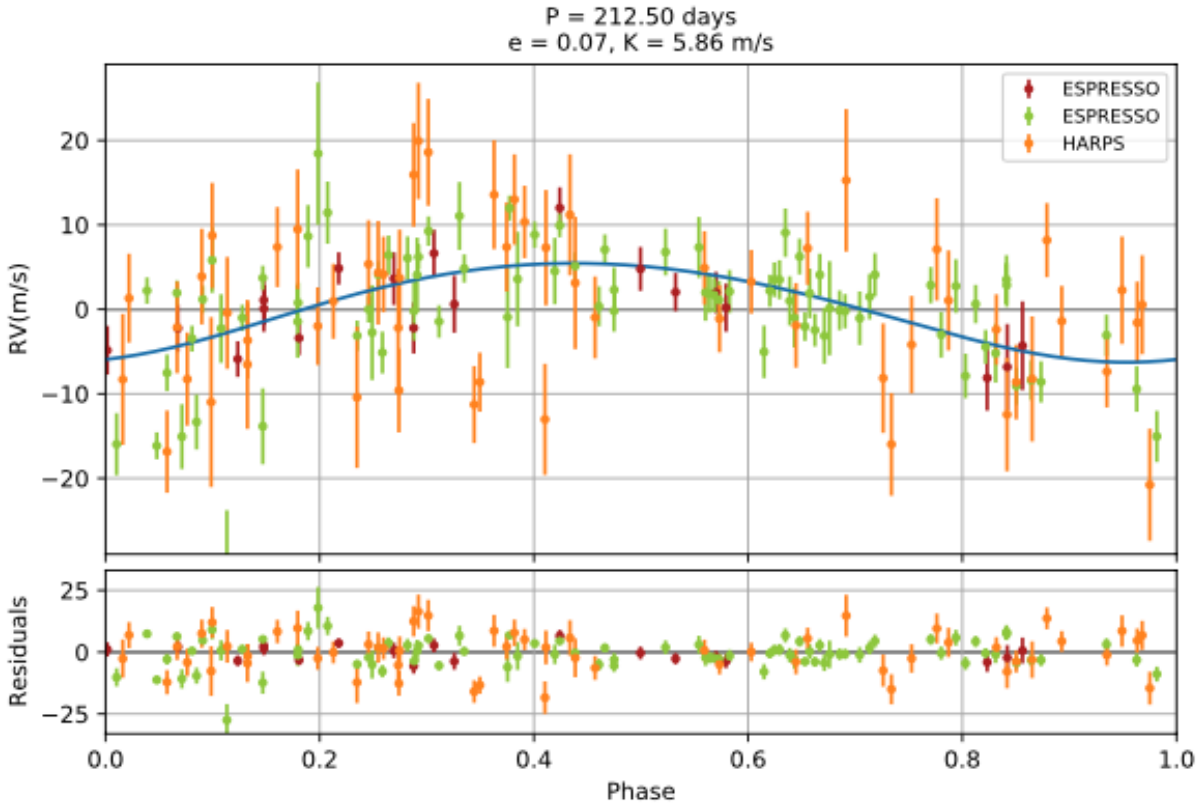

Figure 4.14: Phased Keplerian Radial Velocity (RV) signal calculated from the highest likelihood posterior sample obtained corresponding to a single (N_p = 1) additional Keplerian signal. Above are the exact parameters from the posterior sample used to calculate the model. O-C residuals are plotted below. Orange points show the HARPS data, and the red and green points show ESPRESSO data before and after a calibration lamp change respectively (Faria et al. 2022).

4.3.8 Post-Keplerian effects

The referee report received for Standing et al. (2022) above, suggested that, with the low residual scatter obtained on our SB1 binary targets, our RV values may be sensitive to post-Keplerian effects.

Post-Keplerian effects are those which affect the measured RV signal in a non-Keplerian form. These effects can be long-term (e.g. the orbital precession of the binary orbit), or short term periodic signals (e.g. tidal, light time effects, transverse Doppler, and gravitational redshift) which are described in Kopal (1980a,b); Kopeikin & Ozernoy (1999); Zucker & Alexander (2007); Konacki et al. (2010); Arras et al. (2012); Sybilski et al. (2013).

I calculated the amplitude of post-Keplerian effects on the three binaries in the paper as described in Section 4.3.6 (Section 5.2 of the paper), and found that the amplitude of the effects were below the level of residual RV scatter for these targets and therefore, would not affect the results of this work, with the exception of the gravitational redshift contribution. Sybilski et al. (2013) note that for circular binary orbits, the gravitational redshift and transverse Doppler contributions become constant offsets. These would be absorbed into the systemic velocity fit for the system with `kima` when considering circular binary orbits, and therefore of little consequence, which I confirm. However, this effect must be considered when analysing highly eccentric binary systems. The BEBOP south target sample only contains 5 binary

targets with eccentricities > 0.308 (that of EBLM J0310-31 investigated in Standing et al. (2022)), while the Northern target sample contains 13. Care should be taken when analysing any potential candidate planet signals in these systems.

Tides on the surface of the primary star raised by its proximity to the secondary star also induce a RV signal (Arras et al. 2012). The maximum amplitude of the tidal induced RV signal can be calculated using the following equation adapted from Equation 17 in Arras et al. (2012):

$$v_{\rm tide} \approx 1.13 \ {\rm m\,s^{-1}} \left(\frac{\rm M_p}{\rm M_J}\right) \left(\frac{\rm M_\odot^2}{\rm M(M+M_p)}\right) \times \left(\frac{\rm R}{\rm R_\odot}\right)^4 \left(\frac{\rm 1\ day}{\rm P_{orb}}\right)^3 \tag{4.1}$$

where, $M_{\rm p}$ is the mass of the planet (in our case the secondary star), M is the mass of the primary star, R is the radius of the primary star, and $P_{\rm orb}$ is the binary orbital period. Following Equation 4.1 we can see that there is a heavy dependence on the orbital period on the induced tidal signal. One of the shortest period binary targets in the BEBOP sample is EBLM J1037-25 with a binary orbital period of 4.94 days, and a secondary mass of $\sim$ 0.23 $\rm M_\odot$. Using this target as a worst case scenario, Equation 4.1, gives a maximum tidal RV amplitude of $\sim$ 1.3 $\rm m\,s^{-1}$ (assuming Solar radius). This value is well below the 24.5 $\rm m\,s^{-1}$ RMS scatter on the target. The level of residual scatter for this target is high as the star exhibits stellar activity, though the tidal RV signal may contribute to this scatter. We can therefore conclude that the amplitude for tidally induced RV signals in the BEBOP target list is well below the residual scatter for the entire BEBOP sample (see Figure 4.28).

In Section 4.3.6 (Section 5.2 of the paper), I calculate the effect of binary orbital precession and conclude that as the BEBOP survey continues and the timespan of data increases, binary orbital precession will become the largest non Keplerian signal and will need to be accounted for (see Figure 4.20). Ongoing work to account for this precession within `kima` will be published in Baycroft et al. (in prep) as a direct result of these findings.

When calculating the Post-Keplerian effects for analysis in Section 4.3.6, I found two discrepancies in Sybilski et al. (2013). The first is that the equations for calculating the RV contribution from the gravitational redshift, Equation 8 in Sybilski et al. (2013) and Equation 15 in Konacki et al. (2010), both have an extra factor of 2 within the brackets in the first term when compared to equation 5 in Zucker & Alexander (2007). This seems to be a typographical error shared between Konacki et al. (2010) and Sybilski et al. (2013). Also, the same equations do not contain the periodic $1 + e\cos\nu$ term, instead only multiplying by a factor of e, thus the equations would only return a single value. The correct equation for the radial velocity gravitational redshift contribution is (Zucker & Alexander 2007):

$$\Delta V_{\rm GR} = \frac{K_1(K_1+K_2)}{c\sin^2 i}(1+e\cos\nu) \tag{4.2}$$

where $K_{1,2}$ are the RV semi-amplitudes of the primary and secondary stars respectively, c is the speed of light, i the system's inclination, e the binary orbital eccentricity, and ν the time-dependent true anomaly.

The second discrepancy is that in Sybilski et al. (2013), the light-time effect is calculated using Equation 6 in their paper. This is the same as Equation 12 in Konacki et al. (2010), which both contain a $\sin^2$ term acting on the periodic variation of the signal. Despite this, Sybilski et al. (2013) show that their light-time effect periodically changes to negative velocity in plots a, and b in Figure 4 of that paper. To reproduce the same shape, one must only neglect to square the sin term from the light-time effect equations. I believe this was forgotten during calculation of the light-time effect contributions plotted in their Figure 4. The equation from Sybilski et al. (2013) and Konacki et al. (2010) is correct and as follows (Zucker & Alexander 2007):

$$\Delta V_{\rm LT} = \frac{{K_1}^2}{c} \sin^2(\nu + \omega)(1 + e\cos\nu) \tag{4.3}$$

where ω_1 is the argument of periastron, and the other parameters are as described in Equation 4.2. When attempting to re-create Figure 4a from Sybilski et al. (2013) using Equation 4.3, Figure 4.26 is obtained. Figure 4.26 a), shows the plot from Sybilski et al. (2013) calculated with the following stated values; $M_1 = 1\ M_\odot$, $M_2 = 0.5\ M_\odot$, $\omega = 108°$, inclination= 29°, $P_{\rm bin} = 5$ days, and $e = 0$. Whereas, Figure 4.26 b) shows the resulting signal calculated using the same parameters with Equation 4.3. We can clearly see that the shape of the light time effect signal is different, does not reach negative values, and is out of phase with plot a). The amplitude of the signal is also far greater than in plot a). Figure 4.26 c) shows an attempt at recreating the signal shown in plot a) (Sybilski et al. 2013). In order to recreate the signals, one must neglect to square the sin term in Equation 4.3, and change the stated value for ω to 18°. The shape of the signal then matches that in plot a). Though I was unable to recreate the signal amplitude in plot a), indicating that there are other discrepancies between the signals plotted in plot a) and the text in Sybilski et al. (2013).

4.3.9 Detection limits for the entire BEBOP south survey

To calculate detection limits for the entire BEBOP survey, targets with greater than 15 total observations are selected. Greater than 15 observations are needed to ensure that the binary orbital parameters can be fit, in addition to additional circumbinary planet signals required to calculate the detection limits. Since the southern survey is more established than the northern survey, only southern targets are chosen using data from CORALIE and HARPS. 65 targets satisfy these criterion and these are analysed in this section. Calculating detection limits as in Standing et al. (2022) (Section 4.3), for these 65 southern BEBOP targets yields Figure 4.27. The plot demonstrates BEBOP's repeated ability to detect circumbinary planets with masses greater than a single Jupiter mass, with periods less than roughly half a year. The orange detection limit is that of target EBLM J0608-59 (TOI-1338/BEBOP-1). We can see that it is one of the lowest limits calculated in part due to the 123 ESPRESSO observations obtained on the target (Chapter 6). The green point corresponds to the only detection of a circumbinary planet claimed by BEBOP at this point in time, TOI-1338/BEBOP-1c, see Chapter 6 for further details. The red line is the detection limit calculated for the same target, BEBOP-1, using only HARPS observations, plotted to allow for a fairer comparison to the other limits.

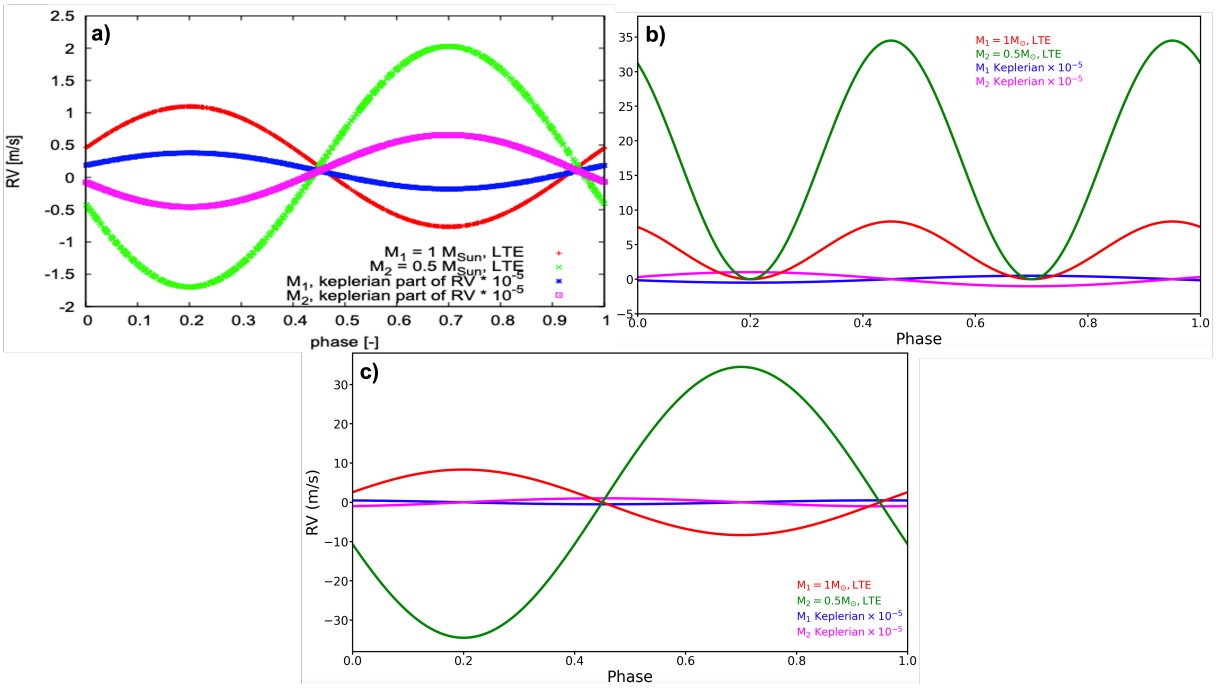

Figure 4.26: a) Plot from Sybilski et al. (2013) showing the light-time effect for the primary star in red, and secondary star in green. Also plotted are the Keplerian RV signals for the primary and secondary stars $\times 10^{-5}$ in blue and magenta respectively. Orbital values for the system are as follows; $M_1 = 1\ M_\odot$, $M_2 = 0.5\ M_\odot$, $\omega = 108°$, inclination= 29°, $P_{bin} = 5$ days, and $e = 0$ (Sybilski et al. 2013). b) The same curves calculated using Equation 4.3 and the above values. c) The same signals calculated using Equation 4.3 without squaring the sin term, and using the above values except with $\omega = 18°$.

The side histogram is calculated from each of the detection limits. The median of these points yields a median semi-amplitude signal of 12.9 m s^{-1} for the primary sample, lower than the signal Jupiter would impart on the Sun with an orbital period less than 1000 days (20.3 m s^{-1}). The secondary sample has a median detection limit at 32.6 m s^{-1}, close to the semi-amplitude signal Jupiter would impart on the Sun with an orbit shorter than a year (28.4 m s^{-1}).

From this analysis we also obtain the level of residual Root Mean Squared (RMS) scatter of our RV data, after having removed the binary signals from each target. The distribution of this scatter can be seen in Figure 4.28. We note that our primary sample has a median RMS approximately 7 m s^{-1} lower than those obtained by the TATOOINE sample (Konacki et al. 2009), whereas our secondary sample has a median scatter around 10 m s^{-1} higher. Here we have values for 43 primary targets, and 23 secondary, where the TATOOINE sample consisted of only 10 targets.

The detection limits demonstrate our ability to probe for lower mass planets around these binaries. For the majority of our targets we are sensitive to Saturn mass planets, and for our best targets we are sensitive to Neptune mass planets at orbital periods less than a year. These results confirm the conclusions in Standing et al. (2022).

After calculating detection limits for the 65 southern survey targets, it becomes possible to calculate the completeness of the southern survey, and in turn the abundance of circumbinary planets. To do this the workflow in Martin et al. (2019) is followed, where the completeness of the survey is defined as the

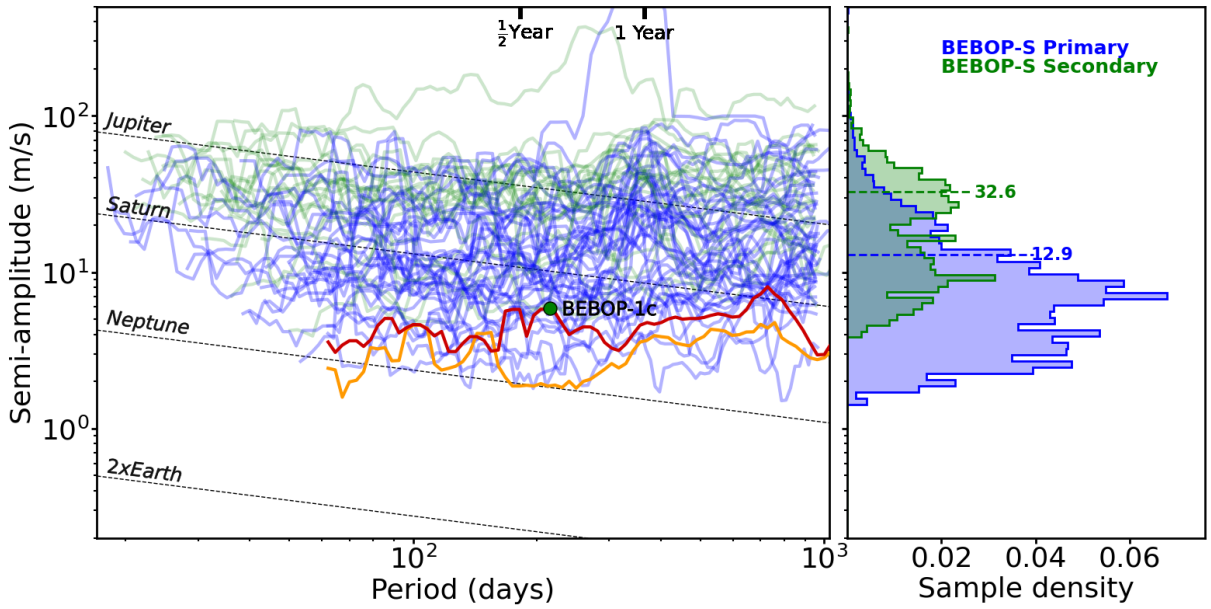

Figure 4.27: Left: detection limits for BEBOP South targets. Blue lines represent the detection limits of the primary BEBOP sample, while the green lines indicate the detection limits of the secondary sample. The orange line illustrates BEBOP-1's detection limit with both HARPS and ESPRESSO data (Chapter 6), along with the green point indicating the detected circumbinary planet BEBOP-1c (Chapter 6). The red line is BEBOP-1's detection limit calculated using only the observations obtained by the HARPS spectrograph as a fairer comparison to the other limits. Right: histogram of detection limits from the left plot for the BEBOP South primary (blue) and secondary (green) targets. Median values of the primary and secondary samples are indicated by the blue and green dashed lines respectively.

fraction of targets for which a planet with a certain mass and period is detectable. This is calculated from the detection limits in Figure 4.27, where below the limit a planet in that system is determined to be undetectable, and above detectable. Converting the detection limits from semi-amplitude into planetary mass, and sorting the detection limits in increasing order in each period bin, allows for the completeness as a function of planetary mass and orbital period to be calculated.

Completeness for the BEBOP south sample can be seen as the red shaded region in Figure 4.29. Dark red corresponds to a completeness of 100%, indicating that in all 65 targets, a planet at this mass and orbital period is able to be detected. This continues to lower completeness values, until the white area is reached, which corresponds to 0% completeness. 0% completeness means that none of the 65 datasets are currently able to detect circumbinary planets at this location in parameter space. We are limited at short orbital periods due to the binary instability region (Section 1.4, Holman & Wiegert (1999)). The detection limit calculations were purposely limited to < 1000 days in this test to save computation time.

Following the calculation of completeness, it becomes possible to calculate the abundance of circumbinary planets. Following the process in Martin et al. (2019) and He et al. (2017), we are able to calculate an upper limit on the abundance of circumbinary planets in regions of parameter space where we are unable to claim any detections. With only a single detection in our data (BEBOP-1c, Chapter 6), the majority of the abundances calculated here are only upper limits.

The abundance upper limit is calculated using the following equation (Martin et al. 2019):

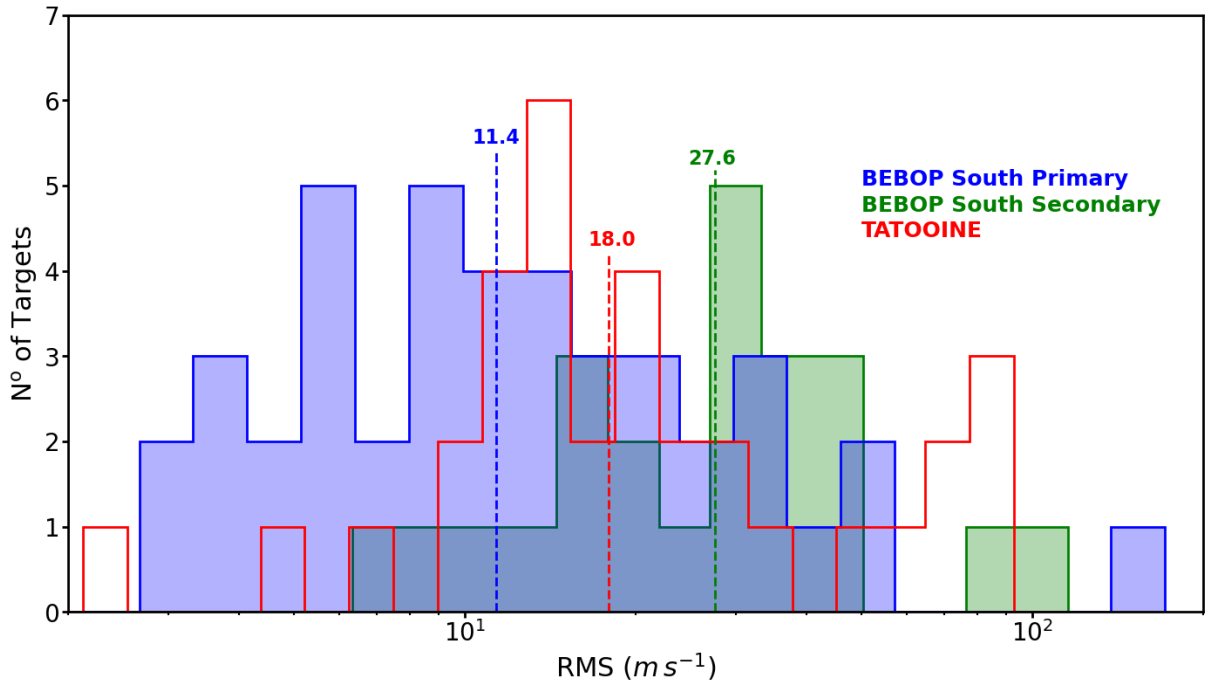

Figure 4.28: Histogram of HARPS residual Root Mean Squared (RMS) scatter after removing the binary signal for the 65 Southern targets for which detection limits were calculated. Blue and green colours represent BEBOP's southern primary (42 targets) and secondary (23 targets) sample respectively. The red histogram represents the RMS values for the primary and secondary stars for each of their SB2 binary targets from each individual instrument from the TATOOINE survey Konacki et al. (2009). Median values for each sample are indicated by the dotted lines in their respective colours.

$$\mathcal{N}_{\rm CBP} = \frac{1-(1-\kappa)^{1/n_{\rm stars}}}{C(P_{\rm c}, m_{\rm c}\sin i_{\rm c})} \tag{4.4}$$

where $\mathcal{N}_{\rm CBP}$ is the upper limit on the number of circumbinary planets, κ is the confidence interval (i.e, for a 2σ, 95% confidence interval $\kappa = 0.95$. All following upper limits on occurrence rates are calculated with a 95% confidence limit), $n_{\rm stars} = 65$ (the number of binary targets used to calculate the survey completeness), and $C(P_{\rm c}, m_{\rm c}\sin i_{\rm c})$ is the average completeness value within the desired region of parameter space.

The white boxes in Figure 4.29 indicate the regions in planetary mass and orbital period for which the abundance of circumbinary planets was calculated. The bounds of these boxes are chosen to be roughly equally spaced in log space, as in Martin et al. (2019). In orbital period the bounds are 37.2, 186.2, and 941.8 days. In planetary mass the bounds are 52.5, 158.9, 476.7, 1430.1, and 4290.3 $M_\oplus$. Just as in Martin et al. (2019) the completeness $C(P_{\rm c}, m_{\rm c}\sin i_{\rm c})$ is taken as the mean value within a particular box (values in the lower right of each box in Figure 4.29), the 2σ upper limit on the completeness is calculated using Equation 4.4, and shown as the white values in the centre of each box in Figure 4.29.

In the lower right box we have our only detection of a circumbinary planet in our southern sample, BEBOP-1c (Chapter 6). Having a detection in the region allows us to calculate the abundance as in Mayor et al. (2011). This is calculated using the following equation (Martin et al. 2019):

$$\mathcal{N}_{\rm CBP} = \frac{1}{n_{\rm stars}} \sum_{i=1}^{n_{\rm det}} \frac{1}{C(P_{\rm c}, m_{\rm c} \sin i_{\rm c})} \tag{4.5}$$

where $n_{\rm det} = 1$ the number of circumbinary planet detections in the region, the other parameters are the same as in Equation 4.4. To calculate the 1σ uncertainty on the abundance, we utilise Poisson statistics using the following equation (Martin et al. 2019):

$$\sigma = 2\frac{\mathcal{N}_{\rm CBP}}{\sqrt{n_{\rm det}}} \tag{4.6}$$

The abundance of circumbinary planets with masses from 52.5 to 158.9 $M_\oplus$, and periods between 186.2 and 941.8 days is therefore $8.9^{+17.9}_{-7.4}$%. Equation 4.7 yields a 1σ uncertainty of ±17.9% for the abundance in this region. However, since there is a single detection in the region, it would not be physical for the lower limit to reach 0%. Therefore, we use a value of $1/65 = 1.5$% signifying a single detection in our sample of 65 systems.

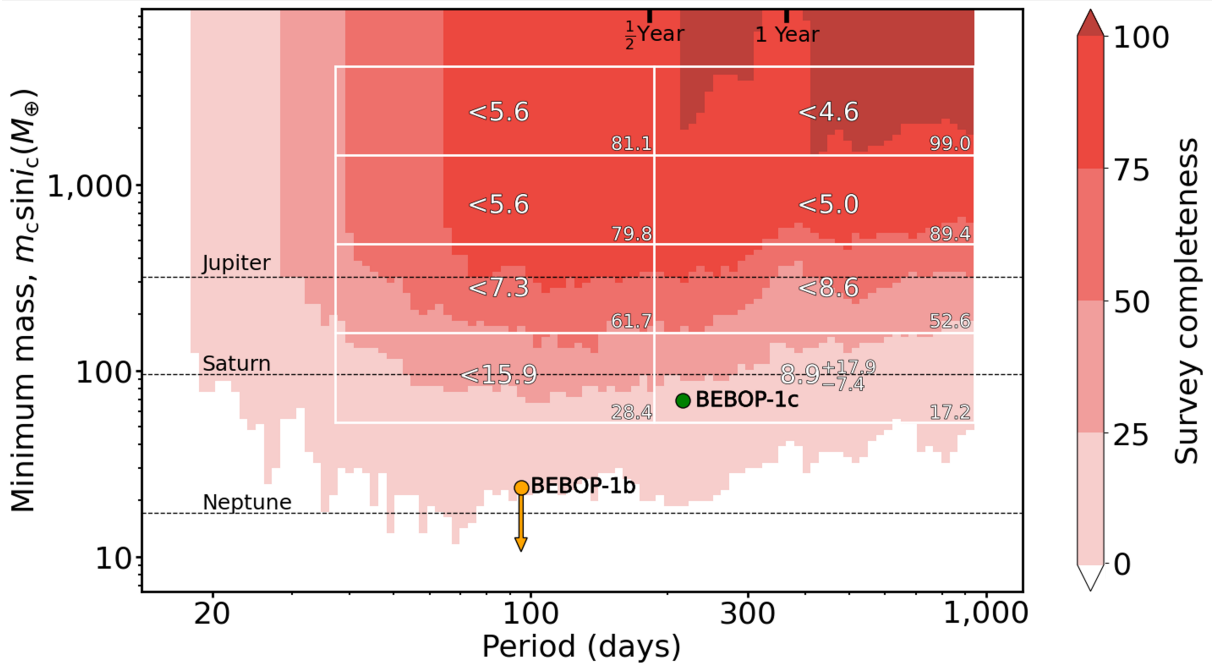

Figure 4.29: Current completeness for the BEBOP south survey consisting of 65 binary targets in planetary mass vs orbital period. The red contours illustrate the completeness of the survey from 0% (white) to 100% (dark red) as in Figure 10 in Martin et al. (2019). The white boxes show the regions in parameter space for which we calculate the abundance of circumbinary planets. The white number in the centre of each box corresponds to the 2σ (95%) upper limit on the abundance, except for the box containing a planetary detection of BEBOP-1c, shown in green (Chapter 6), where the value is the abundance along with its 1σ uncertainty. The white values in the lower right corner of each box is the mean completeness within that particular box. All white values are percentages. The upper limit on the mass for BEBOP-1b is also shown as the orange point with the arrow (Chapter 6).

We can also calculate the probability of finding a planet with a certain mass and period in our current data as described in Martin et al. (2019) with the following equation:

$$D = \xi^{n_{\rm stars} C(P_{\rm c}, m_{\rm c} \sin i_{\rm c})} \tag{4.7}$$

where ξ is chance of a gas giant planet existing around a binary (ξ = 0.1, 10% Martin & Triaud (2014); Armstrong et al. (2014)). Therefore, the probability that we would have detected a circumbinary planet such as Kepler-64 or Kepler-38, which lie in the lower left box in Figure 4.29, is 85.7%.

Armstrong et al. (2014) estimate that $10^{+18}_{-6.5}$% of close binaries have co-planar circumbinary gas giants ($6-10$ $R_\oplus$) with orbital periods between $50-300$ days. To compare our abundance limits with the values in Armstrong et al. (2014), we must first convert their radius limits into Earth masses to be compatible with our completeness values. To do this we assume a planetary density of $\rho_J = 1.33$ g cm^{-3} as in Martin et al. (2019). The > 10 $R_\oplus$ bin in Armstrong et al. (2014) then becomes > 241.5 $M_\oplus$(> 0.76 M_J), taking an upper limit on this mass bin at 13.5 M_J as in Martin et al. (2019), considers only planetary mass objects in the mass range $241.5 - 4290.3$ $M_\oplus$. We are also able to compare our abundance to the $8-10$ $R_\oplus$ bin in Armstrong et al. (2014). Using the same density assumption, we convert this bin into a mass range of $123.9 - 241.5$ $M_\oplus$($0.39 - 0.76$ M_J).

Calculating completeness values for these two regions, and upper limits on abundances with Equation 4.4, yields upper limits on circumbinary planet abundance rates seen in the first table in Table 4.8, where we find that they are in agreement.

The SPOTS survey (Thalmann et al. 2014) was able to place an upper limit on circumbinary planet abundance for orbital distances between $1-300$ AU as seen in the second table in Table 4.8 (Asensio-Torres et al. 2018). Converting $1-300$ AU into orbital period with Equation 1.6, gives $1-5196.2$ years. BEBOP is limited in period sensitivity by our observation timespan, and our completeness was only calculated out to 941.8 days. However, calculating an upper limit in our abundance for the same mass range gives the values seen in the second table in Table 4.8. This is in agreement with the limit imposed by the SPOTS survey (Asensio-Torres et al. 2018) considering that their period range is far larger than our current observational sensitivity.

We are also able to compare our circumbinary gas giant occurrence rates to those around single stars such as described in Cumming et al. (2008), and Wittenmyer et al. (2020). Cumming et al. (2008) calculate an occurrence rate for gas giant planets with an orbital period < 1900 days seen in the third table in Table 4.8. Our upper limit on abundance in the same mass region is slightly lower than that from Cumming et al. (2008) though our bin only extends out to roughly half their orbital period range (third table in Table 4.8).

Wittenmyer et al. (2020) also calculate occurrence rates for gas giant planets around single stars in the three period regions seen in the fourth table in Table 4.8. They do not state the exact upper mass limit that they use to calculate these values, however we take the upper limit as 13.5 M_J. Our upper limits on abundances in these ranges appear to be more optimistic for gas giant circumbinary planets at shorter orbital periods ($30-100$ days) when compared to their occurrence rates around single stars in Wittenmyer et al. (2020), though still in agreement. Our upper limits also agree with the Wittenmyer et al. (2020) rates for the two longer orbital period bins (fourth table in Table 4.8).

In conclusion, while we are sensitive to Jovian circumbinary planets such as Kepler-1647, or TIC-1729 (Table 1.1), we do not detect any in this sample of 65 binary targets. The implication is that they

Table 4.8: Occurrence rates for circumbinary planets calculated in Armstrong et al. (2014), and the SPOTS survey (Asensio-Torres et al. 2018), compared to this work in the upper two tables. Occurrence rates of gas giant planets orbiting single stars calculated in Cumming et al. (2008), and Wittenmyer et al. (2020), compared to this work in the lower two tables. All occurrence rates below are calculated at with a 95% confidence limit.

Comparison between circumbinary planet occurrence rates:

P (days)	M (M_J)	Armstrong et al. (2014)	BEBOP
50 – 300	0.76 – 13.5	$0.0^{+5.9}$%	< 5.3%
50 – 300	0.39 – 0.76	$6.4^{+19.7}_{-2.5}$%	< 9.2%

P (years)	M (M_J)	SPOTS	BEBOP
1 – 5196.2	2 – 15	< 10.5%	-
1 – 2.6	2 – 15	-	< 4.7%

Comparison to occurrence rates of gas giants from single stars:

P (days)	M (M_J)	Cumming et al. (2008)	BEBOP
< 1900*d*	0.3 – 15	8.5 ± 1.3%	-
20 – 941.8	0.3 – 15	-	< 7%

P (days)	M (M_J)	Wittenmyer et al. (2020)	BEBOP
30 – 100	0.3 – 13.5	$0.0^{+1.2}$%	< 7.8%
100 – 300	0.3 – 13.5	$1.7^{+1.9}_{-0.7}$%	< 5.6%
300 – 1000	0.3 – 13.5	$8.0^{+3.7}_{-2.2}$%	< 6.4%

are uncommon, and are in fact difficult to form in nature. Our abundance calculations agree with those of Armstrong et al. (2014) and the SPOTS survey Asensio-Torres et al. (2018) for circumbinary planets, and also agrees with the occurrence rates of gas giants around single stars from Cumming et al. (2008) and Wittenmyer et al. (2020). With observations in the BEBOP survey ongoing in both hemispheres, a more robust limit on the lack of Jovian circumbinary planets out to longer orbital periods and more adequate comparisons with single star occurrence rates will be available soon.

4.4 Candidate circumbinary planet signals

At this stage of the BEBOP observing campaign, with approximately 25-30 observations on each binary target, candidate circumbinary signals begin to emerge from the data. Many still have Bayes Factors far below the 150 threshold in order to claim a detection. I have seen many promising candidates appear (with low Bayes Factors), only to promptly disappear following further observations. Currently, our most promising target other than EBLM J0608-59 (BEBOP-1, Chapter 6), is EBLM J1250+26 in our northern survey. The target itself consists of a 1.02 $M_\odot$ primary star (Stassun et al. 2018), and a 0.363 ± 0.027 $M_\odot$ secondary star on a 72 day period orbit. The candidate signal in question is in fact a 14.9 ± 1.0 M_J circumbinary brown dwarf with a 1384 ± 59 day orbital period on an eccentric $e = 0.35 \pm 0.02$ orbit. Its semi-amplitude signal K= 234.9 ± 6.3 m.s^{-1} can be seen in Figure 4.30. With our current 29 observations we achieve a Root Mean Squared (RMS) scatter on the residuals, after having removed the binary signal,

of ≈ 120.2 m.s^{-1}, which lowers to 5.9 m.s^{-1} after removing the brown dwarf signal. Currently, the Bayes Factor in favour of the additional Brown dwarf signal is $> 10,000$, though additional observations are required to complete the candidate's orbit to ensure a repeating signal.

In addition to this candidate circumbinary brown dwarf, we also have a few promising candidate circumbinary planet signals in our data. The candidate planet with the highest statistical evidence so far is in the EBLM J2359+44 binary system. J2359+44 consists of a 1.373 $M_\odot$ primary star (Stassun et al. 2018), and a 0.310 ± 0.032 $M_\odot$ secondary star on an eccentric $e = 0.48$, 11 day period orbit. The candidate signal has a Bayes Factor of 9.6, far below the required 150 to claim a detection, but large enough to stand out in our sample, and close to the "moderate" evidence strength from the Jeffreys' scale (Trotta 2008). Figure 4.31 shows the candidate circumbinary signal. It has an orbital period of 66.6 ± 0.8 days, a semi-amplitude of 17.3 ± 4.8 m.s^{-1}, and $M \sin i = 0.48 \pm 0.14$ M_J. We currently have 45 observations on this target, with a high RMS scatter of 18.4 m.s^{-1} after removing only the binary. The scatter decreases to 14.1 m.s^{-1} after removing the candidate signal, and explains the low evidence in favour of the planetary signal despite having 45 observations on the target. Our hope is that further observations increase the statistical evidence to the point where we will be able to claim a detection for this candidate within the next year.

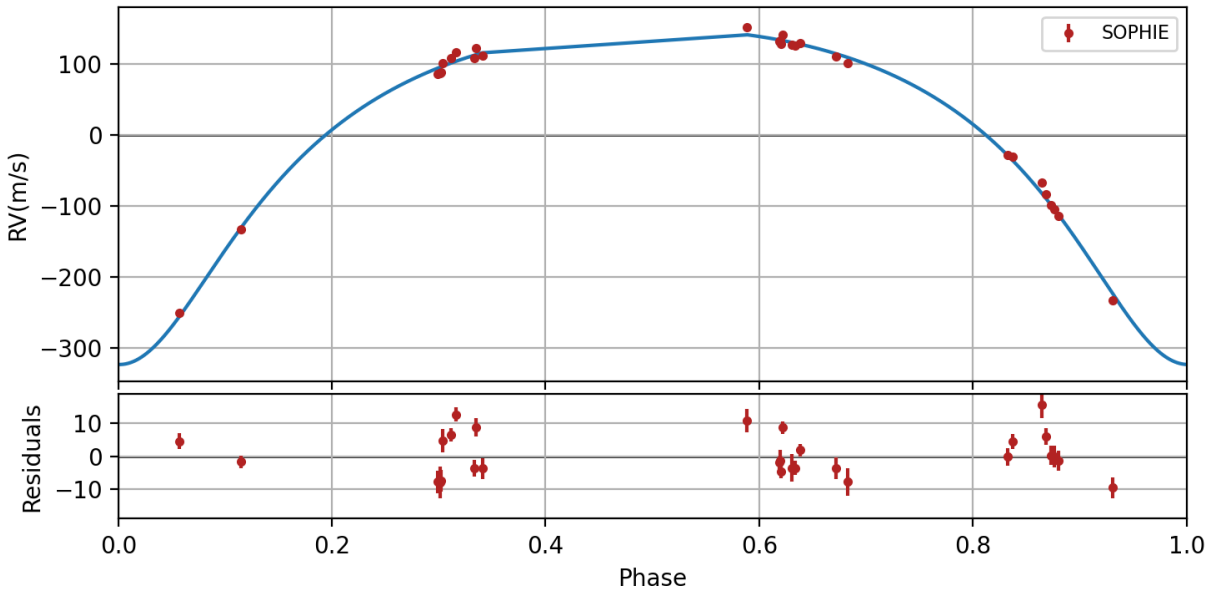

Figure 4.30: Phased Keplerian Radial Velocity (RV) signal calculated from the highest likelihood posterior sample obtained corresponding to an additional candidate brown dwarf signal to the binary EBLM J1250+26. The incomplete orbit is illustrated by the straight line from phase 0.35-0.6. O-C residuals are plotted below. All data was obtained with the SOPHIE spectrograph (Mayor et al. 2003).

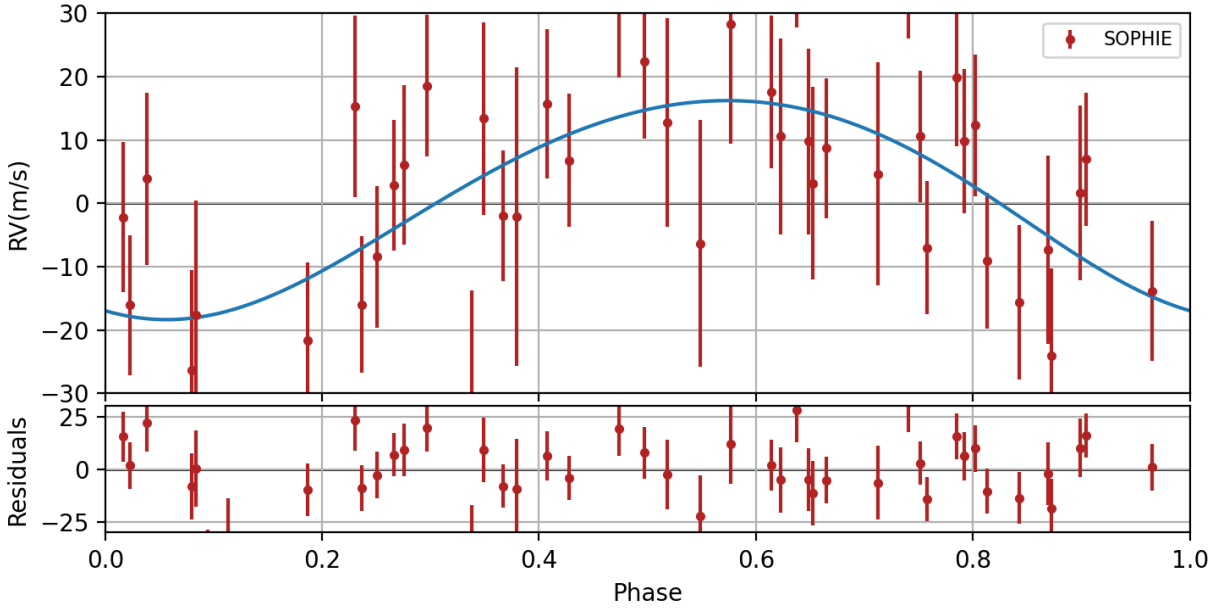

Figure 4.31: Phased Keplerian Radial Velocity (RV) signal calculated from the highest likelihood posterior sample obtained corresponding to an additional candidate circumbinary planet signal to the binary EBLM J2359+44. O-C residuals are plotted below. All data was obtained with the SOPHIE spectrograph (Mayor et al. 2003).

Chapter 5

BEBOP III. Observations and an independent mass measurement of Kepler-16 (AB) b – the first circumbinary planet detected with radial velocities

"Do. Or do not. There is no try."

Yoda, *Star Wars: The Empire Strikes Back*

5.1 My contribution to the paper

Kepler-16 is the brightest of the transiting circumbinary planet hosts discovered with *Kepler* (Doyle et al. 2011). It is also a single line eclipsing binary target, and therefore the most suitable RV target available for the BEBOP survey to use as a proof of concept target (see Section 4.2).

In each of the seven observing runs I have carried out at the OHP in France, I have observed Kepler-16. In total, BEBOP has obtained 143 observations on the target with the SOPHIE spectrograph (Perruchot et al. 2008). I have been closely involved with the RV analysis of these Kepler-16 data throughout my PhD.

For the paper below, I identified outliers in the data as described in Section 4.2.3 and 5.4. I performed a `kima` analysis similarly to that done in Standing et al. (2022) (Section 4.3), providing an independent detection of the circumbinary planet Kepler-16b, as detailed in Section 5.4. Planetary parameters obtained from my analysis can be found in Table 5.1. I also calculated detection limits for the system as in Standing et al. (2022) (Section 4.3), to place constraints on the presence of any additional planetary signals that may be present in our data (see Section 5.4, and Figure 5.3). Finally, I investigated the number of RV

observations required to detect this circumbinary planet by taking subsets of the available data (both subsequently and randomly). Section 5.5 discusses this analysis, with my results plotted in Figure 5.4.

The complete analysis of our BEBOP data on circumbinary planet host Kepler-16 can be found in the paper below, Triaud et al. (2022).

Monthly Notices of the ROYAL ASTRONOMICAL SOCIETY

MNRAS 511, 3561–3570 (2022)
Advance Access publication 2022 February 25

https://doi.org/10.1093/mnras/stab3712

BEBOP III. Observations and an independent mass measurement of Kepler-16 (AB) b – the first circumbinary planet detected with radial velocities

Amaury H.M.J. Triaud [1]★† Matthew R. Standing,[1] Neda Heidari,[2,3,4] David V. Martin [5]‡ Isabelle Boisse,[2] Alexandre Santerne [2] Alexandre C. M. Correia [6,7] Lorena Acuña,[2] Matthew Battley [8,9] Xavier Bonfils,[10] Andrés Carmona,[10] Andrew Collier Cameron [11] Pía Cortés-Zuleta,[2] Georgina Dransfield [1] Shweta Dalal,[12] Magali Deleuil,[2] Xavier Delfosse,[10] João Faria,[13,14] Thierry Forveille,[10] Nathan C. Hara,[15] Guillaume Hébrard,[12] Sergio Hoyer [2] Flavien Kiefer,[12] Vedad Kunovac [1] Pierre F. L. Maxted [16] Eder Martioli [12,17] Nicola J. Miller [16] Richard P. Nelson,[18] Mathilde Poveda,[19,20] Hanno Rein [21] Lalitha Sairam [1] Stéphane Udry[15] and Emma Willett[1]

Affiliations are listed at the end of the paper

Accepted 2021 December 14. Received 2021 December 13; in original form 2021 November 8

ABSTRACT

The radial velocity method is amongst the most robust and most established means of detecting exoplanets. Yet, it has so far failed to detect circumbinary planets despite their relatively high occurrence rates. Here, we report velocimetric measurements of Kepler-16A, obtained with the SOPHIE spectrograph, at the Observatoire de Haute-Provence's 193cm telescope, collected during the BEBOP survey for circumbinary planets. Our measurements mark the first radial velocity detection of a circumbinary planet, independently determining the mass of Kepler-16 (AB) b to be $0.313 \pm 0.039\,M_{Jup}$, a value in agreement with eclipse timing variations. Our observations demonstrate the capability to achieve photon-noise precision and accuracy on single-lined binaries, with our final precision reaching $1.5\,m\,s^{-1}$ on the binary and planetary signals. Our analysis paves the way for more circumbinary planet detections using radial velocities which will increase the relatively small sample of currently known systems to statistically relevant numbers, using a method that also provides weaker detection biases. Our data also contain a long-term radial velocity signal, which we associate with the magnetic cycle of the primary star.

Key words: techniques: radial velocities – planets and satellites: detection – planets and satellites: individual: Kepler-16 – binaries: eclipsing – binaries: spectroscopic.

1 INTRODUCTION

Circumbinary planets are planets that orbit around both stars of a binary star system. Long postulated (Borucki & Summers 1984; Schneider 1994), the first unambiguous discovery of a circumbinary planet came with Kepler-16 (Doyle et al. 2011), detected by identifying three transits within the light curve of an eclipsing binary system monitored by NASA's *Kepler* mission (Borucki et al. 2011). *Kepler* went on to detect another 13 transiting circumbinary planets in 11 systems (Martin 2018; Socia et al. 2020), with another two systems found using *TESS* (Kostov et al. 2020, 2021). A number of circumbinary planets systems are suspected from eclipse timing variations of binaries on the main sequence (e.g. Borkovits et al. 2016; Getley et al. 2017), and stellar remnants (e.g. Marsh et al. 2013; Han et al. 2017) but most are disputed (e.g. Mustill et al. 2013), and some disproven (e.g. Hardy et al. 2015). Other detections include HD 106906 b, in direct imaging (Bailey et al. 2014) and OGLE-2007-BLG-349L(AB)c with the microlensing method (Bennett et al. 2016).

Despite successes with almost every observational methods, no circumbinary planet signal has been detected using radial velocities yet. In addition, radial velocities have detected many planets with masses compatible with currently known circumbinary planets. This is remarkable since radial velocities are one of the earliest, most established and efficient method of exoplanet detection. The system closest to a circumbinary configuration identified thus far is HD 202206 (Correia et al. 2005; see Section 4).

The radial velocity method has a number of advantages over the transit method. First, it is less restrictive in term of the planet's orbital inclination thus providing a weaker bias towards short orbital periods. Furthermore, the signal can be obtained at every orbital phase, and the method is more cost-effective and easier to use over a longer term thanks to using ground-based telescopes (Martin et al. 2019). Additionally, radial velocities provide the planet's mass, its most fundamental parameter. While the transit method can provide a

* E-mail [redacted]
† Based on observations collected at the Observatoire de Haute-Provence (CNRS, France).
‡ NASA Sagan Fellow.

mass when eclipse timing variations are detected, most circumbinary exoplanets unfortunately remain without a robust mass determination with eclipse timing variations mostly providing upper limits (e.g. Orosz et al. 2012; Schwamb et al. 2013; Kostov et al. 2020). Only four of the known circumbinary planets have eclipse-timing mass estimates inconsistent with 0 at $>3\sigma$. The present and future *TESS* and *PLATO* missions (Rauer et al. 2014; Ricker et al. 2014) are set to identify several more transiting circumbinary planet candidates (e.g. Kostov et al. 2020, 2021). However, these are unlikely to produce many reliable mass measurements, in good part due to rather short observational time-spans compared to *Kepler*'s.

Overall, radial velocities are essential to create a sample of circumbinary planets that is both greater in number and less biased than the transit sample. This will allow a deeper understanding of circumbinary planets: their occurrence rate (Martin & Triaud 2014), multiplicity (Orosz et al. 2019; Sutherland & Kratter 2019), formation and evolution (e.g. Armstrong et al. 2014; Chachan et al. 2019; Pierens, McNally & Nelson 2020; Penzlin, Kley & Nelson 2021), and dependence on binary properties (Martin, Mazeh & Fabrycky 2015; Muñoz & Lai 2015; Li, Holman & Tao 2016; Martin 2019).

In 2017 we created the BEBOP survey (Binaries Escorted By Orbiting Planets; Martin et al. 2019), as a blind radial velocity survey for circumbinary planets. Prior to this, the most extensive radial velocity effort had been produced by the TATOOINE survey (Konacki et al. 2009), but the survey unfortunately did not yield any discoveries. One issue likely affected the survey, from which BEBOP learnt a great deal: TATOOINE targeted double-lined binaries, which was logical. Double-lined binaries are brighter, both stars can have model independent mass measurements, and one can, in principle, measure the Doppler displacement caused by a planet on each of the two components. However, disentangling both components from their combined spectrum accurately is a complex task, and despite photon noise uncertainties regularly reaching 2 to 4 m s^{-1}, the survey returned a scatter of order 15 to 20 m s^{-1} (Konacki et al. 2009, 2010). Indeed, Konacki et al. (2010) recommended single-lined binaries as a solution, but too few were known at the time. Since, radial velocities have been used to constrain the binary parameters, which helps refining the planetary parameters, but not to search for circumbinary planets themselves (e.g. Kostov et al. 2013, 2014).

Thanks to the advent of exoplanet transit experiments, increasing amounts of low-mass single-lined eclipsing binaries are being identified (e.g. Triaud et al. 2013, 2017; von Boetticher et al. 2019; Acton et al. 2020; Lendl et al. 2020; Mireles et al. 2020). The BEBOP survey was constructed solely using sufficiently faint secondaries, to avoid detection with spectrographs such that we could, in principle, reach a radial velocity precision comparable to that around single stars of the same brightness. In principle, this ought to provide an accuracy of order 1 m s^{-1}. Our survey is ongoing, and uses the CORALIE, SOPHIE, HARPS, and ESPRESSO spectrographs. Preliminary results were published in Martin et al. (2019; BEBOP I). In Standing et al. (2021, under review, BEBOP II), we describe our observational protocol, the methods we use to detect planets, as well as how we produce detection limits.

In this paper we detail a complementary project to BEBOP's blind search. Between 2016 and 2021 we monitored Kepler-16, a relatively bright (Vmag = 12) single-lined eclipsing binary system with a primary mass $M_1 = 0.65$ M$_\odot$ (a K dwarf), a secondary mass $M_2 = 0.20$ M$_\odot$ (a mid-M dwarf), and an orbital period $P_{\rm bin} = 41.1$ d. The system is 75 pc distant and known to host a circumbinary gas giant planet with a mass $m_{\rm pl} = 0.33$ M$_{\rm Jup}$, and a period $P_{\rm pl} = 229$ d. Our observations demonstrate that we can indeed recover the Doppler reflex signature of a circumbinary planet. Our results act to both validate and assist our broader search for new planets. Furthermore, we can derive a 'traditional' Doppler mass measurement for the planet, to be compared with that derived from photometric eclipse and transit timings. Finally, our long baseline is sensitive to additional planets, in particular to any that would occupy an orbit misaligned to the transiting inner planets.

2 VELOCIMETRIC OBSERVATIONS ON KEPLER-16

Between 2016-07-08 and 2021-06-23, we collected 143 spectra using the high-resolution high-precision fibre-fed SOPHIE spectrograph, mounted on the 193cm at Observatoire de Haute-Provence, in France (Perruchot et al. 2008). The journal of observations can be found in Table A1. All observations were conducted in HE mode (High Efficiency), where some of the instrumental resolution is sacrificed from 75 000 to 40 000 in favour of a 2.5 times greater throughput. We chose this since whilst Kepler-16 is the brightest circumbinary system, it is relatively faint for SOPHIE, with $V \sim 12.0$.

SOPHIE has two fibres: the first stayed on target, while the other was kept on the sky in order to remove any contribution from the Moon-reflected sunlight. Standard calibrations were made at the start of night as well as roughly every 2 h throughout the night to monitor the instrument's zero-point. In addition, we observed one of three standards (HD 185144, HD 9407, and HD 89269 A) in HE mode nightly, which we used to track and correct for any long-term instrumental drift following procedures established in Santerne et al. (2014) and Courcol et al. (2015).

Our radial velocities were determined by cross-correlating each spectrum with a K5V mask. These methods are described in Baranne et al. (1996), and Courcol et al. (2015), and have been shown to produce precisions and accuracies of a few meters per second (e.g. Bouchy et al. 2013; Hara et al. 2020), well below what we typically obtain on this system. As in Baranne et al. (1996), and Pollacco et al. (2008), we correct our data from lunar contamination by first scaling the calculated CCF (cross-correlation function) on fibre A and B (to account for slightly different efficiencies between the two fibres) before subtracting the two CCFs. This is a particularly important procedure for circumbinary planet searches. Most systems observed with SOPHIE are single stars, and the scheduling software informs the observer whether sunlight reflected on the Moon would create a parasitic cross-correlation signal, with a radial velocity that varies predictably with the lunar phase. In such a situation the observation is postponed. In the case of binary observations, ours, the velocity of the primary star keeps changing by km s^{-1}, meaning we could not practically predict possible lunar contamination at the time of acquisition. We also correct our data from the CTI (charge transfer inefficiency) effect following the procedure described in Santerne et al. (2012).

The cross-correlation software produces two key metrics of the shape of the CCF, its FWHM (full width at half-maximum), and its bisector span (as defined in Queloz et al. 2001). In addition, we measure the Hα stellar activity indicator following Boisse et al. (2009). These are provided in Table A1.

Two measurements are immediately excluded from our analysis. On 2017-09-06 (BJD 2458003.32008) and 2018-10-06 (BJD 2458398.33382), when the fibre was mistakenly placed on to another star. This is obvious from the FWHM we extract from these measurement, and from their radial velocity. They are appropriately flagged in Table A1. In the end, we achieve a mean radial velocity precision of ~ 10.6 m s^{-1} on the remaining 141 measurements.

Radial velocity measurements of the primary have also been obtained with TRES and Keck's HIRES (Doyle et al. 2011; Winn et al. 2011). These data sets were not used in this analysis for several reasons. First, the TRES data has a mean precision of 21 m s^{-1}, which would be insufficient to detect the planet. Secondly, the HIRES data, despite offering a precision of a few m s^{-1}, was only taken on a single night and is contaminated by the Rossiter–McLaughlin signal of the eclipse. Finally, by solely using our own SOPHIE data we may produce a near independent detection. In a similar spirit, we do not use any of *Kepler*'s or *TESS*'s photometric data to conduct our search and parameter estimation.

Finally, Bender et al. (2012) collected near-infrared spectra to reveal the secondary's spectral lines (i.e. observing Kepler-16 as a double-lined spectroscopic binary). Similarly, we do not use these measurements in our analysis, although we do use their estimate for the primary mass.

3 MODELLING OF THE RADIAL VELOCITIES

In order to ascertain our capacity to detect circumbinary planets using radial velocities, as an independent method, we decided to use two different algorithms with different methods for measuring a detection probability. Before describing this, we will detail our procedure to remove outliers. As a reminder, we only use SOPHIE data (see above), where Kepler-16 appears as a single-lined binary and we only observe the displacement of the primary star around the system's barycentre.

3.1 Outlier removal

We searched our 141 data for measurements[1] coinciding with a primary eclipse, and likely affected by the Rossiter–McLaughlin effect (McLaughlin 1924; Rossiter 1924; Winn et al. 2011; Triaud 2018). Fortunately no measurements needed to be excluded for this reason.

We also realized that a number of measurements were likely taken under adverse conditions. This is apparent from an unusually low signal-to-noise ratio, but also from large values of the bisector span. Typically used as a stellar activity, or a blend indicator (Queloz et al. 2001; Santos et al. 2002), the span of the bisector slope (bisector span, or bis span) effectively informs us that the line shape varied and therefore that the mean of the cross-correlation function is likely affected. We took the mean of the bisector span measurement and removed all measurements in excess of 3σ away from the mean. Five measurements are excluded this way, all with a bisector span $\gtrsim \pm 100$ m s^{-1}. Excluded measurements are reported in the journal of observations in Table A1 with a flag.

For visual convenience we also exclude one measurement taken on 2018-06-02 (BJD 2458271.53928) on account of its very low signal to noise and correspondingly large uncertainty, seven times greater than the semi-amplitude of Kepler-16 b. Again, this is reported in Table A1 with a flag.

Finally, we remove a measurement obtained on 2017-10-30 (BJD 2458057.38946). This measurement is $\sim 6\sigma$ away from the best-fitting model. It is totally unclear why this is the case since its FWHM, bisector span, and Hα, all appear compatible with other measurements.

After removing these seven outliers, our analysis is performed on the remaining 134 SOPHIE measurements. The exoplanet detection described just below is done twice, without, and with the seven outlying measurements. Their exclusion did not affect our conclusion but refined our parameters. We also reproduced the following fitting procedures by including the previously existing TRES and HIRES data with no discernible differences.

3.2 Analysis using the genetic algorithm YORBIT

YORBIT is a radial velocity fitting tool used for exoplanet detection, described in Ségransan et al. (2011). It assumes Keplerian orbits (see Section 3.5). YORBIT first performs a Lomb–Scargle periodogram of the observations, which is then used to initiate a genetic algorithm that iterates over the orbital period P, the eccentricity e, the argument of periastron ω, the semi-amplitude K, a reference time T_0, and one systemic velocity per data set γ (for conventions, see Hilditch 2001). Once the algorithm has converged on a best solution, the final parameters are estimated by using a least-square fit. The tool has been routinely used to identify small planetary companions successfully (e.g. Mayor et al. 2011; Bonfils et al. 2013), and represents a more traditional, and possibly a more recognized way of identifying a new planetary system than the nested sampler we use subsequently (see Section 3.3). However, YORBIT cannot do a Bayesian model comparison. Instead it computes a false alarm probability (FAP) by performing a bootstrap on the data thousands of times and computing for each iteration a Lomb–Scargle periodogram.

In a first instance, just one Keplerian is adjusted to the SOPHIE data, with YORBIT automatically finding the most prominent signal, that of the secondary star. Following this step, we remove the secondary's signal and search the resulting residuals with a periodogram. This periodogram shows excess power around 230 d with a FAP ~ 0.1 per cent as well as excess power for a signal longer than the range of dates we observed for, which we later associate to a magnetic cycle. To isolate the signal of Kepler-16 b, we fit the secondary's Keplerian to the data, alongside a polynomial function, which is used to detrend that longer signal. Once YORBIT has converged, we search the residuals again with a periodogram, which provides a FAP $\ll 0.01$ per cent (Fig. 1), clearly detecting Kepler-16 b as an additional periodic sinusoidal signal. The FAP obtained with a cubic detrending function is one order of magnitude better than that obtained with a quadratic function, so we chose the former as our baseline detrending.

To obtain results on the system's parameters, we perform a final fit to the data assuming two Keplerians and a cubic detrending function. Results of that fit are found in Table 1. The orbital parameters of the planet are compatible with those produced in Doyle et al. (2011; see Table 1 and Section 3.5 for a discussion). Our final fit produces a reduced $\chi^2_\nu = 1.17 \pm 0.14$, implying no additional complexity is needed to explain the data, and supporting our choice for a circular planetary orbit.[2] In addition, this shows that we can achieve photon-noise precision on single-lined binary to detect circumbinary planets. The model fit to the data is depicted in Fig. 2.

Including seven outliers described in Section 3.1, neither the FAP nor the reduced χ^2_ν are significantly affected.

[1]The first series of 14 measurements were obtained from a catalogue containing erroneous proper motions and epochs, which in turn created a 1.5 km s^{-1} effect in the radial velocity as the Earth's motion was overcompensated. This can be corrected easily, but the error remains within the archival data.

[2]Making a fit with a quadratic function we obtain $\chi^2_\nu = 1.47 \pm 0.15$, for one fewer parameter, justifying our choice for the cubic drift.

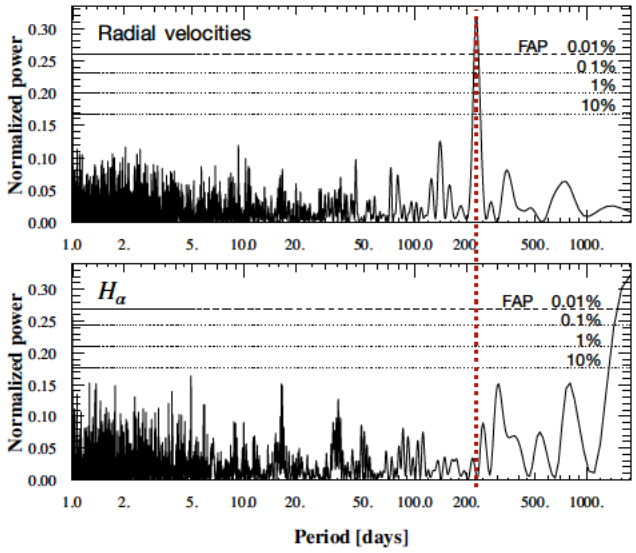

Figure 1. Lomb–Scargle periodogram of Kepler-16's radial velocities (top) and Hα (bottom). The radial velocities are shown after removing the binary motion, and a cubic function. The four lines are, from bottom to top, the 10 per cent, 1 per cent, 0.1 per cent, and 0.01 per cent FAP. There is a highly significant peak around 230 d (vertical red dotted line) that is present in the radial velocities but not in Hα. The Hα measurements contain significant periodogram power at $\gtrsim$ 2000 d, indicating a long-term trend in the chromospheric emission from the primary star.

Table 1. Results of our analysis of the SOPHIE radial velocities only, after removing outliers, that show the fit's Jacobi parameters and their derived physical parameters. They are compared to previous results with 1σ uncertainties provided in the form of the last two significant digits, within brackets. Dates are given in BJD – 2450000. We adopt the KIMA column as our results.

Parameters & units		YORBIT	KIMA	Doyle+ (2011)
Binary parameters				
$P_{\rm bin}$	day	41.077779(54)	41.077772(51)	41.079220(78)
$T_{0,\rm bin}$	BJD	8558.9640(44)	7573.0984(47)	–
$K_{1,\rm bin}$	m s^{-1}	13 678.2(1.5)	13 678.7(1.5)	–
$e_{\rm bin}$	–	0.15989(11)	0.15994(10)	0.15944(62)
$\omega_{\rm bin}$	deg	263.661(40)	263.672(40)	263.464(27)
Planet parameters				
$P_{\rm pl}$	day	228.3(1.8)	226.0(1.7)	228.776(37)
$T_{0,\rm pl}$	BJD	8532.5(4.4)	7535(92)	–
$K_{1,\rm pl}$	m s^{-1}	12.8(1.5)	11.8(1.5)	–
$e_{\rm pl}$	–	0 (fixed)	<0.21	0.0069(15)
$\omega_{\rm pl}$	deg	–	231(65)	$318^{(+10)}_{(-22)}$
System parameters				
γ	km s^{-1}	−33.8137(69)	−33.8065(45)	−32.769(35)
$\sigma_{\rm jitter}$	m s^{-1}	–	$0.070\ ^{+1.104}_{-0.067}$	–
Derived parameters				
M_1	M$_\odot$	0.654(17)*	0.654(17)*	0.6897(35)
M_2	M$_\odot$	0.1963(31)	0.1964(31)	0.20255(66)
$m_{\rm pl}$	M$_{\rm Jup}$	0.345(41)	0.313(39)	0.333(16)
$a_{\rm bin}$	AU	0.2207(18)	0.2207(17)	0.22431(35)
$a_{\rm pl}$	AU	0.6925(67)	0.6880(58)	0.7048(11)

Note. ∗adopted from Bender et al. (2012)

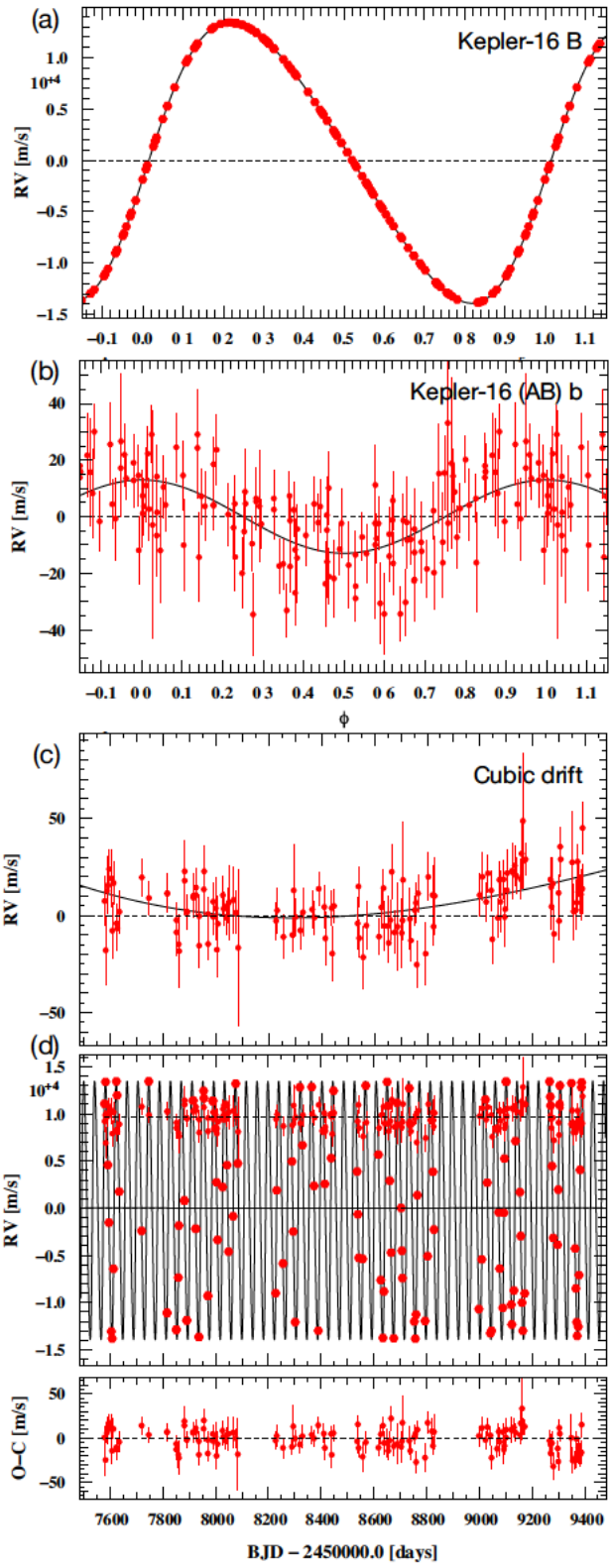

Figure 2. Best-fitting adjustment to the SOPHIE radial velocity data. *a:* Doppler reflex motion caused by the secondary star. *b:* Doppler reflex motion caused by the circumbinary planet. *c:* Cubic drift associated with a magnetic cycle. *d:* Radial velocities as a function of time with a binary+planet+cubic function model. Residuals are displayed below.

3.3 Analysis using the diffusive nested sampler KIMA

KIMA is a tool developed by Faria et al. (2018), which fits a sum of Keplerian curves to radial velocity data. It samples from the posterior distribution of Keplerian model parameters using a diffusive nested sampling algorithm by Brewer & Foreman-Mackey (2016). Diffusive nested sampling allows the sampling of multimodal distributions, such as those typically found in exoplanetary science and radial velocity data (Brewer & Donovan 2015), evenly and efficiently.

KIMA can treat the number of planetary signals (N_p) present in an RV data set as a free parameter in its fit. Since the tool also calculates the fully marginalized likelihood (evidence), it allows for Bayesian model comparison (Trotta 2008) between models with varying N_p. A measure of preference of one Bayesian model over another can be ascertained by computing the 'Bayes Factor' (Kass & Raftery 1995) between the two. The Bayes factor is a ratio of probabilities between the two competing models. Once a value for the Bayes factor has been calculated, we can compare it to the so-called 'Jeffreys' scale' (see Trotta 2008 for more details) to rate the strength of evidence of one model over another.

A more extensive description of our use of KIMA in the context of the BEBOP survey can be found in Standing et al. (2021). For the analysis of the Kepler-16 system, prior distributions were chosen similarly to those used in Faria et al. (2020) with the following notable adaptions. We treat the secondary star as a *known object* with tight uniform priors on its orbital parameters. A log-uniform distribution was used to describe the periods of any additional signals, from $4 \times P_{\rm bin}$ to 1×10^4 d. This inner limit on period is set by the instability limit found in binary star systems (Holman & Wiegert 1999). More details, particularly on the priors we use, can be found in Standing et al. (2021). Just like for the previous analysis using YORBIT, KIMA is only deployed on SOPHIE data, and excluding outliers described in Section 3.1.

Our KIMA analysis of the Kepler-16 data yields a Bayes Factor BF > 10000 in favour of a three Keplerian model (secondary star, planet, and cubic drift). Our posterior shows overdensities at orbital periods of $\approx$230 and $\approx$2000 d, corresponding to the signal of Kepler-16 b and the cubic drift seen in YORBIT. We then apply the clustering algorithm HDBSCAN (McInnes, Healy & Astels 2017) to isolate and extract the resulting planetary orbital parameters, which can be found in Table 1.

3.4 Note on converting fitted parameters to physical values

To convert our semi-amplitudes into masses for M_2 and $m_{\rm pl}$, for the secondary star and planet masses (respectively), we adopt a primary star mass (M_1) from Bender et al. (2012). Software written for exoplanetary usage usually assumes that $m_{\rm pl} \ll M_\star$ (including YORBIT and KIMA); however, this assumption is no longer valid when comparing M_2 to M_1, and a circumbinary planet to both.

First, we find M_2 iteratively using the mass function, following the procedure described in Triaud et al. (2013). Then, we estimate $m_{\rm pl}$ from $K_{1,\rm pl}$ by using the combined mass $M_1 + M_2$. This is because whilst we are only measuring the radial velocity signature of the primary star, the gravitational force of the planet acts on the barycentre of the binary. Had we not done this extra conversion step, we would find significant differences, with erroneous $M_2 = 0.165$ M$_\odot$ and $m_{\rm pl} = 0.29$ M$_{\rm Jup}$ for the YORBIT results.

Differences between our derived parameters (bottom part of Table 1) and those from Doyle et al. (2011) are mainly explained by our adoption of the more accurate M_1 mass from Bender et al. (2012) rather than using the value from Doyle et al. (2011).

3.5 Note on circumbinary planets' orbital elements

The main differences between our fitted parameters and those from Doyle et al. (2011) are caused by our parameters being akin to mean parameters (e.g. the mean orbital period), whereas Doyle et al. (2011) provide osculating parameters, which are the parameters the system had at one particular date, and which constantly evolve following three-body dynamics (Mardling 2013). Also, the planetary signal is significantly more obvious in the *Kepler* transiting data than in our radial velocities. Each measurement within a planetary transit over the primary star produces an SNR = 243 (SNR = 14 when over the secondary). This is why *Kepler* can derive osculating elements, by solving Newton's equations of motion: the planetary motion is resolved orbit after orbit (transit after transit). Comparatively, our radial velocity observations have required multiple orbits of the planet to build up a significant detection. We can therefore only measure a mean period, and are justified in using software which can only adjust non-interacting Keplerian functions.

For example, Doyle et al. (2011) provide a highly precise value of $P_{\rm pl} = 228.776 \pm 0.037$ d, yet this osculating period will vary by approximately ± 5 d over a time-scale of just years. Our measured period of $P_{\rm pl} = 226.0 \pm 1.7$ d has a much higher error with this uncertainty being a combination of our radial velocities being less constraining on the period, and our assumption of a static orbit. The value we obtain with KIMA is 1.6σ compatible with the value found by Doyle et al. (2011).

With respect to the planet mass, we can derive a value with similar precision to that of Doyle et al. (2011) because whilst the transit signature of the planet is much stronger than its radial velocity signature, the transit signature itself carries very little information about the planet's mass. The photodynamical mass derived in Doyle et al. (2011) is dictated by the eclipse timing variations, which have an amplitude of a couple of minutes and have a precision on the order of tens of seconds, producing an SNR close to our radial velocities.

Finally, to validate our assumption that we cannot measure osculating elements with our current data, we used tools described in Correia et al. (2005, 2010) to perform an N-body fit to the radial velocities. This fit finds no improvements in χ^2 indicating that Newtonian effects indeed remain below the detectable threshold.

3.6 A magnetic cycle, and constraints on additional planets

To assess the presence of an external companion causing the additional polynomial signal we notice in our data, we force a two-Keplerian model to fit the data (a circular orbit for the planet and a free-eccentricity orbit for the binary) and analyse the residuals. We find a signal reaching a FAP < 0.01 per cent at orbital periods exceeding the time-span of our data ($\gtrsim 2,000$ d). Long-term drifts can sometimes be caused by magnetic cycles since stellar spots and faculae tend to suppress convective blue-shift, producing a net change in the apparent velocity of a star (Dravins 1985; Meunier, Desort & Lagrange 2010; Dumusque et al. 2011). We perform a Lomb–Scargle periodogram on the Hα activity indicator we extracted from the SOPHIE spectra, and find a FAP < 0.01 per cent. We therefore interpret this long-term radial velocity drift as a magnetic cycle, with a time-scale longer than the time-span of our observations.

The validity of this interpretation can be tested since duration of stellar magnetic cycles scales with stellar rotation periods (for single star; Suárez Mascareño, Rebolo & González Hernández 2016). We

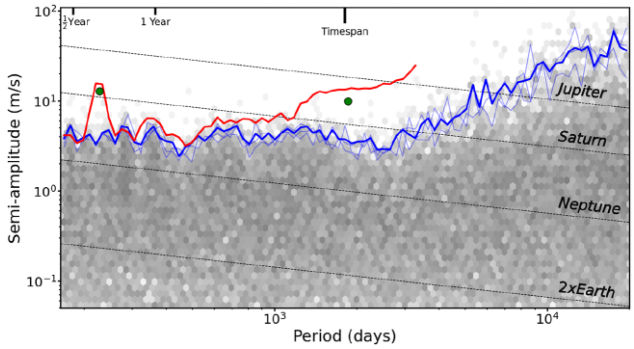

Figure 3. Detection sensitivity to additional planets plotted as semi-amplitude $K_{1,\rm pl}$ as a function of $P_{\rm pl}$. The hexagonal bins depict the density of posterior samples obtained from three separate KIMA runs applied on the Kepler-16 radial velocity data after removing two Keplerian signals shown with green dots. The faded blue lines show detection limits calculated for each of the three runs on the system. The solid blue line shows the detection limit calculated from all posterior samples combined. The solid red line is the outline of the posterior that led to the detection of Kepler-16 b and of a long-term trend associated with a magnetic cycle. The green dots represent the two signals removed from the data to compute the blue detection limit.

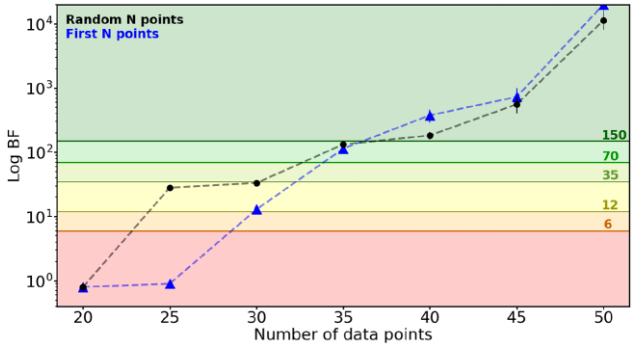

Figure 4. Bayes factors obtained for subsets of data with increasing size. The blue line and triangles indicate the Bayes factors obtained by running KIMA on the first N data points obtained on Kepler-16. The black line and dots show the same but for randomly sampled N data points within the first 3 yr of data. Coloured regions represent various thresholds corresponding to improvements in evidence in favour of the more complex binary + planet model as per the Jeffreys' scale detailed in Standing et al. (2021).

measure the primary star's rotation from the $v\sin i_1$ obtained during the Rossiter–McLaughlin effect by Winn et al. (2011) to the primary's stellar radius obtained by Bender et al. (2012) and obtain a primary rotation $P_{\rm rot,1} = 35.68 \pm 1.04$ d. Following the relation of Suárez Mascareño et al. (2016), with the observed stellar rotation we ought to expect a magnetic cycle on a time-scale of 1900 to 2400 d, which is entirely compatible with the Hα signal and the long-term radial velocity drift.

We now use KIMA as done in Standing et al. (2021) to compute a detection limit on the presence of additional but undetected planetary companions. We first remove the highest likelihood model with two Keplerians (the planet and the long-term drift) from the data, then force $N_{\rm p} = 1$ to obtain a map of all remaining signals that are compatible with the data, but remain formally undetected (the binary is also adjusted at each step). This map is shown as a grey-scale density on Fig. 3. The 99 per cent contour informs us that we are sensitive to companions below the mass of Kepler-16 b up to orbital periods of ∼3000 d. This complements Martin & Fabrycky (2021)'s work who placed detection limits down to Earth-radius planets but only out to periods of 500 d, re-analysing the *Kepler* photometry.

Overall, a picture is emerging of Kepler-16 b as a lonely planet, which has implications for the formation and migration of multi-planet systems in the presence of a potentially destabilising binary (e.g. Sutherland & Kratter 2019).

4 DISCUSSION

Our data clearly shows an independent detection of the circumbinary planet Kepler-16 b, the first time a circumbinary planet is detected using radial velocities, and the first time a circumbinary planet is detected using ground-based telescopes as well. We re-iterate that our model fits are solely made using radial velocities and completely ignore any *Kepler* or other photometric data, to emulate BEBOP's blind search. Importantly, our results show we can achieve a precision close to 1 m s^{-1} on a planetary signal, with the 1σ uncertainties on the semi-amplitudes being only just 1.5 m s^{-1}. This is compatible with the semi-amplitudes of super-Earths and sub-Neptunes (e.g. Mayor et al. 2011). The closest previous detection to a circumbinary planet made from the ground was produced by Correia et al. (2005) on HD 202206, a system comprised of a Sun-like star with an inner companion with mass $m_b \sin i_b = 17.4$ M$_{\rm Jup}$ and orbital period $P_b = 256$ d, and an outer companion with mass $m_c \sin i_c = 2.44$ M$_{\rm Jup}$ and orbital period $P_c = 1383$ d. Benedict & Harrison (2017) claim an astrometric detection of the system that implies a nearly face-on system, with $m_b = 0.89$ M$_\odot$ and $m_c = 18$ M$_{\rm Jup}$, suggesting a circumbinary brown dwarf. However, a dynamical analysis produced by Couetdic et al. (2010) imply such a configuration is unstable and therefore unlikely, favouring instead a more edge-on system.

We first detect Kepler-16 b by using a classical approach to planet detection, via periodograms and FAP, but also perform a second analysis using the diffusive nested sampler KIMA, which allows to perform model comparison and model selection in a fully Bayesian framework. KIMA will be the method of choice for the remainder of the BEBOP survey Standing et al. (2021). The parameters for the planetary companion are broadly compatible with those measured at the time of detection by Doyle et al. (2011), and which have not been revised since. With our current precision it is not possible to determine the eccentricity of the orbit, but we can place an upper limit on it.

Finally, we discuss the detectability of circumbinary systems. We only take the 20 first measurements we collected and run KIMA measuring the Bayes Factor to assess the detectability of Kepler-16 b, where individual uncertainties are similar to the semi-amplitude of the signal, $K_{1,\rm pl}$. We repeat the procedure, measuring BF for each increase of five measurements until we reach a sub-sample containing the 50 first radial velocity measurements (they roughly cover four orbital periods of the planet). We reach a BF >150 (the formal threshold for detection) with the first 40 measurements. We repeat this procedure but instead randomly select 50 measurements within the first 3 yr of data. We run KIMA and measure the Bayes Factor for the first 20 epochs of this sequence of 50 random epochs. We then increase from 20 to 25 until reaching 50. We find that the BF =150 threshold is also passed at 40 measurements. We plot our results in Fig. 4. The results between both series of tests are broadly consistent, except when we only use 25 measurements, with the Bayes Factor growing log-linearly with increasing number of measurements. Thanks to these tests we conclude that just 40 to 45 measurements would have been to formally detect Kepler-16 b with radial velocities.

ACKNOWLEDGEMENTS

First, we would like to thank the staff, in particular the night assistants, at the Observatoire de Haute-Provence for their dedication and hard work, particularly during the COVID pandemic. Secondly, we wish to thank our reviewer, David Armstrong, for reading and commenting our paper. The data were obtained first as part of a DDT graciously awarded by the OHP director (Prog.ID 16.DISC.TRIA), and then by a series of allocations through the French PNP (Prog. IDs 16B.PNP.HEB2, 17A.PNP.SANT, 17B.PNP.SAN2, 18A.PNP.SANT, 18B.PNP.SAN1, 19A.PNP.SANT). The French group acknowledges financial support from the French Programme National de Planétologie (PNP, INSU). This research received funding from the European Research Council (ERC) under the European Union's Horizon 2020 research and innovation programme (grant agreement no. 803193/BEBOP) and from the Leverhulme Trust (research project grant no. RPG-2018-418). EW acknowledges support from the ERC Consolidator Grant funding scheme (grant agreement no. 772293/ASTROCHRONOMETRY). Support for this work was provided by NASA through the NASA Hubble Fellowship grant number HF2-51464 awarded by the Space Telescope Science Institute, which is operated by the Association of Universities for Research in Astronomy, Inc., for NASA, under contract NAS5-26555. PC thanks the LSSTC Data Science Fellowship Program, which is funded by LSSTC, NSF Cybertraining Grant #1829740, the Brinson Foundation, and the Moore Foundation; her participation in the program has benefited this work. SH acknowledges CNES funding through the grant 837319. ACC acknowledges support from the Science and Technology Facilities Council (STFC) consolidated grant number ST/R000824/1. ACMC acknowledges support by CFisUC projects (UIDB/04564/2020 and UIDP/04564/2020), GRAVITY (PTDC/FIS-AST/7002/2020), ENGAGE SKA (POCI-01-0145-FEDER-022217), and PHOBOS (POCI-01-0145-FEDER-029932), funded by COMPETE 2020 and FCT, Portugal.

The radial velocity data are included in the appendix of this paper. The reduced spectra are available at the SOPHIE archive: http://atlas.obs-hp.fr/sophie/. Data obtained under Prog.IDs 16.DISC.TRIA, 16B.PNP.HEB2, 17A.PNP.SANT, 17B.PNP.SAN2, 18A.PNP.SANT, 18B.PNP.SAN1, and 19A.PNP.SANT.

REFERENCES

Acton J. S. et al., 2020, MNRAS, 498, 3115
Armstrong D. J., Osborn H. P., Brown D. J. A., Faedi F., Gómez Maqueo Chew Y., Martin D. V., Pollacco D., Udry S., 2014, MNRAS, 444, 1873
Bailey V. et al., 2014, ApJ, 780, L4
Baranne A. et al., 1996, A&AS, 119, 373
Bender C. F. et al., 2012, ApJ, 751, L31
Benedict G. F., Harrison T. E., 2017, AJ, 153, 258
Bennett D. P. et al., 2016, AJ, 152, 125
Boisse I. et al., 2009, A&A, 495, 959
Bonfils X. et al., 2013, A&A, 549, A109
Borkovits T., Hajdu T., Sztakovics J., Rappaport S., Levine A., Bíró I. B., Klagyivik P., 2016, MNRAS, 455, 4136
Borucki W. J., Summers A. L., 1984, Icarus, 58, 121
Borucki W. J. et al., 2011, ApJ, 728, 117
Bouchy F., Díaz R. F., Hébrard G., Arnold L., Boisse I., Delfosse X., Perruchot S., Santerne A., 2013, A&A, 549, A49
Brewer B. J., Donovan C. P., 2015, MNRAS, 448, 3206
Brewer B. J., Foreman-Mackey D., 2016, preprint (arXiv:1606.03757)
Chachan Y., Booth R. A., Triaud A. H. M. J., Clarke C., 2019, MNRAS, 489, 3896
Correia A. C. M., Udry S., Mayor M., Laskar J., Naef D., Pepe F., Queloz D., Santos N. C., 2005, A&A, 440, 751
Correia A. C. M. et al., 2010, A&A, 511, A21
Couetdic J., Laskar J., Correia A. C. M., Mayor M., Udry S., 2010, A&A, 519, A10
Courcol B. et al., 2015, A&A, 581, A38
Doyle L. R. et al., 2011, Science, 333, 1602
Dravins D., 1985, in Philip A. G. D., Latham D. W., eds, Proc. IAU Symp. 88, Stellar Radial Velocities. L. Davis Press, Schenectady, p. 311
Dumusque X. et al., 2011, A&A, 535, A55
Faria J. P., Santos N. C., Figueira P., Brewer B. J., 2018, J. Open Source Softw., 3, 487
Faria J. P. et al., 2020, A&A, 635, A13
Getley A. K., Carter B., King R., O'Toole S., 2017, MNRAS, 468, 2932
Han Z. T., Qian S. B., Irina V., Zhu L. Y., 2017, AJ, 153, 238
Hara N. C. et al., 2020, A&A, 636, L6
Hardy A. et al., 2015, ApJ, 800, L24
Hilditch R. W., 2001, An Introduction to Close Binary Stars. Cambridge Univ. Press, Cambridge, p. 392
Holman M. J., Wiegert P. A., 1999, AJ, 117, 621
Kass R. E., Raftery A. E., 1995, J. Am. Stat. Assoc., 90, 773
Konacki M., Muterspaugh M. W., Kulkarni S. R., Hełminiak K. G., 2009, ApJ, 704, 513
Konacki M., Muterspaugh M. W., Kulkarni S. R., Hełminiak K. G., 2010, ApJ, 719, 1293
Kostov V. B., McCullough P. R., Hinse T. C., Tsvetanov Z. I., Hébrard G., Díaz R. F., Deleuil M., Valenti J. A., 2013, ApJ, 770, 52
Kostov V. B. et al., 2014, ApJ, 784, 14
Kostov V. B. et al., 2020, AJ, 159, 253
Kostov V. B. et al., 2021, AJ, 162, 234
Lendl M. et al., 2020, MNRAS, 492, 1761
Li G., Holman M. J., Tao M., 2016, ApJ, 831, 96
Mardling R. A., 2013, MNRAS, 435, 2187
Marsh T. R. et al., 2013, MNRAS, 437, 475
Martin D. V., 2018, Populations of Planets in Multiple Star Systems. Springer, Berlin, p. 156
Martin D. V., 2019, MNRAS, 488, 3482
Martin D. V., Fabrycky D. C., 2021, AJ, 162, 84
Martin D. V., Triaud A. H. M. J., 2014, A&A, 570, A91
Martin D. V., Mazeh T., Fabrycky D. C., 2015, MNRAS, 453, 3554
Martin D. V. et al., 2019, A&A, 624, A68
Mayor M. et al., 2011, preprint (arXiv:1109.2497)
McInnes L., Healy J., Astels S., 2017, J. Open Source Softw., 2, 205
McLaughlin D. B., 1924, ApJ, 60, 22
Meunier N., Desort M., Lagrange A. M., 2010, A&A, 512, A39
Mireles I. et al., 2020, AJ, 160, 133
Muñoz D. J., Lai D., 2015, Proc. Natl. Acad. Sci., 112, 9264
Mustill A. J., Marshall J. P., Villaver E., Veras D., Davis P. J., Horner J., Wittenmyer R. A., 2013, MNRAS, 436, 2515
Orosz J. A. et al., 2012, ApJ, 758, 87
Orosz J. A. et al., 2019, AJ, 157, 174
Penzlin A. B. T., Kley W., Nelson R. P., 2021, A&A, 645, A68
Perruchot S. et al., 2008, in McLean I. S., Casali M. M., eds, Proc. SPIE Conf. Ser. Vol. 7014, Ground-based and Airborne Instrumentation for Astronomy II. SPIE, Bellingham, p. 70140J
Pierens A., McNally C. P., Nelson R. P., 2020, MNRAS, 496, 2849
Pollacco D. et al., 2008, MNRAS, 385, 1576
Queloz D. et al., 2001, A&A, 379, 279
Rauer H. et al., 2014, Exp. Astron., 38, 249
Ricker G. R. et al., 2014, in Oschmann J. M., Jr., Clampin M., Fazio G. G., MacEwen H. A., eds, Proc. SPIE Conf. Ser. Vol. 9143, Space Telescopes and Instrumentation 2014: Optical, Infrared, and Millimeter Wave. SPIE, Bellingham, p. 914320
Rossiter R. A., 1924, ApJ, 60, 15
Santerne A. et al., 2012, A&A, 545, A76
Santerne A. et al., 2014, A&A, 571, A37
Santos N. C. et al., 2002, A&A, 392, 215
Schneider J., 1994, Planet. Space Sci., 42, 539

Schwamb M. E. et al., 2013, ApJ, 768, 127
Ségransan D. et al., 2011, A&A, 535, A54
Socia Q. J. et al., 2020, AJ, 159, 94
Standing M. R. et al., 2021, preprint (arXiv:2112.05652)
Suárez Mascareño A., Rebolo R., González Hernández J. I., 2016, A&A, 595, A12
Sutherland A. P., Kratter K. M., 2019, MNRAS, 487, 3288
Triaud A. H. M. J., 2018, The Rossiter-McLaughlin Effect in Exoplanet Research. Springer, Berlin, p. 2
Triaud A. H. M. J. et al., 2013, A&A, 549, A18
Triaud A. H. M. J. et al., 2017, A&A, 608, A129
Trotta R., 2008, Contemp. Phys., 49, 71
von Boetticher A. et al., 2019, A&A, 625, A150
Winn J. N. et al., 2011, ApJ, 741, L1

SUPPORTING INFORMATION

Supplementary data are available at *MNRAS* online.

Please note: Oxford University Press is not responsible for the content or functionality of any supporting materials supplied by the authors. Any queries (other than missing material) should be directed to the corresponding author for the article.

APPENDIX A: JOURNAL OF OBSERVATIONS

[1]*School of Physics & Astronomy, University of Birmingham, Edgbaston, Birmingham, B15 2TT, UK*

Table A1. Journal of observations containing our SOPHIE data. Flags indicate whether the measurement are excluded from our fiducial analysis with the following reason: W, wrong star; B, bisector outlier; U, high uncertainty; O, other. Dates are given in BJD – 2400000. $V_{\rm rad}$ are the measured radial velocities with their uncertainties $\sigma_{V_{\rm rad}}$. FWHM is the Full With at Half Maximum of the Gaussian fitted to the cross correlation function, and *contrast* is its amplitude. Bis. span is the span of the bisector slope. Uncertainties on FWHM and bis. span are $2 \times \sigma_{V_{\rm rad}}$. H_α is the equivalent width of H_α, and its uncertainty σ_{H_α}.

flag	BJD-2400000 [days]	$V_{\rm rad}$ [km s^{-1}]	$\sigma_{V_{\rm rad}}$ [km s^{-1}]	FWHM [km s^{-1}]	contrast	bis. span [km s^{-1}]	H_α	σ_{H_α}
	57578.42404	– 22.7567	0.0126	10.4138	22.7274	– 0.0233	0.2119	0.0022
B	57581.57256	– 20.3465	0.0444	10.4924	13.0881	– 0.1227	0.2184	0.0055
	57582.52743	– 20.4322	0.0176	10.3201	27.2220	– 0.0199	0.2046	0.0036
	57587.43166	– 23.9495	0.0113	10.2935	25.8863	0.0192	0.2031	0.0021
	57591.44122	– 29.2376	0.0146	10.2883	26.1452	0.0538	0.2117	0.0029
	57595.47979	– 35.3428	0.0096	10.3340	29.0424	0.0125	0.2039	0.0020
	57604.43905	– 46.8841	0.0145	10.4605	25.3376	– 0.0054	0.2147	0.0028
	57607.38886	– 47.6294	0.0145	10.4123	28.2874	0.0037	0.2135	0.0030
	57612.47728	– 40.2406	0.0110	10.3402	28.9602	0.0079	0.2116	0.0023
	57623.37736	– 20.3825	0.0100	10.2928	29.0664	– 0.0093	0.2032	0.0020
	57626.38491	– 21.8607	0.0110	10.3395	28.9280	0.0329	0.2063	0.0022
	57634.40704	– 32.0631	0.0109	10.3925	28.9876	– 0.067	0.2092	0.0023
	57719.26505	– 36.2183	0.0095	10.3290	28.9030	0.0201	0.1966	0.0018
	57746.26923	– 20.3795	0.0084	10.3404	29.0733	– 0.0067	0.2122	0.0016
	57815.65363	– 44.9376	0.0098	10.3132	27.1330	– 0.0004	0.2095	0.0018
	57815.67731	– 44.8993	0.0083	10.3249	29.1040	0.0086	0.2080	0.0016
	57850.59947	– 46.6829	0.0091	10.3250	27.0881	0.0033	0.2069	0.0017
	57850.62308	– 46.7070	0.0119	10.2789	28.0442	– 0.0021	0.2067	0.0022
	57858.58652	– 41.1658	0.0146	10.2378	23.9695	– 0.0255	0.1882	0.0025
	57860.61247	– 35.6563	0.0186	10.2443	23.5034	0.0100	0.1941	0.0032
	57881.49587	– 33.0003	0.0175	10.2694	22.2896	– 0.0211	0.2216	0.0030
	57881.51944	– 33.0316	0.0158	10.2409	25.8066	0.0089	0.2109	0.0029
	57890.53416	– 45.6792	0.0089	10.2779	27.3843	0.0160	0.1951	0.0016
	57890.57816	– 45.7231	0.0081	10.2384	27.7725	– 0.0009	0.1910	0.0015
	57914.55102	– 22.4041	0.0110	10.2004	25.3872	– 0.0078	0.2151	0.0020
	57914.57472	– 22.4272	0.0084	10.2139	27.9878	0.0084	0.2134	0.0016
	57924.49590	– 35.9753	0.0099	10.2853	27.2617	0.0267	0.1996	0.0018
	57924.52118	– 36.0181	0.0103	10.2534	28.8795	0.0171	0.2012	0.0020
	57936.48767	– 47.4623	0.0106	10.2734	26.9318	0.0141	0.1932	0.0020
	57936.51133	– 47.4660	0.0113	10.3536	28.5829	– 0.0057	0.1917	0.0021
	57954.37721	– 21.3857	0.0134	10.2930	25.3470	0.0145	0.2031	0.0024
	57955.36873	– 22.1650	0.0129	10.2899	25.3384	– 0.0119	0.2043	0.0022
	57970.44413	– 43.0893	0.0085	10.2438	28.2732	0.0268	0.1914	0.0016
	57970.46806	– 43.1358	0.0082	10.2520	28.9462	0.0077	0.1877	0.0015
	57989.42736	– 22.4627	0.0097	10.2269	27.1918	0.0127	0.1965	0.0017
	57989.45189	– 22.4383	0.0091	10.2555	29.0876	– 0.0119	0.1930	0.0017
	57999.37737	– 25.3762	0.0160	10.2317	23.9715	– 0.0013	0.1971	0.0027
W	58003.32008	– 3.1611	0.0199	7.5424	24.2589	0.0161	0.2016	0.0045
	58003.42095	– 31.0632	0.0141	10.1974	23.2722	– 0.0428	0.1954	0.0023
	58007.42352	– 37.1754	0.0142	10.3020	28.2437	0.0059	0.1924	0.0027
	58026.32236	– 31.5767	0.0100	10.2828	26.6464	0.0082	0.2004	0.0018
	58029.34747	– 24.2823	0.0086	10.2444	31.1481	– 0.0078	0.1962	0.0018

Table A1 *– continued*

flag	BJD-2400000 [days]	$V_{\rm rad}$ [km s^{-1}]	$\sigma_{V_{\rm rad}}$ [km s^{-1}]	FWHM [km s^{-1}]	contrast	bis. span [km s^{-1}]	H_α	σ_{H_α}
B	58034.33565	− 20.4064	0.0114	10.2145	31.4902	− 0.0954	0.1925	0.0024
	58038.28757	− 22.8921	0.0085	10.2171	29.0859	− 0.0010	0.1947	0.0016
	58043.30107	− 29.2555	0.0088	10.1869	27.6237	0.0084	0.1888	0.0016
	58049.33656	− 38.4188	0.0190	10.3105	23.6222	− 0.0004	0.2151	0.0033
O	58057.38946	− 47.4170	0.0127	10.3516	27.6078	0.0028	0.1924	0.0022
	58066.32858	− 34.6758	0.0173	10.2573	23.9592	0.0012	0.2000	0.0029
	58076.24290	− 20.6229	0.0109	10.2381	26.3816	0.0227	0.1993	0.0020
	58084.24172	− 29.0736	0.0402	10.3369	17.3316	0.0183	0.2143	0.0061
	58227.56803	− 42.8215	0.0095	10.3294	29.2382	0.0159	0.1975	0.0018
	58231.59284	− 31.9304	0.0115	10.3272	28.2728	− 0.0126	0.1911	0.0022
	58255.55341	− 39.6783	0.0111	10.2862	26.8276	− 0.0023	0.1972	0.0020
U	58271.53928	− 35.2297	0.0775	10.4414	14.1731	0.0514	0.2170	0.0113
	58289.48662	− 28.8597	0.0086	10.2324	27.6608	0.0124	0.1940	0.0016
	58294.41403	− 36.2932	0.0238	10.1405	19.6541	− 0.0463	0.1980	0.0038
	58301.52589	− 45.8824	0.0094	10.2594	27.0071	− 0.0092	0.1856	0.0017
	58319.49236	− 21.0086	0.0095	10.232	27.3731	− 0.0159	0.1864	0.0017
	58329.35035	− 27.1417	0.0123	10.1726	26.8217	0.0135	0.1895	0.0024
	58364.49871	− 20.9710	0.0095	10.2804	29.4757	0.0077	0.1917	0.0018
	58373.38714	− 31.4460	0.0085	10.2349	28.9319	− 0.0064	0.1959	0.0017
	58389.28389	− 46.7948	0.0085	10.2759	28.4801	− 0.0032	0.1936	0.0017
W	58398.33382	2.0217	0.0162	7.6074	33.8799	− 0.0066	9999.99	9999.99
	58410.34703	− 25.6250	0.0107	10.2377	30.7540	0.0084	0.1970	0.0023
	58414.31942	− 31.2461	0.0135	10.2164	26.4540	− 0.0110	0.2059	0.0026
	58438.23468	− 28.5063	0.0086	10.2149	28.7501	− 0.0001	0.2048	0.0017
	58440.32791	− 23.9560	0.0141	10.4258	30.7245	0.0284	0.2063	0.0030
	58447.28753	− 21.3746	0.0085	10.2282	30.6147	− 0.0060	0.1972	0.0018
	58536.69186	− 29.9300	0.0131	10.2127	26.6076	− 0.0381	0.1960	0.0026
	58539.69622	− 34.4673	0.0101	10.3190	28.0285	− 0.0214	0.1959	0.002
	58542.70128	− 39.0813	0.0096	10.2536	28.4771	− 0.0302	0.2042	0.0019
	58557.68116	− 39.1923	0.0161	10.2757	27.2871	0.0405	0.2019	0.0033
	58569.61968	− 20.8305	0.0122	10.2296	27.7821	− 0.0081	0.2002	0.0024
	58617.59111	− 28.1421	0.0091	10.2460	28.7484	− 0.0038	0.2015	0.0018
	58626.46789	− 41.4286	0.0107	10.2794	25.8409	0.0075	0.2010	0.0020
	58634.53897	− 47.5651	0.0093	10.2481	26.5013	− 0.0039	0.2018	0.0018
	58638.43325	− 42.6407	0.0126	10.2794	28.4741	− 0.0223	0.2039	0.0026
	58650.53936	− 20.4374	0.0152	10.1724	26.3894	0.0132	0.2030	0.0031
	58654.49571	− 22.9659	0.0097	10.2282	28.3680	− 0.0006	0.1971	0.0019
	58660.56745	− 30.9076	0.0102	10.2163	28.9174	− 0.0113	0.1984	0.0022
	58665.57318	− 38.5290	0.0140	10.2965	27.5442	0.0455	0.1981	0.0028
	58675.57952	− 47.5981	0.0109	10.3365	27.6547	0.0017	0.1965	0.0022
	58687.61864	− 22.6485	0.0225	10.3376	23.7336	0.0388	0.2054	0.0043
	58703.54677	− 33.7950	0.0175	10.3134	26.0287	0.0192	0.2010	0.0036
	58706.50803	− 38.3266	0.0100	10.2295	28.0761	− 0.0120	0.1982	0.0020
	58708.50232	− 41.2314	0.0301	10.2930	16.0707	− 0.0426	0.1994	0.0047
B	58732.43751	− 20.3947	0.0302	10.2203	25.1441	− 0.1346	0.2322	0.0062
	58734.44238	− 21.1078	0.0155	10.2528	27.1499	− 0.0207	0.2124	0.0031
	58738.38163	− 24.8845	0.0105	10.1784	27.7775	− 0.0244	0.2003	0.0021
	58753.33846	− 45.8380	0.0075	10.2737	28.6564	− 0.0095	0.202	0.0016
	58757.43639	− 47.6475	0.0099	10.3475	28.4233	0.0141	0.2001	0.0020
	58760.37181	− 45.0829	0.0118	10.2839	28.1836	0.0119	0.1973	0.0024
	58765.41646	− 32.4426	0.0094	10.2947	28.2387	0.0005	0.2029	0.0019
	58794.31837	− 45.7701	0.0157	10.3120	26.8288	− 0.0071	0.2012	0.0031
	58804.24157	− 38.9032	0.0122	10.3048	27.9886	0.0424	0.2025	0.0024
	58820.22529	− 24.4962	0.0149	10.3393	26.6102	− 0.0071	0.2153	0.0030
	58824.24004	− 29.9520	0.0094	10.2552	28.2000	0.0245	0.2090	0.0019
	58828.27635	− 36.0832	0.0198	10.4292	23.1762	− 0.0434	0.2019	0.0034
B	58919.69124	− 47.3685	0.0208	10.3504	24.6286	− 0.1229	0.2077	0.0041
	58998.56140	− 44.5035	0.0109	10.3115	28.8681	0.0086	0.1939	0.0022
	59009.49993	− 39.2485	0.0122	10.2756	27.7224	− 0.0107	0.2039	0.0025
	59023.55894	− 22.3117	0.0099	10.2759	28.5419	− 0.0080	0.1996	0.0019
	59030.43413	− 31.1164	0.0095	10.2358	28.4005	0.0120	0.1979	0.0019
	59042.42642	− 47.0737	0.0101	10.2934	28.2747	0.0043	0.2012	0.0020
	59046.54366	− 46.7980	0.0123	10.2777	28.0726	− 0.0441	0.1967	0.0026

Table A1 – *continued*

flag	BJD-2400000 [days]	$V_{\rm rad}$ [km s^{-1}]	$\sigma_{V_{\rm rad}}$ [km s^{-1}]	FWHM [km s^{-1}]	contrast	bis. span [km s^{-1}]	H_α	σ_{H_α}
	59067.42681	− 25.4159	0.0097	10.2439	28.0315	0.0085	0.1974	0.0019
	59073.55426	− 34.2494	0.0093	10.3336	28.3985	0.0340	0.2080	0.0019
	59077.48604	− 40.2255	0.0157	10.2866	27.4415	0.0209	0.2072	0.0034
	59089.39809	− 44.3841	0.0099	10.3046	28.1461	0.0012	0.2066	0.0020
	59093.41074	− 34.3069	0.0151	10.2234	26.0449	− 0.0083	0.2102	0.0031
	59095.45922	− 28.5598	0.0098	10.1601	27.3818	0.0041	0.1988	0.0020
	59101.49898	− 20.3988	0.0089	10.2738	28.4152	− 0.006	0.2009	0.0017
	59102.51980	− 20.4328	0.0122	10.5231	27.0339	0.0343	0.1998	0.0022
	59121.39686	− 44.0417	0.0142	10.2192	24.6636	− 0.0090	0.2162	0.0028
	59123.35979	− 46.1410	0.0093	10.2626	27.3614	0.0051	0.2093	0.0018
	59131.39916	− 42.5350	0.0104	10.2861	28.3114	0.0065	0.2073	0.0021
	59137.28463	− 26.7021	0.0091	10.2698	28.7466	0.0254	0.2025	0.0018
	59154.32126	− 32.1154	0.0102	10.3170	26.7867	− 0.0023	0.2072	0.0019
	59157.36523	− 36.7752	0.0177	10.2287	25.1757	0.0102	0.2177	0.0035
	59162.32683	− 43.8233	0.0349	10.6452	24.2053	− 0.0007	0.2148	0.0072
	59165.27801	− 46.8031	0.0093	10.3282	28.3817	0.0336	0.2066	0.0019
	59172.32740	− 42.8424	0.0082	10.4652	28.6099	− 0.0162	0.2052	0.0016
B	59181.27395	− 21.7546	0.0168	10.3768	31.0919	− 0.1028	0.1955	0.0039
	59266.69524	− 20.3963	0.0109	10.3016	28.3442	0.0245	0.2087	0.0022
	59269.69460	− 22.0169	0.0109	10.3060	28.0074	0.0154	0.2067	0.0022
	59270.67941	− 22.9506	0.0118	10.2768	26.9761	0.0561	0.2142	0.0024
	59275.70395	− 29.3537	0.0133	10.2461	26.0009	− 0.0098	0.2156	0.0027
	59280.69715	− 36.9685	0.0146	10.2385	27.3492	0.0137	0.2127	0.0030
	59297.61346	− 37.7124	0.0090	10.3029	28.4720	0.0267	0.1983	0.0018
	59299.64512	− 31.8527	0.0094	10.3205	28.1204	− 0.0358	0.202	0.0019
	59303.60959	− 22.8602	0.0096	10.2401	27.2753	0.0383	0.1987	0.0019
	59305.61783	− 20.8265	0.0088	10.2858	28.0542	0.0050	0.2126	0.0018
	59349.50200	− 20.5659	0.0262	10.4567	25.5230	0.0576	0.2089	0.0054
	59354.55499	− 24.8984	0.0143	10.2426	28.2716	0.0149	0.2148	0.0031
	59363.59631	− 38.0943	0.0097	10.2586	27.9776	0.0149	0.2057	0.0020
	59366.52159	− 42.3251	0.0116	10.2845	28.0478	0.0281	0.2116	0.0024
	59369.57437	− 45.8980	0.0086	10.3087	28.8846	− 0.0363	0.2094	0.0018
	59371.53106	− 47.3490	0.0106	10.3614	28.6411	− 0.0433	0.2137	0.0022
	59375.55836	− 46.3745	0.0088	10.2746	28.9782	0.0130	0.2074	0.0018
	59378.56443	− 40.9102	0.0100	10.3196	28.9479	− 0.0039	0.2053	0.0021
	59382.54493	− 29.7562	0.0129	10.2722	28.2695	0.0240	0.2016	0.0027
	59387.49783	− 21.0110	0.0123	10.2471	26.8552	0.0086	0.2108	0.0024
	59388.44241	− 20.4912	0.0133	10.2164	26.7626	0.0178	0.2056	0.0027

[2]*Aix Marseille Univ, CNRS, CNES, LAM, Marseille, France*
[3]*Department of Physics, Shahid Beheshti University, Tehran, Iran*
[4]*Laboratoire J.-L. Lagrange, Observatoire de la Côte d'Azur, Université de Nice-Sophia Antipolis, CNRS, Campus Val-rose, F-06108 Nice Cedex 2, France*
[5]*Department of Astronomy, The Ohio State University, 4055 McPherson Laboratory, Columbus, OH 43210, USA*
[6]*CFisUC, Departamento de Física, Universidade de Coimbra, P-3004-516 Coimbra, Portugal*
[7]*IMCCE, UMR8028 CNRS, Observatoire de Paris, PSL Université, 77 av. Denfert-Rochereau, F-75014 Paris, France*
[8]*Department of Physics, University of Warwick, Gibbet Hill Road, Coventry CV4 7AL, UK*
[9]*Centre for Exoplanets and Habitability, University of Warwick, Gibbet Hill Road, Coventry CV4 7AL, UK*
[10]*Université Grenoble Alpes, IPAG, 38000, Grenoble, CNRS, IPAG, F-38000 Grenoble, France*
[11]*Centre for Exoplanet Science / SUPA, School of Physics and Astronomy, University of St Andrews, North Haugh, St Andrews, Fife, KY16 9SS, UK*
[12]*Institut d'Astrophysique de Paris, UMR7095 CNRS, Université Pierre & Marie Curie, 98bis boulevard Arago, F-75014 Paris, France*
[13]*Instituto de Astrofísica e Ciências do Espaço, Universidade do Porto, CAUP, Rua das Estrelas, P-4150-762 Porto, Portugal*
[14]*Departamento de Física e Astronomia, Faculdade de Ciências, Universidade do Porto, Rua do Campo Alegre, P-4169-007 Porto, Portugal*
[15]*Observatoire Astronomique de l'Université de Genève, Chemin de Pegasi 51, CH-1290 Versoix, Switzerland*
[16]*Astrophysics Group, Keele University, ST5 5BG, UK*
[17]*Laboratório Nacional de Astrofísica, Rua Estados Unidos 154, 37504-364, Itajubá - MG, Brazil*
[18]*Astronomy Unit, Queen Mary University of London, Mile End Road, London E 14NS, UK*
[19]*Université Paris Est Créteil and Université de Paris, CNRS, LISA, F-94010 Créteil, France*
[20]*Université Paris-Saclay, UVSQ, CNRS, CEA, Maison de la Simulation, F-91191, Gif-sur-Yvette, France*
[21]*Department of Physical and Environmental Sciences, University of Toronto at Scarborough, Toronto, Ontario M1C 1A4, Canada*

This paper has been typeset from a TEX/LATEX file prepared by the author.

Chapter 6

BEBOP-1c: The first circumbinary planet discovered with radial velocities

"There's always a bigger fish."

Qui-Gon Jinn, *Star Wars: The Phantom Menace*

On my way into the office one morning in the summer of 2019, I checked my emails on the train and found an exciting email from Amaury. *TESS* had detected its first circumbinary planet transit. Not only this, but it was in a binary system observed by us in the BEBOP south sample, EBLM J0608-59!

We rushed into action, searching for any trace of this roughly Saturn sized planet in our current data. Unfortunately, our CORALIE and HARPS data only allowed us to probe masses down to roughly 1 M_J in the system, and therefore we could see no trace of this planetary signal. Nevertheless, we provided Veselin Kostov our RV data for inclusion in their discovery paper (Kostov et al. 2020). The data allowed them to accurately determine the central binary motion and masses. Three transits of planet 'TOI-1338b' were observed by *TESS* in total, originally discovered by high school summer intern Wolf Cukier. The first page of the discovery paper is included in Section **??**.

Undeterred by our inability to detect the planet in our RV data, Amaury and I applied for additional observations through Director's Discretionary Time (DDT) on ESO's ESPRESSO spectrograph (Pepe et al. 2021). ESPRESSO is a high-resolution spectrograph situated in Paranal observatory on the Very Large Telescope (VLT) specialising in high-precision RV observations for exoplanet detection (Pepe et al. 2021). DDT is reserved for targets which require urgent observations which cannot wait for the usual observational proposal windows.

We were awarded this DDT time and obtained a further 20 observations with ESPRESSO, along with several further HARPS observations. Even with this data, we were unable to see any trace of the $\approx$ 95 day

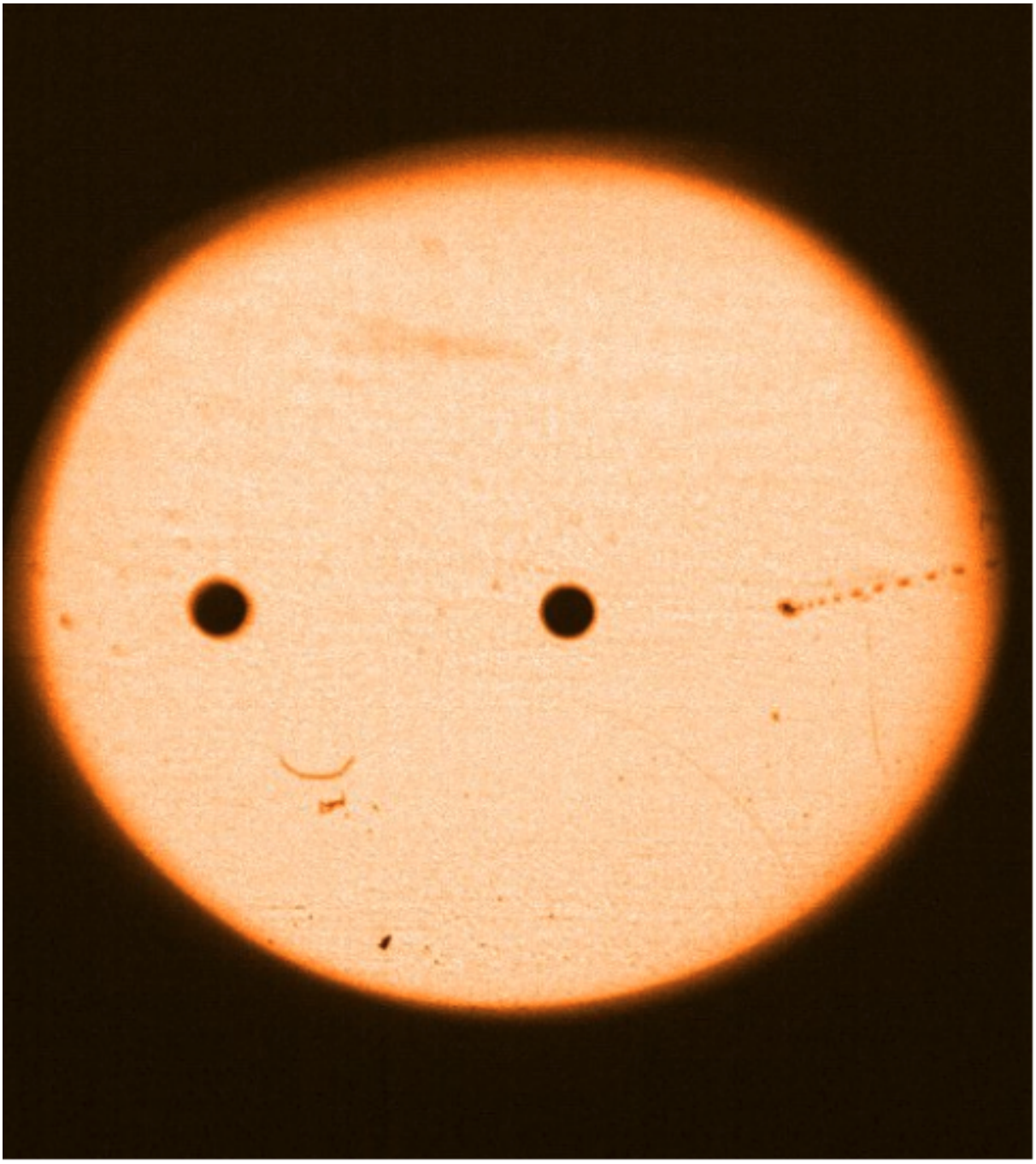

Figure 6.1: ESPRESSO instrument field of view illuminated by an homogeneous source shows ESPRESSO smiling. Picture and caption from ESPRESSO user manual .

period transiting planet. Though a signal was starting to appear out of the noise at a longer $\approx$ 220 day period.

As the rest of the UK was settling in to the first lockdown caused by the COVID-19 pandemic, I was busy writing a telescope proposal, seeking further ESPRESSO observations. For this proposal, I developed a script to simulate RV observations with any number of Keplerian signals. The script allows the user to select the number of observations required. Each simulated observation time is determined

by a random offset in night and time. The amplitude of these random offsets are specified by the user. The uncertainty of each observation is determined in a similar fashion, along with the level of scatter introduced randomly to each observation with a set amplitude. The script also allows for the use of observation times and uncertainties of current data.

From their photodynamical fit, Kostov et al. (2020) estimate the mass of the planet at 33 ± 20 $M_{\oplus}$. Assuming the lowest mass of 13 $M_{\oplus}$, analysis of my simulations showed that to confirm the inner transiting planet TOI-1338b, along with the additional ≈ 220 day candidate signal, we would require an additional 38 hours of ESPRESSO observations spread over two observing periods. Spreading out the observations would allow us to cover two orbital periods of the inner planet, and a full orbit of the outer candidate signal. In order to cover two orbital periods we applied for a 'monitoring proposal', so named as the target is monitored for longer than one observing period.

The requested time was awarded with the highest priority. The proposal ranked in the 1st quartile of all proposals for the telescope, and in the 1st quartile of all proposals during the observing period.

Results from the analysis of this data can be found in the following sections.

6.1 The ESPRESSO Pipeline

Once observations are taken at the VLT with ESPRESSO, the raw observational data require reduction using the ESPRESSO pipeline to obtain the RV values required for analysis.

The ESPRESSO pipeline can be downloaded from here[a], and its user manual is available in the same web page. The pipeline applies several corrections to the raw data based on the calibration data available.

Each '.fits' file downloaded can have an uncompressed size of > 300 MB, and for a single raw observation data file with all associated raw calibrations, the compressed file size can amount to ≈ 30 GB. Due to the file sizes involved, I recommend installing the pipeline and downloading the data on a computer with adequate storage (> 1 TB) to avoid having to reduce the data in batches. Though with large observing runs, this may be unavoidable.

In Appendix A, I present a step-by-step guide to using the ESPRESSO pipeline (V.2.3.5).

6.1.1 FWHM larger in ESPRESSO compared to HARPS

When initially experimenting with the EBLM J0608-59 data, I noticed in my data quality sheets (Section 4.2.3) that the Full Width at Half Maximum (FWHM) of the ESPRESSO data was larger than expected, and in fact larger than the FWHM from our HARPS data on the same target. With ESPRESSO's higher resolution, one would expect the width of the CCF to be smaller.

Puzzled by this, I contacted Pedro Figuera ESO staff astronomer and the ESO helpdesk with the query. After providing further details along with my inspection of individual spectral lines, the ESPRESSO consortium were consulted and a conclusion was reached. The FWHM of individual spectral lines are smaller with ESPRESSO when compared to those obtained with HARPS as is expected. However, due to

[a] https://www.eso.org/sci/software/pipelines/espresso/espresso-pipe-recipes.html

differences in the line weighting schemes and algorithms for CCF computation between the HARPS and ESPRESSO pipelines, the HARPS data reduced with the HARPS pipeline will have a smaller FWHM when compared to ESPRESSO data reduced with the ESPRESSO pipeline for the same target.

This information is now part of the data reduction *'Frequently Asked Questions (FAQ)'*, and can be viewed here[b].

6.2 Detection of circumbinary planet TOI-1338/BEBOP-1c

Following the re-opening of Paranal and La Silla observatories after COVID closures, final observations of EBLM J0608-59 (TOI-1338) were collected in March 2022. Once I had reduced and analysed the HARPS and ESPRESSO data combined, I was able to claim a formal detection of a 215 day period, 69 $M_\oplus$ second circumbinary planet around the EBLM J0608-59 binary star system, my first planet detection. This makes EBLM J0608-59/TOI-1338 the first entry in the BEBOP catalogue of circumbinary planet systems and henceforth BEBOP-1. This second planet, TOI-1338/BEBOP-1c, is the first circumbinary planet discovered by RV observations alone, with TOI-1338/BEBOP-1 being the second multi-planetary circumbinary system discovered.

Unfortunately, our final RV data-set yields no trace of the RV signal caused by the 95 day period transiting planet TOI-1338/BEBOP-1b published in Kostov et al. (2020). With our data, we can place a 99% upper limit on the mass of BEBOP-1b at < 23.6 $M_\oplus$. Therefore, with a radius of 6.9 $R_\oplus$ (Kostov et al. 2020), the inner planet has a mean planetary density < 0.39 g.cm^{-3}, which is less dense than a Victoria Sponge cake![c]

The full analysis on the system can be found in the paper below. I lead the following research, applied for and obtained the observing time, reduced and analysed the RV data, and wrote and organised the manuscript. Co-author contributions are as follows: Lalitha Sairam performed the stellar activity analysis confirming the planetary nature of the planet, and wrote the 'Stellar activity' section. Vedad Kunovac created the majority of the figures for the paper. Amaury H. M. J. Triaud revised and assisted with the generation of the manuscript. Gavin Coleman and Richard P. Nelson carried out formation simulations for the system and wrote the 'System formation' section. Alexandre C. M. Correia performed a stability analysis on the system, and wrote the 'System dynamics' section, assisted by David V. Martin. Thomas A. Baycroft identified outliers in the RV data, and calculated the False Inclusion Probability (FIP) and True Inclusion Probability (TIP) for the system, writing the associated subsection, with assistance from Nathan Hara. Georgina Dransfield calculated the Transmission Spectroscopy Metric (TSM) for the inner planet and wrote the 'Prospects for atmospheric follow-up with JWST' section.

The journal of observations providing the RV data used in the analysis has been removed from the paper to save space, it can be found in the online version. Alternatively, I would be happy to provide it upon request.

[b] https://www.eso.org/sci/data-processing/faq/should-i-expect-the-fwhm-of-the-cross-correlation-function-ccf-of-espresso.html

[c] https://bakerpedia.com/processes/specific-gravity-cakes/

The First Circumbinary Planet Discovered with Radial Velocities

Matthew R. Standing[1*], Lalitha Sairam[1], David V. Martin[2,3], Amaury H. M. J. Triaud[1], Alexandre C. M. Correia[4,5], Vedad Kunovac[6], Gavin Coleman[7], Thomas A. Baycroft[1], Isabelle Boisse[8], Andrew Collier Cameron[9], Georgina Dransfield[1], João P. Faria[10,11], Michaël Gillon[12], Nathan C. Hara[13], Coel Hellier[14], Jonathan Howard[1], Ellie Lane[1], Rosemary Mardling[15], Pierre F. L. Maxted[14], Nicola J. Miller[14], Richard P. Nelson[7], Jerome A. Orosz[16], Franscesco Pepe[13], Alexandre Santerne[8], Daniel Sebastian[1], Stéphane Udry[13], William F. Welsh[16]

[1]School of Physics and Astronomy, University of Birmingham, Edgbaston, Birmingham B15 2TT, UK

[2]Department of Astronomy, The Ohio State University, 4055 McPherson Laboratory, Columbus, OH 43210, USA

[3]NASA Sagan Fellow

[4]CFisUC, Departamento de Física, Universidade de Coimbra, 3004-516 Coimbra, Portugal

[5]IMCCE, UMR8028 CNRS, Observatoire de Paris, PSL Université, 77 av. Denfert-Rochereau,75014 Paris, France

[6]Lowell Observatory, 1400 W. Mars Hill Rd., Flagstaff, AZ 86001, USA

[7]Astronomy Unit, Queen Mary University of London, Mile End Road, London E1 4NS, UK

[8]Aix Marseille Univ, CNRS, CNES, Institut Origines, LAM, Marseille, France

[9] Centre for Exoplanet Science / SUPA, School of Physics and Astronomy, University of St Andrews, North Haugh, St Andrews, Fife, KY16 9SS, UK

[10] Instituto de Astrofíisica e Ciências do Espaço, Universidade do Porto, CAUP, Rua das Estrelas, 4150-762 Porto, Portugal

[11] Departamento de Física e Astronomia, Faculdade de Ciências, Universidade do Porto, Rua do Campo Alegre, 4169-007 Porto, Portugal

[12] Astrobiology Research Unit, University of Liège, Allée du 6 août 19 (B5C), 4000 Liège (Sart-Timan), Belgium

[13] Observatoire Astronomique de l'Université de Genève, Chemin de Pegasi 51, 1290 Versoix, Switzerland

[14] Astrophysics Group, Keele University, ST5 5BG, UK

[15] School of Physics and Astronomy, Monash University, Victoria, 3800, Australia

[16] Department of Astronomy, San Diego State University, 5500 Campanile Drive, San Diego, CA 92182, USA

We report the detection of a gas-giant planet in orbit around both stars of an eclipsing binary star system that also contains the smaller, inner transiting planet TOI-1338b. The new planet, called BEBOP-1c, was discovered using radial-velocity data collected with the HARPS and ESPRESSO spectrographs. Our analysis reveals it is a $0.2\ \mathrm{M_{Jup}}$ circumbinary planet with a period of 215 days. This is the first detection of a circumbinary planet using radial-velocity observations alone, and makes BEBOP-1 only the second confirmed multiplanet circumbinary system to date. We do not detect the smaller inner transiting planet with radial-velocity data, and can place an upper limit on the inner planet's mass at $23.6\ \mathrm{M_{\oplus}}$ with 99% confidence. The inner planet is the first circumbinary planet amenable for atmospheric characterisation, using the James Webb Space Telescope.

Circumbinary planets are planets that orbit both stars of a central binary. They were once confined to science fiction, but the discovery of Kepler-16b (*1*) paved the way for the discovery of 14 transiting planets in 12 binary systems, by the *Kepler* (*2*) and *TESS* (*3*) missions. Of the 12 transiting circumbinary planet systems discovered to date only one hosts multiple circumbinary planets, Kepler-47. Kepler-47 b, d and c have orbital periods of 49.5, 187.4, and 303.2 days respectively (*4*), with c's orbit placing it within the system's habitable zone. Planet forming disks around binaries are harsh environments for planet formation to take place, and circumbinary planet discoveries provide insights into the formation and migration mechanisms at play in these unique environments (*5–8*).

Of the 14 confirmed transiting circumbinary planets discovered to date, there are only significant mass detections (different from zero at $> 2\sigma$) for six of them. These are: Kepler-34 b and 35 b (*9*), TIC 17290098 b (*10*), Kepler-16 b (*1, 11*), Kepler-47 c and d (*4*). Where the masses were determined from binary eclipse timing variations (ETV's) alone. For the remaining eight

circumbinary planets only upper limits can be placed on their masses, because the ETV's are on the order of only seconds or minutes, and hence difficult to measure. Their masses could therefore be much lower than expected and reveal several inflated objects, ideal targets for atmospheric transmission follow-up observations (*12*). To correctly characterise these planets, accurate masses are required.

To increase the number of known circumbinary planets, and to provide accurate masses for systems discovered with the transit method, we initiated a radial-velocity observing survey dedicated to circumbinary planet detection called Binaries Escorted By Orbiting Planets (BEBOP) (*13*). Systems followed by BEBOP are on average 4 visual magnitudes brighter than circumbinary systems identified with *Kepler* (*13*). Radial velocities are less restricted to the edge-on and shorter orbital periods found by the transit method (*14*). Despite initial challenges in bringing radial-velocity precision for binaries down to values where planets can be detected (*15*), recent results have produced an independent detection of Kepler-16b with a precision of $1.5\ \mathrm{m.s^{-1}}$, resulting in a planetary mass in agreement with ETV measurements (*11*).

The first circumbinary planet discovered by NASA's Transiting Exoplanet Survey Satellite (TESS) (*3*) was TOI-1338 b (*16*). TOI-1338 is low mass eclipsing binary system, which consists of a $1.13\ \mathrm{M_\odot}$ F8-type primary star with a visual magnitude of $V = 11.7$ (*16, 17*), and a $0.31\ \mathrm{M_\odot}$ M-dwarf companion. This system was already being monitored with radial velocities with HARPS (*18*) as part of the BEBOP project, where the target was known as EBLM J0608-59 (*13, 17*). Radial-velocity data available at the time were unable to detect any trace of TOI-1338b, the $33 \pm 20\ \mathrm{M_\oplus}$, Saturn-sized planet announced by Kostov et al. (2020) (*16*). To constrain the mass of this planet, we used the ESPRESSO spectrograph at the Very Large Telescope (*19*). Meanwhile we continued to observe with HARPS intermittently in order to combine both datasets more easily, and in order to mitigate observatory closures caused by the COVID pandemic. In total, we collected 123 ESPRESSO, and 61 HARPS spectra covering a timespan

of 1472 days.

We analyse our radial-velocity data with the diffusive nested sampler implemented in `kima` (*20*). Further details can be found in the supplementary material, but we note here that a particularly useful feature of `kima` is that the number of planetary signals in the data can be included as a free parameter in the analysis. The number of planets detected is determined from the ratio of evidence between models with different number of planets. The radial-velocity data favours a one-planet model over a zero-planet model with a ratio of probability (Bayes factor) $> 9,300$ (where > 150 is the typical threshold for detection). The same analysis provides a Bayes factor of only 1.4 in favour of a two-planet model over a one-planet model, far below the detection threshold. Therefore, only one planetary signal is formally detected in our data.

Figure 1 depicts a histogram of the posterior samples obtained from our analysis. There are two peaks, one at the binary orbital period of 14.6 days, and a single additional excess at 215.1 days. Since this periodicity does not correspond to the 95 day period of the transiting planet (*16*), and an outer orbit significantly improves the fit, we conclude the detected planetary signal is likely that of an additional, outer circumbinary planet within the system. We therefore give the system the name BEBOP-1, becoming the first entry in the BEBOP catalog for circumbinary planets detected with radial velocities, with the new signal being BEBOP-1c. Figure 2 shows a phase-folded plot of the radial-velocity variation caused by BEBOP-1c, with a semi-amplitude $K_{\rm c} = 5.89 \pm 0.97$ $\rm m.s^{-1}$, corresponding to a minimum mass $m_{\rm c} \sin i_{\rm c} = 0.217 \pm 0.035$ $\rm M_{Jup}$. Parameters of the binary and planetary orbits, obtained from our model fit to the radial velocities are available in Table 1. We calculate the True Inclusion Probability (TIP) (*21, 22*) for our posterior samples which also provides a clear $> 99.9\%$ probability of the presence of a planetary signal at a period of 215.1 days. Further details can be found in the supplementary material.

Stellar magnetic activity can produce periodic modulations in radial velocity over a wide

range of timescales sometimes mimicking a planetary companion (*23*). To verify if this is the case for the BEBOP-1c signal, we search for periodic signals in five spectroscopic activity indices (see supplementary material for details).

Stellar activity has been shown to affect most, if not all of these five indices at once (*24*). In our case, only two show any signal. Furthermore, at shorter periods neither Ca II H+K nor Hα indices produce any significant peak. Combining the stellar radius and projected rotational velocity of BEBOP-1, a rotation period of 19 ± 3 days has been reported (*16*). We do not find any statistically significant signal at the estimated rotation period.

Our analysis of activity indices rules out any association between the 215 day radial-velocity variation and stellar activity, supporting the hypothesis for BEBOP-1c's planetary nature. Further details and figures are provided in the supplementary material.

A visual inspection of *TESS* lightcurves shows no transit of BEBOP-1c, however, thanks to orbital circulation, transits are expected to occur in due time. Circumbinary orbits exhibit nodal precession. This changes the orientation of a circumbinary planet's orbital plane with respect to both the binary and the observer. This makes a planet change from a transiting to a non-transiting configuration (*14, 25*) as has been seen in a few systems (*26, 27*). Using an analytic criterion (*28, 29*), we find that BEBOP-1c is *guaranteed to eventually transit* mainly because the binary is so well-aligned with our line of sight ($I_{\rm bin} = 89.658^\circ$) combined with the rather large size of the primary star ($R_{\rm A} = 1.299 R_\odot$). Whilst BEBOP-1c will *eventually* transit, we are unable to predict when and how frequently. Its precession period is of order 119 years, during which time there will be two periods of transitability of a duration depending on BEBOP-1c's orbital inclination.

While we are confident the radial-velocity signal we detect is that of a circumbinary planet, it is also worth verifying whether the system as we propose it is plausible. A global stability analysis of the system shows it is stable when the two circumbinary planets are in nearly circu-

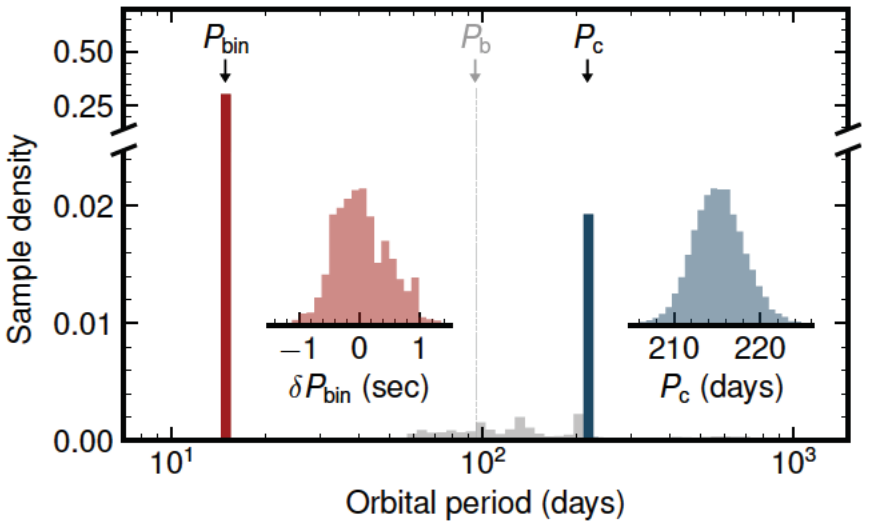

Figure 1: Histogram periodogram of posterior samples obtained from a `kima` run on the BEBOP-1 system. The 14.6 day binary period along with the 215.6 day period of BEBOP-1c can be clearly seen, and are highlighted in red and blue respectively. The inlaid plots show a zoom on these two peaks. No significant peak from BEBOP-1b can be seen in these posterior samples.

lar and coplanar orbits (see supplementary material). More precisely, the eccentricities of both planets cannot exceed 0.1, in agreement with the best fit solution (Table 1). The inclination of planet c, i_c, is unconstrained by the radial velocities, however, thanks to orbital stability arguments, it cannot be higher than 40° with respect to the orbital plane of the binary, corresponding to a maximum mass of $m_{\max,c} = 0.28\ \mathrm{M_{Jup}}$.

The influence of the central binary means that circumbinary planets have unique formation pathways, and it is noteworthy that the system discussed in this paper is only the second system known to host multiple planets. Hydrodynamical simulations have shown that the preference for observed circumbinary planets to be located close to the stability boundary can be explained by formation at large distances in circumbinary discs, followed by inwards migration and stalling at the edge of the inner cavities formed by the central binaries (*30–32*). We have utilised a purpose-built simulation code to study the formation of circumbinary planets as

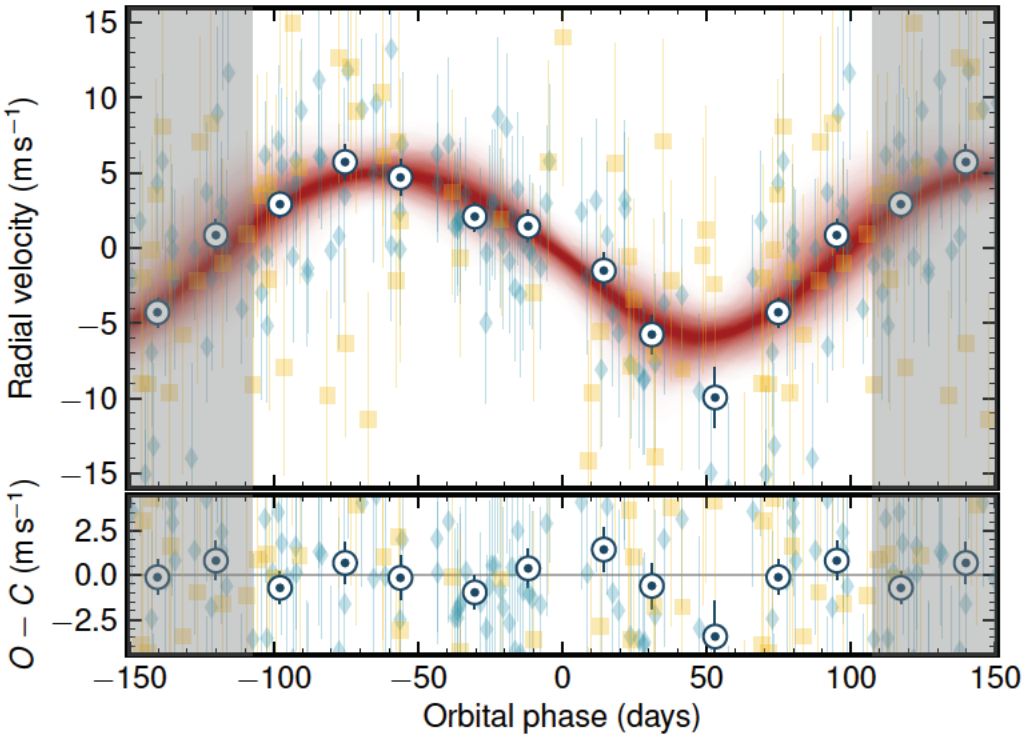

Figure 2: Phased Keplerian Radial-Velocity (RV) models of BEBOP-1c with ESPRESSO (blue diamonds) and HARPS (orange squares) data along with associated residuals after removing the binary signal. RV data is binned by 0.1 phase units ($\sim$21.6 days) and illustrated by the circular points. Red Keplerian models are based on 500 randomly drawn posterior samples from a `kima` run, shaded from the 50^{th} to 99^{th} percentiles. The shaded regions display the repeating signal.

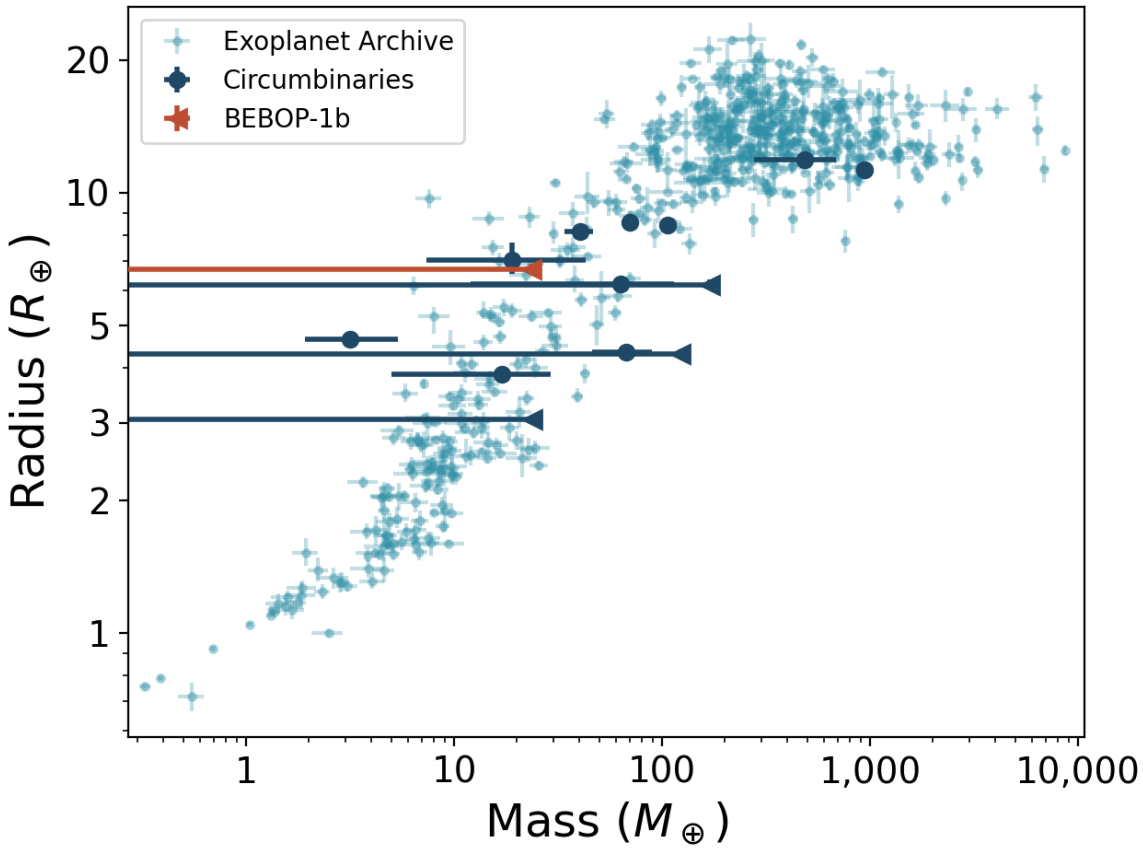

Figure 3: Radius vs Mass plot of all transiting circumbinary planets (dark blue) and planets orbiting single stars (light blue). BEBOP-1b is highlighted in orange, with one of the lowest densities known. The newly-discovered BEBOP-1c is not on the graph since it does not transit. For the single star planets we restrict the sample to planets with mass and radius percentage errors less than 20%.

a means of understanding plausible formation scenarios for the BEBOP-1 system. The model includes the N-body integrator MERCURY6, adapted to include a central binary system (*33, 34*), and it incorporates prescriptions for a viscous circumbinary disc that includes the effects of an eccentric, precessing central cavity and photoevaporative winds (*35*), pebble accretion onto planetary seeds (*36*), planet migration (*37*), and gas accretion onto growing planets (*38, 39*). Our suite of simulations produced numerous systems that were qualitatively similar to BEBOP-1 (see additional material), with BEBOP-1b and c analogues landing on stable orbits at their observed locations.

With no detection of the 95 day planet in our data the best we can do is to calculate a detection limit for this period region. We find that BEBOP-1b has a mass $< \ 23.6\ \mathrm{M}_{\oplus}$ with 99% confidence. This is a tighter constraint than, but compatible with, the $33 \pm 20\ \mathrm{M}_{\oplus}$ from ETV's (*16*). Combined with a planetary radius of $\approx 6.9\ \mathrm{R}_{\oplus}$ (*16*), BEBOP-1b has a maximum mean planetary density $< 0.39\ \mathrm{g.cm}^{-3}$. This allows us to calculate the Transmission Spectroscopy Metric (TSM) (*12*) for planet b using the upper limit on the mass ($< \ 23.6\ \mathrm{M}_{\oplus}$); this yields a minimum TSM value of > 27 (see supplementary material). Of the now 15 known circumbinary exoplanets, BEBOP-1b is the only one for which James Webb Space Telescope transmission spectroscopy can currently be pursued. If we are to unveil the mysteries of circumbinary Tatooine-like exo-atmospheres, the BEBOP-1 system provides a new hope.

References

1. L. R. Doyle, *et al.*, *Science* **333**, 1602 (2011).

2. W. J. Borucki, *et al.*, *Science* **327**, 977 (2010).

3. G. R. Ricker, *et al.*, *Journal of Astronomical Telescopes, Instruments, and Systems* **1**, 14003 (2015).

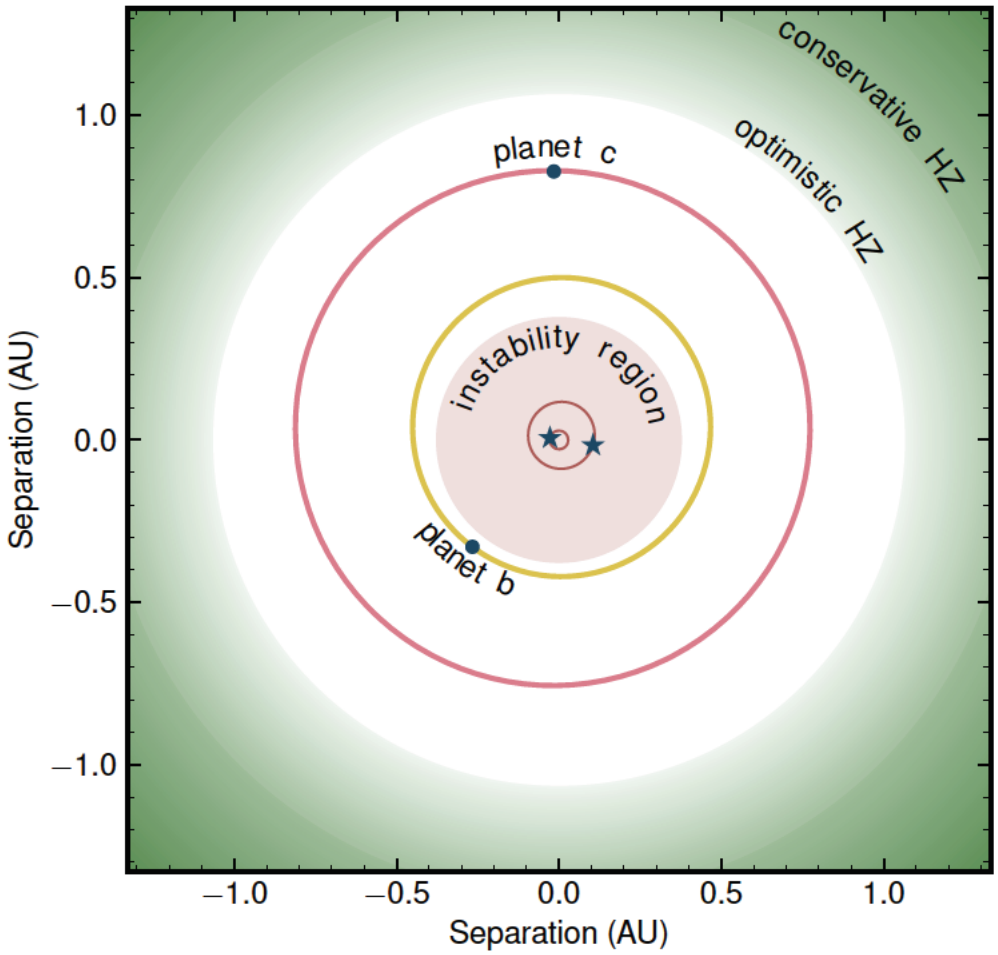

Figure 4: Overview of the BEBOP-1 system along with the extent of the systems habitable zone. The conservative habitable zone is shown by the dark green region, while the optimistic habitable zone is shown by the light green region. Binary stars are marked by the blue stars in the centre. BEBOP-1c's orbit is shown by the red orbit models, based on 500 randomly drawn posterior samples from a `kima` run, shaded from the 50^{th} to 99^{th} percentiles. BEBOP-1b's orbit is shown by the yellow models, and is also based on 500 random samples drawn from the posterior in its discovery paper (*16*).

Table 1: BEBOP-1 system orbital parameters from our analysis of the ESPRESSO and HARPS radial velocities, after removing outliers. 1σ uncertainties are provided as the last two significant digits, within brackets. Dates are given in BJD - 2,450,000. * from Kostov et al. (2020) (*16*), ** from Triaud et al. (2017) (*17*).

Binary parameters		
$P_{\rm bin}$	day	14.6085576(65)
$T_{0,\rm bin}$	BJD	8206.16755(94)
$K_{1,\rm bin}$	$\rm km\,s^{-1}$	21.61693(71)
$e_{\rm bin}$	–	0.155518(30)
$\omega_{\rm bin}$	rad	2.05572(26)
M_1	$\rm M_\odot$	1.127(69)*
R_1	$\rm R_\odot$	1.345(46)*
M_2	$\rm M_\odot$	0.313(12)
$a_{\rm bin}$	AU	0.1321(25)
$T_{\rm eff,1}$	K	6050(80)*
$V_{\rm mag,1}$	–	11.72(02)*
Spectraltype	–	F8**
Planet b parameters		
$P_{\rm b}$	day	95.174(35)*
$K_{\rm b}$	$\rm m\,s^{-1}$	$< 2.6(0.1)$
$e_{\rm b}$	–	0.0880(43) *
$m_{\rm b}$	$\rm M_\oplus$	$< 23.6(0.9)$
$m_{\rm b}$	$\rm M_{Jup}$	$< 0.0742(29)$
$a_{\rm b}$	AU	0.4607(88)*
$\rho_{\rm b}$	$\rm g.cm^{-3}$	$< 0.39^{+0.02}_{-0.01}$
Planet c parameters		
$P_{\rm c}$	day	215.1(3.0)
$T_{0,\rm c}$	BJD	8130.1(39.3)
$K_{\rm c}$	$\rm m\,s^{-1}$	5.89(0.97)
$e_{\rm c}$	–	< 0.15
$\omega_{\rm c}$	rad	3.78(94)
$m_{\rm c}\sin i_{\rm c}$	$\rm M_\oplus$	69.1(11.2)
$m_{\rm c}\sin i_{\rm c}$	$\rm M_{Jup}$	0.217(35)
$a_{\rm c}\sin i_{\rm c}$	AU	0.793(15)
System parameters		
γ	$\rm km\,s^{-1}$	30.7620(11)
Instrumental		
$\rm Jitter_{HAR}$	$\rm m\,s^{-1}$	$5.2^{+1.6}_{-2.2}$
$\rm Jitter_{ESP19}$	$\rm m\,s^{-1}$	$3.0^{+2.2}_{-2.5}$
$\rm Jitter_{ESP21}$	$\rm m\,s^{-1}$	4.4(0.6)
$\rm RV\ Offset_{ESP19}$	$\rm m\,s^{-1}$	$-146.4^{+1.9}_{-1.7}$
$\rm RV\ Offset_{ESP21}$	$\rm m\,s^{-1}$	-151.0(1.3)

4. J. A. Orosz, *et al.*, *The Astrophysical Journal* **157**, 174 (2019).

5. S. Meschiari, *ApJ* **752**, 71 (2012).

6. S. Lines, Z. M. Leinhardt, S. Paardekooper, C. Baruteau, P. Thebault, *ApJl* **782**, L11 (2014).

7. A. Pierens, C. P. McNally, R. P. Nelson, *MNRAS* **496**, 2849 (2020).

8. D. V. Martin, E. Fitzmaurice, *MNRAS* (2022).

9. W. F. Welsh, *et al.*, *Nature* **481**, 475 (2012).

10. V. B. Kostov, *et al.*, *The Astrophysical Journal* **162**, 234 (2021).

11. A. H. M. J. Triaud, *et al.*, *MNRAS* **511**, 3561 (2022).

12. E. M. R. Kempton, *et al.*, *PASP* **130**, 114401 (2018).

13. D. V. Martin, *et al.*, *A&A* **624**, A68 (2019).

14. D. V. Martin, A. H. M. J. Triaud, *A&A* **570**, A91 (2014).

15. M. Konacki, M. W. Muterspaugh, S. R. Kulkarni, K. G. Hełminiak, *ApJ* **704**, 513 (2009).

16. V. B. Kostov, *et al.*, *The Astrophysical Journal* **159**, 253 (2020).

17. A. H. Triaud, *et al.*, *A&A* **608**, A129 (2017).

18. F. Pepe, *et al.*, *The Messenger* **110**, 9 (2002).

19. F. Pepe, *et al.*, *A&A* **645**, A96 (2021).

20. J. P. Faria, N. C. Santos, P. Figueira, B. J. Brewer, *The Journal of Open Source Software* **3**, 487 (2018).

21. N. C. Hara, N. Unger, J.-B. Delisle, R. Díaz, D. Ségransan, *arXiv e-prints* p. arXiv:2105.06995 (2021).

22. N. C. Hara, T. de Poyferré, J.-B. Delisle, M. Hoffmann, *arXiv e-prints* p. arXiv:2203.04957 (2022).

23. D. Queloz, *et al.*, *A&A* **379**, 279 (2001).

24. J. Gomes da Silva, *et al.*, *A&A* **534**, A30 (2011).

25. J. Schneider, *Planetary Space Science* **42**, 539 (1994).

26. V. B. Kostov, *et al.*, *The Astrophysical Journal* **784**, 14 (2014).

27. W. F. Welsh, *et al.*, *ApJ* **809**, 26 (2015).

28. D. V. Martin, A. H. Triaud, *MNRAS* **449**, 781 (2015).

29. D. V. Martin, *MNRAS* **465**, 3235 (2017).

30. A. Pierens, R. P. Nelson, *A&A* **472**, 993 (2007).

31. A. Pierens, R. P. Nelson, *A&A* **478**, 939 (2008).

32. A. B. T. Penzlin, W. Kley, H. Audiffren, C. M. Schäfer, *A&A* **660**, A101 (2022).

33. J. E. Chambers, *MNRAS* **304**, 793 (1999).

34. J. E. Chambers, E. V. Quintana, M. J. Duncan, J. J. Lissauer, *The Astrophysical Journal* **123**, 2884 (2002).

35. G. A. L. Coleman, T. J. Haworth, *MNRAS* **514**, 2315 (2022).

36. M. Lambrechts, A. Johansen, *A&A* **572**, A107 (2014).

37. S.-J. Paardekooper, C. Baruteau, W. Kley, *MNRAS* **410**, 293 (2011).

38. G. A. L. Coleman, J. C. B. Papaloizou, R. P. Nelson, *MNRAS* **470**, 3206 (2017).

39. S. T. S. Poon, R. P. Nelson, G. A. L. Coleman, *MNRAS* **505**, 2500 (2021).

Author contributions

The BEBOP project was established by DVM, and AHMJT, building on work by the WASP consortium that involved AHMJT, IB, ACC, MG, CH, PFLM, FP, AS and SU. The radial velocity (RV) data used in this manuscript were secured and obtained by MRS, AHMJT, LS, DVM, VK, DS, TAB, PFLM, NJM, and AS and their reduction involved MRS, AHMJT, FP and SU. The observational campaign was led by MRS for ESPRESSO observations, and AHMJT for HARPS. RV analysis was led by MRS with assistance from AHMJT, DVM, and JPF. Outliers in RV data were identified by TAB, and MRS. Detection limit analysis was performed by MRS, JH, and EL with help from JPF. TIP and FIP analysis was carried out by TAB, and NCH. Analysis of stellar activity was carried out by LS, MRS, and AHMJT. Independent stability analysis on the system was carried out by ACMC, and DVM with inputs from RM. Formation pathway simulations were carried out by GALC and RPN. The Transmission Spectroscopy Metric (TSM) was calculated by GD. The system was identified to have an inner transiting planet TOI-1338/BEBOP-1b by DVM, JAO and WFW. VK prepared the majority of figures in the paper. All co-authors assisted in writing and reviewing the manuscript.

Acknowledgments

We would like to thank the ESO staff at La Silla and Paranal for their continued support throughout this work, especially through the COVID pandemic. With special thanks to our ESPRESSO support astronomer M. Wittkowski.

We also thank all of the observers who took part in the HARPS timeshare and were instrumental in collecting data for this projects. We particularly thank X. Dumusque and F. Bouchy for their work organising the timeshare.

This paper is based on observations collected at the European Southern Observatory under ESO programmes 103.2024, 106.216B, 1101.C-0721 and 106.212H. This research has made use of the services of the ESO Science Archive Facility.

This work made use of the Astropy, numpy, pandas, scipy, corner, and matplotlib packages.

This research received funding from the European Research Council (ERC) under the European Union's Horizon 2020 research and innovation programme (grant agreement n° 803193/BEBOP) and from the Leverhulme Trust (research project n° RPG-2018-418).

MRS would like to acknowledge the support of the UK Science and Technology Facilities Council (STFC).

ACMC acknowledges support from CFisUC (UIDB/04564/2020 and UIDP/04564/2020), GRAVITY (PTDC/FIS-AST/7002/2020), PHOBOS (POCI-01-0145-FEDER-029932), and ENGAGE SKA (POCI-01-0145-FEDER-022217), funded by COMPETE 2020 and FCT, Portugal. The stability maps were performed at the OBLIVION Supercomputer (HPC Center - University of Évora), funded by ENGAGE SKA and by the BigData@UE project (ALT20-03-0246-FEDER-000033).

VK acknowledges support from NSF award AST2009501.

The project leading to this publication has received funding from the french government under the "France 2030" investment plan managed by the French National Research Agency (reference : ANR-16-CONV-000X / ANR-17-EURE-00XX) and from Excellence Initiative of Aix-Marseille University - A*MIDEX (reference AMX-21-IET-018). This work was supported by the "Programme National de Planétologie" (PNP) of CNRS/INSU.

JPF is supported in the form of a work contract funded by national funds through Fundação

para a Ciência e a Tecnologia (FCT) with reference DL57/2016/CP1364/CT0005.

ACC acknowledges support from STFC consolidated grant numbers ST/R000824/1 and ST/V000861/1, and UKSA grant number ST/R003203/1.

MG is FNRS Senior Research Associate

This research utilised Queen Mary's Apocrita HPC facility, supported by QMUL Research-IT (http://doi.org/10.5281/zenodo.438045).

Supplementary materials

Collected Observations

Modelisation of the data

Stellar Activity

System Dynamics

System Formation

Prospects for atmospheric follow-up with JWST

Journal Of Radial-Velocity Observations

Tables S1 to S4

Figures S1 to S7

References *(40-68)*

Supporting Online Material

In this supplementary material we present additional methods and details in support of our main article "The First Circumbinary Planet Discovered with Radial Velocities". The material is organised as follows, in Section 1 we describe the collected observations for the discovery, along with outlier removal. Section 2 presents the orbital fitting and data analysis techniques utilised, along with constraints on additional planetary companions in the system. Section 3 provides an overview of the stellar activity analysis on the system. In Section 4 we discuss the stability of the system, and in Section 5 we discuss formation pathways for the planetary system. Section 6 hosts discussion on atmospheric follow-up observations of system. The Radial-Velocity data used in the analysis is available in Section 7.

1 Collected Observations

BEBOP-1 was selected for the Binaries Escorted By Orbiting Planets (BEBOP) programme (*1*) from a large sample of low-mass eclipsing binaries identified by the EBLM project (*2*) under the name EBLM J0608-59. Those binaries were detected as part of the Wide Angle Search for Planets (WASP), as candidate transiting planet which were later shown with using radial velocities to be "false positive" eclipsing binaries. To be part of the EBLM and BEBOP sample, a system needs to be a single-lined eclipsing binary. For identification and selection,

the southern sample exclusively used the CORALIE spectrograph ($R \sim 45,000$; mounted on the 1.2m *Euler* Swiss telescope, at La Silla, Chile).

The BEBOP sample represents a sub-sample of the EBLM sample, where the binaries are selected to optimise planet-finding capability. The main discriminator is the obtainable radial-velocity precision, which is typically a function of magnitude. There is also a bias to wider (5 days) binaries, since rapid rotation due to tidal locking broadens spectral lines and reduces precision. Fortunately, the *Kepler* results in fact show a dearth of planets transiting the tightest binaries (*3*). We also progressively remove binaries where a long-term radial velocity trend reveals a presence of a third star, which is believed to have a detrimental impact on planet occurrence (*3*). Finally, systems are also removed based on simple activity indicators just as the line bisector (*4*). Greater details about the selection process can be found in (*1*).

There exists 55 radial velocities obtained with CORALIE, which are not used in this paper. Their typical uncertainty is $25\ \mathrm{m\,s^{-1}}$, much higher than the signal we identify. Some of them were used to determine the spin–orbit angle of the binary (*5*).

1.1 HARPS

HARPS is a high-resolution, high-precision échelle spectrograph built for the detection of exo-planets (*6*). It has a resolution $R \sim 100,000$ and typically achieves a long-term stability under $1\ \mathrm{m\,s^{-1}}$. It is mounted on the ESO 3.6m telescope at La Silla, Chile.

The southern BEBOP sample, including BEBOP-1 (under the name J0608-59) were observed by HARPS under two ESO large observing programmes (prog.ID 1101.C-0721 and 106.212H; PI Triaud). BEBOP-1 received 61 spectra between the dates of 2018-04-08 and 2022-04-18. Typically exposure times of 1800s were obtained, with a median radial-velocity precision of $5.73\ \mathrm{m\,s^{-1}}$.

HARPS data were reduced by HARPS Data Reduction Software (DRS) version 3.5 (which

is hosted at the Observatory of Geneva, and will be made public in a few months). A description of how the DRS works can be found in (*7*) and in (*8*). Spectra are correlated using a weighted numerical mask matching the spectral type of the target producing a cross-correlation function (CCF). A Gaussian function is fitted to the CCF to find the mean radial velocity.

Version 3.5 of the DRS is not very different from the version held by ESO but it allowed us to recorrelate the spectra with our own specification. The standard DRS is built to study single, slow rotating stars. It assumes two quantities: a common mean radial velocity for all spectra of a given system, and a correlation window of $30\ \mathrm{km\,s^{-1}}$ on either side of that mean velocity. In the case of binaries, the velocity changes according to the binary phase. In addition some of the BEBOP sample targets rotate fast enough that a $30\ \mathrm{km\,s^{-1}}$ window is not adequate. Using version 3.5 allowed us to centre the correlation window to the observed velocity at each epoch, thus ensuring the same set of absorption lines are used to produce the radial velocities, epoch after epoch. For BEBOP-1 we used the standard $30\ \mathrm{km\,s^{-1}}$ correlation window and a G2 mask to produce the cross-correlation window. The reduction software provides the radial velocity, its uncertainty (determined from photon noise and the line width), the line width (FWHM), the span of the bisector slope (Bis_Span), and automatically produced corrections to the barycentre of the Solar system.

All HARPS data are available at the ESO public archive by searching for J0608-59, and can be found in Table 2 in this supplementary material.

1.2 ESPRESSO

Following the discovery of TOI-1338b (*9*), 20 radial-velocity measurements were obtained in 2019 with the ESPRESSO spectrograph located in Paranal, Chile (*10*) in an attempt to confirm the planet and more accurately constrain its mass (Prog.ID 103.2024, PI Triaud). Exposure times were typically $900\ \mathrm{s}$ in length and yielded a median precision of $2.83\ \mathrm{m\,s^{-1}}$. These data

combined with previously obtained HARPS spectra yielded no detection of BEBOP-1b, but hinted at the presence of an outer companion planet with an orbital period of ≈ 200 days. To confirm this candidate planet and attempt to detect the inner transiting planet, a further 103 ESPRESSO spectra were obtained with exposure times of 900 s yielding a median precision of $2.63\ \mathrm{m\,s^{-1}}$ (Prog.ID 106.216B PI Standing). Of these 103 measurements, 3 were obtained during the primary eclipse of the binary, and 1 during the transit of planet b. These 4 observations have been discarded from our analysis as they are affected by the Rossiter-McLaughlin effect, which we do not model here (*11, 12*).

In our radial-velocity analysis, we fit for an offset between ESPRESSO data obtained in 2019, and those in 2021, post COVID closures. This $4.6\ \mathrm{m\,s^{-1}}$ offset, though small, was introduced by calibration lamp change during the COVID closure of telescope in 2020 (*13*). Our 2019 dataset was obtained after the fibre change on the instrument in 2019. Without accounting for this offset the planetary signal is still detected in the data. COVID closure of both the La Silla and Paranal observatories delayed the collection of data on this system and by consequence the discovery of this planet by a year. Complete phase coverage of BEBOP-1c's orbit was finally achieved when the final data points were collected in March 2022.

ESPRESSO data were reduced using version 2.3.3 of the ESPRESSO pipeline (publicly available at ESO) with a procedure similar to that used to HARPS, but adapted to ESPRESSO. Each cross correlation function was obtained with a G2 template spectra, step size of $0.5\ \mathrm{km\,s^{-1}}$, and a $300\ \mathrm{km\,s^{-1}}$ window centered on the radial velocity of the binary. To summarise, we have 123 ESPRESSO observations in total, with 20 observations in ESPRESSO 2019, and 103 in ESPRESSO $2021/2022$. The total timespan of the HARPS and ESPRESSO combined is 1472 days.

All ESPRESSO data are available at the ESO public archive by searching for J0608-59. All radial-velocity data used in our analysis can be found in Tables 2-4 in this supplementary

material.

1.3 TESS

BEBOP-1 was a target for the radial-velocity survey before the launch of TESS. It was then later discovered to contain a 95-day transiting planet (TOI-1338b, aka BEBOP-1b), based on four sectors of TESS data (three in short cadence, 120 seconds). More data has been taken in the years since. These data are mentioned here for completeness but we do not include them in the analysis; BEBOP-1c is an independent radial-velocity discovery.

1.4 Outlier Removal

Outliers were identified using two methods. The first involves a-priori finding outliers in the span of the bisector slope (Bis_Span, a measure of line shape (*4*)) and Full Width at Half Maximum (FWHM), and excluding these. The radial-velocity analysis in this paper used this method. The second method uses a student-t distribution to account for outliers as part of the sampling process (e.g. (*14*)), we use this to check the results from the first method.

For the a-priori removal, each set of points was fit as a mixture model with inlier and outlier populations, following the method described in Hogg et al. (2010) (*15*). For both FWHM and Bis_Span, the inlier model was simply a constant with a small scatter allowed in addition to the uncertainties (which were taken as double the radial-velocity uncertainty). The outlier model also fits a constant but with a very wide population scatter.

We use PyMC3 (*16*) to fit a mean and scatter for both the inlier and outlier distributions, as well as a parameter f for the proportion of points that are outliers, the prior on f is a $\beta[1.5, 9]$ distribution favouring a low proportion of outliers. These parameters are then used to calculate the probability of the i^{th} point being an outlier for each posterior using the following equation:

$$P_{i,out} = \frac{fL_{i,out}}{fL_{i,out} + (1-f)L_{i,in}} \tag{1}$$

where $L_{i,out}$ and $L_{i,in}$ are the likelihoods for the i^{th} point in the respective outlier and inlier distributions.

The power of this method is in removing the human factor from outlier identification, and not having to resort to sigma-clipping which does not usually consider measurement uncertainties. A total of 17 outliers are identified this way.

For the second method, we ran the fits on the whole dataset including outliers, accounting for them by using a student-t distribution, this allows outliers in radial velocity to be directly found, rather than relying on the Bis_Span and FWHM indicators. This method identifies 8 outliers of which 5 are shared with the 17 outliers identified in method 1; 3 points are particularly strong outliers in the student-t method all of which were identified in method 1. Importantly, the resulting detection of BEBOP-1c and non-detection of BEBOP-1b remain, and all the parameters from the student-t fit are consistent with those found removing the outliers a-priori.

In summary: 3 outliers are identified in the HARPS data in FWHM one of which is also identified in Bis_Span and is such a strong outlier it is suspected that the wrong star was observed; 1 outlier is identified in the ESPRESSO 2019 data in FWHM; and 13 outliers are identified in the ESPRESSO $2021/2022$ data in FWHM (2 of which are also identified in Bis_Span). Data points identified as outliers are flagged in Tables 2-4 of this supplementary material. We denote outliers, excluded from the analysis, with the following flags: Wrong star W, Bis_Span B, FWHM F, During binary transit R, during planetary transit P.

2 Modeling of the data

2.1 Kima

For the radial-velocity analysis we use the `kima` package (*17*). `kima` models radial-velocity data with a sum of Keplerian functions from $N_{\rm p}$ orbiting planets, and estimates the posterior distributions for each of the orbital parameters.

Table 1: Prior distributions for the binary and planetary RV model signals in `kima`

Parameter	Unit	Prior distribution	
		Binary	Planet
N_p		1	$\mathcal{U}(0, 3)$
P	days	$\mathcal{U}(14.61 \pm 0.01)$	$\mathcal{LU}(4 \times P_\mathrm{bin}, 2000)$
K	$\mathrm{m\,s^{-1}}$	$\mathcal{U}(21617 \pm 15)$	$\mathcal{MLU}(0.1, 100)$
e		$\mathcal{U}(0.1556 \pm 0.001)$	$\mathcal{K}(0.867, 3.03)$
ϕ		$\mathcal{U}(0, 2\pi)$	
ω		$\mathcal{U}(0, 2\pi)$	
σ_jit	$\mathrm{m\,s^{-1}}$	$\mathcal{LU}(0.01, 67)$	
γ	$\mathrm{m\,s^{-1}}$	$\mathcal{U}(30761 \pm 100)$	

Notes: N_p denotes the Number of Planetary Keplerian signals to fit to the data. P_bin denotes the Period of the binary. $\mathcal{U}$ denotes a uniform prior with an upper and lower limit, $\mathcal{LU}$ is a log-uniform (Jeffreys) prior with upper and lower limits, $\mathcal{MLU}$ is a modified log-uniform prior with a knee and upper limit, and $\mathcal{K}$ is a Kumaraswamy prior (*22*) which takes two shape parameters (*23*).

To sample the posterior distribution `kima` uses a Diffusive Nested Sampling (DNS) approach (*18*). This provides `kima` with estimates on the evidence for each model, allowing for model comparison (*19, 20*). This model comparison can then be used to compare the ratio of evidences between models with different numbers of Keplerian signals. Importantly, the number of planets N_p is a free parameter like any other.

The radial-velocity analysis follows that described in Standing et al. (2022) (*8*) and Triaud et al. (2022) (*21*). Prior distributions used in our analysis can be found in Table **1**.

2.2 Resulting fit

The `kima` combined fit of our HARPS and ESPRESSO data favours a single planet model in addition to the binary orbit with a Bayes factor of $> 9\,300$. The Bayes factor is the ratio of the Bayesian evidence between two competing models. In our case the Bayes factor is the number of posterior samples obtained with $\mathrm{N_p}$ planetary signals, over those with $\mathrm{N_p} - 1$. The Bayes factor value indicates the measure of support in favour of one model over the other (*8, 24, 25*).

A Bayes factor value of > 150 indicates very strong evidence (*8, 26*) in favour of a single

planet in addition to the binary orbit.

When searching for the inner transiting planet in the data we obtain a Bayes factor of 1.4 in favour of two planetary signals. This is categorised as inconclusive evidence of any further signals in the data.

Forcing a fit on a 95 day Keplerian signal yields no clear signal corresponding to BEBOP-1b with posterior samples having a semi-amplitude consistent with $0\ \mathrm{m.s}^{-1}$. This fit still produces a clear detection of BEBOP-1c.

To obtain orbital parameters for the system, we follow the same procedure as detailed in Standing et al. (2022) (*8*). Proposed posterior samples with orbits which cross one another, or into the instability region of the binary, are removed. The remaining samples are clustered with the `HDBSCAN` clustering algorithm (*27*). Clusters corresponding to the binary and BEBOP-1c are then plotted using the `Corner` package (*28*). Orbital parameters are then determined as the 50^{th} percentile, with 1σ uncertainties estimated from the 14^{th} and 84^{th} percentiles of the cluster. Corner plots for the binary and BEBOP-1c can be seen in Figures **1** and **2** respectively.

2.3 Constraints on BEBOP-1b and further planetary companions

Using `kima` as in Standing et al. (2022), and Triaud et al. (2022) (*8, 21*) we calculate a detection limit on additional undetected planetary signals in the radial-velocity data. Firstly, we remove the highest likelihood Keplerian model corresponding to BEBOP-1c from the data. Following this, to calculate the detection limit we fix $N_{\mathrm{p}} = 1$ in our fit, include the binary with tight priors on its parameters, and obtain posterior samples of all remaining signals which are compatible with the data. This method is conceptually similar to that described in Tuomi et al. (2014) (*29*), where the sampler is forced to fit an additional signal to the data. Any signals found are compatible with the data, but as of yet undiscovered, since only one planetary signal is present in our original fit.

The resulting posterior samples can be seen as a greyscale density plot in Figure 3, with a blue 99% contour corresponding to our detection limit. The blue limit demonstrates that we are sensitive to additional sub-Saturn mass planets for periods out to 2000 days, while we are sensitive to Neptune mass planets near the instability limit.

We note a density of posterior samples at periods around 100 days in agreement with the presence of BEBOP-1b seen in *TESS* photometry (*9*). Following the findings described in Standing et al. (2022) (*8*), we calculate an additional detection limit to place an upper limit on the mass of BEBOP-1b. This limit is calculated in the same manner as the blue line, though only using posterior samples with eccentricities < 0.1 (the approximate upper limit on the eccentricity of BEBOP-1b (*9*), and a value allowed by our orbital stability analysis). A running mean is applied on the red eccentricity cut line to ensure > 1000 samples are in each bin. The resulting red detection limit demonstrates our sensitivity to circular planets at the orbital period of BEBOP-1b is $\approx 2.6 \pm 0.1$ $\mathrm{m.s^{-1}}$. This allows us to place an upper limit on the mass of BEBOP-1b of 23.6 ± 0.9 $M_\oplus$. With a radius of ≈ 6.9 $R_\oplus$, we calculate the mean density of BEBOP-1b to be < 0.39 $\mathrm{g.cm^{-3}}$

The uncertainty of the detection limit is determined by performing numerical experiments with `kima`. We first generate a radial-velocity timeseries, following a Gaussian distribution, with dates following a log-uniform distribution. Then we run `kima` just like any other system and produce a large number of posteriors (in our case 685,000). Following that, we compute a detection limit like in Standing et al. (2022) (*8*) and call this our fiducial case. The next step is to calculate detection limits for many subsamples of the posterior and measure their fractional distance to the fiducial detection limit. We find that the fractional error in the position of subsamples' detection limits follows a square root law. Consequently, we fit these data with a function $y = a\,x^{-1/2}$, where y is the fractional uncertainty of the detection limit at a given orbital period and x is the number of posterior within a given posterior subsamples. We find

$a = 15.1 \pm 0.3$. We use this relation to represent an uncertainty on Fig. 4.

2.3.1 FIP and TIP

We compute the True Inclusion Probability (TIP) and False Inclusion Probability (FIP) for a signal being present in the data over various frequency bins (*30*). Plotting this in a periodogram gives similar information to the detection limit described above. However, where the detection limits give us information about an upper limit on the mass of a potential planetary signal, the TIP periodogram effectively gives us the probability of there being a planetary signal at that given period. It has been shown that using this metric as a detection criterion is optimal in the context of exoplanet detection (*31*). We find 3 peaks in the TIP periodogram further to the detected planet c at: 97, 386 and 756 days with respective TIPs of 0.27, 0.34 and 0.84. This is shown in Figure 4 which shows the FIP and TIP periodograms.

3 Stellar Activity

Chromospheric emission lines observed in the stellar spectrum often trace stellar magnetic activity. Here we describe the activity indices measured and used in our analysis. We used the open-source package `actin` (*32*) to measure the Ca II H&K, He I, sodium D doublet (Na D a and b), Ca I and Hα activity indices.

First we compute a generalised Lomb-Scargle (GLS) periodogram (*33*) of each activity indicators, from individual instruments, and using the combined dataset. In Figure 6 (a,b), we show the window function of each individual and combined datasets and the periodogram of radial velocity. We compute false alarm probability levels of 10%, 1% and 0.1% using a bootstrap randomisation of the dataset. We consider a signal to be significant if the false alarm probability level is $< 0.1\%$. We searched for periodic signals of chromospheric activity indicators to investigate the possibility of BEBOP-1c's period $P_{\rm c}$ being produced by magnetic

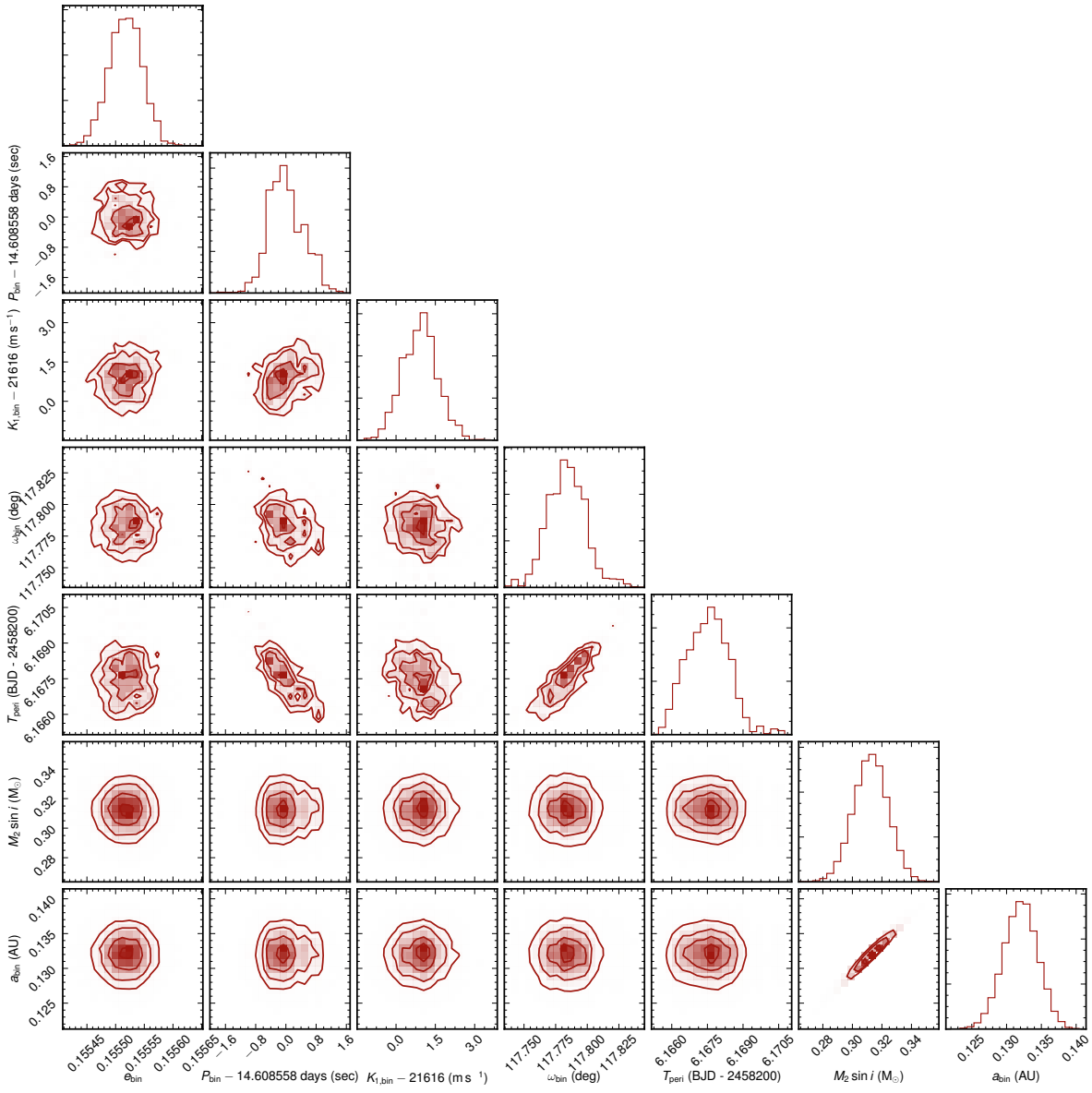

Figure 1: Corner plot of posterior sample distributions for the Binary stars orbital parameters; eccentricity, orbital period, semi-amplitude, argument of periastron, time of periastron passage, $M \sin i$ in Solar masses, and semi-major axis.

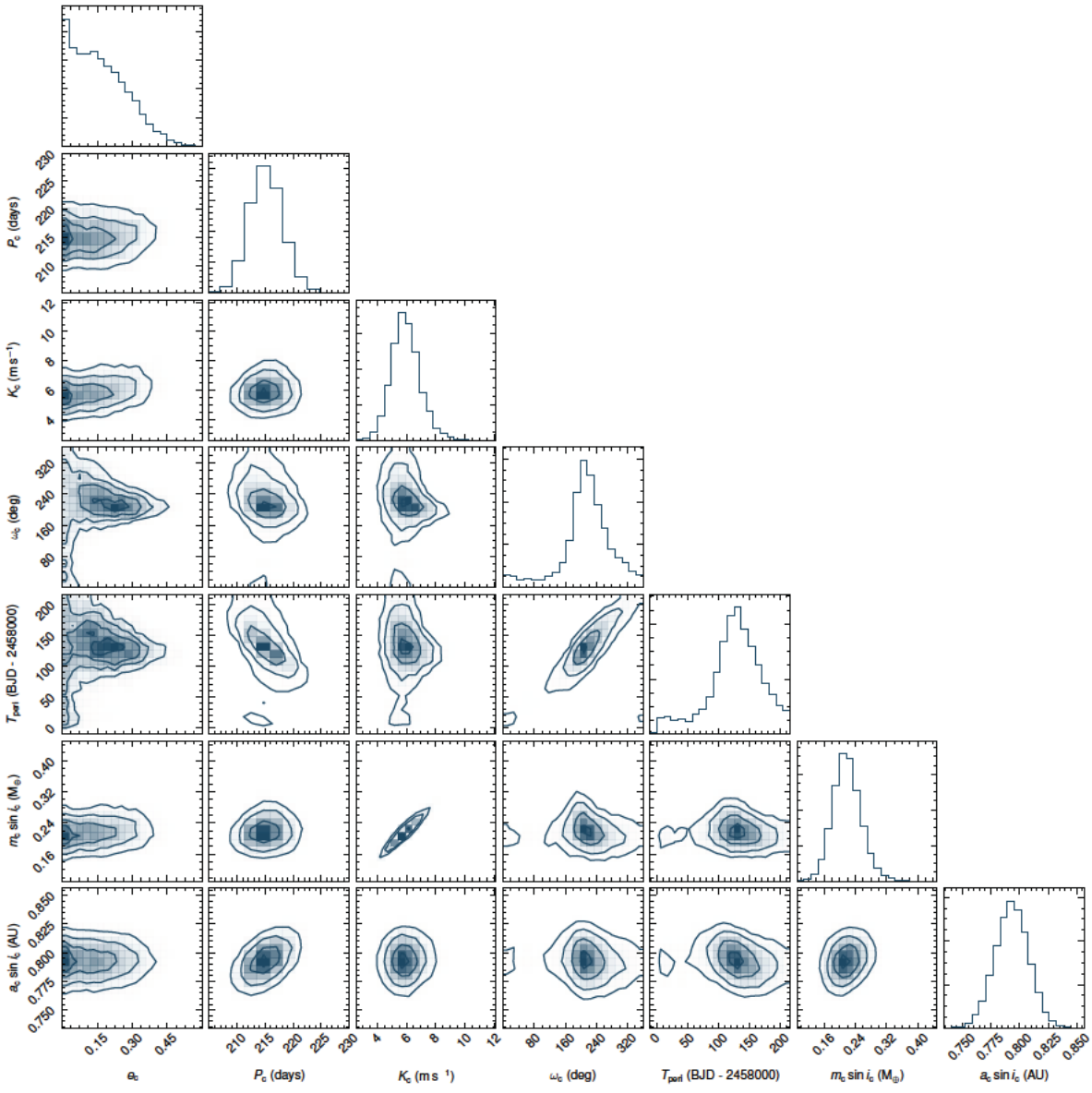

Figure 2: Corner plot of posterior sample distribution for BEBOP-1c orbital parameters; eccentricity, orbital period, semi-amplitude, argument of periastron, time of periastron passage, $M \sin i$ in Earth masses, and semi-major axis.

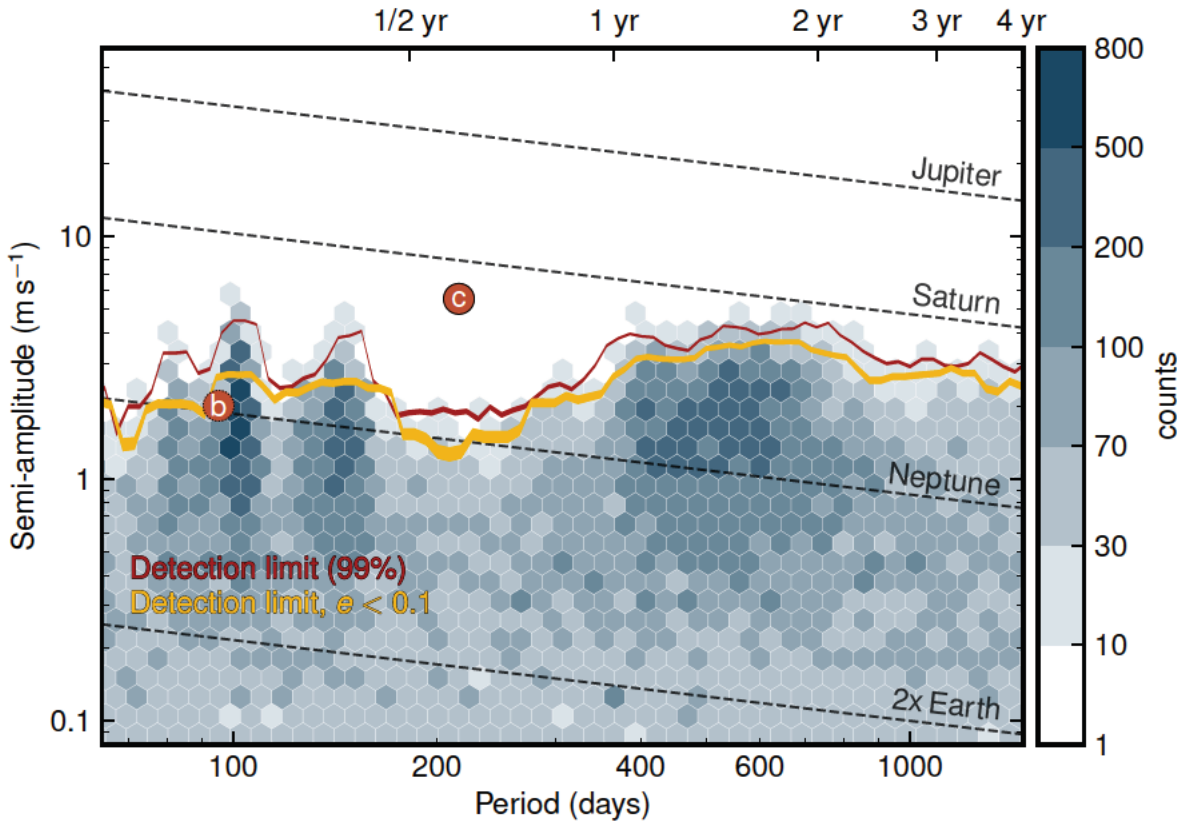

Figure 3: Hexbin plot denoting the density of $\sim 100\,000$ posterior samples obtained from four separate `kima` runs on BEBOP-1 Radial-Velocity (RV) data with $N_{\rm p}$ fixed $= 1$. The red line shows the calculated 99% detection limit, along with its associated error. Point 'c' indicates the position of detected planet BEBOP-1c, and point 'b' that of planet BEBOP-1b undetected in RV data alone. The orange line shows the detection limit on samples with eccentricity < 0.1 (the upper limit on BEBOP-1b's eccentricity (*9*)).

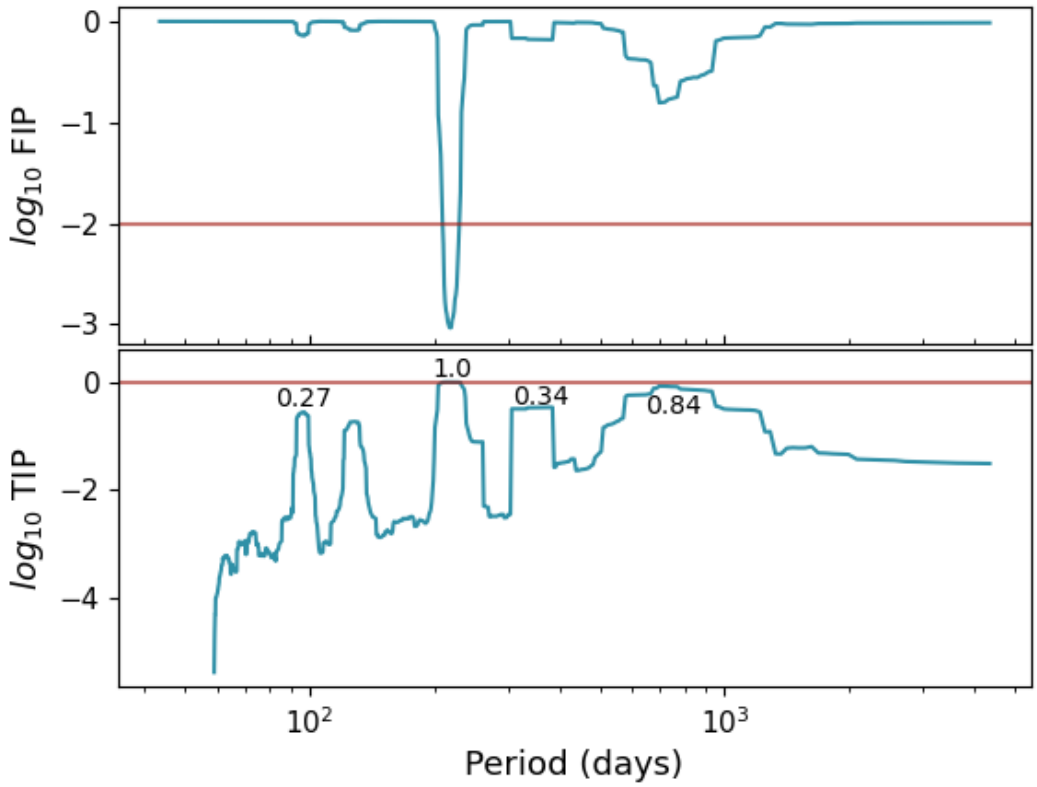

Figure 4: Top: False Inclusion Probability (FIP) periodogram showing the clear detection of BEBOP-1c at ≈ 215 days. Bottom: True Inclusion Probability (TIP) periodogram showing the significance of any other peaks with TIP > 0.2. The second highest peak occurs at ≈ 756 days with a significance of 84%, a lower peak with significance of 27% is found at $\approx$ 97 days, corresponding to the period of BEBOP-1b.

activity of BEBOP-1A (the primary). Figure 6 (c-g) depicts the periodogram of Ca II, Hα, Na D, He I and Ca I indices. None of the activity indicators shows any significant signal at or near P_c ($\sim$ 215 d). We see significant period at $\sim$ 7.5 d in Na D (FAP $\sim$0.1%) and He I (FAP $\sim$1%), however, the nature of these signals are not obvious. We see weak signals in Hα at 270 d caused by a combination of window function and a long-period term, however, the signal is not significant. In addition, the activity time series shown in Figure 7 does not show any obvious modulation.

We searched All-Sky Automated Survey (ASAS; (*34*)) archival data to constraint the rotation period and to investigate the nature of the BEBOP-1c signal. The ASAS observations spanning over 10 years. The ASAS data shows a strong signal at 61 d (10% false alarm probability) which could be related to stellar rotation ($\sim 3P_{\rm rot}$).

In addition, analysis of the radial-velocity bisector shows no correlation with the $\sim$ 215 d signal, yielding a Pearson Correlation co-efficient of < 0.052.

The ASAS data and activity indicators do not show any significant signal at $\sim$ 215 d, therefore this signal is likely planetary in nature.

4 System dynamics

In this section we deal with various aspects of the orbital dynamics of BEBOP-1, first looking at the stability of the system, and then estimating whether the outer planet, BEBOP-1c, will show transits at some point into the future.

4.1 Orbital Stability

The orbital solution given in Table 1 in the main text shows a compact two-planet circumbinary system ($a_{\rm bin} = 0.13$, $a_{\rm b} = 0.46$ and $a_{\rm c} = 0.79$ au). The inner planet has a maximum mass similar to Neptune ($m_{\rm b} = 23.6$ $M_\oplus$) and is close to the circumbinary stability boundary (*9, 35*),

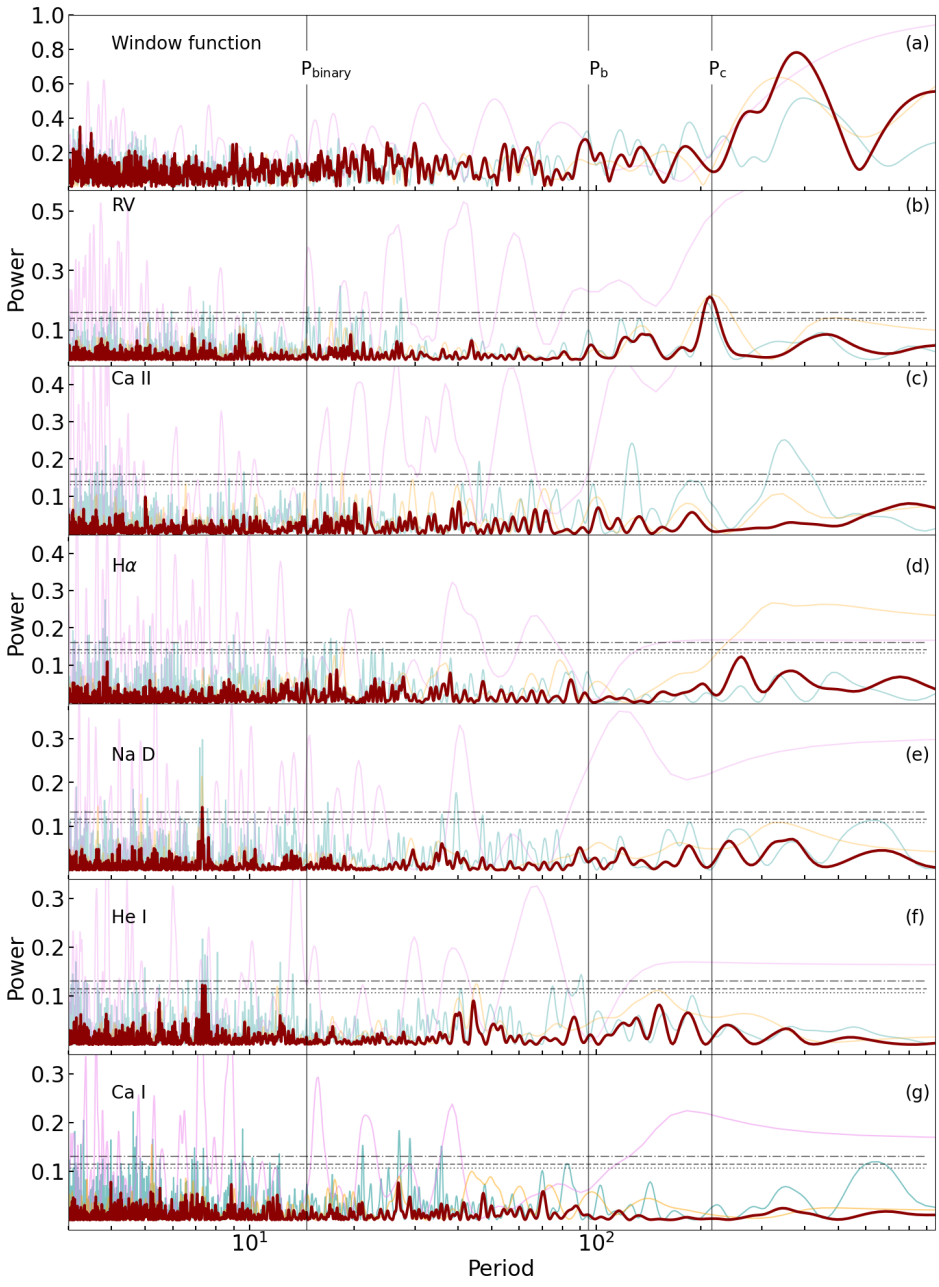

Figure 5: Generalised Lomb-Scargle periodogram of BEBOP-1 spectroscopic data. The top panel shows the window function of the combined dataset (dark red). b, Periodogram of the radial-velocity measurements. c-g, Periodogram for Ca II, Hα, Na D, He I and Ca I index. The cyan, violet and orange curves corresponds to HARPS, ESPRESSO 2019 and ESPRESSO 2021/2022, respectively, and the dark red curves correspond to the combined dataset. The horizontal lines represent the bootstrapped false alarm probability levels of 10% (dotted), 1% (dashed), and 0.1% (dotted dash). The vertical solid lines indicate the binary period and planetary periods (P_b and P_c).

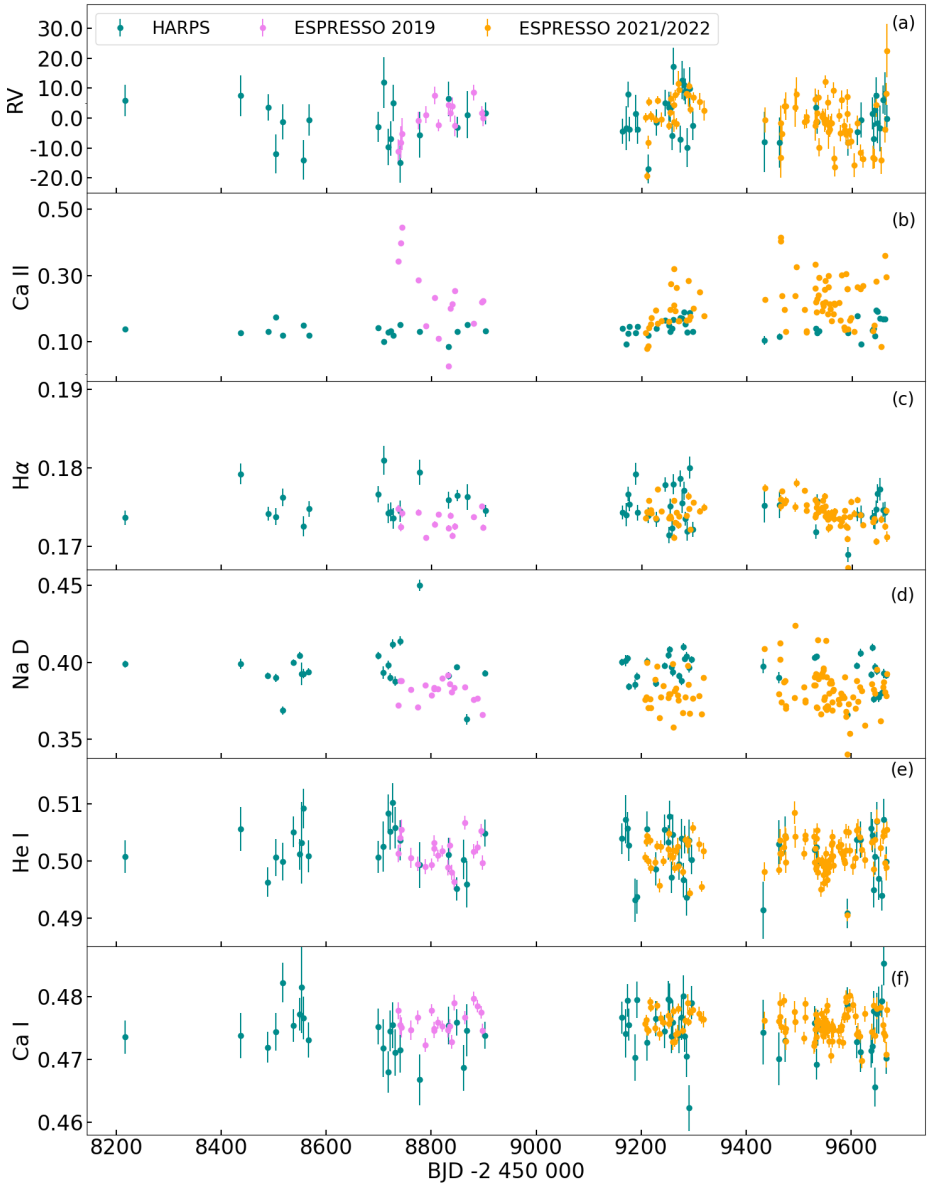

Figure 6: Radial velocity, Ca II, Hα, Na D, He I and Ca I timeseries for BEBOP-1.

while the outer planet minimum mass is similar to Saturn ($m_{\rm c} = 0.22\,{\rm M_{Jup}}$). As a consequence, we expect strong mutual gravitational interactions between the stars and the planets. In order to study the stability of the system, we performed a global frequency analysis (*36, 37*) in the same way as achieved for other circumbinary planetary systems (*38*). In our analysis, we always consider for the inner planet its maximal mass, which can be seen as a superior limit for stability. Moreover, the mass of this planet is relatively small and does not impact much the stability, and so smaller masses do not change much the global picture described here.

The system is integrated on a regular 2D mesh of initial conditions in the vicinity of the best fit (Table 1 main text). Each initial condition is integrated for 5000 yr, and a stability indicator, $\Delta = |1 - n_{b'}/n_b|$, is computed. Here, n_b and n'_b are the main frequency of the mean longitude of the inner planet over 2500 yr and 5000 yr, respectively, calculated via the frequency analysis (*37*). Note that while the osculating mean motion varies over a single planetary orbit as a result of energy exchange with the binary and planet c, n_b calculated over time intervals much longer than any resonant variations is constant for stable systems, while it drifts for unstable systems until one of the planets escapes. The results are reported in color, where yellow represents strongly chaotic trajectories with $\Delta > 10^{-2}$, while extremely stable systems for which $\Delta < 10^{-8}$ are shown in purple/black. Orange indicates the transition between the two, with $\Delta \sim 10^{-4}$.

Observationally, only the inner planet's eccentricity is well-constrained: $e_{\rm b} = 0.088 \pm 0.004$ (*9*). In contrast, only an upper limit can be placed for the outer, non-transiting planet: $e_{\rm b} < 0.15$ (Table 1 main text).

Therefore, in a first experiment, we explore the stability of the system in the plane $(e_{\rm b}, e_{\rm c})$, assuming coplanar orbits. The results are shown in Figure 7. We observe that that the eccentricities of both planets must be smaller than 0.1 to ensure a stable system. Moreover, since we already have for the inner planet $e_{\rm b} \approx 0.1$ (*9*), the only remaining possibility for the outer planet

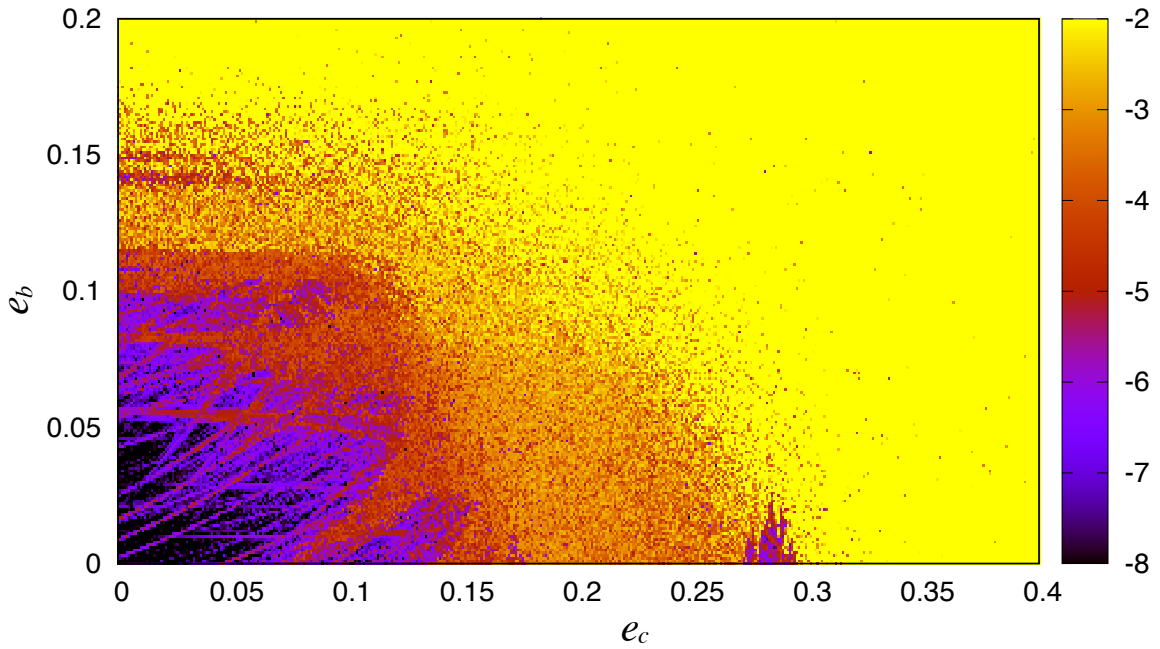

Figure 7: Stability analysis of the BEBOP-1 system in the plane $(e_{\rm c}, e_{\rm b})$, assuming coplanar orbits. For fixed initial conditions (Table 1 main text), the parameter space of the system is explored by varying the eccentricities of both planets, with a step size of 0.001. For each initial condition, the system is integrated over 5000 yr and a stability indicator is calculated which involved a frequency analysis of the mean longitude of the inner planet (see text). Chaotic diffusion is indicated when the main frequency of the mean longitude varies in time. Yellow points correspond to highly unstable orbits, while purple points correspond to orbits which are likely to be stable on a billion-years timescales.

is $e_{\rm c} \approx 0$. We thus adopt $e_{\rm c} = 0$ in the following stability analyses.

The inner planet is not detected in the radial-velocity data, its presence can only be inferred from photometric measurements (*9*). Therefore, in a second experiment, we explore the stability of the inner planet orbit, by varying the orbital period and the eccentricity of this planet, assuming coplanar orbits (Figure 8). This allow us to test the compatibility of the two independent observational datasets. We observe that the inner planet lies in a small stability region that is shaped by the presence of the binary system on the left hand side and by the presence of the massive outer planet on the right hand side. We thus conclude that the two planet circumbinary

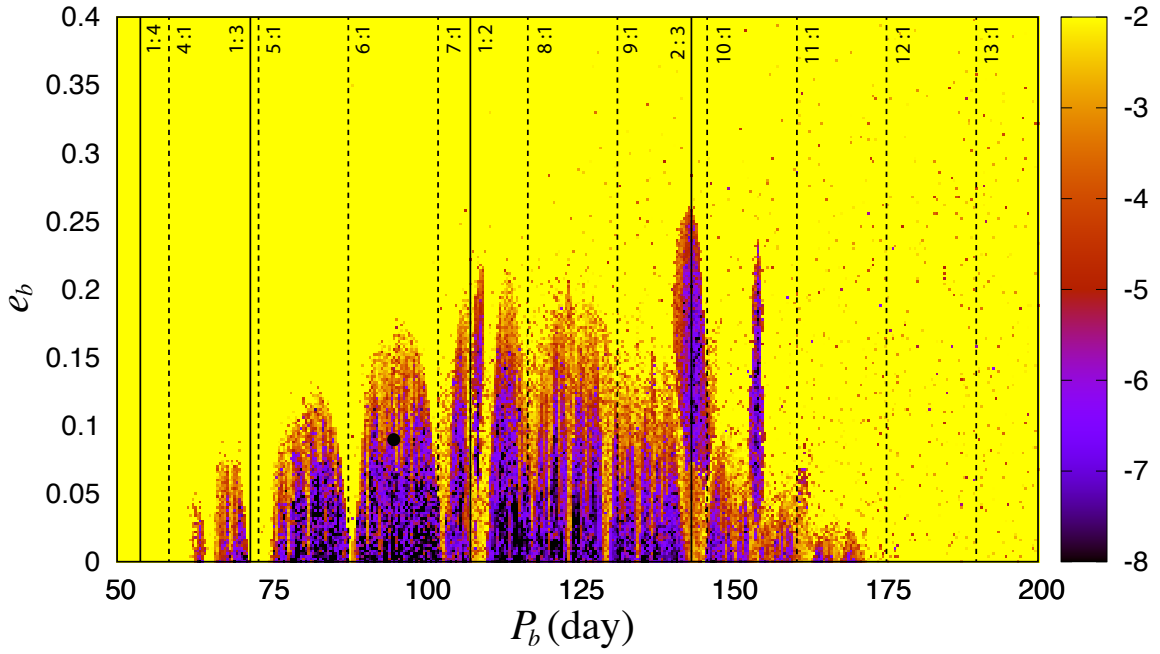

Figure 8: Stability analysis of the BEBOP-1 system in the plane $(P_{\rm b}, e_{\rm b})$, assuming coplanar orbits. For fixed initial conditions (Table 1 main text), the parameter space of the system is explored by varying the orbital period $P_{\rm b}$ and the eccentricity $e_{\rm b}$ of the inner planet. The step size is 0.4 day in orbital period and 0.002 in eccentricity. The black dot gives the best fit parameters for the inner planet (*9*). The color codes are the same from Figure 7, the dashed black lines indicate resonances with the binary, and the solid black lines resonances with the outer planet BEBOP-1c.

solution is reliable. However, we assumed $e_{\rm c} = 0$ to draw the stability map obtained in Figure 8. As we increase the eccentricity of the outer planet, the small stable region is quickly degraded and completely disappears for $e_{\rm c} > 0.1$, in conformity with the results shown in Figure 7. Figure 8 shows that the inner planet, BEBOP-1b, is surrounded by unstable regions. If the planet migrated to its current location, it would have to pass through two resonances with the outer planet. This could indicate consequences for formation migration in the system.

The radial-velocity technique alone is unable to constrain the inclination, $I_{\rm c}$, and the longitude of the node, $\Omega_{\rm c}$, of the outer planet. As a result, we can only determine the minimum value of its mass, which corresponds to a coplanar system ($I_{\rm c} = 90$), that we have been assuming

in previous analyses. However, contrarily to the inner planet, the outer planet does not transit, and thus cannot be exactly in the same orbital plane of the remaining bodies in the system. In a final experiment, we explore the stability of the system, by varying the inclination and the longitude of the node of the outer planet (Figure 9). We observe that the system can be stable within a circle centred at the coplanar solution, which corresponds to mutual inclinations smaller than 40°. A larger stability regions also exists centred at ($\Omega_{\rm c} = 180^{\circ}, I_{\rm c} = 90^{\circ}$), but it corresponds to mutual inclinations higher than 120°, that is, to retrograde orbits, which are more unlikely from a formation point-of-view. As we change $I_{\rm c}$, the mass of the outer planet increases. At the boundary of stability, $I_{\rm c} = 90^{\circ} \pm 40^{\circ}$, we get a maximum mass for the outer planet, $m_{\rm max,c} = 0.28$ $\mathrm{M_{Jup}}$. Again, we assumed $e_{\rm c} = 0$ to draw the stability map obtained in Figure 10. As we increase the eccentricity of the outer planet, the radius of the stable circle quickly shrinks and completely disappears for $e_{\rm c} > 0.1$, in conformity with the results shown in Figure 7.

4.2 Possible transits of BEBOP-1c

Orbits of circumbinary planets exhibit nodal precession. This changes the orientation of the planet's orbit with respect to both the binary and the observer. This means that a planet changes from a transiting to non-transiting configuration (*39, 40*). The precession timescale is typically on the order of decades, and hence can be observable with long baselines such as Kepler and TESS. Kepler-413 exhibited this on-off transit sequence (*41*). Kepler-453 did not start transiting until half way through the Kepler mission (*42*).

(*43, 44*) derived an analytic criterion for if a planet will ever enter transitability on the primary (A) or secondary (B) star during its precession cycle:

$$\Delta I > \left| \frac{\pi}{2} - I_{\rm bin} \right| - \sin^{-1} \left(\frac{a_{\rm A,B}}{a_{\rm p}} \sin \left| \frac{\pi}{2} - I_{\rm bin} \right| + \frac{R_{\rm A,B}}{a_{\rm p}} \right), \tag{2}$$

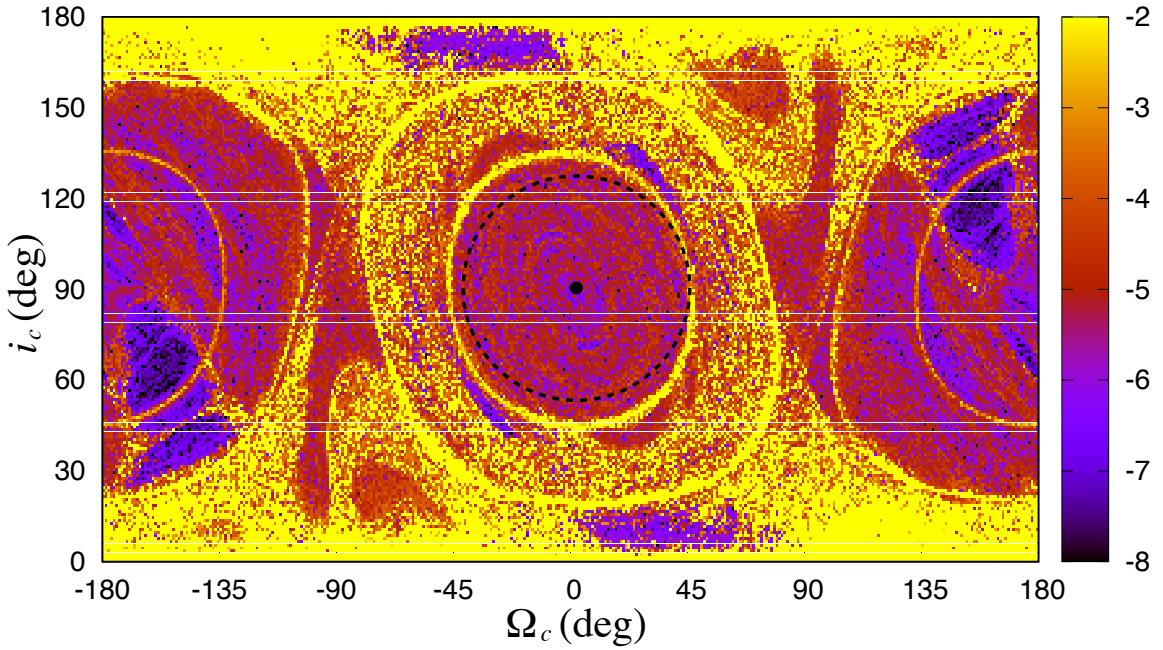

Figure 9: Stability analysis of the BEBOP-1 system in the plane $(\Omega_{\rm c}, I_{\rm c})$. For fixed initial conditions (Table 1 main text), the parameter space of the system is explored by varying the inclination $I_{\rm c}$ and the longitude of the node $\Omega_{\rm c}$ of the outer planet, with a step size of 1°. The black dot gives the best fit parameters, while the dashed circle corresponds to mutual inclinations equal to 40°. The color codes are the same from Figure 7.

where ΔI is the mutual inclination between the planet and binary orbit. It may seem counter-intuitive at first that a planet-binary misalignment makes transitability *more* likely. The reason is that the planet's sky inclination oscillates around the binary's sky inclination, with an amplitude equal to ΔI. A higher ΔI therefore makes it more likely that the planet's inclination will become close to $90°$, and hence transitability. For eclipsing binaries $I_{\rm bin}$ is near $90°$, and hence the vast majority of circumbinary planets orbiting eclipsing binaries will eventually transit.

Placing the BEBOP-1c values into Eq. 2 yields $\Delta I_{\rm min} = -0.11°$ for the primary star. The negative inclination criterion means that BEBOP-1c is *guaranteed to eventually transit* regardless of what its mutual inclination is. This is mainly because the binary is so well-aligned with our line of sight ($I_{\rm bin} = 89.658°$) and the primary star is rather large ($R_{\rm A} = 1.299 R_{\odot}$). Whilst we think that BEBOP-1c is guaranteed to *eventually* transit, we are unable to predict when and how frequently. The precession period is

$$P_{\rm prec} = P_{\rm p} \frac{16}{3} \left(\frac{a_{\rm p}}{a_{\rm bin}} \right)^2 \frac{1}{\cos \Delta I}, \tag{3}$$

where we assume circular orbits (*39, 45*). For BEBOP-1c $P_{\rm prec} = 119$ years, assuming ΔI is close to zero, as is the case of the known circumbinary planets. With modern advances in medical science, there is a chance that the authors will live to see BEBOP-1c transit.

5 System formation

The coplanarity between the planet and binary orbit planes for the circumbinary planets that have been discovered so far strongly suggests that these planets were formed in circumbinary protoplanetary discs that were themselves closely aligned with the binary orbit plane. We present here the results from a suite of simulations of circumbinary planet formation that were performed to examine plausible scenarios for the origin of the BEBOP-1b & c system.

5.1 Circumbinary disc and N-body model

Our simulations were performed using a newly developed code designed specifically to examine the formation of circumbinary planet systems. The code employs the N-body symplectic integrator MERCURY6, adapted to include a central binary system (*46, 47*). The code utilises the 'close-binary' algorithm (*46*) that calculates the temporal evolution of the positions and velocities of each body in the simulations with respect to the centre of mass of the binary stars, subject to gravitational perturbations from both stars and other large bodies. The evolution of the circumbinary disc is calculated using a 1D viscous α–disc model (*48*), where the equilibrium temperature is calculated by balancing irradiation heating from the central stars, background heating from the residual molecular cloud, viscous heating and blackbody cooling. Hydrodynamical simulations have shown that circumbinary discs develop precessing eccentric inner cavities, with their sizes and eccentricities being dependant on the properties of the binary and disc (*49, 50*). To mimic the formation of this cavity, we use a variable α model fitted to results from 2D hydrodynamic simulations using FARGO3D (*51*), that show that the mass flux through the cavity remains roughly constant within the region around the binary. Our approach to accounting for the precession and eccentricity of this cavity is described below. The model also includes a prescription for photoevaporative winds, resulting from high-energy photons from both the central stars and nearby stars, that remove gas from the discs on a time scale determined by the adopted flux of high energy photons (*52, 53*).

5.2 Planet migration

Planets with masses that significantly exceed a Lunar-mass undergo migration because of gravitational interaction with the surrounding disc. Type I migration is included in the model via torque formulae that take account of Lindblad and corotation torques (*54*). If a planet becomes massive enough to form a gap in a disc (*55*), its migration changes from type I to type

II. When transitioning from type I to type II migration the model accounts for gap formation self-consistently by calculating the torque acting on the disc due to the planet, with the back-reaction driving migration (*56*). Planets in the vicinity of the inner cavity of the circumbinary disc will experience time variable forces arising from its eccentricity and precession. To account for this, the model includes additional forces that are obtained by interpolating from a force map that has been generated from 2D hydrodynamic simulations of a circumbinary disc with binary parameters equal to those inferred for the BEBOP-1 system. These were performed using FARGO3D (*51*).

5.3 Planetary growth

The growth of planetary seeds in the model occurs via pebble accretion, and once a planet exceeds an Earth mass it starts to accrete gas from the disc. Pebble accretion models have shown that as protoplanetary discs evolve, dust coagulates into pebbles and settles in the midplane, where the pebbles drift inwards (*57*). This creates a pebble production front that expands outwards over time. As the pebbles drift through the disc, they encounter planetary embryos which can accrete the pebbles with an efficiency that depends on the disc and planet properties (*58,59*). Gas accretion is modelled using a recently developed empirical fit (*60*) to the results of detailed 1D envelope structure models (*61*) that account for local disc conditions. We note these models predict that gas accretion starts off very slowly and speeds up as the core and envelope grow in mass. Hence, the onset of gas accretion does not generally result in the formation of a gas giant planet because the envelope contracts on its Kelvin-Helmholtz timescale.

5.4 The resulting circumbinary planet systems

The simulations were initiated by placing 42 planetary seeds throughout the disc between 2 and 20 au, with eccentricities and inclinations distributed uniformly up to $e = 0.02$ and $i = 0.5°$,

respectively. The initial masses of the seeds were set to equal one tenth of the transition mass, which is where pebble accretion becomes efficient as the planetary core begins to accrete from the entirety of its Hill sphere as opposed to its Bondi sphere. These initial masses were between 10^{-4} and $10^{-3} M_{\oplus}$ and are consistent with recent simulations of planetary embryo formation within protoplanetary discs based on gravitational collapse (*62*).

Figure 11 shows the mass and semimajor axis evolution from an example simulation that formed a planetary system similar to BEBOP-1. Black points show the final masses and semi-major axes of the surviving planets, whilst the vertical black dashed line denotes the stability boundary (*63*). The red triangle and plus sign indicate the locations of BEBOP-1b and c.

The formation of this system occurred as follows. As the pebble front moved outwards, the planets on the most circular orbits were able to accrete pebbles efficiently, allowing a number of them to grow to masses greater than an Earth mass. These planets began to migrate, generally in towards the central cavity, and continued to accrete drifting pebbles as well as gas. The central cavity in the disc provides a positive surface density gradient in the gas, and this allowed corotation torques to balance Lindblad torques for planets arriving there, resulting in migration stalling. Hence, inward migrating planets started to congregate near the outer edge of the cavity, with some resonant chains forming. As the planets continued to grow in mass, two planets with masses $\sim 10 M_{\oplus}$ collided, forming a more massive core. This planet was then able to accrete gas more efficiently and entered a brief period of runaway gas accretion to become a gas giant. As the planet's mass increased, it migrated in closer towards the central stars, pushing planets interior to it into the cavity, and closer to the stability boundary. This resulted in the inner-most planets being ejected from the system as they crossed the stability boundary and were gravitationally scattered by the central stars, although the planet destined to become the BEBOP-1b analogue remained outside of the boundary. The gas giant planet opened a gap in the disc and began to undergo slow inwards type II migration, whilst continuing to accrete

gas through the gap at the viscous supply rate. After 1.8 Myr the disc reached the end of its life and was fully dispersed due to photoevaporative winds, and the giant planet stopped accreting and migrating, leaving both planets with masses and semimajor axes similar to those inferred from the observations. The system was allowed to evolve for a further 8 Myr, during which time it remained stable, yielding the final system shown in figure 11.

This evolution scenario was a common outcome for a number of simulated systems, with planets growing through pebble accretion at large radii in the disc, before migrating in towards the central cavity. Planets congregated there, leading to collisions and some ejections. Figure 12 shows the mass versus semimajor axis for all planets formed in the simulations, with the colour coding showing the metallicity of the system in comparison with the Solar value (this determines the mass in pebbles assumed in the models). Planets shown by grey points have been lost from the systems through collisions with more massive planets or by ejection. The black dashed line shows the stability boundary, whilst the black triangle and plus sign show the masses and locations of BEBOP-1b and c.

The figure shows that formation of BEBOP-1b analogues is a relatively common outcome of the simulations, with numerous super-Earth and Neptune mass planets being formed with similar orbital periods. This is unsurprising given that these planets become trapped relatively easily around the cavity, close to the observed location of BEBOP-1b. For BEBOP-1c, this planet has fewer simulated planets in its proximity, a result of its observed mass. At this mass, planets are in a runaway gas accretion regime, where they quickly grow to masses greater than Saturn's. Indeed, in our best fit simulation, the gas giant planet had a mass roughly twice that inferred for BEBOP-1c. In our best fitting simulations, runaway gas accretion was initiated close to the end of the disc lifetimes, which limited the amount of gas that could be accreted by the planets. This necessity for appropriate timing could indicate that BEBOP-1c formed very late in the disc lifetime.

Looking at the metallicities required to form the planets, no systems with half the Solar metallicity were able to form systems similar to BEBOP-1. This was because cores with sufficient mass to undergo efficient gas accretion were unable to form. On the other hand, systems with twice the Solar metallicity were too effective at forming massive cores, resulting in too many gas giant planets forming, and few planets with masses comparable to BEBOP-1b remaining in the system, making them poor fits for comparison. These results show that the metallicity of the system, and how efficiently dust is converted into planets, is important for determining the architectures of circumbinary planet systems.

6 Prospects for atmospheric follow-up with JWST

In order to assess the suitability of BEBOP-1b for atmospheric characterisation using transmission spectroscopy, we calculate its Transmission Spectroscopy Metric (TSM) as established by Kempton et. al. (2018) (*64*). A planet's TSM is proportional to the SNR that could be achieved by observations using *JWST*, and it depends on the planet's mass, radius and equilibrium temperature, and the host star's radius and J-band magnitude.

Calculation of BEBOP-1b's equilibrium temperature is non-trivial; its non-zero eccentricity and changing irradiation levels caused by the binary mean that the temperature oscillates between minimum and maximum values. Full modelling of this, as was done in Kane & Hinkel (2013) (*65*), is beyond the scope of this paper, so we estimate a mean equilibrium temperature based on two extremes: when the secondary star is closest and furthest to the planet. The equilibrium temperature calculated from the irradiation of just the primary star is $501\,\mathrm{K}$, and the motion of the secondary star will cause the true equilibrium temperature to vary between $603 - 659\,\mathrm{K}$.

We calculate the TSM following Kempton et al. (2018) (*64*) using a mean $\mathrm{T_{eq}} = 630\,\mathrm{K}$ and the mass upper limit of $\mathrm{M_b} < 23.6\,\mathrm{M_\oplus}$ in the first instance, yielding a TSM of 27. This value

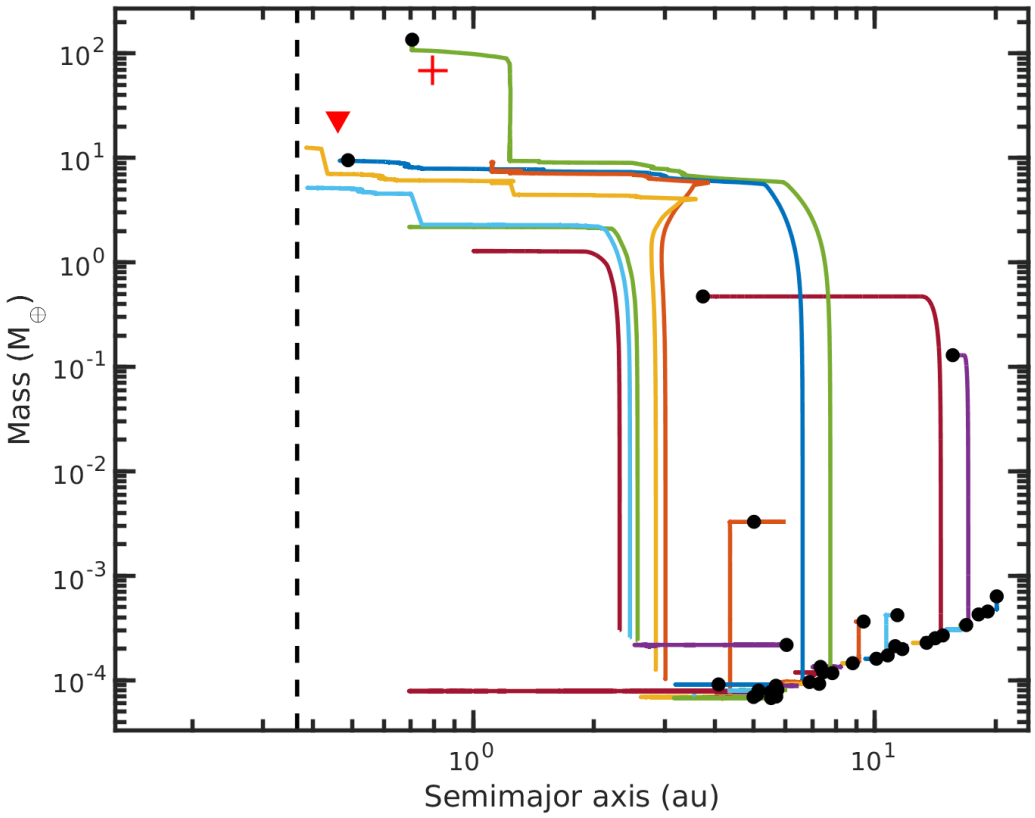

Figure 10: Evolution of the mass versus semimajor axes for the best matching simulated planetary system formed through pebble accretion to BEBOP-1. Black dots represent the final masses and locations of the planets, whilst the red triangle and plus show the observed locations of BEBOP-1b and 1c respectively. The black dashed line denotes the stability limit for the system (*63*).

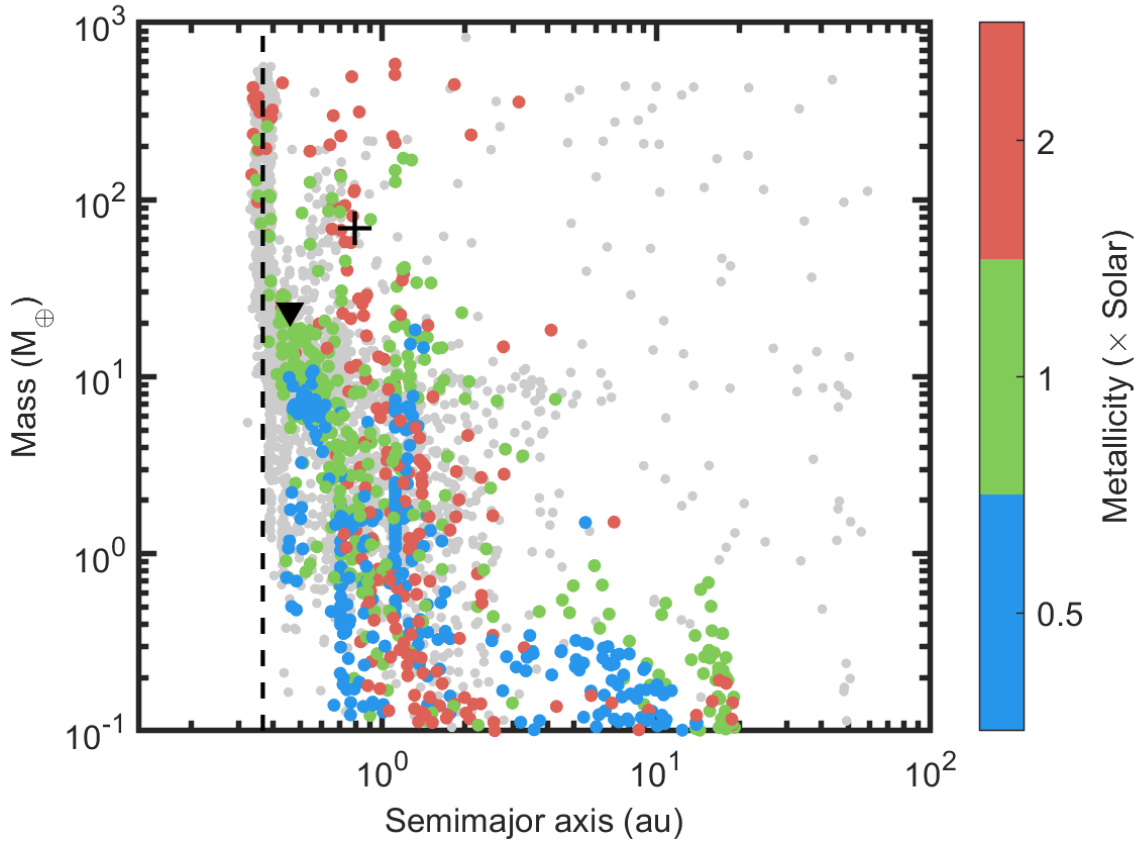

Figure 11: A mass versus semimajor axes plot showing all planets formed in simulations. Different colour points show the initial metallicity of the sytems, whilst the grey points show planets there were lost, either through accretion into other planets, or ejection from the system. BEBOP-1b and 1c are denoted by the black triangle and plus symbols. The black dashed line denotes the stability limit for the system (*63*).

is below the suggested JWST cut-off of 96 for planets in the sub-Jovian regime. However, the mass used for this calculation is the upper limit; a lower mass would imply a larger scale height and therefore a significantly larger TSM.

In Figure 13 we present the TSM of BEBOP-1b as compared to other known exoplanets. Its position shows that even the lower limit of its TSM range compares favourably with other sub-Jovian sized planets in its temperature regime. We have indicated with an arrow the range of TSMs possible for a mass down to $10\,\mathrm{M}_{\oplus}$, which would imply a mean density of $0.17\,\mathrm{g/cm^3}$, comparable to Kepler-47c, for example (*66*).

We also note that crucially, of the now 15 known circumbinary exoplanets, BEBOP-1b is the only one for which observations of this kind can currently be pursued. Most Kepler systems are too faint (e.g. Kepler-47 with a $\mathrm{Jmag} = 13.970$ (*67*), or Kepler-34 with a $\mathrm{Jmag} = 13.605$ (*67*)), and others such as Kepler-16 no longer transit (*68*). Therefore, despite the challenges it may present, BEBOP-1b is our only possibility to shed light on the atmospheric make-up of circumbinary planets.

References

1. D. V. Martin, *et al.*, *A&A* **624**, A68 (2019).

2. A. H. Triaud, *et al.*, *A&A* **608**, A129 (2017).

3. D. V. Martin, T. Mazeh, D. C. Fabrycky, *MNRAS* **453**, 3554 (2015).

4. D. Queloz, *et al.*, *A&A* **379**, 279 (2001).

5. V. Kunovac Hodžić, *et al.*, *MNRAS* **497**, 1627 (2020).

6. M. Mayor, *et al.*, *The Messenger* **114**, 20 (2003).

7. A. Baranne, *et al.*, *A&As* **119**, 373 (1996).

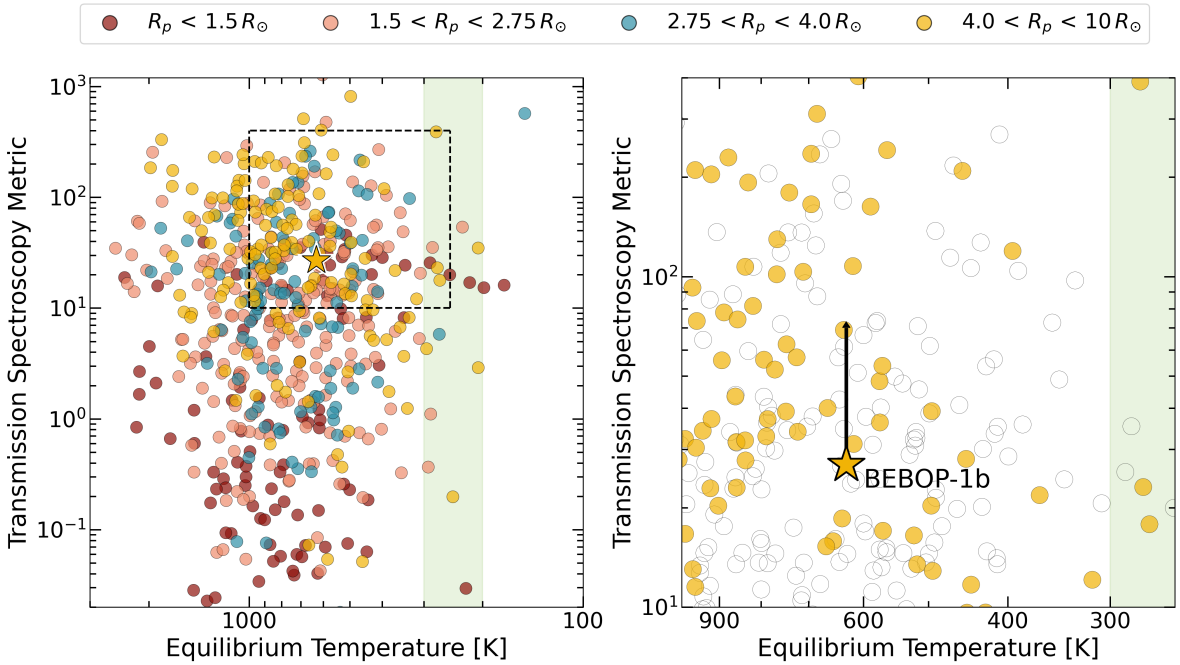

Figure 12: Transmission spectroscopy metric as a function of equilibrium temperature for planets with measured masses. Planets are coloured according to their size range, with BEBOP-1b plotted as a yellow star as it falls into the sub-Jovian regime of $4.0 < \mathrm{R_p} < 10\mathrm{R_\oplus}$. In both panels we show in light green the position of the temperate zone between $200 - 300\mathrm{K}$. In the right hand panel we zoom in on the vicinity of BEBOP-1b and indicate with a black arrow the range of possible TSMs for a mass down to $10\mathrm{M_\oplus}$. Data for this plot was retrieved from the NASA Exoplanet Archive (*69*) on May 18th 2022.

8. M. R. Standing, *et al.*, *MNRAS* **511**, 3571 (2022).

9. V. B. Kostov, *et al.*, *The Astrophysical Journal* **159**, 253 (2020).

10. F. Pepe, *et al.*, *A&A* **645**, A96 (2021).

11. A. H. M. J. Triaud, *The Rossiter-McLaughlin Effect in Exoplanet Research* (2018), p. 2.

12. V. Kunovac Hodžić, A. H. M. J. Triaud, H. M. Cegla, W. J. Chaplin, G. R. Davies, *MNRAS* **502**, 2893 (2021).

13. J. P. Faria, *et al.*, *A&A* **658**, A115 (2022).

14. E. Agol, *et al.*, **2**, 1 (2021).

15. D. W. Hogg, J. Bovy, D. Lang, *arXiv e-prints* p. arXiv:1008.4686 (2010).

16. J. Salvatier, T. Wiecki, C. Fonnesbeck, *arXiv e-prints* p. arXiv:1507.08050 (2015).

17. J. P. Faria, N. C. Santos, P. Figueira, B. J. Brewer, *The Journal of Open Source Software* **3**, 487 (2018).

18. B. J. Brewer, L. B. Pártay, G. Csányi, *Statistics and Computing* **21**, 649 (2011).

19. F. Feroz, S. T. Balan, M. P. Hobson, *MNRAS* **415**, 3462 (2011).

20. B. J. Brewer, *arXiv e-prints* p. arXiv:1411.3921 (2014).

21. A. H. M. J. Triaud, *et al.*, *MNRAS* **511**, 3561 (2022).

22. P. Kumaraswamy, *Journal of Hydrology* **46**, 79 (1980).

23. D. M. Kipping, *MNRAS* **434**, L51 (2013).

24. R. E. Kass, A. E. Raftery, *Journal of the American Statistical Association* **90**, 773 (1995).

25. R. Trotta, *Contemporary Physics* **49**, 71 (2008).

26. H. Jeffreys, *Theory of probability* (Oxford University Press, 1961).

27. L. McInnes, J. Healy, S. Astels, *The Journal of Open Source Software* **2** (2017).

28. D. Foreman-Mackey, *The Journal of Open Source Software* **1**, 24 (2016).

29. M. Tuomi, H. R. A. Jones, J. R. Barnes, G. Anglada-Escudé, J. S. Jenkins, *MNRAS* **441**, 1545 (2014).

30. N. C. Hara, N. Unger, J.-B. Delisle, R. Díaz, D. Ségransan, *arXiv e-prints* p. arXiv:2105.06995 (2021).

31. N. C. Hara, T. de Poyferré, J.-B. Delisle, M. Hoffmann, *arXiv e-prints* p. arXiv:2203.04957 (2022).

32. J. Gomes da Silva, P. Figueira, N. Santos, J. Faria, *The Journal of Open Source Software* **3**, 667 (2018).

33. M. Zechmeister, M. Kürster, M. Endl, *A&A* **505**, 859 (2009).

34. G. Pojmanski, **47**, 467 (1997).

35. B. Quarles, S. Satyal, V. Kostov, N. Kaib, N. Haghighipour, *ApJ* **856**, 150 (2018).

36. J. Laskar, **88**, 266 (1990).

37. J. Laskar, *Physica D Nonlinear Phenomena* **67**, 257 (1993).

38. A. C. M. Correia, *et al.*, *A&A* **440**, 751 (2005).

39. J. Schneider, *Planetary Space Science* **42**, 539 (1994).

40. D. V. Martin, A. H. M. J. Triaud, *A&A* **570**, A91 (2014).

41. V. B. Kostov, *et al.*, *The Astrophysical Journal* **784**, 14 (2014).

42. W. F. Welsh, *et al.*, *ApJ* **809**, 26 (2015).

43. D. V. Martin, A. H. Triaud, *MNRAS* **449**, 781 (2015).

44. D. V. Martin, *MNRAS* **465**, 3235 (2017).

45. F. Farago, J. Laskar, *MNRAS* **401**, 1189 (2010).

46. J. E. Chambers, E. V. Quintana, M. J. Duncan, J. J. Lissauer, *The Astrophysical Journal* **123**, 2884 (2002).

47. J. E. Chambers, *MNRAS* **304**, 793 (1999).

48. N. I. Shakura, R. A. Sunyaev, *A&A* **24**, 337 (1973).

49. A. Pierens, R. P. Nelson, *A&A* **556**, A134 (2013).

50. D. Thun, W. Kley, G. Picogna, *A&A* **604**, A102 (2017).

51. P. Benítez-Llambay, F. S. Masset, *ApJs* **223**, 11 (2016).

52. C. P. Dullemond, D. Hollenbach, I. Kamp, P. D'Alessio, *Protostars and Planets V* pp. 555–572 (2007).

53. I. Matsuyama, D. Johnstone, L. Hartmann, *ApJ* **582**, 893 (2003).

54. S.-J. Paardekooper, C. Baruteau, W. Kley, *MNRAS* **410**, 293 (2011).

55. A. Crida, A. Morbidelli, F. Masset, **181**, 587 (2006).

56. D. N. C. Lin, J. Papaloizou, *ApJ* **309**, 846 (1986).

57. M. Lambrechts, A. Johansen, *A&A* **572**, A107 (2014).

58. M. Lambrechts, A. Johansen, *A&A* **544**, A32 (2012).

59. A. Johansen, M. Lambrechts, *Annual Review of Earth and Planetary Sciences* **45**, 359 (2017).

60. S. T. S. Poon, R. P. Nelson, G. A. L. Coleman, *MNRAS* **505**, 2500 (2021).

61. G. A. L. Coleman, J. C. B. Papaloizou, R. P. Nelson, *MNRAS* **470**, 3206 (2017).

62. G. A. L. Coleman, *MNRAS* **506**, 3596 (2021).

63. M. J. Holman, P. A. Wiegert, *The Astrophysical Journal* **117**, 621 (1999).

64. E. M. R. Kempton, *et al.*, *PASP* **130**, 114401 (2018).

65. S. R. Kane, N. R. Hinkel, *ApJ* **762**, 7 (2013).

66. J. A. Orosz, *et al.*, *The Astrophysical Journal* **157**, 174 (2019).

67. R. M. Cutri, *et al.*, *VizieR Online Data Catalog* p. II/246 (2003).

68. L. R. Doyle, *et al.*, *Science* **333**, 1602 (2011).

69. R. L. Akeson, *et al.*, **125**, 989 (2013).

6.3 Attempt to view the secondary stars' CCF

After the first set of ESPRESSO DDT observations were obtained for J0608-59 (BEBOP-1), the COVID-19 pandemic closed both the La Silla, and Paranal observatories in Chile. With no more data being obtained on the target, the possibility of claiming a detection of TOI-1338b or BEBOP-1c was on hold. However, with 20 high precision spectroscopic ESPRESSO observations available, I attempted to view the CCF of the secondary star in the SB1 system through stacking the observations. This would transform an SB1 system into an SB2, something which had not been achieved at the time, and as the brightest SB1 system observed with ESPRESSO, J0608-59 presented the perfect opportunity to attempt this for the first time.

The observations are first correlated with the M5 spectral mask available for use in the ESPRESSO pipeline. Using an M5 mask should increase the correlation of the mask with any observed spectral signatures of the secondary M-dwarf star, and in turn increase its CCF signal. At this stage the correlation window is set to be wide enough to enclose the entire radial-velocity motion of the secondary star. The Keplerian signal of the secondary star can be calculated by multiplying the inverse of the primary RV's by the mass ratio of the binary ($Q = M_1/M_2$). The peak-to-peak amplitude of the secondary radial-velocity motion is then the span of these RV values. For the secondary star, BEBOP-1B, the span of its RV signal is $\sim 142\ \mathrm{km\,s^{-1}}$. The spectra is therefore correlated with a window of $200\ \mathrm{km\,s^{-1}}$ each side of the systemic velocity of the system (corresponding to a total window size of $400\ \mathrm{m\,s^{-1}}$).

Normalising the CCFs, and then phase folding them onto the binary orbital motion, with an added y-offset for each observation, yields Figure 6.18. The characteristic Gaussian signal caused by the primary star can be seen easily. Red crosses are plotted at the calculated velocity of the secondary star, though no minima can be seen in these locations, confirming the SB1 nature of J0608-59. See Section 4.2.3 for further details on ensuring BEBOP targets are truly single line eclipsing binaries.

Centering these CCFs at a velocity of $0\ \mathrm{m\,s^{-1}}$ by subtracting the RV signal of the primary, moves each observation into the primary stars reference frame. This allows for the combination of all individual CCFs into a 'Master' CCF through calculating the median (Figure 6.19). No signal from the secondary star is expected to be seen in the master CCF as this plot is in the primary stars reference frame, and the radial-velocity motion of the secondary spans 10's of $\mathrm{km\,s^{-1}}$.

Subtracting the 'master' CCF from each individual CCF removes the primary star's dominating signal, leaving residual CCFs which could contain the signal from the secondary star. Following the same logic and centering the residual CCFs on the motion of the secondary star places the observations into the secondary star's reference frame (Figure 6.20).

Finally, combining these residual CCFs should form a 'master' secondary star CCF. Calculating the median through all of the residuals yields the master residual CCF (Figure 6.21). Unfortunately, zooming in on zero velocity reveals no signal from the secondary star. Some lower regions are visible, but they do not exceed the noise of the master residual CCF, yielding no detection of the secondary star's CCF.

Repeating the process using G2 and F5 masks yields similar results. Varying the mass of the secondary in small increments, to verify that the secondary CCFs were being centered on the correct location, also

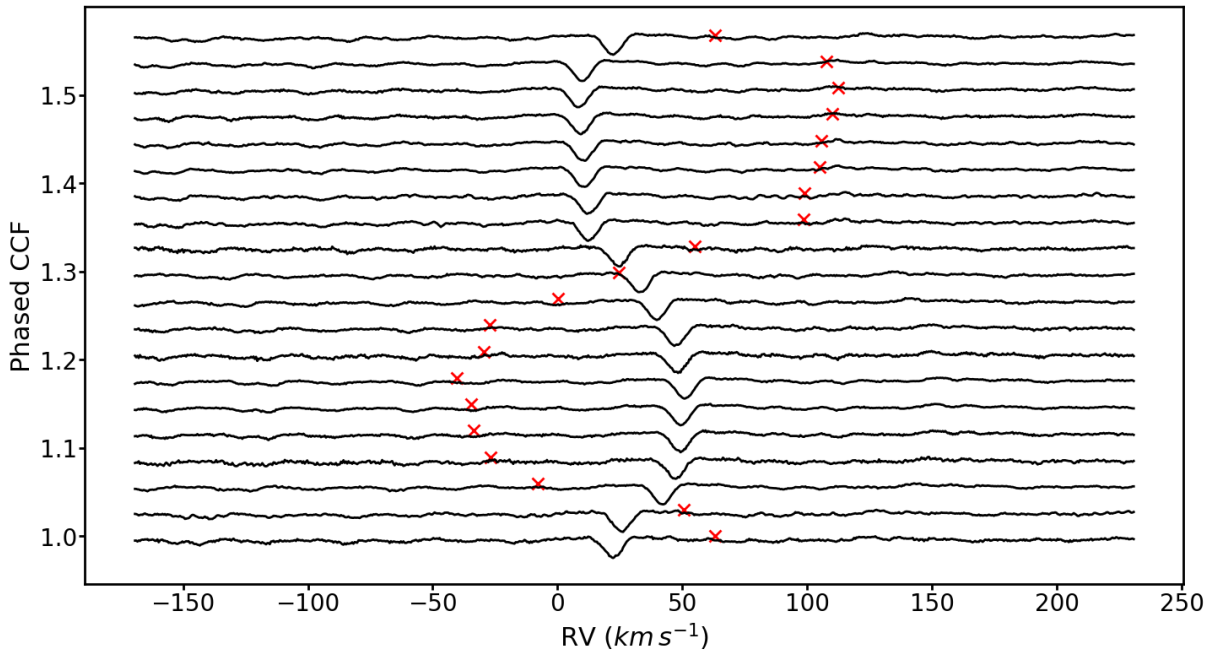

Figure 6.18: Plot of the phase folded CCF curves from the 20 DDT ESPRESSO observations of SB1 J0608-59/BEBOP-1. Each row corresponds to a different observation with an arbitrary offset applied. The phased motion of the primary star around the systemic velocity of the system can be seen by the Gaussian dips in each line. Red crosses mark the expected velocity of the secondary stars CCF signal.

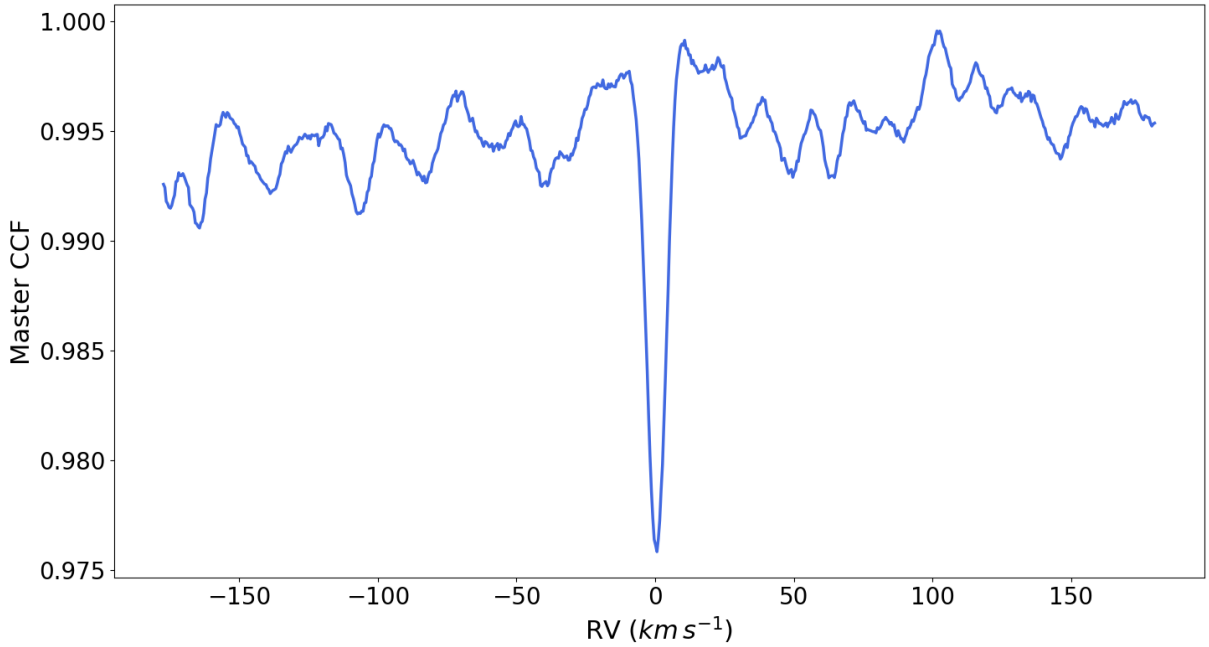

Figure 6.19: Master CCF plot calculated from taking the median of the 20 DDT ESPRESSO observations of SB1 J0608-59/BEBOP-1 seen in Figure 6.18 centered at a radial velocity of 0 km s^{-1}.

yielded similar results. Therefore, with the 20 ESPRESSO observations available at this time, the CCF of J0608-59/BEBOP-1's secondary star remained elusive.

Following the completion of the observing program on ESPRESSO, we now posses a total of 123 observations. Future work will involve an attempt to combine all of these observations in a similar way,

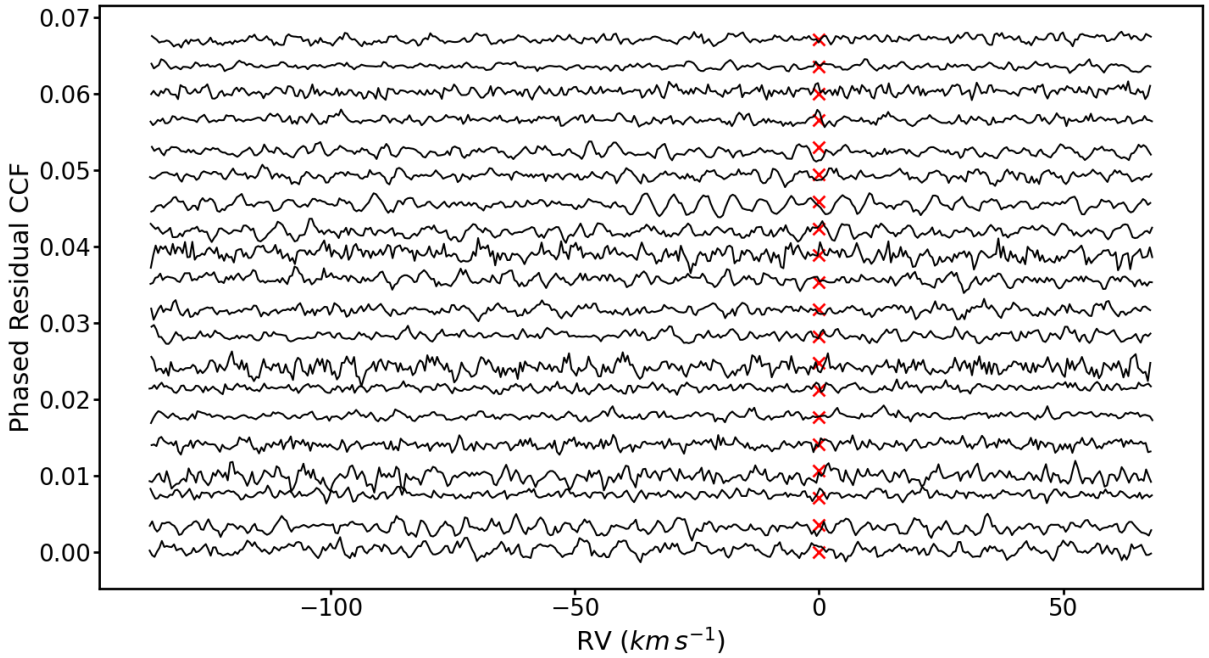

Figure 6.20: Plot of the phase folded residual CCF curves after having subtracted the 'master' CCF from the 20 DDT ESPRESSO observations of SB1 J0608-59/BEBOP-1. Each row corresponds to a different observation with an arbitrary offset applied. Red crosses mark the expected velocity of the secondary star's CCF signal, the CCF's have been moved to the secondary stars reference frame.

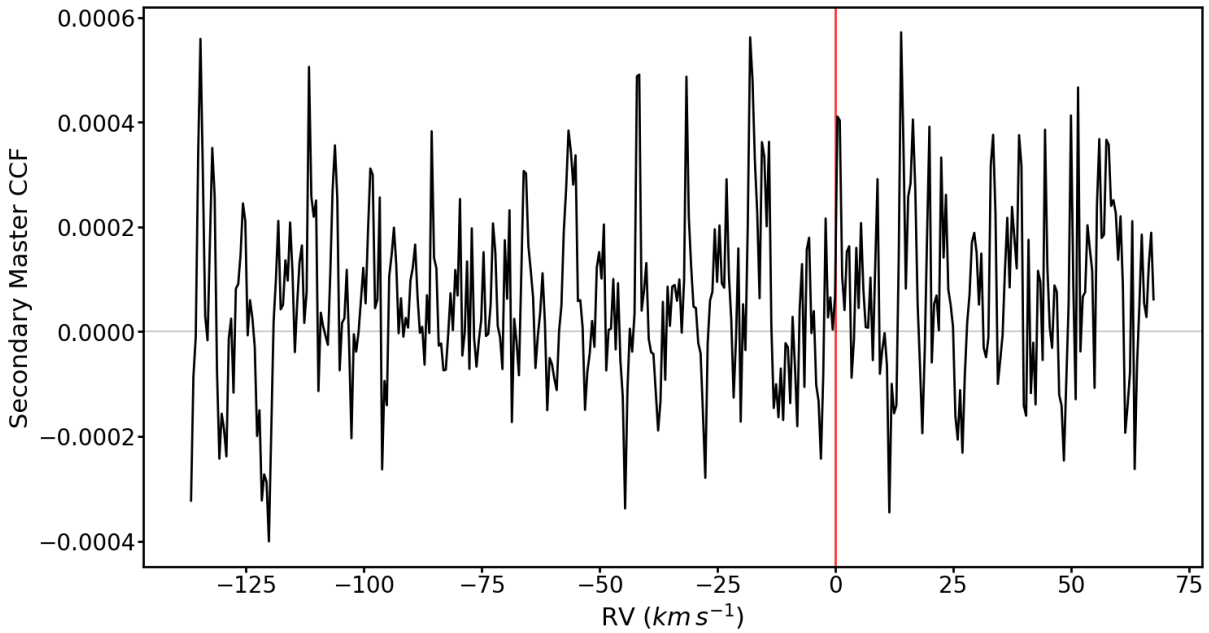

Figure 6.21: Secondary master CCF plot calculated from taking the median of the 20 DDT ESPRESSO observations of SB1 J0608-59/BEBOP-1 seen in Figure 6.20 centered at a radial velocity of 0 km s^{-1}. The red line shows the zero velocity reference frame of the secondary star, where the secondary star's CCF is expected to be seen. No signal from the secondary star (BEBOP-1B) can be seen.

with the hope that an additional 103 observations will allow the detection of the elusive signal of the secondary star.

Chapter 7

Conclusions & Future Work

"So long, and thanks for all the fish."

Douglas Adams, *The Hitchhiker's Guide to the Galaxy*

The aim of this thesis was to investigate the possibility of detecting circumbinary planets using Radial Velocity (RV) observations alone. Of the 14 circumbinary planets previously discovered orbiting main sequence binary stars, all of them have been found in transit by space telescopes which cost hundreds of millions of dollars, *Kepler* (Borucki et al. 2010) and *TESS* (Ricker et al. 2015). Due to the inherent differences between planets orbiting single stars to those orbiting binary star systems, circumbinary planets are difficult objects to observe. However, by expanding on lessons learnt from the TATOOINE survey (Konacki et al. 2009), the BEBOP survey (Martin et al. 2019) has finally broken through this observational barrier. BEBOP has now yielded both the first RV detection of a known circumbinary planet, Kepler-16b (Doyle et al. 2011) in Triaud et al. (2022) (Chapter 5), and the first RV discovery of a new circumbinary planet, TOI-1338/BEBOP-1c (Chapter 6), with ground-based radial-velocity observations alone. These breakthroughs have demonstrated an ability to discover these fascinating objects with accessible, and more cost-effective ground-based observatories.

With only 15 circumbinary planets having been detected, calculating accurate occurrence rates for these objects is important for guiding further observations into discovering the underlying demographics of these planets. My work on the analysis of RV data with `kima` has allowed me to develop a robust and efficient method of calculating detection limits for RV surveys (Chapter 4, Standing et al. (2022)). This method avoids the need to carry out computationally expensive injection recovery tests, which often assume circular orbits in their calculation. In Standing et al. (2022), I find that assuming circular orbits yields over optimistic detection limits by around $20-40\%$. Using `kima` and nested sampling to calculate these limits instead, negates the need to assume circular orbits as planetary eccentricity can be

fit simultaneously at little to no extra computational cost. Applying this method to the BEBOP sample demonstrates our ability to probe masses down to that of Neptune around the best of our targets, with sub-Saturn sensitivity on our brightest targets out to periods of ≈ 1000 days (Figure 4.27, Standing et al. (2022)).

Having calculated detection limits for the southern BEBOP targets, I then calculated the completeness of the survey, and in turn the occurrence rates of circumbinary planets (Section 4.3, Figure 4.29). Table 4.8 compares our occurrence rates for circumbinary planets to those from Armstrong et al. (2014) and the SPOTS survey (Asensio-Torres et al. 2018), and finds that they are in agreement.

Comparing BEBOP occurrence rates of circumbinary gas giant planets to those of gas giants orbiting single stars from Cumming et al. (2008) and Wittenmyer et al. (2020), we also find that they are broadly consistent.

However, I note that the occurrence rate values used here for circumbinary planets are calculated before the BEBOP survey is complete. Once completed, I will combine the northern and southern target detection limits, and re-calculate these occurrence rate values with the longest orbital period range allowed by our observational timespan. Obtaining further observations on each target will lower the detection limits, improving the completeness of the survey, and probing into longer orbital periods. Doubling the number of systems in the sample by including the northern targets will yield more precise occurrence rate limits, while including any confirmed candidates, along with Kepler-16b (from the northern targets), will allow true occurrence rates to be calculated in more areas of parameter space.

At this point in the survey, we have demonstrated our sensitivity to circumbinary planets, and have several candidate circumbinary planet signals, along with a circumbinary brown dwarf signal to be confirmed with further observations. We are limited in our planet search by the high level of residual RMS scatter present after having removed the binary in some of our targets. Future work is needed to attempt to fit for and remove this scatter. We are uncertain on the origin of this scatter, it could be caused by stellar variability, post-Keplerian effects (Chapter 4), or even undetected circumbinary planet signals. Fitting for post-Keplerian effects in `kima`, along with applying Gaussian Process (GP) to fit for stellar activity, may allow the level of scatter to be reduced, revealing many more circumbinary planet candidate signals as of yet hidden in our data. PhD student Thomas Baycroft will continue my work on the BEBOP survey, he will also attempt to include post-keplerian fits to the binary RV data in an attempt to reduce the residual scatter and improve our survey sensitivity.

In Chapter 6, I introduced the first entry in the BEBOP planetary catalogue TOI-1338/BEBOP-1c, BEBOP's first circumbinary planet discovery, a 69 $M_\oplus$ planet on a 215 day orbit around a 14.6 day period binary star system. The system itself was already known to host an inner circumbinary planet detected by transit in *TESS* photometry (Kostov et al. 2020), TOI-1338/BEBOP-1b, a 6.9 $R_\oplus$ planet on a 95 day orbit. Originally, we set out to confirm this discovery with RV observations, and were awarded time on the ESPRESSO spectrograph. Unfortunately we were unable to detect the smaller inner planet

TOI-1338/BEBOP-1b, and are only able to place an upper limit on its mass of < 23.6 $M_\oplus$ with 99% confidence, down from the 33 ± 20 $M_\oplus$ in (Kostov et al. 2020). In the process we discovered the second planet in the system, TOI-1338/BEBOP-1c, making the system the second multi-planetary circumbinary system discovered. With further observations, we will be able to determine the mass of the inner transiting planet, and ascertain the presence of any further planetary companions in the TOI-1338/BEBOP-1 system.

The planet TOI-1338/BEBOP-1c currently does not transit the central binary stars, though it is likely to transit at some point (Chapter 6, Standing et. al 2022 (In review)). PhD student Georgina Dransfield will monitor *TESS* (Ricker et al. 2015) lightcurves of TOI-1338/BEBOP-1 for any new planetary transits or ETV signals on the binary transits. Georgina will utilise the SPECULOOS (Delrez et al. 2018) and Antarctic Search for Transiting ExoPlanets (ASTEP) (Guillot et al. 2015) telescopes to capture any further planetary transits from the ground.

In Chapter 6, I described an attempt to view the Cross Correlation Function (CCF) signal of the secondary star in the single-line (SB1) TOI-1338/BEBOP-1 system. Unfortunately, I was unable to combine 20 ESPRESSO observations in a way which would reveal this signal. My hope is that including the remaining 103 ESPRESSO observations will reveal the secondary CCF and allow absolute masses for both stars to be determined. With absolute masses from both stars the absolute mass for TOI-1338/BEBOP-1c can be calculated.

During my PhD I have made contributions to several other bodies of work. Kostov et al. (2020), announces the detection of *TESS*'s first circumbinary planet orbiting the TOI-1338 system. In this system, observed in the BEBOP survey as EBLM-J0608-59, I later discovered an additional circumbinary planet with Radial Velocity (RV) observations alone (see Chapter 6). For the TOI-1338 paper we provided our RV observations to determine the binary stars motion and masses. Some of these observations I personally obtained through an observing run at La Silla observatory in Chile. I also analysed our RV data for any trace of the 95 day orbital period *TESS* planet, but found none. This analysis was not included in the final paper.

For Swayne et al. (2021), Kostov et al. (2021), and Sebastian et al. (2022) I contributed to the collection of data through carrying out observing runs at the OHP. I also contributed some primary analysis for TIC-1729 (Kostov et al. 2021), and EBLM IX (Sebastian et al. 2022).

I regularly operate the SPECULOOS telescopes remotely, facilitating some of the observations for the discovery of the two transiting super-Earth planets announced in Delrez et al. (2022).

I also reduced archival ESPRESSO data using the pipeline as described in Section 6.1 for Dransfield et al. (2022), before carrying out initial RV analysis along with contributing to the text of the final paper.

Finally, I will conclude this thesis by stating that the future for circumbinary planet research looks to be very exciting. The field has progressed steadily since I started my PhD, with the new TESS circumbinary planet discoveries (Kostov et al. 2020, 2021), along with our work in the BEBOP survey,

rekindling the excitement in the field which was first developed when Kepler-16b was discovered in Doyle et al. (2011).

When I began my PhD, no sessions on circumbinary planets were being held at any conferences. Through my work detailed in this thesis, I was asked to become part of the scientific organising committee for a special session focusing on circumbinary planets at the European Astronomical Society (EAS) conference 2022, where I chaired a session as a PhD student.

Transit missions utilising long stares have proved to be important for the discovery of transiting circumbinary planets, due to their longer orbital periods from the instability limit close to the binary stars (Holman & Wiegert 1999). As such, the *PLAnetary Transits and Oscillations of stars (PLATO)* mission (Rauer et al. 2014), planned for launch in 2026, will likely double the number of known circumbinary planets. With this mission comes a great opportunity for astronomers to discover and characterise more of these objects.

It is my hope that this work inspires others to search for, and discover many more circumbinary planets, and perhaps somewhere out there, there is a real-life Tatooine waiting to be discovered.

GUIDE TO THE ESPRESSO PIPELINE

> "The Hitch-Hiker's Guide has already supplanted the great Encyclopaedia Galactica as the standard repository of all knowledge and wisdom, ... , it scores over the older, more pedestrian work in two important respects. First, it is slightly cheaper; and secondly it has the words '*DON'T PANIC*' inscribed in large friendly letters on its cover."
>
> Douglas Adams, *The Hitchhiker's Guide to the Galaxy*

Here I will describe a step-by-step guide on the reduction of ESPRESSO data using the ESPRESSO pipeline (V.2.3.5). The ESPRESSO pipeline can be downloaded from here[a], and its user manual is available in the same web page.

Downloading data from the ESO archive

- File sizes for each observations and the numerous calibrations associated with them are large, therefore when downloading ESPRESSO data from the ESO data archive, I recommend using the shell script option.
- When downloading, ensure the associated raw calibrations for each observation are also downloaded by selecting the appropriate option.
- Once obtained, the shell script must be given execute permission by running the following command in the command line: '`chmod +x downloadscript.sh`'.
- The script can then be run by executing '`./downloadscript.sh`'.
- If the data to be downloaded is proprietary you will be prompted to sign in to your ESO account with relevant permissions to access the data in question.

[a] https://www.eso.org/sci/software/pipelines/espresso/espresso-pipe-recipes.html

- Once the download has completed, a folder titled '*data_with_raw_calibs*' will contain the compressed observation and associated calibration files. These will need to be uncompressed before data reduction can take place. To do this, navigate into the folder in command line and execute the following command '`gunzip -v *.Z`' (the '`-v`' option will allow you to track its progress).

Running the pipeline

- If you plan to run the pipeline via a remote connection use the '-Y' command when ssh-ing into the workstation.
- To run the pipeline via the Graphical User Interface (GUI) execute '`esoreflex espresso`'.
- Once the GUI has appeared, to point the code to the correct data we must change the working directories by clicking on them and then manually selecting the correct directories from the resulting window.
- The input directory '*ROOT_DATA_DIR*' should be set to the directory which contains the '*data_with_raw_calibs*' folder.
- The input directory '*RAW_DATA_DIR*' should be set to the '*data_with_raw_calibs*' folder.
- '*CALIB_DATA_DIR*' should not be changed, and points the pipeline to the calibration information installed with the pipeline.
- Output directory '*END_PRODUCTS_DIR*' is the location where the pipeline stores the output files from each run, and where the reduced and correlated data will reside.
- Before running the pipeline ensure to set the option '*Tools-Animate at run time*' to a value (10 ms is sufficient). This highlights the step which the pipeline is on as it reduces your data and allows you to track its progress.
- Finally to run the pipeline, click the blue 'play' button. A red square will highlight the step in the flow diagram the pipeline is currently at.
- At the '*Data_Set Selection*' step, a window will appear and allow you to select which observations you wish to run through the pipeline.
- Once the pipeline reaches the '*Science Reduction*' step, another window will appear in which you can set the CCF correlation settings such as stellar mask, RV centre, step-size, and window-size by clicking on the 'RV' tab in the upper right of the window.
- Clicking on the *CCF_A* button in the lower left of this window will display the current plot of the CCF, along with the Barycentric Julian Date (BJD) of the observation and calculated RV value and uncertainty.
- Two check boxes on the right of the window allow the values set in the '*RV*' tab to be used in subsequent runs on the same dataset, and can also suppress this window from appearing, allowing the pipeline to continue to the next observation without interruption.
- If the CCF correlation settings were changed, clicking '*Re-run Recipe*' will re-correlate the data with the input values. To continue to the next observation, click '*Continue Workflow*'.

- Once the pipeline has correlated each observation selected at the '*Data_Set Selection*' step, a window will appear at the '*ProductExplorer*' step allowing the user to inspect the reduced data. Select 'continue' to finish the reduction process.

Exploring the output data

- The output data will be located in the folder selected in 'Output directory'. The data products created for each observation will be located within a folder named as the data and time the reduction pipeline was initiated (e.g. '$2021-01-05T10:48:32$').
- A folder for each observation selected for reduction will be located within this folder (e.g 'ESPRE.2020-12-24T04:12:44.930').
- Within these folders all data products created by the pipeline for the observation are stored as '.fits' files.
- The 'CCF_A' files contain the observations' BJD, RV, uncertainties, bisector and FWHM values, along with any other relevant information.

List of Figures

1.1 An illustration of the planets orbiting TRAPPIST-1 compared to the scale of the Solar system. All planets can be seen to orbit well within the orbital distance of Mercury. Credit: NASA/JPL-Caltech 4

1.2 Plot of planet mass in Jupiter masses against orbital period in days for all confirmed exoplanets. Planets are coloured and shaped based on their discovery method. Data taken from the NASA Exoplanet Archive as of February 2022. 8

1.3 The solar spectrum. Absorption lines can be seen as the vertical dark lines in the spectrum. Credit: NOAO/NSO/Kitt Peak FTS/AURA/NSF 11

1.4 Figure of the cross correlation method for calculating the Radial Velocity RV of a star adapted from Roy et al. (2016). Left: Black dashed observed stellar absorption spectra and coloured template spectra in wavelength space. Colours represent the shifting of the template from shorter (blue) wavelengths to longer (red) wavelengths. Green represents the wavelength at which the template matches the observed spectra. Right: Resulting Cross Correlation Function CCF calculated at each step. The instantaneous radial velocity is then obtained from the centre of a gaussian fit to the CCF. 12

1.5 Top: Schematic of a binary star systems orbital motion at four different times through one orbit. Bottom: Phased radial velocity plot showing the same orbit of the binary star J1928-38. Red points are RV data from the HARPS spectrograph as part of the BEBOP survey (see Chapter 4). The blue line is a Keplerian RV signal fit to the data. The semi-amplitude K of the binary signal is shown. Inspired by Martin (2017a). 13

1.6 Schematic of planetary orbit around a single star. The periastron is the location on the planets orbit where it is closest to its star. f is known as the 'true anomaly' and denotes the angle from the periastron direction to the orbital position of the planet. ω is the argument of periastron, and denotes the angle from the line of nodes to the periastron direction. i is the orbital inclination of the system. Figure adapted from Rebound Orbital elements. 14

1.7 Figure from Berdyugina (2005) illustrating the effect of a starspot on the spectral line profile of a star. The dashed lines in the lower row of plots indicate a model with no spots present, and the solid lines those of the star with the spot. 16

1.8 Right: CCF of HD166435 spectra. Left: bisector of the CCF. Here we can see the boundaries which define the top and bottom of the bisector slope, V_0 is an arbitrary offset. Both plot CCF contrast against RV. Figure from Queloz et al. (2001b). 17
1.9 An illustration of transits and occultations from Winn (2010). As can be seen, there is a dip in brightness as the planet passes in front of the star, the "transit". The combined flux from the system increases slightly as the planets day side comes into view. Then as the "occultation" occurs, the reflected component of stellar flux is blocked by the star and the total flux decreases to the stellar value. 18
1.10 Direct imaging of quadruple exoplanet system HR 8799, obtained from Marois et al. (2010). A time-lapse of the planets' motion over 7 years is also available by clicking here. 21
1.11 Histogram of number of planets per star with orbital periods < 100 days against planet radius, modified from (Fulton et al. 2017). Shaded regions illustrate the radius definitions of super-Earths (red) and sub-Neptunes (blue). 24
1.12 Plot from Weiss et al. (2018) which shows the system architectures of *Kepler* multi-planetary systems with at least 4 planets. Each row depicts a planetary system (name left), and each planet is plotted against its semi-major axis (AU) in log space. The size of each point depicts the planet's radius, and colour depicts their equilibrium temperature. 26
1.13 ALMA dust continuum image of the protoplanetary disk surrounding the star HL Tau from ALMA Partnership et al. (2015). 28
1.14 Luke Skywalker stares longingly at the binary sunset on his circumbinary home planet of "Tatooine", as John Williams's "Binary Sunset" theme swells into its crescendo. *Star Wars IV - A New Hope* (Lucas et al. 1977). 32
1.15 Schematic of planetary orbits within binary star systems. Left: A circumbinary planetary system, consisting of a close binary with the primary star (yellow), and secondary star (red), orbited by a circumbinary planet (green). The red shaded region surrounding the binary depicts the instability region. Right: A circumprimary/secondary planetary system, within a wide binary. The primary star (yellow) is orbited by a circumprimary planet (green), and the secondary star (red) is orbited by a circumsecondary planet (green). Adapted from Martin (2017a). 32
1.16 Lightcurve of Kepler-16 from Doyle et al. (2011) over ≈ 600 days. Primary eclipses of the binary are marked in blue, secondary binary eclipses in yellow. The transits of the planet as it passes in front of the primary star green, and the transits of the planet in front of the secondary star in red. 35

1.17 Plot of *Kepler* circumbinary planet periapse distance, $a_p(1-e_p)$ against the instability limit from Equation 1.17. The red region depicts the unstable region surrounding the binaries. Kepler-47's multi-planetary system is depicted by the grey circles in comparison to the blue squares for the single planet systems. The right hand plot is zoomed in to the instability limit excluding Kepler-1647. Planets are labelled by their *Kepler* numbers. Plot taken from Martin (2018). 36

2.1 Illustration of the sampling levels at each stage for classic and diffusive nested sampling. For the bi-modal distribution shown, classic nested sampling could have difficulty exploring both islands of probability. However, diffusive nested sampling allows particles to travel more freely to isolated nodes of higher likelihood through lower levels. Figure from Brewer et al. (2009). 41

2.2 An example of a DNS run where the two stages of a run can be seen. The initial rising stage, where new likelihood levels are created until the maximum number of levels have been reached. During this stage the particle is still able to explore lower levels, allowing more freedom in exploration. Once the limit of the number of levels have been created, the particle is free to explore all levels with uniform weightings. 42

2.3 Default `kima` plots from posterior samples obtained from a `kima` run on the example data for system 51-Peg. a) Shows the phased keplerian plot of the data with the posterior Keplerian model with the highest likelihood, along with its associated residuals. b) Shows a histogram of the number of posterior samples with N_p. In this case N_p was allowed to vary uniformly between 0 and 1, as can be seen all posterior samples are found with $N_\mathrm{p} = 1$, showing a definite detection of 51-Peg b as in Mayor & Queloz (1995). 43

2.4 Histogram of the number of posterior samples with associated N_p from a `kima` run on radial velocity data for the EBLM J0608-59 (TOI-1338/BEBOP-1) system (Chatper 6). The chosen N_p is decided from the Bayes factor as discussed in the text, and is displayed in red. 45

2.5 Plot of the eccentricity vs orbital period of posterior samples obtained from a `kima` run on radial velocity data for EBLM J0608-59 (BEBOP-1). The thick red line corresponds approximately to the exclusion zone created by the instability region of the binary stars, the blue cluster of points at $\approx$ 14.6 days. The thick green lines mark the approximate exclusion zone carved by BEBOP-1c, the green cluster of points at $\approx$ 220 days. Black points are valid samples which are not part of a cluster, while the orange points are clustered, representing the third densest region of samples. The faded grey points represent posterior planetary orbits which cross with another planet, or the instability region in their proposed systems. 50

2.6 Top panel: log-likelihood (L) vs enclosed prior mass (X). Green points indicate samples at which new levels were created. Lower panel: Posterior weights of the saved particles. A successful run should show a single peak as above (Brewer & Foreman-Mackey 2016). Plot obtained from `kima`. 52

2.7 Corner plot of posterior samples from green cluster in Figure 2.5 corresponding to TOI-1338/BEBOP-1c. Figure created using corner package (Foreman-Mackey 2016). 57

3.1 Power density spectrum (gray) and the smoothed spectrum (black) around the p-mode oscillation frequencies. The 68% confidence interval of the fit mode frequencies are shown as the vertical shaded regions. Colors denote the angular degree,l, where blue is $l = 0$, orange is $l = 1$, and green is $l = 2$. 62

3.2 Échelle diagram showing oscillation frequencies modulo the large separation ($\Delta\nu = 69.0$) supplied by each team: MV (circles), IWR (squares), MBN (diamonds), and WJC (triangles). The colors represent the angular degrees, l, that were considered. The shaded regions represent 68% confidence interval of the frequencies in the final fit. Several mixed modes (diverging modes along the $l = 1$ ridge) were suggested, but could not be verified by the other teams, and so were not included in the final fit. 62

3.3 Spectral energy distribution of λ^2 For. Red symbols represent the observed photometric measurements, where the horizontal bars represent the effective width of the passband. The photometric measurements are $B_T V_T$ magnitudes from *Tycho-2*, the $BVgri$ magnitudes from APASS, the JHK_S magnitudes from *2MASS*, the W1–W4 magnitudes from *WISE*, and the G magnitude from *Gaia*. Blue symbols are the model fluxes from the best-fit Kurucz atmosphere model (black) 63

3.4 Top: Kiel diagram showing the literature values (purple) and seismic values (red; see Table 2) of λ^2 For. Dashed lines indicate evolutionary tracks spanning a mass range of $0.8 - 2M_\odot$, in increments of $0.2M_\odot$. Literature values are presented in Table D.1. Bottom: Masses and radii of the literature sources with a combination of log g with either mass or radius in comparison to the seismic estimates. 64

3.5 Top: Observational RV data (blue) of λ^2 For, from AAT, Keck, and HARPS, phase-folded at a period of 17.25 days. The phase-folded best-fit model is shown in red, with the model uncertainties in shaded red. Bottom: Residual RV after subtracting the best-fit RV model. The dashed lines indicate the standard deviation, $\sigma = 2.64$ m/s, of the residual. 65

3.6 Periodograms of the HARPS RV data (blue), the spectral line bisector span (orange), and the cross-correlation function full-width at half maximum (FWHM, green). The FWHM and bisector span were only available for the HARPS data, and so the AAT and Keck data are not included in the power spectra shown here. The full vertical line shows the period of λ^2 For b, and the dashed line is the secondary 33 day periodicity. The comb of peaks around the orbital period of λ^2 For b are caused by the observational window function, as is the case for many of the peaks around the 33 day periodicity. 65

3.7 Stability map (MEGNO) for a particle at different periods and inclinations, in the presence of the known planet λ^2 For b. The color bar indicates the linear scale of the MEGNO statistic, for which darker colors represent a higher degree of orbital divergence (chaos) on timescales of 10^5 orbits of λ^2 For b. Lighter shaded regions denote stable orbits. The upper range of the color bar has been truncated at a MEGNO value of 4 for clarity. The marginalized posterior distribution of the 33-day orbit is shown in green, with the median indicated by the square symbol. Orbits in resonance with λ^2 For b are indicated by vertical dashed lines. Additional resonances are not marked for clarity. The solid black square denotes the period and eccentricity of λ^2 For b. 66

3.8 Resulting counts over time for different *TESS* data reduction pipelines. The Buzasi Corr time series very effectively removes most of the long-period variability; however, the SPOC time series still shows the lowest variance in the frequency range around the p-mode envelope. . . 69

3.9 Corner plot of the rotational splitting and inclination angle posterior distributions from the seismic fit, consisting of 10^5 samples. The marginalized posterior distributions are shown in the diagonal frames. The dashed vertical lines show the 16th, 50th, and 84th percentiles of the distributions at $i = 38^{+31}_{-26}$ degrees and $\nu_{rot} = 1.2 \pm 0.9$ for the inclination and rotational splitting respectively. The lower left frame shows a 2D histogram of the distributions (black). The shaded red curve shows the rotational splittings corresponding to $v \sin i = 2.5 \pm 0.1$km/s from Ammler-von Eiff Reiners (2012) and a stellar radius of $R_* = 1.63 \pm 0.04 R_\odot$. 69

3.10 Marginalized posterior of the N_p parameter in the `kima` fit to the RV measurements of λ^2 For. The number of samples in each bin corresponds to the likelihood, while the ratio of the height of each bin indicates the Bayes factor of one configuration over another. Comparing the cases of $N_p = 0$ and $N_p = 1$ the Bayes factor is effectively infinite, indicating that there is at least one planet in the system. In contrast, the ratio between $N_p = 2$ and $N_p = 1$ is low, with a Bayes factor of 1.67, suggesting that there is little evidence to support a two-planet configuration. 70

3.11 Corner plot of the orbital parameters from the `kima` fit: the eccentricity e, the orbital period P, velocity semi-amplitude K, and the projected planet mass M. 70

4.1 Histograms of the visual magnitude of BEBOP's northern (top), and southern (bottom) SB1 binary targets, in comparison to TATOOINE's SB2 binary target sample in red. The blue and green histograms represent BEBOP's primary and secondary samples respectively. Median values for each sample are indicated by the dotted lines in their respective colours. 75

4.2 Histogram of median RV uncertainties obtained in observations with the HARPS spectrograph (Mayor et al. 2003) for BEBOP's northern (top), and southern (bottom) SB1 binary targets, in comparison to TATOOINE's SB2 binary target sample. Colours and median values in both plots are depicted as in Figure 4.1. The TATOOINE sample consists of the uncertainties for the primary and secondary stars for each of their SB2 binary targets from each individual instrument. 76

4.3 Top: Histogram of median SNR at 260 nm obtained in observations with the SOPHIE spectrograph (Perruchot et al. 2008) for BEBOP's northern SB1 binary targets. Bottom: Histogram of median SNR at 260 nm obtained in observations with the HARPS spectrograph (Mayor et al. 2003) for BEBOP's southern (bottom) SB1 binary targets. Colours and median values in both plots are depicted as in Figure 4.1. 77
4.4 A picture of the Swiss 1.2 m telescope located at ESO's Las Silla Observatory in Chile taken when I visited in 2019, just before being invited for pisco sours with the Swiss observers at the start of the night. 79
4.5 A picture of myself at ESO's 3.6 m telescope located at the Las Silla Observatory in Chile when I visited in 2019. 80
4.6 Left: A Picture of the dome housing the 1.93 m telescope located at the OHP in France taken at twilight during one of my many observing runs there. Right: A picture of the 1.93 m telescope within the dome. 81
4.7 A picture of the four 8.2 m UT's of the VLT at Paranal observatory, Chile. Superimposed are the light tunnels connecting to the instruments such as the ESPRESSO spectrograph used in this work. Also visible are the three smaller 1.8 m AT's. Image credit: ESO. 82
4.8 Combined instrument data quality sheet for CORALIE, and HARPS J0228+05 data. Dataset statistics can be found in the top panel. The remaining panels are plots of FWHM, Bisector, SNR (at 550 nm), and RV uncertainty against measurement number. Datapoints which lie further than 2σ from the median values in each window (per instrument) are indicated by red crosses. There are two CORALIE instruments in this plot as a fibre change introduced an RV offset. Observations before and after the change are therefore treated as from separate instruments. 84
4.9 Plot of the phase folded CCF curves from SB1 J0310-31 observations. Each row in each of the four plots corresponds to a different observation. The lower row of plots has the binary CCF centered at 0 $\mathrm{km\,s^{-1}}$. Plots in the left column have values below the median for each observation shaded red. Plots in the right column are the same phase diagrams drawn with a colour-map. 85
4.10 Plot of the phase folded CCF curves from 10 SOPHIE observations of SB2 HD 78418. Plots are the same as in Figure 4.9. A second CCF can be seen clearly in all observations moving in opposition to the primary star. 86

4.11 Data-sheet produced from a `kima` run on J0608-59 (BEBOP-1, Chapter 6) data. The statistics at the top provide quick-look information. The following two plots show the highest likelihood posterior sample with the chosen number of planetary signals (N_p) along with its residuals. Orange points show the HARPS data, and the red and green points show ESPRESSO data before and after a calibration lamp change respectively (Faria et al. 2022). The third plot shows the FWHM - mean FWHM, with all three plots against BJD (days) - 2,450,000. Below this on the left is a plot of the bisector slope vs RV value for each data-set. The upper plot to the right of the bisector plot shows the residual values having subtracted the only the binary star's signal. Below this, the plot shows a modified version of Figure 2.4, log(number of posterior samples) vs number of planets. The associated Bayes Factors for each number of signals are plotted above their associated number, with the vertical red line indicating the chosen N_p signals displayed in the plots. The grey histogram represents the raw `kima` posterior samples, and the blue histogram shows number of posterior samples in each bin after having removed any crossing orbits. The lowest plot in the data sheet shows a histogram of the number of posterior samples vs orbital period. The red line on this plot indicates the timespan of the data, and the green line a year. 87

4.12 Plot of bisector slope against residual RV values after having subtracted the binary signal for southern target EBLM J0407-23. Red and green data points are CORALIE and HARPS data respectively with associated uncertainties. Anti-correlation here indicates the presence of stellar activity. 88

4.13 Phased Keplerian binary Radial Velocity (RV) signal for J0608-59 calculated from the highest likelihood posterior sample obtained. Above are the exact parameters from the posterior sample used to calculate the model. O-C residuals are plotted below. Orange points show the HARPS data, and the red and green points show ESPRESSO data before and after a calibration lamp change respectively (Faria et al. 2022). 89

4.15 Best fit phased RV models for a) = J0310-31, b) = J1540-09, c) = J1928-38 with associated residuals. Doppler motion of the primaries seen here are caused by the secondary stars. Residuals have an RMS = 3.2, 3.8, and 3.0 m s^{-1}, respectively. 93

4.16 Hexbin plot denoting the density of posterior samples obtained from three separate `kima` runs on J0310-31 with $N_{\rm p}$ fixed = 1, as a grayscale. Faded blue lines show detection limits calculated from each individual run on the system as described in the text. The solid blue line shows the detection limit calculated from all posterior samples combined. Coloured symbols indicate the Bayes factor results of injection/recovery tests and correspond to the colour bar on the right. Circles are for injected static Keplerian sinusoidal signals, whereas triangles are for N-body simulated injected signals. The Keplerian and N-body signals are injected at the same orbital periods but are represented slightly offset horizontally here for visual clarity. The faded red dashed lines show masses of solar system planets for comparison. 97

4.17 Same as in figure 2 but for three separate kima runs on J1540-09 (a), and J1928-38 (b) with N_p fixed = 1. All injected signals here are static Keplerian sinusoidal. 98
4.18 Plot of Bayes Factor (BF) vs number of posterior samples from a kima run with a 227.57 d, 3.16 m s^{-1} injected signal in J0310-31. In blue, we show the cumulative Bayes factor as a function of the number of posterior samples. The blue line shows the BF values, and and their running uncertainty are drawn as the shaded blue region. We add one red dot after 10 $N_p = 0$ samples to show the BF value then, with their uncertainties. The horizontal red line shows the final BF value calculated with all posterior samples. 99
4.19 Hexbin plot of posterior samples for J0310-31 as in figure 2. The coloured lines here indicate the detection limits calculated with the posterior samples split into five even phase bins with the black line representing the phase bin containing $\phi = 0$. 99
4.20 Plot of residual radial velocity amplitude as a function of time, after removing a Keplerian binary signal from N-body simulated J0310-31 radial-velocity dataset. Simulated data are computed with rebound including the binary and an orbiting circumbinary planet with P_p = 74.59 d and K_p = 6.32 m s^{-1}. To reveal the Newtonian perturbation, we plot one point for each night over the entire duration of our dataset. The blue line depicts 1.3× RMS within bins 45 day wide. We use this line as a visual guide to the amplitude of the effect. The shaded orange region illustrates the RMS scatter obtained on the data we collected on J0310-31. The *bow-tie* shape of the residuals is caused by apsidal motion of the binary ($\dot{\omega}_{bin}$), caused by the planet, which a Keplerian model does not include. 99
4.21 a) Phased RV residuals from the best fit model of J0310-31 simulated binary and additional post-Newtonian effects only. Residuals have an RMS = 0.07 m s^{-1}. b) Semi-amplitude vs period plot of posterior samples from a kima run on the residuals seen in plot a). Posterior samples are located at half, third and a quarter of J0310-31's binary orbital period. 100
4.22 Hexbin plot of posterior samples obtained from three separate kima runs on J0310-31 with an additional 486d signal located at the green point, with N_p free between 0 and 3. The blue line shows the detection limit as seen in Fig. 2. Faded red lines show detection limits calculated from each individual run on the system after having removed the most likely $N = 1$ signal from the data. The solid red combines all these posterior samples together. 100
4.23 Hexbin plot of posterior samples and blue detection limit for J0310-31 as in figure 2. The Red and green lines here indicate the same limit calculated from posterior samples with eccentricities < 0.1 and < 0.5 respectively. Horizontal coloured lines show the mean semi-amplitude of the three coloured detection-limits out to 1000 days. 101
4.24 Plot of the percentage difference between detection limits calculated with all posterior samples, and posterior samples with eccentricities < 0.1 and < 0.5 in red and green respectively for J0310-31 from figure 9. Solid coloured lines represent a running mean taken on the faded coloured lines. 101

4.25 Mass vs period plot showing the three detection limits from this work as blue lines in comparison to confirmed exoplanets as grey circles, and transiting circumbinary planets as pink diamonds. Solar System planets are depicted as yellow dots for reference. Circumbinary planets in order of increasing period; Kepler-47 b, Kepler-413 b, TOI-1338 b, Kepler-38 b, Kepler-35 b, Kepler-64 b, Kepler-1661 b, Kepler-47 d, TIC-1729 b, Kepler-16 b, Kepler-453 b, Kepler-34 b, Kepler-47 c, Kepler-1647 b. Arrows illustrate planets with upper mass limits with the symbol placed to give a 2σ upper limit. 102

4.14 Phased Keplerian Radial Velocity (RV) signal calculated from the highest likelihood posterior sample obtained corresponding to a single ($N_p = 1$) additional Keplerian signal. Above are the exact parameters from the posterior sample used to calculate the model. O-C residuals are plotted below. Orange points show the HARPS data, and the red and green points show ESPRESSO data before and after a calibration lamp change respectively (Faria et al. 2022). . 106

4.26 a) Plot from Sybilski et al. (2013) showing the light-time effect for the primary star in red, and secondary star in green. Also plotted are the Keplerian RV signals for the primary and secondary stars $\times 10^{-5}$ in blue and magenta respectively. Orbital values for the system are as follows; $M_1 = 1\ M_\odot$, $M_2 = 0.5\ M_\odot$, $\omega = 108°$, inclination= 29°, $P_{bin} = 5$ days, and $e = 0$ (Sybilski et al. 2013). b) The same curves calculated using Equation 4.3 and the above values. c) The same signals calculated using Equation 4.3 without squaring the sin term, and using the above values except with $\omega = 18°$. 109

4.27 Left: detection limits for BEBOP South targets. Blue lines represent the detection limits of the primary BEBOP sample, while the green lines indicate the detection limits of the secondary sample. The orange line illustrates BEBOP-1's detection limit with both HARPS and ESPRESSO data (Chapter 6), along with the green point indicating the detected circumbinary planet BEBOP-1c (Chapter 6). The red line is BEBOP-1's detection limit calculated using only the observations obtained by the HARPS spectrograph as a fairer comparison to the other limits. Right: histogram of detection limits from the left plot for the BEBOP South primary (blue) and secondary (green) targets. Median values of the primary and secondary samples are indicated by the blue and green dashed lines respectively. 110

4.28 Histogram of HARPS residual Root Mean Squared (RMS) scatter after removing the binary signal for the 65 Southern targets for which detection limits were calculated. Blue and green colours represent BEBOP's southern primary (42 targets) and secondary (23 targets) sample respectively. The red histogram represents the RMS values for the primary and secondary stars for each of their SB2 binary targets from each individual instrument from the TATOOINE survey Konacki et al. (2009). Median values for each sample are indicated by the dotted lines in their respective colours. 111

4.29 Current completeness for the BEBOP south survey consisting of 65 binary targets in planetary mass vs orbital period. The red contours illustrate the completeness of the survey from 0% (white) to 100% (dark red) as in Figure 10 in Martin et al. (2019). The white boxes show the regions in parameter space for which we calculate the abundance of circumbinary planets. The white number in the centre of each box corresponds to the 2σ (95%) upper limit on the abundance, except for the box containing a planetary detection of BEBOP-1c, shown in green (Chapter 6), where the value is the abundance along with its 1σ uncertainty. The white values in the lower right corner of each box is the mean completeness within that particular box. All white values are percentages. The upper limit on the mass for BEBOP-1b is also shown as the orange point with the arrow (Chapter 6). 112

4.30 Phased Keplerian Radial Velocity (RV) signal calculated from the highest likelihood posterior sample obtained corresponding to an additional candidate brown dwarf signal to the binary EBLM J1250+26. The incomplete orbit is illustrated by the straight line from phase 0.35-0.6. O-C residuals are plotted below. All data was obtained with the SOPHIE spectrograph (Mayor et al. 2003). 115

4.31 Phased Keplerian Radial Velocity (RV) signal calculated from the highest likelihood posterior sample obtained corresponding to an additional candidate circumbinary planet signal to the binary EBLM J2359+44. O-C residuals are plotted below. All data was obtained with the SOPHIE spectrograph (Mayor et al. 2003). 116

5.1 Lomb-Scargle periodogram of Kepler-16's radial velocities (top) and Hα (bottom). The radial velocities are shown after removing the binary motion, and a cubic function. The four lines are, from bottom to top, the 10%, 1%, 0.1% and 0.01% false alarm probabilities. There is a highly significant peak around 230 days (vertical red dotted line) that is present in the radial velocities but not in Hα. The Hα measurements contain significant periodogram power at $\gtrsim$ 2000 days, indicating a long-term trend in the chromospheric emission from the primary star. 122

5.2 Best fit adjustment to the SOPHIE radial velocity data. *a:* Doppler reflex motion caused by the secondary star. *b:* Doppler reflex motion caused by the circumbinary planet. *c:* Cubic drift associated with a magnetic cycle. *d:* radial velocities as a function of time with a binary+planet+cubic function model. Residuals are displayed below. 122

5.3 Detection sensitivity to additional planets plotted as semi-amplitude $K_{1,\mathrm{pl}}$ as a function of P_{pl}. The hexagonal bins depict the density of posterior samples obtained from three separate Kima runs applied on the Kepler-16 radial velocity data data after removing two Keplerian signals shown with green dots. The faded blue lines show detection limits calculated for each of the three runs on the system. The solid blue line shows the detection limit calculated from all posterior samples combined. The solid red line is the outline of the posterior that led to the detection of Kepler-16 b and of a long-term trend associated with a magnetic cycle. The green dots represent the two signals removed from the data to compute the blue detection limit. 124

5.4 Bayes factors obtained for subsets of data with increasing size. The blue line and triangles indicate the Bayes factors obtained by running KIMA on the first N data points obtained on Kepler-16. The black line and dots show the same but for randomly sampled N data points within the first 3 years of data. Coloured regions represent various thresholds corresponding to improvements in evidence in favour of the more complex binary + planet model as per the Jeffreys' scale detailed in Standing et al. (2021). 124

6.1 ESPRESSO instrument field of view illuminated by an homogeneous source shows ESPRESSO smiling. Picture and caption from ESPRESSO user manual 130

6.2 Histogram periodogram of posterior samples obtained from a `kima` run on the BEBOP-1 system. The 14.6 day binary period along with the 215.6 day period of BEBOP-1c can be clearly seen, and are highlighted in red and blue respectively. The inlaid plots show a zoom on these two peaks. No significant peak from BEBOP-1b can be seen in these posterior samples. 138

6.3 Phased Keplerian Radial-Velocity (RV) models of BEBOP-1c with ESPRESSO (blue diamonds) and HARPS (orange squares) data along with associated residuals after removing the binary signal. RV data is binned by 0.1 phase units (~21.6 days) and illustrated by the circular points. Red Keplerian models are based on 500 randomly drawn posterior samples from a `kima` run, shaded from the 50^{th} to 99^{th} percentiles. The shaded regions display the repeating signal. 139

6.4 Radius vs Mass plot of all transiting circumbinary planets (dark blue) and planets orbiting single stars (light blue). BEBOP-1b is highlighted in orange, with one of the lowest densities known. The newly-discovered BEBOP-1c is not on the graph since it does not transit. For the single star planets we restrict the sample to planets with mass and radius percentage errors less than 20%. 140

6.5 Overview of the BEBOP-1 system along with the extent of the systems habitable zone. The conservative habitable zone is shown by the dark green region, while the optimistic habitable zone is shown by the light green region. Binary stars are marked by the blue stars in the centre. BEBOP-1c's orbit is shown by the red orbit models, based on 500 randomly drawn posterior samples from a `kima` run, shaded from the 50^{th} to 99^{th} percentiles. BEBOP-1b's orbit is shown by the yellow models, and is also based on 500 random samples drawn from the posterior in its discovery paper (Kostov et al. 2020). 142

6.6 Corner plot of posterior sample distributions for the Binary stars orbital parameters; eccentricity, orbital period, semi-amplitude, argument of periastron, time of periastron passage, $M \sin i$ in Solar masses, and semi-major axis. 159

6.7 Corner plot of posterior sample distribution for BEBOP-1c orbital parameters; eccentricity, orbital period, semi-amplitude, argument of periastron, time of periastron passage, $M \sin i$ in Earth masses, and semi-major axis. 160

6.8 Hexbin plot denoting the density of ∼ 100 000 posterior samples obtained from four separate `kima` runs on BEBOP-1 Radial-Velocity (RV) data with N_p fixed = 1. The red line shows the calculated 99% detection limit, along with its associated error. Point 'c' indicates the position of detected planet BEBOP-1c, and point 'b' that of planet BEBOP-1b undetected in RV data alone. The orange line shows the detection limit on samples with eccentricity < 0.1 (the upper limit on BEBOP-1b's eccentricity (Kostov et al. 2020)). 161

6.9 Top: False Inclusion Probability (FIP) periodogram showing the clear detection of BEBOP-1c at ≈ 215 days. Bottom: True Inclusion Probability (TIP) periodogram showing the significance of any other peaks with TIP > 0.2. The second highest peak occurs at ≈ 756 days with a significance of 84%, a lower peak with significance of 27% is found at ≈ 97 days, corresponding to the period of BEBOP-1b. 162

6.10 Generalised Lomb-Scargle periodogram of BEBOP-1 spectroscopic data. The top panel shows the window function of the combined dataset (dark red). b, Periodogram of the radial-velocity measurements. c-g, Periodogram for Ca II, Hα, Na D, He I and Ca I index. The cyan, violet and orange curves corresponds to HARPS, ESPRESSO 2019 and ESPRESSO 2021/2022, respectively, and the dark red curves correspond to the combined dataset. The horizontal lines represent the bootstrapped false alarm probability levels of 10% (dotted), 1% (dashed), and 0.1% (dotted dash). The vertical solid lines indicate the binary period and planetary periods (P_b and P_c). 164

6.11 Radial velocity, Ca II, Hα, Na D, He I and Ca I timeseries for BEBOP-1. 165

6.12 Stability analysis of the BEBOP-1 system in the plane (e_c,e_b), assuming coplanar orbits. For fixed initial conditions (Table 1 main text), the parameter space of the system is explored by varying the eccentricities of both planets, with a step size of 0.001. For each initial condition, the system is integrated over 5000 yr and a stability indicator is calculated which involved a frequency analysis of the mean longitude of the inner planet (see text). Chaotic diffusion is indicated when the main frequency of the mean longitude varies in time. Yellow points correspond to highly unstable orbits, while purple points correspond to orbits which are likely to be stable on a billion-years timescales. 167

6.13 Stability analysis of the BEBOP-1 system in the plane (P_b,e_b), assuming coplanar orbits. For fixed initial conditions (Table 1 main text), the parameter space of the system is explored by varying the orbital period P_b and the eccentricity e_b of the inner planet. The step size is 0.4 day in orbital period and 0.002 in eccentricity. The black dot gives the best fit parameters for the inner planet Kostov et al. (2020). The color codes are the same from Figure 7, the dashed black lines indicate resonances with the binary, and the solid black lines resonances with the outer planet BEBOP-1c. 168

6.14 Stability analysis of the BEBOP-1 system in the plane (Ω_c,I_c). For fixed initial conditions (Table 1 main text), the parameter space of the system is explored by varying the inclination I_c and the longitude of the node Ω_c of the outer planet, with a step size of 1°. The black dot gives the best fit parameters, while the dashed circle corresponds to mutual inclinations equal to 40°. The color codes are the same from Figure 7. 170
6.15 Evolution of the mass versus semimajor axes for the best matching simulated planetary system formed through pebble accretion to BEBOP-1. Black dots represent the final masses and locations of the planets, whilst the red triangle and plus show the observed locations of BEBOP-1b and 1c respectively. The black dashed line denotes the stability limit for the system (Holman & Wiegert 1999). 177
6.16 A mass versus semimajor axes plot showing all planets formed in simulations. Different colour points show the initial metallicity of the sytems, whilst the grey points show planets there were lost, either through accretion into other planets, or ejection from the system. BEBOP-1b and 1c are denoted by the black triangle and plus symbols. The black dashed line denotes the stability limit for the system (Holman & Wiegert 1999). 178
6.17 Transmission spectroscopy metric as a function of equilibrium temperature for planets with measured masses. Planets are coloured according to their size range, with BEBOP-1b plotted as a yellow star as it falls into the sub-Jovian regime of $4.0 < R_p < 10R_\oplus$. In both panels we show in light green the position of the temperate zone between 200 – 300K. In the right hand panel we zoom in on the vicinity of BEBOP-1b and indicate with a black arrow the range of possible TSMs for a mass down to $10M_\oplus$. Data for this plot was retrieved from the NASA Exoplanet Archive (Akeson et al. 2013) on May 18th 2022. 180
6.18 Plot of the phase folded CCF curves from the 20 DDT ESPRESSO observations of SB1 J0608-59/BEBOP-1. Each row corresponds to a different observation with an arbitrary offset applied. The phased motion of the primary star around the systemic velocity of the system can be seen by the Gaussian dips in each line. Red crosses mark the expected velocity of the secondary stars CCF signal. 186
6.19 Master CCF plot calculated from taking the median of the 20 DDT ESPRESSO observations of SB1 J0608-59/BEBOP-1 seen in Figure 6.18 centered at a radial velocity of 0 km s^{-1}. . . . 186
6.20 Plot of the phase folded residual CCF curves after having subtracted the 'master' CCF from the 20 DDT ESPRESSO observations of SB1 J0608-59/BEBOP-1. Each row corresponds to a different observation with an arbitrary offset applied. Red crosses mark the expected velocity of the secondary star's CCF signal, the CCF's have been moved to the secondary stars reference frame. 187

6.21 Secondary master CCF plot calculated from taking the median of the 20 DDT ESPRESSO observations of SB1 J0608-59/BEBOP-1 seen in Figure 6.20 centered at a radial velocity of 0 $\mathrm{km\,s^{-1}}$. The red line shows the zero velocity reference frame of the secondary star, where the secondary star's CCF is expected to be seen. No signal from the secondary star (BEBOP-1B) can be seen. 187

List of Tables

1.1 Orbital parameters for discovered circumbinary planets and their binary hosts. 33

2.1 Table of Bayes Factors (BF) along with corresponding probability, sigma values (standard deviations away from the mean of a normal distribution), and the "Jeffreys' scale" from Standing et al. (2022); Trotta (2008). 45

3.1 Stellar model settings for the different teams. A single entry is used where all three teams used the same input physics. 63
3.2 Model parameters for λ^2 For using seismic and non-seismic constraints. 63
3.3 Best-fit orbital parameters of λ^2 For b 65
3.4 Oscillation frequencies with angular degree l of λ^2 For 69
3.5 Literature sources for T_{eff} and log g values shown in Fig.4 70
3.6 HARPS observing program PIs and IDs for data used in this work. 70

4.1 Updated binary, system and derived parameters for the investigated binary systems. Uncertainties are given in the brackets, as the last two significant figures, except for $\sigma_{\rm jit}$ where uncertainties can be significantly asymmetric. 94
4.2 Table of Bayes Factors (BF) along with corresponding probability, sigma values (standard deviations away from the mean of a normal distribution), and the "Jeffreys' scale" adapted from Trotta (2008). 95
4.3 Prior distributions used in RV model for binary and planetary signals in `kima` 95
4.4 J0310-31 Keplerian insertion and recovery results 105
4.5 J0310-31 Rebound simulated N-body insertion and recovery results 105
4.6 J1540-09 Keplerian insertion and recovery results 105
4.7 J1928-38 Keplerian insertion and recovery results 105
4.8 Occurrence rates for circumbinary planets calculated in Armstrong et al. (2014), and the SPOTS survey (Asensio-Torres et al. 2018), compared to this work in the upper two tables. Occurrence rates of gas giant planets orbiting single stars calculated in Cumming et al. (2008), and Wittenmyer et al. (2020), compared to this work in the lower two tables. All occurrence rates below are calculated at with a 95% confidence limit. 114

5.1 Results of our analysis of the SOPHIE radial velocities only, after removing outliers, that show the fit's Jacobi parameters and their derived physical parameters. They are compared to previous results with 1σ uncertainties provided in the form of the last two significant digits, within brackets. Dates are given in BJD - 2,450,000. We adopt the KIMA column as our results. 122

5.2 Journal of Observations containing our SOPHIE data. Flags indicate whether the measurement are excluded from our fiducial analysis with the following reason: W, wrong star; B, bisector outlier; U, high uncertainty; O, other. Dates are given in BJD - 2,400,000. $V_{\rm rad}$ are the measured radial velocities with their uncertainties $\sigma_{V_{\rm rad}}$. FWHM is the Full With at Half Maximum of the Gaussian fitted to the cross correlation function, and *contrast* is its amplitude. Bis. span is the span of the bisector slope. Uncertainties on FWHM and bis. span are $2 \times \sigma_{V_{\rm rad}}$. H$\alpha$ is the equivalent width of Hα, and its uncertainty σ_{H_α}. 126

6.1 BEBOP-1 system orbital parameters from our analysis of the ESPRESSO and HARPS radial velocities, after removing outliers. 1σ uncertainties are provided as the last two significant digits, within brackets. Dates are given in BJD - 2,450,000. * from Kostov et al. (2020), ** from Triaud et al. (2017). 143

6.2 Prior distributions for the binary and planetary RV model signals in `kima` 155

Bibliography

ALMA Partnership et al., 2015, ApJ, 808, L3

Agol E., Fabrycky D. C., 2018, in Deeg H. J., Belmonte J. A., eds, , Handbook of Exoplanets. p. 7, doi:10.1007/978-3-319-55333-7_7

Akeson R. L., et al., 2013, PASP, 125, 989

Alibert Y., Mordasini C., Benz W., 2004, A&A, 417, L25

Anglada-Escudé G., López-Morales M., Chambers J. E., 2010, ApJ, 709, 168

Armstrong D. J., Osborn H. P., Brown D. J. A., Faedi F., Gómez Maqueo Chew Y., Martin D. V., Pollacco D., Udry S., 2014, MNRAS, 444, 1873

Arras P., Burkart J., Quataert E., Weinberg N. N., 2012, MNRAS, 422, 1761

Asensio-Torres R., et al., 2018, A&A, 619, A43

Baştürk Ö., Dall T. H., Collet R., Lo Curto G., Selam S. O., 2011, A&A, 535, A17

Bailey V., et al., 2014, ApJ, 780, L4

Baliunas S. L., Donahue R. A., Soon W., Henry G. W., 1998, in Donahue R. A., Bookbinder J. A., eds, Astronomical Society of the Pacific Conference Series Vol. 154, Cool Stars, Stellar Systems, and the Sun. p. 153

Baranne A., et al., 1996, A&AS, 119, 373

Barragán O., Gandolfi D., Antoniciello G., 2019, MNRAS, 482, 1017

Bashi D., Zucker S., Adibekyan V., Santos N. C., Tal-Or L., Trifonov T., Mazeh T., 2020, A&A, 643, A106

Bayes T., Price M., 1763, Philosophical Transactions, 53, 370

Bean J. L., Raymond S. N., Owen J. E., 2021, Journal of Geophysical Research (Planets), 126, e06639

Beaugé C., Nesvorný D., 2012, ApJ, 751, 119

Beavers W. I., Herczeg T. J., Lui A., 1986, ApJ, 300, 785

Benedict G. F., Harrison T. E., 2017, AJ, 153, 258

Bennett D. P., et al., 2016, AJ, 152, 125

Berdyugina S. V., 2005, Living Reviews in Solar Physics, 2, 8

Beuermann K., et al., 2010, A&A, 521, L60

Bodenheimer P., Hubickyj O., Lissauer J. J., 2000, Icarus, 143, 2

Boisvert J. H., Nelson B. E., Steffen J. H., 2018, MNRAS, 480, 2846

Bonavita M., Desidera S., Thalmann C., Janson M., Vigan A., Chauvin G., Lannier J., 2016, A&A, 593, A38

Borucki W. J., Summers A. L., 1984, Icarus, 58, 121

Borucki W. J., et al., 2010, in American Astronomical Society Meeting Abstracts #215. p. 101.01

Borucki W. J., et al., 2012, ApJ, 745, 120

Bouchy F., Queloz D., 2007, in Afonso C., Weldrake D., Henning T., eds, Astronomical Society of the Pacific Conference Series Vol. 366, Transiting Extrapolar Planets Workshop. p. 193

Bourrier V., et al., 2018, A&A, 619, A1

Brewer B. J., Foreman-Mackey D., 2016, arXiv e-prints, p. arXiv:1606.03757
Brewer B. J., Pártay L. B., Csányi G., 2009, arXiv e-prints, p. arXiv:0912.2380
Brewer B. J., Pártay L. B., Csányi G., 2011, Statistics and Computing, 21, 649
Bryan M. L., Knutson H. A., Lee E. J., Fulton B. J., Batygin K., Ngo H., Meshkat T., 2019, AJ, 157, 52
Bryson S., et al., 2021, AJ, 161, 36
Buchhave L. A., et al., 2012, Nature, 486, 375
Cabrera J., et al., 2014, ApJ, 781, 18
Chachan Y., et al., 2020, AJ, 160, 201
Chambers J., 2010, in Seager S., ed., , Exoplanets. pp 297–317
Correia A. C. M., Udry S., Mayor M., Laskar J., Naef D., Pepe F., Queloz D., Santos N. C., 2005, A&A, 440, 751
Croll B., et al., 2017, ApJ, 836, 82
Cumming A., Butler R. P., Marcy G. W., Vogt S. S., Wright J. T., Fischer D. A., 2008, PASP, 120, 531
D'Angelo G., Durisen R. H., Lissauer J. J., 2010, in Seager S., ed., , Exoplanets. pp 319–346
Dawson R. I., Johnson J. A., 2018, ARA&A, 56, 175
Dawson R. I., Murray-Clay R. A., 2013, ApJ, 767, L24
Delorme P., et al., 2013, A&A, 553, L5
Delrez L., et al., 2018, in Marshall H. K., Spyromilio J., eds, Society of Photo-Optical Instrumentation Engineers (SPIE) Conference Series Vol. 10700, Ground-based and Airborne Telescopes VII. p. 107001I (arXiv:1806.11205), doi:10.1117/12.2312475
Delrez L., et al., 2022, arXiv e-prints, p. arXiv:2209.02831
Doyle L. R., et al., 2011, Science, 333, 1602
Doyle A. P., Davies G. R., Smalley B., Chaplin W. J., Elsworth Y., 2014, MNRAS, 444, 3592
Dransfield G., et al., 2022, MNRAS,
Dumusque X., et al., 2015, ApJ, 814, L21
Duquennoy A., Mayor M., 1991, How Many Single Stars Among Solar Type Stars?. pp 39–43, doi:10.1007/3-540-54752-5_186
Dvorak R., Froeschle C., Froeschle C., 1989, A&A, 226, 335
Edwards B., et al., 2019, Experimental Astronomy, 47, 29
Esa ., 1997, VizieR Online Data Catalog, p. I/239
Fabrycky D., Tremaine S., 2007, ApJ, 669, 1298
Faria J. P., Santos N. C., Figueira P., Brewer B. J., 2018, The Journal of Open Source Software, 3, 487
Faria J. P., et al., 2020, A&A, 635, A13
Faria J. P., et al., 2022, A&A, 658, A115
Fauchez T. J., et al., 2019, ApJ, 887, 194
Fischer D. A., Valenti J., 2005, ApJ, 622, 1102
Ford E. B., Joshi K. J., Rasio F. A., Zbarsky B., 2000, ApJ, 528, 336
Foreman-Mackey D., 2016, The Journal of Open Source Software, 1, 24
Fulton B. J., et al., 2017, AJ, 154, 109
Fulton B. J., Petigura E. A., Blunt S., Sinukoff E., 2018, PASP, 130, 044504
Gaia Collaboration et al., 2016, A&A, 595, A1
Gardner J. P., et al., 2006, Space Sci. Rev., 123, 485
Gaudi B., 2010, Microlensing by Exoplanets. pp 79–110
Gill S., et al., 2019, A&A, 626, A119

Gillon M., Jehin E., Magain P., Chantry V., Hutsemékers D., Manfroid J., Queloz D., Udry S., 2011, in European Physical Journal Web of Conferences. p. 06002 (arXiv:1101.5807), doi:10.1051/epjconf/20101106002

Gillon M., et al., 2017, Nature, 542, 456

Gliese W., 1957, Astronomisches Rechen-Institut Heidelberg Mitteilungen Serie A, 8, 1

Gomes da Silva J., Santos N. C., Bonfils X., Delfosse X., Forveille T., Udry S., 2011, A&A, 534, A30

Gómez Maqueo Chew Y., et al., 2014, A&A, 572, A50

Gonzalez G., 1997, MNRAS, 285, 403

Gray D. F., 2008, The Observation and Analysis of Stellar Photospheres

Greaves J. S., et al., 2021, Nature Astronomy, 5, 655

Greene T. P., Line M. R., Montero C., Fortney J. J., Lustig-Yaeger J., Luther K., 2016, ApJ, 817, 17

Gregory P. C., 2005, ApJ, 631, 1198

Guillot T., et al., 2015, Astronomische Nachrichten, 336, 638

Guinan E. F., Ribas I., 2001, ApJ, 546, L43

Haisch Karl E. J., Lada E. A., Lada C. J., 2001, ApJ, 553, L153

Hardy A., et al., 2015, ApJ, 800, L24

He M. Y., Triaud A. H. M. J., Gillon M., 2017, MNRAS, 464, 2687

Hebb L., et al., 2009, ApJ, 693, 1920

Hilditch R. W., 2001, An Introduction to Close Binary Stars

Hogg D. W., Foreman-Mackey D., 2018, ApJS, 236, 11

Hogg D. W., Bovy J., Lang D., 2010, arXiv e-prints, p. arXiv:1008.4686

Holl B., et al., 2022, arXiv e-prints, p. arXiv:2206.05439

Holman M. J., Wiegert P. A., 1999, AJ, 117, 621

Horner J., Wittenmyer R., Hinse T., Marshall J., Mustill A., 2014, arXiv e-prints, p. arXiv:1401.6742

Howard A. W., et al., 2010, Science, 330, 653

Howard A. W., et al., 2012, ApJS, 201, 15

Hsu D. C., Ford E. B., Ragozzine D., Ashby K., 2019, AJ, 158, 109

Huang C., Wu Y., Triaud A. H. M. J., 2016, ApJ, 825, 98

Izidoro A., Raymond S. N., 2018, in Deeg H. J., Belmonte J. A., eds, , Handbook of Exoplanets. p. 142, doi:10.1007/978-3-319-55333-7_142

Jeffreys H., 1946, Proceedings of the Royal Society of London Series A, 186, 453

Jeffreys H., 1961, Theory of probability. Oxford University Press

Jenkins J. M., et al., 2015, AJ, 150, 56

Kass R. E., Raftery A. E., 1995, Journal of the American Statistical Association, 90, 773

Kasting J. F., Whitmire D. P., Reynolds R. T., 1993, Icarus, 101, 108

Kepler J., 1609, Astronomia nova.

Kipping D. M., 2009, MNRAS, 392, 181

Kipping D. M., 2013, MNRAS, 434, L51

Kley W., Haghighipour N., 2014, A&A, 564, A72

Konacki M., 2005, ApJ, 626, 431

Konacki M., Muterspaugh M. W., Kulkarni S. R., Hełminiak K. G., 2009, ApJ, 704, 513

Konacki M., Muterspaugh M. W., Kulkarni S. R., Hełminiak K. G., 2010, ApJ, 719, 1293

Kopal Z., 1980a, Ap&SS, 70, 329

Kopal Z., 1980b, Ap&SS, 71, 65

Kopeikin S. M., Ozernoy L. M., 1999, ApJ, 523, 771
Kostov V. B., Mccullough P. R., Hinse T. C., Tsvetanov Z. I., Hébrard G., Díaz R. F., Deleuil M., Valenti J. A., 2013, The Astrophysical Journal, 770, 52
Kostov V. B., et al., 2014, The Astrophysical Journal, 784, 14
Kostov V. B., et al., 2016, The Astrophysical Journal, 827, 86
Kostov V. B., et al., 2020, AJ, 159, 253
Kostov V. B., et al., 2021, arXiv e-prints, p. arXiv:2105.08614
Kumaraswamy P., 1980, Journal of Hydrology, 46, 79
Lagrange A. M., et al., 2016, A&A, 586, L8
Lambrechts M., Johansen A., 2012, A&A, 544, A32
Latham D. W., et al., 2011, ApJ, 732, L24
Lendl M., et al., 2020, MNRAS, 492, 1761
Libby-Roberts J. E., et al., 2020, AJ, 159, 57
Lin D. N. C., Papaloizou J., 1986, ApJ, 309, 846
Lin D. N. C., Bodenheimer P., Richardson D. C., 1996, Nature, 380, 606
Lines S., Leinhardt Z. M., Paardekooper S., Baruteau C., Thebault P., 2014, ApJ, 782, L11
Lissauer J. J., Stevenson D. J., 2007, in Reipurth B., Jewitt D., Keil K., eds, Protostars and Planets V. p. 591
Lovis C., Fischer D., 2010, in Seager S., ed., , Exoplanets. pp 27–53
Lovis C., Pepe F., 2007, A&A, 468, 1115
Lubow S. H., Ida S., 2010, in Seager S., ed., , Exoplanets. pp 347–371
Lucas G., Hammill M., Ford H., Fischer C., et al., 1977, Star Wars IV - A New Hope, Lucasfilm Ltd., 20th Century Fox
Luque R., Pallé E., 2022, arXiv e-prints, p. arXiv:2209.03871
Lustig-Yaeger J., Meadows V. S., Lincowski A. P., 2019, AJ, 158, 27
MacKay D. J., Mac Kay D. J., et al., 2003, Information theory, inference and learning algorithms. Cambridge university press
Mardling R. A., Aarseth S. J., 2001, MNRAS, 321, 398
Marois C., Zuckerman B., Konopacky Q. M., Macintosh B., Barman T., 2010, Nature, 468, 1080
Marsh T. R., et al., 2014, MNRAS, 437, 475
Martin D., 2017a, PhD thesis, https://nbn-resolving.org/urn:nbn:ch:unige-963253
Martin D. V., 2017b, MNRAS, 465, 3235
Martin D. V., 2018, Populations of Planets in Multiple Star Systems. p. 156, doi:10.1007/978-3-319-55333-7_156
Martin D. V., Fitzmaurice E., 2022, MNRAS,
Martin D. V., Triaud A. H. M. J., 2014, A&A, 570, A91
Martin D. V., Triaud A. H., 2015, MNRAS, 449, 781
Martin D. V., et al., 2019, A&A, 624, A68
Mayor M., Queloz D., 1995, Nature, 378, 355
Mayor M., et al., 2003, The Messenger, 114, 20
Mayor M., et al., 2011, arXiv e-prints, p. arXiv:1109.2497
McInnes L., Healy J., Astels S., 2017, The Journal of Open Source Software, 2
McLaughlin D. B., 1924, ApJ, 60, 22
Meschiari S., 2012, ApJ, 752, 71
Morbidelli A., Raymond S. N., 2016, Journal of Geophysical Research (Planets), 121, 1962

Morbidelli A., Lunine J. I., O'Brien D. P., Raymond S. N., Walsh K. J., 2012, Annual Review of Earth and Planetary Sciences, 40, 251

Mugrauer M., Neuhäuser R., Mazeh T., Guenther E., Fernández M., Broeg C., 2006, Astronomische Nachrichten, 327, 321

Mulders G. D., Pascucci I., Apai D., 2015, ApJ, 798, 112

Murray C. D., Correia A. C. M., 2010, in Seager S., ed., , Exoplanets. pp 15–23

Mustill A. J., Marshall J. P., Villaver E., Veras D., Davis P. J., Horner J., Wittenmyer R. A., 2013, MNRAS, 436, 2515

Nagasawa M., Ida S., Bessho T., 2008, ApJ, 678, 498

Nelson R. P., 2003, MNRAS, 345, 233

Neveu-VanMalle M., et al., 2014, A&A, 572, A49

Nielsen M. B., et al., 2020, A&A, 641, A25

Ormel C. W., Ida S., Tanaka H., 2012, ApJ, 758, 80

Orosz J. A., et al., 2012a, Science, 337, 1511

Orosz J. A., et al., 2012b, ApJ, 758, 87

Orosz J. A., et al., 2019, AJ, 157, 174

Owen J. E., Wu Y., 2013, ApJ, 775, 105

Owen J. E., Wu Y., 2017, ApJ, 847, 29

Paardekooper S.-J., Leinhardt Z. M., Thébault P., Baruteau C., 2012, ApJ, 754, L16

Penzlin A. B. T., Kley W., Nelson R. P., 2021, A&A, 645, A68

Pepe F., et al., 2002, The Messenger, 110, 9

Pepe F., et al., 2021, A&A, 645, A96

Perruchot S., et al., 2008, in McLean I. S., Casali M. M., eds, Society of Photo-Optical Instrumentation Engineers (SPIE) Conference Series Vol. 7014, Ground-based and Airborne Instrumentation for Astronomy II. p. 70140J, doi:10.1117/12.787379

Petigura E. A., 2015, PhD thesis, University of California, Berkeley

Pierens A., Nelson R. P., 2013, A&A, 556, A134

Pierens A., Nelson R. P., 2018, MNRAS, 477, 2547

Pierens A., McNally C. P., Nelson R. P., 2020, MNRAS, 496, 2849

Pinhas A., Madhusudhan N., Clarke C., 2016, MNRAS, 463, 4516

Pollacco D. L., et al., 2006, PASP, 118, 1407

Queloz D., et al., 2001a, The Messenger, 105, 1

Queloz D., et al., 2001b, A&A, 379, 279

Quirrenbach A., 2010, Astrometric Detection and Characterization of Exoplanets. pp 157–174

Raghavan D., et al., 2010, ApJS, 190, 1

Rappaport S., Sanchis-Ojeda R., Rogers L. A., Levine A., Winn J. N., 2013, ApJ, 773, L15

Rauer H., et al., 2014, Experimental Astronomy, 38, 249

Raymond S. N., 2006, ApJ, 643, L131

Raymond S. N., Izidoro A., 2017, Icarus, 297, 134

Raymond S. N., Kokubo E., Morbidelli A., Morishima R., Walsh K. J., 2014, in Beuther H., Klessen R. S., Dullemond C. P., Henning T., eds, Protostars and Planets VI. p. 595 (arXiv:1312.1689), doi:10.2458/azu_uapress_9780816531240-ch026

Ricker G. R., et al., 2015, Journal of Astronomical Telescopes, Instruments, and Systems, 1, 14003

Roberge A., Kamp I., 2010, in Seager S., ed., , Exoplanets. pp 269–295

Rosenthal L. J., et al., 2021, arXiv e-prints, p. arXiv:2112.03399

Rossiter R. A., 1924, ApJ, 60, 15

Roy A., Chakraborty A., Mahadevan S., Chaturvedi P., Prasad N. J. S. S. V., Shah V., Pathan F. M., Anandarao B. G., 2016, in Evans C. J., Simard L., Takami H., eds, Society of Photo-Optical Instrumentation Engineers (SPIE) Conference Series Vol. 9908, Ground-based and Airborne Instrumentation for Astronomy VI. p. 99086R (arXiv:1607.06485), doi:10.1117/12.2232833

Santos N. C., et al., 2002, A&A, 392, 215

Santos N. C., Israelian G., Mayor M., 2004, A&A, 415, 1153

Schneider J., 1994, Planet. Space Sci., 42, 539

Schwamb M. E., et al., 2013, The Astrophysical Journal, 768, 127

Seager S., Lissauer J. J., 2010, Introduction to Exoplanets. pp 3–13

Seager S., Sasselov D. D., 2000, ApJ, 537, 916

Sebastian D., et al., 2022, MNRAS,

Sigurdsson S., Stairs I. H., Moody K., Arzoumanian K. M. Z., Thorsett S. E., 2008, in Fischer D., Rasio F. A., Thorsett S. E., Wolszczan A., eds, Astronomical Society of the Pacific Conference Series Vol. 398, Extreme Solar Systems. p. 119

Skilling J., 2006, Bayesian analysis, 1, 833

Slawson R. W., et al., 2011, AJ, 142, 160

Socia Q. J., et al., 2020, AJ, 159, 94

Sousa-Silva C., Seager S., Ranjan S., Petkowski J. J., Zhan Z., Hu R., Bains W., 2020, Astrobiology, 20, 235

Sousa S. G., et al., 2008, A&A, 487, 373

Standing M. R., et al., 2022, MNRAS, 511, 3571

Stassun K. G., et al., 2018, AJ, 156, 102

Steffen J. H., et al., 2012, Proceedings of the National Academy of Science, 109, 7982

Strassmeier K. G., 2009, A&ARv, 17, 251

Swayne M. I., et al., 2021, arXiv e-prints, p. arXiv:2106.07276

Sybilski P., Konacki M., Kozłowski S. K., Hełminiak K. G., 2013, MNRAS, 431, 2024

Thalmann C., et al., 2014, A&A, 572, A91

Thorsett S. E., Arzoumanian Z., Camilo F., Lyne A. G., 1999, ApJ, 523, 763

Tinetti G., et al., 2007, Nature, 448, 169

Tinetti G., et al., 2018, Experimental Astronomy, 46, 135

Traub W., Oppenheimer B., 2010, Direct Imaging of Exoplanets. pp 111–156

Triaud A. H. M. J., 2018, The Rossiter-McLaughlin Effect in Exoplanet Research. p. 2, doi:10.1007/978-3-319-55333-7_2

Triaud A. H. M. J., et al., 2013, A&A, 549, A18

Triaud A. H., et al., 2017, A&A, 608, A129

Triaud A. H. M. J., et al., 2022, MNRAS, 511, 3561

Trotta R., 2008, Contemporary Physics, 49, 71

Tuomi M., Jones H. R. A., Barnes J. R., Anglada-Escudé G., Jenkins J. S., 2014, MNRAS, 441, 1545

Vallenari A., et al., 2022, Gaia DR3 documentation Chapter 19: Performance verification, Gaia DR3 documentation, European Space Agency; Gaia Data Processing and Analysis Consortium, id. 19

Van Eylen V., Agentoft C., Lundkvist M. S., Kjeldsen H., Owen J. E., Fulton B. J., Petigura E., Snellen I., 2018,

MNRAS, 479, 4786
Vanderburg A., et al., 2015, Nature, 526, 546
Venturini J., Guilera O. M., Haldemann J., Ronco M. P., Mordasini C., 2020, A&A, 643, L1
Veras D., 2016, Royal Society Open Science, 3, 150571
Ward W. R., 1997, Icarus, 126, 261
Weiss L. M., et al., 2018, AJ, 155, 48
Welsh W. F., et al., 2012, Nature, 481, 475
Welsh W. F., Orosz J. A., Carter J. A., Fabrycky D. C., 2014, in Haghighipour N., ed., Vol. 293, Formation, Detection, and Characterization of Extrasolar Habitable Planets. pp 125–132 (arXiv:1308.6328), doi:10.1017/S1743921313012684
Welsh W. F., et al., 2015, ApJ, 809, 26
Winn J., 2010, Exoplanet Transits and Occultations. pp 55–77
Winn J. N., Fabrycky D. C., 2015, ARA&A, 53, 409
Winn J. N., et al., 2011, ApJ, 741, L1
Wittenmyer R. A., et al., 2013, ApJS, 208, 2
Wittenmyer R. A., Bergmann C., Horner J., Clark J., Kane S. R., 2019, MNRAS, 484, 4230
Wittenmyer R. A., et al., 2020, MNRAS, 492, 377
Wolszczan A., 1994, Science, 264, 538
Wolszczan A., Frail D. A., 1992, Nature, 355, 145
Zucker S., Alexander T., 2007, ApJ, 654, L83
von Boetticher A., et al., 2017, A&A, 604, L6